DEVELOPMENT OF HIGH TEMPERATURE CREEP RESISTANT ALUMINIUM BASED SAND CAST MAGNESIUM ALLOYS

A THESIS SUBMITTED TO
THE GRADUATE SCHOOL OF NATURAL AND APPLIED SCIENCES
OF
MIDDLE EAST TECHNICAL UNIVERSITY

BY

EMRAH YALINIZ

IN PARTIAL FULFILLMENT OF THE REQUIREMENTS
FOR
THE DEGREE OF MASTER OF SCIENCE
IN
METALLURICAL AND MATERIALS ENGINEERING

JUNE 2018

Approval of the thesis:

DEVELOPMENT OF HIGH TEMPERATURE CREEP RESISTANT ALUMINIUM BASED SAND CAST MAGNESIUM ALLOYS

Submitted by **EMRAH YALINIZ** in partial fulfillment of the requirements for the degree of **Master of Science in Metallurgical and Materials Engineering Department, Middle East Technical University** by,

Prof. Dr. Halil Kalıpçılar
Dean, Graduate School of **Natural and Applied Sciences** _____

Prof. Dr. Hakan Gür
Head of Department, **Metallurgical and Materials Engineering** _____

Prof. Dr. Ali Kalkanlı
Supervisor, **Metallurgical and Materials Eng. Dept., METU** _____

Examining Committee Members:

Prof. Dr. Fahrettin Öztürk
Mechanical Eng. Dept., Ankara Yıldırım Beyazıt University _____

Prof. Dr. Ali Kalkanlı
Metallurgical and Materials Engineering Dept., METU _____

Prof. Dr. İshak Karakaya
Metallurgical and Materials Engineering Dept., METU _____

Prof. Dr. Rıza Gürbüz
Metallurgical and Materials Engineering Dept., METU _____

Prof. Dr. Zafer Evis
Department of Engineering Sciences, METU _____

Date: 13.06.2018

I hereby declare that all information in this document has been obtained and presented in accordance with academic rules and ethical conduct. I also declare that, as required by these rules and conduct, I have fully cited and referenced all material and results that are not original to this work.

Name, Last name: Emrah YALINIZ

Signature:

ABSTRACT

DEVELOPMENT OF HIGH TEMPERATURE CREEP RESISTANT ALUMINIUM BASED SAND CAST MAGNESIUM ALLOYS

Yalınız, Emrah

M.S., Department of Metallurgical and Materials Engineering Department

Supervisor: Prof. Dr. Ali Kalkanlı

June 2018, 213 pages

The aim of this thesis is to develop alternative sand casting aluminum based magnesium alloys to substitute current sand castable helicopter transmission housing magnesium alloys such as ZE41A and EV31A. AZ91 magnesium alloy has also been preferred for helicopter transmission housing material. However, the lower creep resistance above 120 ^{o}C due to the presence of β-($Mg_{17}Al_{12}$) phase in the microstructure and showing varying mechanical properties in different section thicknesses limit the usage of AZ91 in the modern helicopter transmission housings. This thesis has been aimed to eliminate these disadvantages of AZ91 alloy by adding different alloying elements.

The aim of alloying elements e.g. Si, Sr, Ca and Sn addition to AZ91 alloy is to form high temperature creep resistant phases in the microstructure and decrease casting defects such as interdendritic porosity in order to obtain desired mechanical properties. Although simultaneous addition of 0.7 % Si, 0.5 % Ca and 0.9 % Sn addition to AZ91 alloy decreases the grain size, porosity percentage of the alloy is higher than even that of AZ91 alloy, which causes reduction of tensile test results. The test results show simultaneous addition of 0.7 % Si, 0.4 % Sr, 0.6 % Sn elements

together with 0.1 % Al-5Ti-1B to AZ91 alloy results in higher tensile test results in comparison to ZE41A and AZ91 magnesium alloys. The decrease in volume fraction of β-($Mg_{17}Al_{12}$) phase network was achieved with addition of Sr and Sn elements to obtain a high creep resistant magnesium alloy. The elements like Sr and Sn provide the modification of mechanically detrimental "Chinese script" morphology of Mg_2Si to polygonal and square-like shape, which is beneficial both at room and elevated temperature properties. The test results indicate the structural integrity in variable casting thicknesses achieved after the alloying elements (0.7 % Si, 0.4 % Sr and 0.6 % Sn) and grain refiner (0.1 % Al-5Ti-1B) addition to AZ91 alloy.

Keywords: Magnesium sand casting, modified Mg_2Si phase, magnesium transmission housings, creep resistant magnesium alloys

ÖZ

YÜKSEK SICAKLIK SÜRÜNME DİRENCİNE SAHİP KUMA DÖKÜM ALÜMİNYUM ESASLI MAGNEZYUM ALAŞIMLARININ GELİŞTİRİLMESİ

Yalınız, Emrah
M.S., Metalurji ve Malzeme Mühendisliği Bölümü
Tez Yöneticisi: Prof. Dr. Ali Kalkanlı
Haziran 2018, 213 sayfa

Bu tezin temel amacı, günümüzdeki helikopter güç aktarma sistemleri dişli kutularında kullanılmakta olup kum kalıba dökülebilen ZE41A ve EV31A magnezyum alaşımlarının yerine geçebilecek alüminyum içeren magnezyum alaşımlarını geliştirmektir. Geçmişte AZ91 magnezyum alaşımı da helikopter transmisyon mahfazalarında tercih edilmekteydi. Bununla birlikte, mikroyapısındaki β-($Mg_{17}Al_{12}$) fazının 120 ^{o}C üzerinde düşük sürünme sebep olması ve farklı kesit alanlarındaki çok değişken mekanik özellikler göstermesi AZ91 alaşımın modern helikopter transmisyon mahfazalarında kullanımı kısıtlamaktadır. Bu tez, AZ91 alaşımının bu dezavantajlarını farklı alaşım elementleri ekleyerek gidermek için oluşturulmuştur.

Si, Sr, Ca and Sn gibi alaşımlandırma elementlerinin AZ91 alaşımına eklenmesi, mikroyapıda yüksek sürünme direncine sahip fazların oluşması ve döküm hatalarını azaltarak istenen mekanik özellikleri elde etmek içindir. AZ91 alaşımına 0.7% Si, 0.5% Ca ve 0.9% Sn elementlerinin eklenmesi tane boyutunu azalırken, alaşımının

porozite yüzdesinin AZ91 alaşımından bile yüksek olması çekme testi sonuçlarında azalmaya neden olmaktadır. Test sonuçları, 0.7% Si, 0.4% Sr, 0.6% Sn elementlerine ek olarak 0.1% Al-5Ti-1B tane incelticinin AZ91 alaşımına birlikte eklenmesiyle ZE41A ve AZ91 alaşımlarına kıyasla daha yüksek çekme testi sonuçları elde edildiğini göstermiştir. Sr and Sn elementlerinin eklenmesiyle β-($Mg_{17}Al_{12}$) faz ağının azalması, daha yüksek sürünme direncine sahip bir magnezyum alaşımın elde edilmesi sağlamıştır. Sr and Sn gibi elementlerin mekanik olarak zararlı "Çin Yazısı" Mg_2Si morfolojisinin, oda ve yüksek sıcaklık özelliklerini iyileştiren poligonal ya da karemsi şekle modifikasyonunu sağlanmıştır. Test sonuçları AZ91 alaşımına eklenenen alaşım elementlerinin (0.7 % Si, 0.4% Sr ve 0.6% Sn) ve tane inceltinin (0.1% Al-5Ti-1B) farklı döküm kalınlıklarında yapısal bütünlüğü sağladığını göstermektedir.

Anahtar Kelimeler: Magnezyum kuma döküm, modifiye edilmiş Mg_2Si fazı, magnezyum transmisyon mahvazaları, sürünme dirençli magnezyum alaşımları

To My Family

&

To My Love,

İrem

ACKNOWLEDGEMENTS

Fistly and foremost, I would like to thank my supervisor, Prof. Dr. Ali Kalkanlı for his continuous guidance, support, and instruction. His kindness and thoughtfulness aided me in both my academic and personal endeavors.

I also have a great appreciation to the casting laboratory technican, Ali Osman Atik, for his help during experimental setup and procedures. Appreciation also goes to my colleague, Enver Burak Aldoğan, for his assistance during all steps of thesis from experimental setup to optical and scanning electron microscopy analysis. Without his help, this study would not be finished. I would also thank to Cemre Metin Poyraz and Kadir Özgün Köse for their support about scanning electron microscope analysis. For digital and real time radiography tests, special thanks to Tuğçe Kaleli and Fehmi Ümit Akçaoğlu, respectively, for their patience and support during the tests.

The financial support from the Undersecretariat of Turkish Defense under favour of "MÜGE Project" was necessary for completion of this dissertation and is well appreciated. I would like to express my appreciation to Turkish Aerospace Industries Inc. is greatly acknowledged for their suport.

I would express my gratitude to my parents, brother and sister whose support, patience and constant encouragement helped me throughout this study. My deepest appreciation is expressed to them for their love, understanding, and inspiration.

Finally, I would like to thank my love, İrem, for her lifelong love and support. Her constant encouragement helped me overcome the many difficulties I faced throughout my study. I could not have done it without her patience. My deepest

thanks to İrem for her patience when I was studying instead of spending time together.

TABLE OF CONTENTS

LIST OF TABLES

TABLES

LIST OF FIGURES

FIGURES

LIST OF SYMBOLS

Abbreviations

AMS	Aerosapce Material Specification
BCC	Body-Centered Cubic
CD	Continuous Decomposition
cm	Centimeter
d	Average Grain Size
dT/dt	Cooling Rate
DD	Discontinuous Decomposition
DSC	Differential Scanning Calorimetry
DTA	Differential Thermal Analysis
EDX (EDS)	Energy Dispersive X-ray
El.	Elongation
FCC	Face-Centered Cubic
FR	Freezing Range
GRF	Growth Restriction Factor
HCP	Hexagonal Close-Packed
HV	Vickers Hardness
ICP-AES	Inductively Coupled Plasma-Atomic Emission Spectrometry
LPP	Liquidus Peak Parameter where $d\theta/dt>0$
L_v	Latent Heat of Fusion Per Unit Volume
mm	Millimeter
METU	Middle East Technical University
MMPDS	Metallic Materials Properties Development Handbook
MPa	Megapascal
OM	Optical Microscope
SEM	Scanning Electron Microscope/Microscopy
TAI	Turkish Aerospace Industries, Inc.

T_E	Eutectic Temperature
T_L	Liquidus Temperature
T_m	Melting Point of the Liquid
t_{rec}	Duration of Recalescence
T_S	Solidus Temperature
UTS	Ultimate Tensile Strength
UC	Undercooling
YS	Yield Strength
wt. %	Weight Percent
ΔH	Change in Enthalpy
ΔS	Change in Entropy
ΔG_v	Net Bulk Free Energy
θ_n	Initial Temperature Primary Dendrites Nucleation
θ_{min}	Unsteady State Growth Temperature
θ_g	Recalescence of Steady State Growth Temperature
$\Delta\theta_{rec}$	Recalescence Undercooling
ΔG_r	Total Free Energy Change
ΔT	Temperature Difference

Elements

Al	Aluminium
B	Boron
Be	Beryllium
C	Carbon
Ca	Calcium
Ce	Cerium
Cl	Chlorine
Cu	Copper
F	Fluorine

Fe	Iron
La	Lanthanum
Mg	Magnesium
Mn	Manganese
Nd	Neodymium
Ni	Nickel
O	Oxygen
Pr	Praseodymium
Sb	Antimony
Si	Silicon
Sr	Strontium
Ti	Titanium
V	Vanadium
Zn	Zinc
Zr	Zirconium

Greek Symbols

σ_y	Yield Strength
σ_0	Friction Stress
k_y	Locking Parameter
ε	Cooling Rate
r_c	Critical Nucleus Radius
m	Slope of the Liquidus Line
k	Equilibrium Partition Coefficient
C_0	Initial Solute Concentration in the Melt
μ	Micron
r^*	Critical Nucleus
δ	Planar Disregistry Factor
γ_{ml}	Interfacial Surface Tension Between Mould and Liquid

γ_{sm}	Interfacial Surface Tension Between Solid and Mould
γ_{sl}	Interfacial Surface Tension Between Solid and Liquid Interface
θ	Wetting Angle
ΔG^*_{homo}	The Necessary Energy for Homogeneous Nucleation
θ_d	Angle Between Two Low Index Directions in (hkl)
$d_{[uvw]}$	Lattice Spacing in the Direction of $[uvw]$

CHAPTER 1

INTRODUCTION

1.1 Background and Objectives

The need for light weighting of transportation system has been a governing focus in materials design and production. The largest impact of light weighting components in aerospace and automotive industries is known as in structural and powertrain parts. These parts could be made from magnesium (Mg), aluminum (Al) or steel in accordance with their requirements. Due to the very high strength to density ratio, magnesium is an inevitable alternative in these components used in aerospace and automotive industries to reduce weight. Based on this issue, there has been a competition between aluminum and magnesium in castings used in these industries. In addition, this contest is also valid in between magnesium alloys to substitute one another.

This investigation is focused on promising magnesium alloys used in powertrain casings of helicopter power transmission systems as an alternative to commercial magnesium alloys and a substitution of current aluminum alloys. Moreover, the studied magnesium alloys could also be seen as a candidate for automotive powertrain casting applications due to some similar material requirements for helicopter powertrain casings.

The trend in powertrain components has been focused on the substitution of low cost and fulfilling the room and elevated temperature magnesium alloys for steel and

aluminum components [1,2]. This trend has revived the studies on the development of magnesium alloys containing different alloying elements such as aluminum, alkaline earth and rare earth additions [3]. Although there are several studies have been examined the microstructure and creep behavior with different alloying elements, there is a limited understanding of the influence of alloying additions on solidification characteristics, castability, microstructure and radiographic quality.

The main focus for a substitution or developing of a magnesium alloy for powertrain applications is related with fulfilling the desired mechanical properties, which includes the room temperature, high temperature creep and fatigue properties. These requirements shall be thought as together for the usage of powertrain casing material for the substitution of an existing one. This necessity has stimulated the development of several candidate magnesium alloys for powertrain applications that contain several alloying elements such as Al, Si, Sr, Ca, Sb Sn, Bi, and RE. Although many investigations have been conducted related with the microstructure, mechanical and creep behavior of several magnesium alloys for the case by case, there remains limited understanding of the element additions on these properties together. The element selections and their amounts in this study were selected based on the literature review and experimental results to achieve optimum mechanical and metallurgical properties. Due to these reasons, the promising magnesium alloys in this study has a challenge in terms of combining these different fields in one study.

It is also worth to note that because of the complexity and containing complicated integral oil channels, the most appropriate method for production of complex helicopter gearboxes is sand casting. In order to simulate the actual helicopter gearbox casting method, sand casting method for the experiments has been chosen in this research although it has many difficulties to overcome for production. Moreover, in the literature there is a very limited knowledge about the process parameters for sand casting of magnesium alloys to make a basis for the future experiments. Generally, experiments in this field on the literature are based on the permanent

mould casting method. However, this does not reflect the actual production method for helicopter transmission housings. Due to this reason, at the beginning of this study, the experiments have been focused on to find the optimum sand casting process parameters such as sand grain size, binder, hardener, their application time, moulding parameters, casting temperature etc. for magnesium sand casting. During the optimization of these parameters, alloying elements selection with their optimum amounts has also been studied.

The recent studies were based on Mg-Al binary system, where the amount of Al addition changes between 5 and 9 wt. %. Aluminum alloying to magnesium provides the increase of strength, castability and corrosion resistance of magnesium alloys at a low price range in comparison to other alloying candidates. However, creep resistance of this system is very low when the temperatures goes above 120 ^{o}C whereas operating temperature for powertrain components is typically in between 150 to 200 ^{o}C [4,5]. Thermally unstable β-$Mg_{17}Al_{12}$ phase formation with Al alloying is responsible for poor creep resistance. Due to this reason, development of creep resistant magnesium alloys containing Al has focused on the searching of new alloying elements hindering or decreasing the formation this phase.

The current studies show that Si addition to Mg-Al alloys provides an improvement in creep properties due to the formation of thermally stable Mg_2Si in the microstructure. Si containing Mg-Al alloys such as AS41 and AS21 have been used in automotive powertrain applications. These alloys replaced the cast iron crank case and transmission housings by saving nearly 50 kg in weight [6]. Mg_2Si formation with the addition of Si to Mg-Al alloys brings very effective strengthening Mg_2Si particles exhibiting high melting temperature (1085 ^{0}C), low density, high elastic modulus and low thermal expansion coefficient [6,7,8]. Mg_2Si phase has also superior properties to $Mg_{17}Al_{12}$ in terms of hardness (460 HV) [7, 8]. The challenge for this phase is prone to formation of undesirable and coarse Chinese script morphology under lower solidification rates (like in sand casting) causing the

decrease of the mechanical properties at ambient temperatures [1,6,9]. Due to this reason, the refining of Mg_2Si particles in sand casting is crucial to obtain optimum mechanical properties at room temperature (RT).

The refinement and/or modification of Mg_2Si particles could be achieved with addition of Ca, Sr and Sb elements in accordance with the recent studies. For example, the study conducted by Sirinivasan et al. [10] shows that the addition of 0.2 wt.% Sb to AZ91-0.5%Si alloy provides the modification of Chinese script Mg_2Si phase to fine polygonal shape. (In this thesis, the compositions are given in weight percent unless otherwise indicated.) Sr is also known as another modification element for Mg_2Si phase together with the grain refiner in Mg-Al-Si alloys. Chinese script Mg_2Si phase was almost eliminated with 0.4 wt% Sr addition to AS31 magnesium alloy and changed to irregular blocky shape [11,12]. In Mg-5Al-1Zn-1Si-0.2Ca, grain refinement and modification effect of Ca have also been determined [13]. The study conducted by Pans's group also indicated that 0.6 % Sn to AZ61-0.7Si alloy provided the refinement in the Chinese script morphology Mg_2Si phase in the alloy [11,15,44].

In the light of the brief introduction, the main objective of this research is to find an alternative magnesium alloy usable in high temperature applications such as helicopter transmission housing applications. The base magnesium alloy for the comparison has been selected as AZ91 due to the some commercial aerospace transmission casings already produced from this alloy and several studies conducted with this alloy.

The specific aims of this research are:

1) To develop a sand casting technique with optimum process parameters for magnesium alloys
2) To characterize the as-cast and heat-treated microstructure as a function of composition for the studied magnesium alloys
3) To develop a basic understanding of alloying element addition on solidification characteristics of magnesium alloys by comparing the cooling curves
4) To investigate the effect of alloying element addition on the tensile properties and microstructure of the studied alloys
5) To understand the reason of fracture after tensile test by fractography analysis
6) To estimate the creep resistance of studied alloys by comparing the microstructural overview with the literature data

This thesis contains five chapters with the following detailed explanations in order to specify each stage.

Chapter 1 provides a general idea, background and objective of the thesis. In addition, brief introduction of magnesium alloys with their advatages and disadvantages is also given. Some examples of magnesium casting parts from aerospace and automotive industries are presented to provide general application areas of magnesium cast parts in the industry.

Chapter 2 gives a detailed theoretical background and literature review about magnesium and its alloys. This chapter starts with metallurgical information about magnesium and explanation about their identification system by introducing their alloy designation. Magnesium alloys are divided into two groups in accordance with containing Zr or not. General mechanical properties obtained from Aerospace Material Specifications (AMS) for some Zr containing and Zr-free magnesium alloys

are also summarized in order to compare the test results obtained in this thesis. A comprehensive review about the difficulty of sand casting of magnesium alloys and their melt contol are also given under this chapter to explain the difficulties faced during the experiments. Infuence of alloying elements on Mg-Al based alloys together with their optimum addition range are listed. Literature review about the purpose of alloying elements and property enhancement on Mg-Al alloys are covered. Alloying element effects on the properties especially creep and tensile are explained in detail to see where the literature is about this issue. The general literature review about solidification and grain refinement in addition to particular studies about magnesium alloys are also provided in this chapter. Casting defects for magnesium castings and fractography results of some studies are presented for evaluation and comparison.

Chapter 3 explains the materials and experimental procedure used in this study. Magnesium alloys used in this thesis with their compositional ranges were prepared with AZ31 base alloy, master alloys and grain refiners, when necessary. The microstructural investigation was conducted by optical microscope (OM) and Scanning Electron Microspcope (SEM) having EDS capability. In order to evaluate the effect of different casting thicknesses on mechanical properties, different specimen conditions were obtained from the mould system and tested. T6 heat treatment is applied to all alloy systems in order to compare as-cast and heat treated microstructures. Tensile tests after radiographic inspection are performed at RT with Instron 5985 electromechanical test machine. Grain size and porosity measurement techniques with their details are provided in this chapter. Cooling curve analysis method with data acquisition system is provided to understand procedure followed up during thermal analysis evaluation.

Chapter 4 shows all metallurgical and mechanical test results. Cooling curve analysis, X-ray diffraction (XRD) and radiographic test results before tensile test, optical microstructure analysis, SEM-EDS resultS evaluation, grain size and porosity

measurements constitute the metallurgical evaluation after the tensile test. Fractography results taken from the fracture of tensile specimens are also presented in this chapter.

Chapter 5 summarizes the findings of this study and possible future work according to the obtained test results to meet the requirement of magnesium casting components in industry.

1.2 Magnesium Alloys with Advantages and Disadvantages

Magnesium alloys have been gaining more attention for aerospace and automotive industries due to their lower density together with combination of good mechanical properties to substitute aluminum alloys currently dominating the industry [1].

The major advantages of magnesium alloys in the industry can be given as follows [16,17, 18, 19]:

- Lightest structural metal
- High strength-to-weight ratio
- Good castability
- Good machinability
- Acceptable weldability under controlled atmosphere
- Excellent damping capability

However, the usage of magnesium is still not on the expected levels because of the general drawbacks given below [16,19]:

- Low elastic modulus compared to aluminum and steel

- Limited cold workability and toughness
- Limited strength and creep resistance at high temperatures
- Poor corrosion resistance in some environments

The main challenges for broad magnesium usage are related with the disadvantages of magnesium alloys provided as below [6]:

- Higher reactivity during melting
- Higher cost than other commercial casting alloys
- Short maintenance intervals because of corrosion behavior
- Corrosion initiation due to wear, abrasion and mechanical damage despite of coatings against corrosion
- Dissimilar metal joints and moisture exposure because of poor engineering design

1.3 Magnesium Casting Applications

1.3.1 Magnesium Sand Casting in Aerospace Industries

Magnesium has been extensively preferred in helicopter transmission housings, aircraft engines, air frames and landing wheels in aerospace industry. The main reason for usage of magnesium castings in this industry is the high strength to density ratio together with the desired room and elevated temperature properties, fatigue behavior and good machinability. AZ91E, ZE41A, EV31A, QE22 and WE43 are typical magnesium alloys used in helicopter and aircraft applications because of their creep strength and improved corrosion resistance [19,20].

An example of gearbox housings of helicopter transmission system is provided in Fig. 1.1. This casting has been used in Sikorsky CH53E helicopter main transmission housing produced from AZ91E magnesium alloy. The net weight and height of this casting are approximately 300 kg and 1220 mm, respectively. This part is known as the largest aerospace magnesium sand casting part in the world [21, 22, 23]. Other example of magnesium sand casting products is presented in Fig. 1.2. The main transmission of AH 64 Block III is poured with using EV31A (Elektron 21®) (Fig. 1.2). This helicopter is known as the first aerospace certified helicopter using rare earth containing magnesium alloy EV31A. This magnesium alloy is known as the latest developed magnesium alloy in industry [22].

Fig. 1.1 Sikorsky CH53E main casing produced from AZ91 magnesium alloy [22]

These parts are produced with using very complex assembled sand cores. An example of this type of mould assembly is given in Fig. 1.3. This mold assembly contains more than 100 cores. The final part after casting is also given in Fig. 1.3 [22].

Fig. 1.2 AH64 Block III main transmission casing produced from EV31A [22]

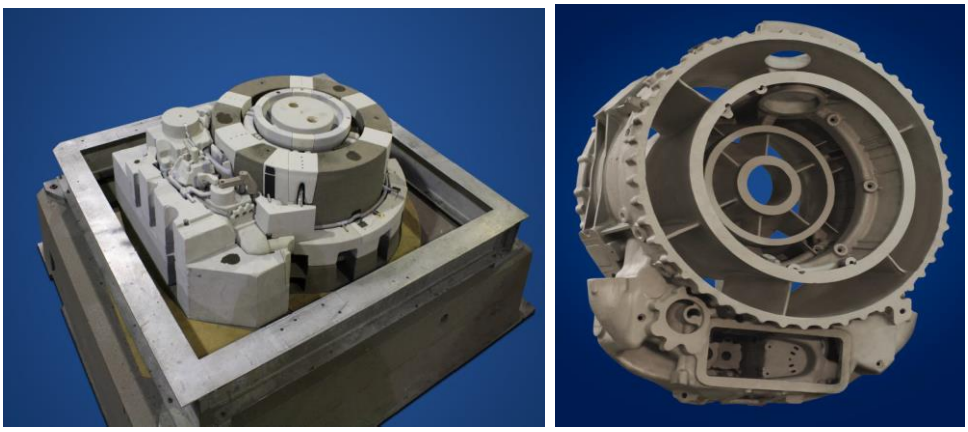

Fig. 1.3 (a) Mold assembly for P&WC 535 Air Inlet (b) P&WC 535 Air Inlet [22]

CHAPTER 2

THEORETICAL BACKGROUND AND LITERATURE REVIEW

2.1 Magnesium

Magnesium (Mg) was discovered by Sir Humphrey Davy in 1808. It is the sixth most abundant element on the earth comprising 2.7 % of the earth's crust and 0.13% of word's ocean water. It is known as the lightest structural metal having a density of ~ 1.738 g/cm^3 at 20 ^{0}C, which is approximately 85% lighter than steel and 35% lighter than Al. Therefore, magnesium and its alloys are seen as potential candidates to replace denser metals such as iron, steel and aluminum in industry [24]. However, magnesium as a pure metal, like most other pure metals, is soft with low mechanical properties and moderate ductility. Its mechanical properties, corrosion resistance and castability could be improved with alloying [7,18,26].

As far as the crystal structure of magnesium is regarded, magnesium has hexagonal closed packed (HCP) crystal structure (a=0.32092 nm and c=0.52105 nm at RT). (Fig. 2.1) It has only two independent basal slip system [18]. Due its crystallographic nature, deformation at lower temperatures is very limited. In addition, it is very sensitive to corrosion in a marine environment. This is not only coming from its electronegativity but also related with its impurities such as Fe, Ni, Cu that adversely affect corrosion behavior [6,18,26]. Pure magnesium is not generally used in industry. However, it is preferred in the alloying form with other metals. The general alloying elements and alloying designation systems are explained in Section 2.2.

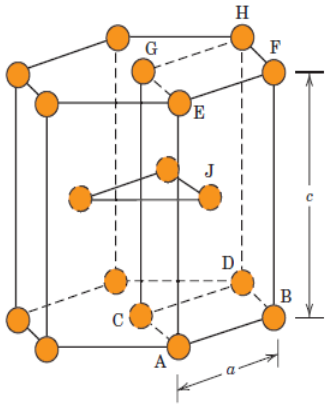

Fig. 2.1 The hexagonal close-packed crystalline structure example [26]

Casting process is a dominant fabricating method for magnesium parts. Sand casting has been main production method for large and complex aerospace castings [31,32]. The aerospace components need higher level of structural integrity to obtain consistent properties in every section of the part [29]. Hence, consistent material properties in all over the part are very crucial for castings in magnesium aerospace castings.

2.2 Magnesium Alloy Designation

Commercially produced gravity (sand or investment) casting magnesium alloys are currently based on the basic alloy systems according to their major alloying elements: aluminum, zinc, manganese, zirconium and rare earths [30]. These alloy systems are categorized as follows and their alloy families are given in parenthesis:

- Magnesium-aluminum-zinc-manganese (AZ, AM, AJ, AE, AS)
- Magnesium-zinc-rare earths-zirconium (ZE, ZK)
- Magnesium-silver-rare earths-zirconium (EZ, EK, EV, EQ)
- Magnesium-rare earths-zirconium (WE)

Identification of commercial magnesium alloys is determined in accordance with the practice established in 1952 by the American Society for Testing and Materials [30]. ASTM B591 [31] defines the codification system to designate magnesium alloys. This alloy designation consists of two letters followed by two numbers. Code designations are based on chemical composition limits. The first alphabet letter identifies the major alloying element and the second one denotes the second major alloying element. The following number represents the respective weight percentage amounts of major alloying elements defined by first two alphabet letters. A serial letter at the end of this designation explains the development stage or degree of purity of the corresponding alloy system. This final letter explains the whether there is any initial and subsequent developments on the particular alloy presents or not. Their composition is slightly different than the first and one another; but, this does not affect the basic designation.

The temper designation coding system for magnesium alloy is illustrated in ASTM B296. Temper system can be as fabricated (F), solution heat-treated & naturally aged (T4), only artificially aged (T5) and solution heat-treated & artificially aged (T6) according to ASTM B296 [33,122]. Fig. 2.2 summarizes the coding system of magnesium alloy explained in this paragraph for one typical example for AZ91. “A” represents aluminum, the greatest amount alloying element in the alloy; “Z” indicates zinc, which is the second greatest amount element in the alloy. “9” in the designation means that the rounded off mean aluminum weight percentage is between 8.6 and 9.4; “1” expresses the rounded of mean zinc percentage is in the range of 0.6 and 1.4. “E” represents the fifth composition of this alloy registered with ASTM [30]. Temper code – T6 indicates that the alloy is solution heat-treated & artificially aged heat treatment condition.

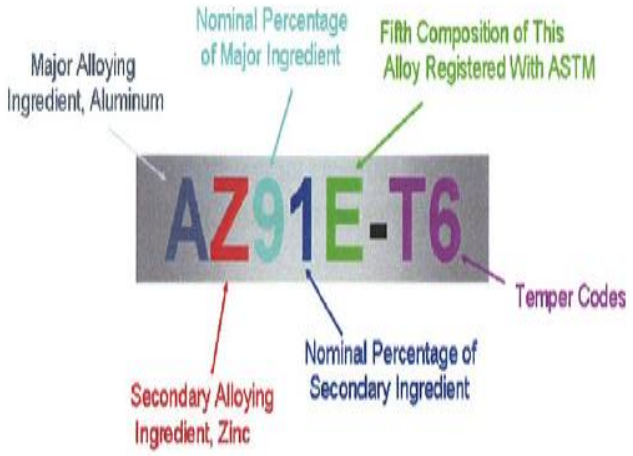

Fig. 2.2 ASTM B591 Magnesium alloy identification system (Artwork courtesy of ASTM, www.astm.org.) [31]

The notation approved by ASTM for major elements added to magnesium alloys by a specific letter is given in Table 2.1 [30].

Table 2.1 Designation of elements in magnesium alloy system

Symbol	Element	Symbol	Element	Symbol	Element
A	Aluminum	K	Zirconium	V	Gadolinium
B	Bismuth	M	Manganese	Z	Zinc
C	Copper	Q	Silver	W	Yttrium
E	Rare Earth Elements	S	Silicon		
J	Strontium	T	Tin		

Although AZ an AM series magnesium alloys have several advantages as a common casting alloys, they suffer from microporosity in sand and permanent mold castings. The creep properties of Al containing Mg alloys could be improved by addition of calcium, tin, strontium or rare earth elements. The current aim of the aerospace magnesium alloys containing aluminum is to achieve high integrity of properties in the parts together with the desired creep resistance [30].

2.3 Major Alloy System for Magnesium

2.3.1 Zirconium Free Magnesium Alloys

The first commercially used magnesium sand casting alloys were formed by additions of aluminum, zinc and manganese to magnesium. Aluminum addition to magnesium improves both the yield and tensile strength and enhances hardness. Zinc promotes castability and yield strength with bringing some loss of ductility. AZ and AM series magnesium alloys belong to this group. Dowmetal C (AZ92) and Dowmetal H (AZ63) were known as early magnesium sand casting alloys. Due to the greater ductility and fracture toughness requirements of automotive applications, magnesium alloys such as AM60, AM50 and AM20 are used [6, 32].

The lower creep resistance of current Mg-Al alloys above 125 ^{o}C is seen as their major drawback, which makes inadequate these alloys for elevated temperature applications. In automotive industry, transmission cases produced with casting operate at temperatures up to 175 ^{o}C, engine blocks up to 200 ^{o}C, even pistons works temperature above 300 ^{o}C [1,25]. However, in industrial applications, most of casting customers does not need an alloy with a service temperature of 250 ^{o}C.

2.3.1.1 AZ91 Magnesium Alloy

AZ91 magnesium alloy is a well understood and most widely used magnesium alloy having a satisfactory combination of RT strength and ductility in addition to good corrosion resistance. Due to these reasons, it is usually taken as a “benchmark” in order to compare the properties of other and newer alloys [25,17]. This alloy can be preferred in both aerospace and automotive applications due to its castability, wide

range of mechanical properties at RT and satisfactory corrosion resistance [6,33,34]. In addition to this, its cost is more feasible than the other magnesium alloys available in the market. Main disadvantage of this alloy is its susceptibility to creep mechanism at temperatures higher than 120 ^{0}C. Additionally, it has also problem with fatigue properties [37]. The reason for lower creep resistance is based on the observation of low melting point β-$Mg_{17}Al_{12}$ precipitation coarsening easily at high temperatures [1,33].

Solutionizing treatment of AZ91 magnesium alloy results in the decomposition of supersaturated α-Mg solid solution, which is observed in two mechanisms: discontinuous decomposition (DD) and continuous decomposition (CD). Generally, initiation of DD precipitates starts preferentially at the grain boundaries and then growing inside of the grains in a coarse laminate shape during early stage of ageing. CD precipitates occur in the fine form of β dispersion at the remnant region of grain where the DD products are not observed. It was concluded according to the results that DD shape is harmful to mechanical properties due to the weakness of the alloy at these zones while CD shape phase products are beneficial [38]. It was also noted that discontinuous precipitation of β-$Mg_{17}Al_{12}$ at grain boundaries and its migration into the grains during growth accelerate grain boundary sliding at elevated temperature. Due to this reason, the general focusing point in AZ91 alloy to increase creep resistance is to obtain thermally stable phase formation at grain boundaries [35].

Fig. 2.3 shows the general as-cast microstructure of AZ91 alloy together with its SEM and EDS analysis. Main phase constituents are α-Mg matrix, massive and lamellar $Mg_{17}Al_{12}$ phases [10]. Solution heat treated and as-cast microstructure of AZ91 are also provided in Fig. 2.4. As seen in this figure, all massive $Mg_{17}Al_{12}$ phase is dissolved into the matrix with solutioning heat treatment [29].

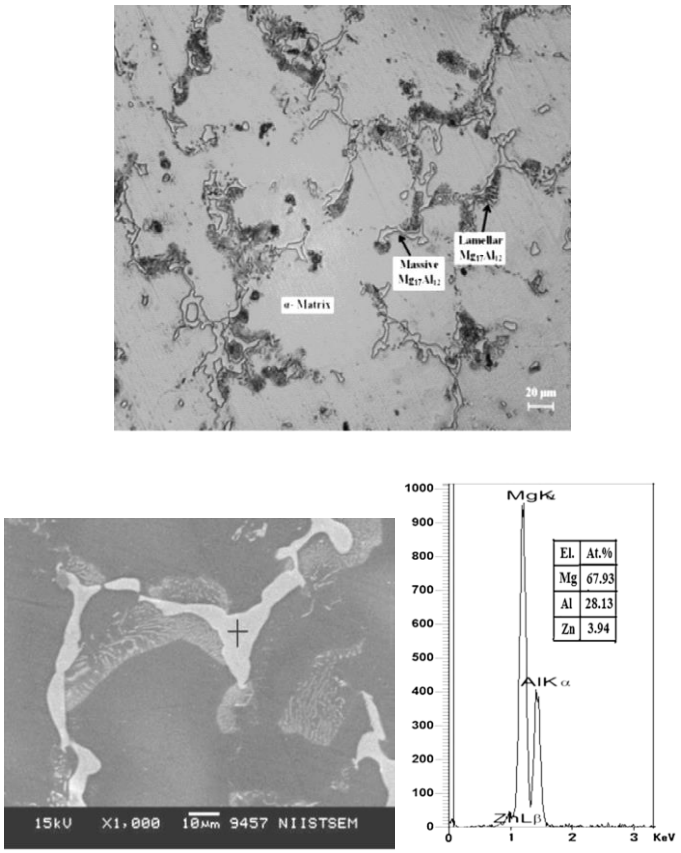

Fig. 2.3 Microstructure of as-cast AZ91 alloy (b) and SEM image with EDS analysis of massive $Mg_{17}Al_{12}$ phase [10,33]

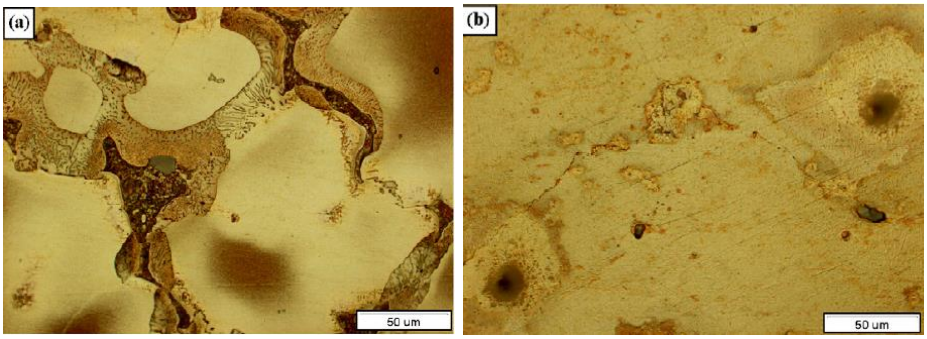

Fig. 2.4 Microstructure of AZ91 (a) as-cast (b) after solution treatment [29]

2.3.2 Zirconium Containing Magnesium Alloys

F. Sauerwald [20] observed the special grain refining effect of zirconium (Zr) on pure magnesium in 1937. In addition this effect, zirconium behaves as a "collector" and takes away several impurity elements such as iron, hydrogen and aluminum. Therefore, zirconium is not preferred in magnesium-aluminum alloys due to the reaction between zirconium and aluminum [20]. ZE41A has been the most commercially sand casting magnesium alloy in the industry. The major disadvantage of this alloy is its poorer corrosion resistance as compared to AZ91E, WE43A and EV31A. However, it should be significantly noted that the minimum yield strength (YS) of specimens cut from casting for ZE41A is higher than the ultimate tensile strength (UTS) of those for AZ91E. This alloy has been preferred for complex castings of aerospace applications as indicated in 1.3.1 [9,25].

The latest generation magnesium-rare earth-zinc-zirconium alloy Elektron 21 (EV31A) is currently used in the aerospace industry. It contains neodymium and gadolinium to improve mechanical properties and castability without foundry problems. In addition, small amount zinc is added to improve castability without sacrificing corrosion resistance. The complete set of database given in the Metallic Materials Properties Development (MMPDS) [39] has been supported with the results obtained from the production of castings.

2.3.3 Mechanical Properties of Magnesium Alloys

Before giving detail explanations between tensile properties of test pieces cut from castings and separately cast test bars for magnesium alloys, some general information can be foreseen.

a) The test pieces cut form in thick regions show more tendency towards microporosity, especially, when these regions are not properly fed. This will certainly decrease UTS and elongation values.
b) Alloys with microporosity parallel to the casting surface are less affected in tensile properties in thick or changing sections than those showing microporosity perpendicular to the surface.
c) Due to the variety of chilling rates, different microstructures can arise, which may modify the material properties, except any effects resulting form change in grain size, for instance, the amount and continuity of a network of degenerate eutectic at the grain boundaries [20].

2.3.3.1 Tensile Property Requirements of Magnesium Alloys

The study performed by Srinivasan et al. [40] also showed the mechanical property variation of AZ91D alloy even in plate casting. The picture of plate casting wth specimen locations and their mechanical test results, grain size and porosity percentages are presented in Fig. 2.5 and Table 2.2, respectively.

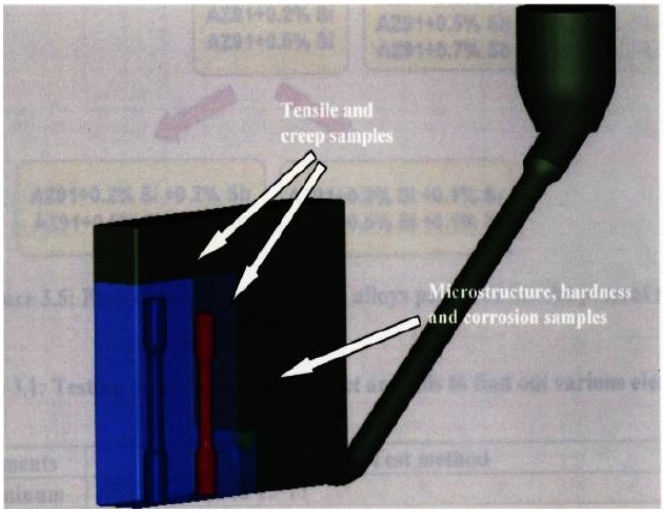

Fig. 2.5 Schematic diagram showing plate casting and sample locations [40]

Table 2.2 Mechanical property variation in AZ91D alloy along the wall thicknesses of plate casting [40]

Sample Location	YS, MPa	UTS, MPa	% El.	Grain Size μm	% Porosity
Center region of casting plate	92	173	2.8	110	2.35
Wall side region of casting plate	120	210	4	80	1.98

Mechanical properties of magnesium alloys used in industry are presented in Table 2.3. This table also contains main alloying elements of the alloys together with their Aerospace Material Specifications (AMS). According to the experiments, cut up specimen properties of zirconium alloy castings are close to those of separately cast test bars. However, more difference exists in aluminum containing magnesium alloy. This situation is expressed with the alloys given in Table 2.3. Mechanical properties of AZ91 show much more variation in different conditions in comparison to non-aluminum containing magnesium alloys such as ZE41A, EV31A and WE43B.

2.4 Magnesium Sand Casting Technology

Some important principles from the physical and chemical reactivity of magnesium are listed below. During design of gating, risering system and pouring, these factors shall be taken into consideration to obtain desired metallurgical and mechanical properties.

- Suitable inhibitors must be selected and added to the sand in order to prevent possible reactions between magnesium and moisture.
- The flow of metal shall be as smooth as possible to minimize oxidation.

- Due to the low density of magnesium, “hydrostatic” pressure helping to fill the mould is relatively low. Therefore, sands must be permeable and ventilation of mould shall be well enough in order to prevent the risk of blows and misruns.
- Necessity of generous risers because of low volume heat capacity [20]

Table 2.3 Mechanical properties of current industrial magnesium alloys [30]

Alloy	AMS	Minimum Tensile Properties			Properties Apply To:
		YS (MPa)	UTS (MPa)	% E	
		110	235	3	Separate cast bars
AZ91C/E-T6	4437 4446 [41] [42]	100 83	176 134	0.75	Specimens cut from castings; average of 4+ bars Specimens cut form castings; any 1 bar
ZE41A-T5	4439 [43]	134 120	200 180	2.5 2.0	Separate cast bars Specimens cut from castings; coupons
WE43B-T6	4427 [44]	173 152 128 159	220 217 197 190	2.0 2.0	Separate cast bars Specimens cut from castings Separate cast bars at 250 ^{0}C Specimen cut from castings at 250 ^{0}C
EV31A-T6 Elektron 21	4429 [45]	145 145 155	249 249 228	2 2	Separate cast bars Specimens cut from castings; coupons Specimen cut from castings at 250 ^{0}C

There are several exceptions in magnesium sand castings in comparison to other metal sand castings. These exceptions are as follows:

- the necessity of chemical inhibitors

- compensation of low fluid metal pressure of magnesium in comparison to aluminum
- low heat content of magnesium related issue [30]

Magnesium oxidizes readily in a molten state. Oxidation can also continue in the mold during and after pouring. Direct interaction of molten magnesium with mold atmosphere could cause reaction with oxygen or moisture in sand. Inhibitors are added to sand to prevent the latter reaction. The CO_2 process has become very popular for core making in magnesium foundries. CO_2 hardened resins are preferred to prevent the moisture related problems in the sand mould [30]. If the gassing time is properly controlled, collapsibility can be enough without the necessity for additives to promote later disintegration [20]. Improved filter system shall also be preferred because future disposal regulations will limit the further usage of fluxes. [21] Cover gases such as SF_6 and SO_2 instead of flux should be used to decrease possibility of foreign materials coming from flux materials [21,25]. [29,47]

2.4.1 Gating Systems for Magnesium Sand Casting

During gating practices of magnesium alloys, the low density of magnesium and oxidation tendency of magnesium shall be taken into consideration. Low density consideration is also significant to fill the mold completely without turbulence. Turbulence results in undesirable oxide formation in the molten metal stream, which affects the mechanical properties adversely and causes unacceptable inclusions in the castings. Some suggestions for designing gating systems for magnesium include:

- Any falling of metal above 10 mm in the cavity will probably cause oxides in castings.
- The usage of a pouring cup is suggested to make the pouring sprue full.

- Filters or screens shall be preferred to remove as many oxides as possible. Origin of these oxides could be molten magnesium or the reaction occurred in the gating system.
- In order to achieve mechanical and metallurgical requirements on magnesium castings, the metal velocity shall be below 0.5 m/s in any location of the system [30].

2.4.2 Risering, Chilling, and Filtering Systems for Magnesium Sand Casting

The general purpose of risers on a casting is the compensation of shrinkage contraction during liquid metal solidification. Last solidification area must be risers in order to obtain effective solidification mechanism. Magnesium alloys have very high tendency to shrinkage formation due to their long freezing range. For example, freezing range of AZ91 magnesium alloy is about 130 ^{o}C in comparison to 60 ^{o}C for that of A356 Aluminum cast alloy. In order to compensate shrinkage in these alloys there is a requirement of more and larger risers. The usage of insulated sleeves could also be thought to improve the feeding efficiency of risers.

The use of chills aims to achieve steeper thermal gradient in the solidifying part and enhance the feeding efficiency of risers. The other aim of chill usage is to speed up the solidification rate in thick sections, which are not risered, in order to avoid formation of local shrinkage defects. In addition, local mechanical property improvement by obtaining fine grain structure can also be assured with chills. Metal chills, if used, should be free of rust and moisture, positioned in the proper location and monitored to prevent wear. [30]

2.5 Melt Control of Magnesium

In addition to general liquid metal handling issues, magnesium needs much more safety concerns due to its reactivity and oxidizing tendency. In order to avoid contact between oxygen environment and molten magnesium, extra process design consideration should be taken into consideration. This issue becomes very critical and significant when the molten magnesium temperature is increased and/or oxide formation accelerated alloying elements specific to magnesium alloys are added into magnesium alloy [19,25]. Proper melt protection also provides high level of melt cleanliness and minimum hydrogen pickup. Due to weak and impermeable oxide film on the surface of magnesium melt in comparison to an aluminum melt, melt protection of magnesium requires even greater attention.

For sand casting of magnesium, an alloy specific casting cover flux could be used to avoid oxygen contact with liquid magnesium surface. Recently, a protective cover gas such as SF_6 and SO_2 is preferred in many magnesium castings to prevent oxidation (burning) in the melting crucible. The maintenance of safety gas mixture and control of their mixture levels are also very critical. Cover gases such as SF_6 and SO_2 should be used at their minimum required levels to decrease their cost and environmental impacts [19,25,46].

2.6 Effect of Alloying Elements on Magnesium Alloys

There are different methods of strengthening of magnesium alloys via alloying. These methods include solid solution strengthening, precipitation hardening and dispersion strengthening. Aim of the magnesium is to improve its properties such as strength, formability and corrosion resistance. The elements used in magnesium cast alloys for alloying are Al, Zn, Zr, Y and rare earth (RE) elements. Other minor

alloying elements used in cast magnesium alloys are Be, Ca, Si, Sr, Sn, Sb and Bi to enhance the properties such as castability, RT strength, high temperature strength, grain size, formability, and oxidation resistance [21,25,41].

From the literature, general observations of magnesium alloying can be expressed as follows:

a) Continuous solid solutions are only possible with hexagonal metals such as Zn, Cd, Be, Ti and Zr.
b) Due to the electropositive nature of magnesium, it has a tendency to compound formation with less electropositive metals such as those of Groups IVB and VIB as well as with elements such as carbon (C) and Si.
c) Probability of the extensive solid solution formation of other elements with magnesium in terms of atomic size compatibility restricts the atomic size of those less than 15 percent. In order to obtain solid solution strengthening, the elements shall have an atomic diameter higher than that of Mg (3.2 Å) and these elements are listed in Fig. 2.6 [20,46].

Carapella [20] represents the elements where the size factor favours solid solution formation with magnesium. The most favorable size factor of elements making the solid-solution with magnesium is illustrated in Fig. 2.6. The relation between the maximum solid solubility and misfit in each group of constant valency has also been shown in Fig. 2.6. This figure also indicates the manner how the solid solution formation possibility with the solute vacancy from two, the effect being stronger for a lower valency solute [20].

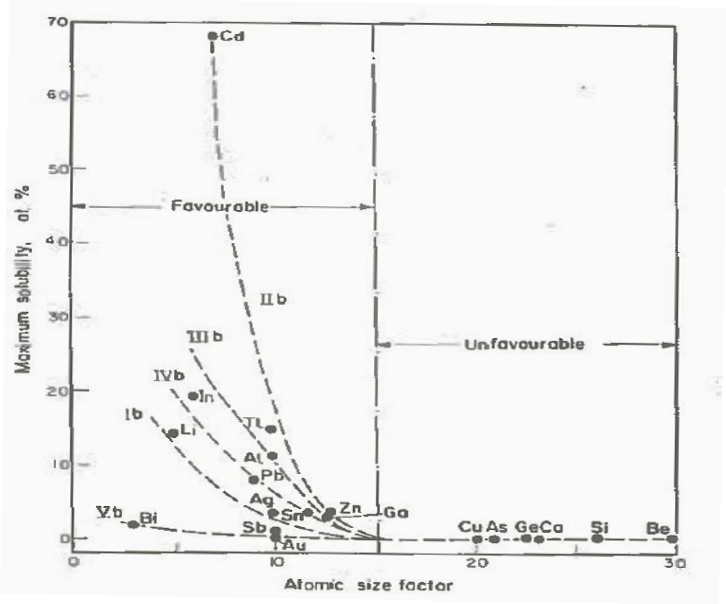

Fig. 2.6 Influence of atomic size on the solid solubility of various B group elements in magnesium (after Carapella) [20]

When the solid solution of alloying elements with magnesium is not established, compound formation could occur. The intermetallic phases could be important to obtain strengthening for creep resistance, recrystallization and texture. The stability of the intermetallic compounds is generally related with the melting point. In addition to this, it is also affected by the maximum solubility and the eutectic composition and temperature. This correlation is shown by Carapella with subsequent amendments in Fig. 2.7 and Fig. 2.8 [20].

The eutectic composition will be directly related with the melting point of the compound. In addition to this, it was concluded that as the percentage of solute decreases, melting point of the compound increases. In the real metals, the various interactions of different effects can make nonsense of such simple interpretations,

however, the latter at least helps to create a qualitative basis for "explaining" the generalizations expressed in Fig. 2.8 [20].

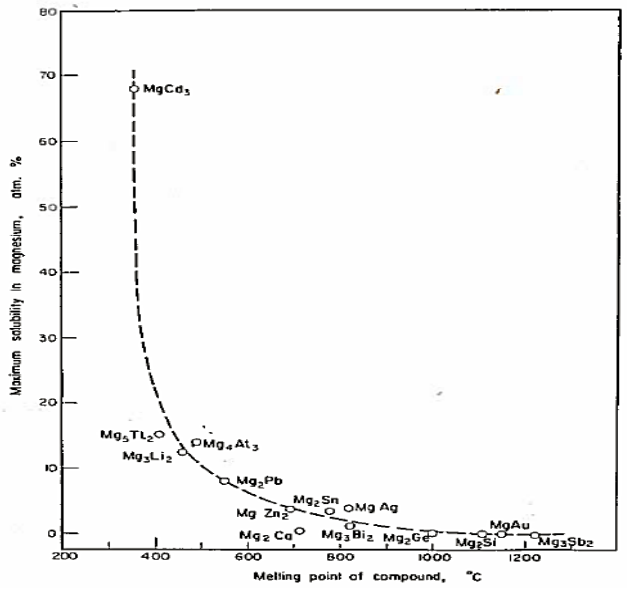

Fig. 2.7 Relationship between melting point of compound and maximum solubility in magnesium (after Carapella) [20]

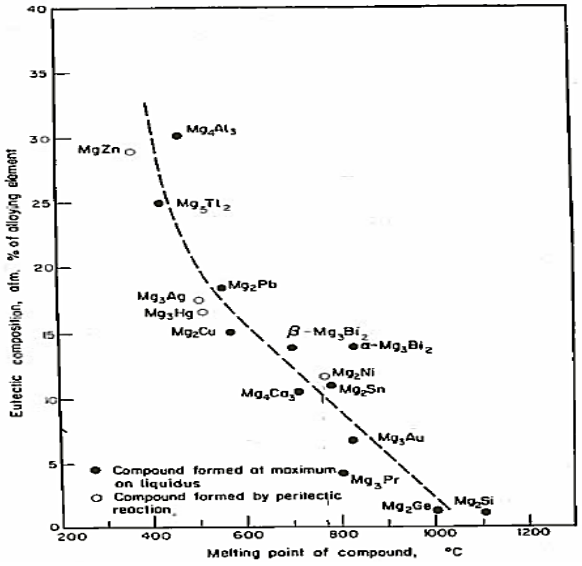

(a)

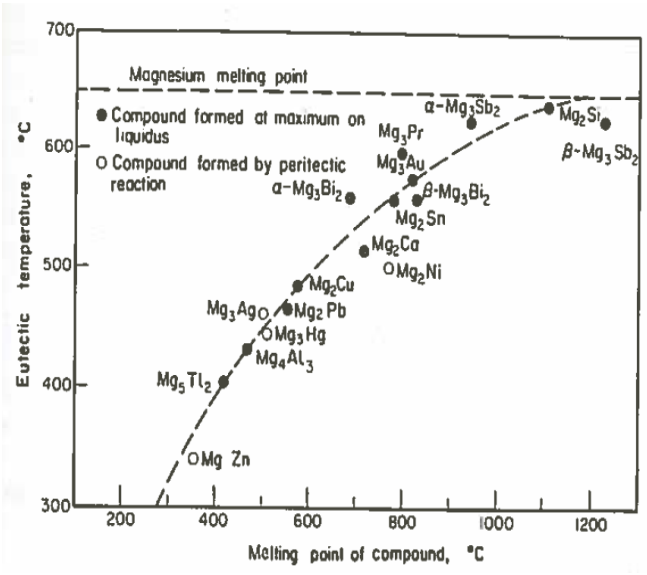

(b)

Fig. 2.8 a) Relationship between compound melting point and eutectic composition (after Carapella) (b) Relationship between compound melting point and eutectic composition (after Carapella) [20]

Raynor et al. [20] has pointed that the magnesium products with Group V elements increase the stability with Mg_2X type compound formation raising the eutectic temperature, where X= Pb, Sn, Ge and Si. Si and Ge. In addition to this, the greatest depression of the freezing point is obtainable with the rare earth elements. Other elements showing enhanced depression are Ca and Sr in which, in addition to Mg_aX type compound formation, the atomic size is reasonably under the favorable zone for solid solution formation [20]. Elements of group IV and V elements such as Si, Sn, Sb and Bi forms line compounds with magnesium, which is high melting temperature and good strengtheners for magnesium alloys [48]. Some elements such as Sb, Cd and Li show less depression of the freezing points than at first sight expectation. Antimony (Sb) forms a strong compound, Mg_3Sb_2, melting over 1200 ^{0}C, and has a favorable size factor, so that relatively little freezing point depression could be foreseen [20].

Following categories are formed by considering the binary systems with the elements given in this table showing appreciable solubility fall roughly.

- Continuous solid solutions: Cd
- Peritectic systems: In, Mn*, Zr*(In order of decreasing solubility at eutectic point)
- Eutectic systems with solid solubility exceeding about 1 percent
    - Pb, Tl, Ag*, Sn, Al*, Bi, Zn*,Ga, Li*, Os, Th*, Hg, (Nd, Pr)*
- Eutectic systems with solid solubility up to 1 percent (roughly in decreasing order of eutectic composition)
    - Eutectic composition > 5 percent: Au, Sb, Cu, Ni, Ce*, Sr, Ca, Ba, La
    - Eutectic composition < 5 percent: Co, Ge, Fe, Si

      Eutectic systems with liquid miscibility gap: Na [20]

Before giving the detail of alloying element addition effects to magnesium alloys, the brief summary of alloying elements to magnesium with respect to castability, mechanical and corrosion properties is provided in Table 2.4.

2.6.1 Effect of Al alloying on Magnesium Alloys

The most widely used element in alloying of magnesium is aluminum. The solid solubility of Al in Mg is 12.7 % at 435 ^{o}C and decreases to less than 2 % at RT as seen in the binary phase diagram of Mg-Al system presented in Fig. 2.9 [30]. The industrial magnesium casting alloys contain less than 10 % aluminum.

Table 2.4 General influence of elements used in magnesium alloys [6,38,39,40,47, 48]

Alloying Element	Melting-casting Behavior	Mechanical and technological properties	Corrosion behavior I/M produced
Al	Castability improvement, Microporosity formation tendency	Solid solution strengthener , precipitation hardening effect at low temperatures	Negligible influence
Ca	Effective grain refiner, slight suppression of oxidation during melting	Creep property improvement	Detrimental influence
Mn	Fe amount controller with Fe-Mn precipitates Precipitate refiner	Creep property improvement	Detrimental Fe controller
Sr	Helping reduction of microporosity Decreases surface energy of liquid magnesium	Helps morphological modification of Mg_2Si phase Creep property improvement	Minor influence
Si	Decreases in castability, Mg_2Si formation for elevated temperature .	Improves creep properties.	Detrimental influence
Zn	Castability improvement Microscoporosity tendency	Precipitation hardening effect , Creep property improvement Brittlenes and hot shortness tendency withour Zr addition	Minor influence, Detrimental Cu controller

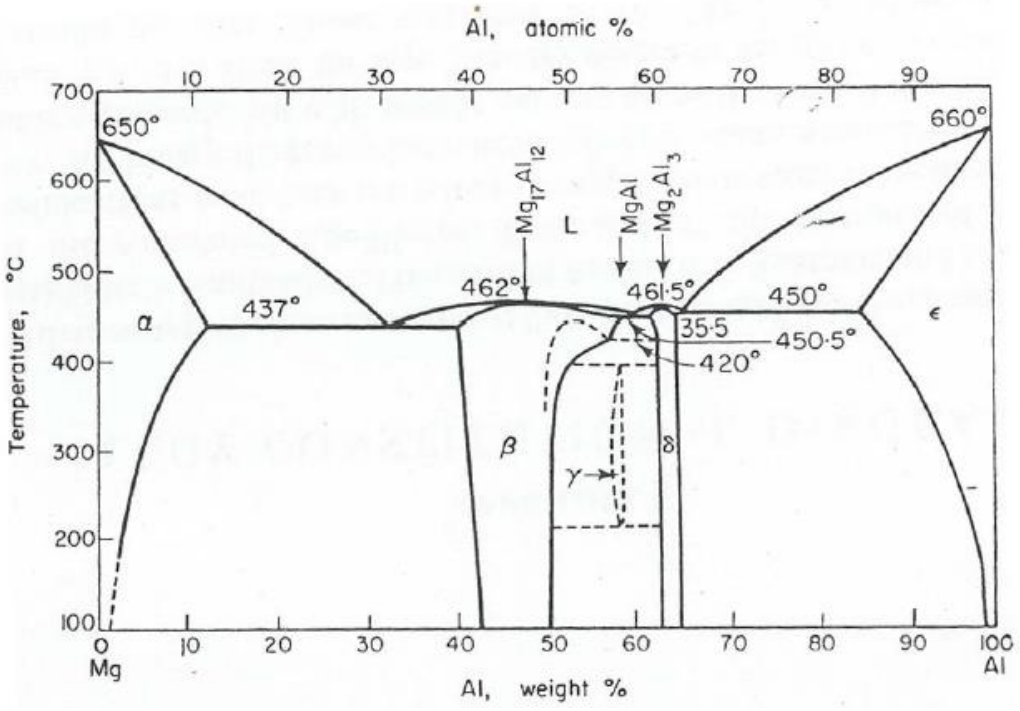

Fig. 2.9 Mg-Al binary phase diagram [30]

Due to the precipitation hardening of $Mg_{17}Al_{12}$ intermetallic compound under the solvus line, aluminum addition to magnesium leads to increase in the tensile strength by solid solution. In addition, Al alloying to magnesium increases the corrosion resistance together with the improvement in castability [6,38,39,40]. Aluminum alloying also brings the advantage in reduction of the grain size [30].

Aluminum containing magnesium alloys have an intermetallic β-($Mg_{17}Al_{12}$) phase at inter-dendritic regions and grain boundaries. $Mg_{17}Al_{12}$ is the main strengthening phase in Mg-Al alloys.One intermetallic compound shows all homopolar, heteropolar and normal metallic characteristics. In addition, tetragonal structure of $Mg_{17}Al_{12}$ was also reported with a crystal structure parameter a = 10.50 nm and c = 10.19 nm [47]. Precipitation of $Mg_{17}Al_{12}$ phase from supersaturated α-Mg is observed in two different ways: discontinuous and continuous precipitations. The discontinuous

precipitation means the mixtured formation of a lamellar mode of α-Mg-β-($Mg_{17}Al_{12}$) and massive $Mg_{17}Al_{12}$ phase. The other one precipitates uniformly within the supersaturated α-Mg [5]. The disadvantage of discontinuous $Mg_{17}Al_{12}$ phase at the grain bundaries is to reduce ductility due to its shape and morphology. However, by solution and aging treatments, its morphology and distribution can also be modified. For example, due to unstability of the eutectic phase in Mg-Al alloys, the complete dissolution of $Mg_{17}Al_{12}$ phase via heat treatment is observed [54]. By long term solution treatment (24 hours), in addition to dissolution of $Mg_{17}Al_{12}$ phase, re-precipitation of discontinuous fine plate like phase was also detected [47].

The melting point of β-($Mg_{17}Al_{12}$) phase is approximately 462 ^{o}C and it has poor thermal stability and partly metallic bonding. Temperatures above 120-130 ^{o}C causes the coarsening and softening of $Mg_{17}Al_{12}$ phase. Therefore, above this temeperature range, this phase could not act to prevent grain boundary sliding. It can be considered to have lower aluminum content in Mg-Al alloys in order to achieve desired elevated temperature properties. Due to the structure difference between cubic crystal $Mg_{17}Al_{12}$ and hexagonal closed packed α-Mg matrix, the interface between these phases is also fragile [41,48]. The mechanical properties change of AZ91 with respect to temperature was illustrated by Srinivasan et al. [40] as shown in Fig. 2.10. The softening and coarsening of $Mg_{17}Al_{12}$ phase with increasing temperature is the main cause of decrease in UTS and YS values.

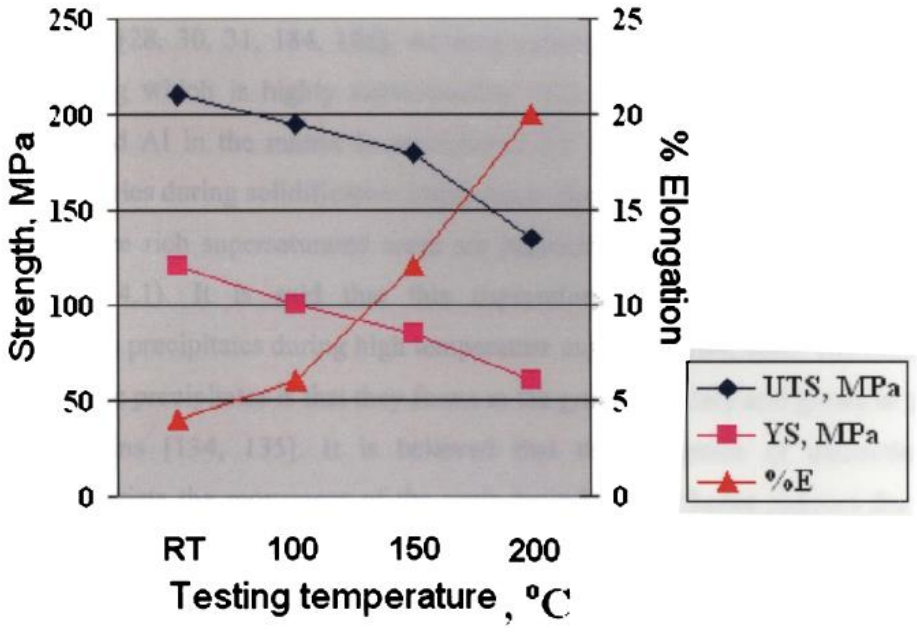

Fig. 2.10 Tensile property variation of AZ91 at different temperatures [40]

As a creep mechanism in magnesium alloys, both grain boundary sliding and diffusion-controlled dislocation climb are observed depending on the alloy systems, microstructure and stress-temperature regimes [1,25,42]. Due to the poor thermal stability and discontinuous precipitation of β-$Mg_{17}Al_{12}$ phase, substantial grain boundary sliding at elevated temperature is observed in Al based Mg alloys. In addition, creep deformation of these alloys is accelerated at elevated temperatures with both aluminum solute diffusion in the magnesium matrix and self-diffusion of magnesium. Because of these reasons, creep properties of aluminum containing magnesium alloys should be increased to be usable in elevated temperature applications. The main ways of improving creep resistance of these type alloys are summarized below [1,10, 25,42]:

- Suppressing $Mg_{17}Al_{12}$ phase formation
- Pinning grain boundary sliding

- Decreasing diffusion in magnesium matrix
- Solid solution strengthening
- Precipitation hardening
- Particle strengthening introducing second phase

The slow cooling rate in Mg-Al alloys (typically occurred in sand casting) leads to formation of continuous and/or discontinuous precipitation in the supersaturated areas of α-Mg phase as shown in Fig. 2.11. Generally, discontinuous precipitation is located on the neighborhood of α-Mg near the β-$Mg_{17}Al_{12}$ phase due to higher contents of aluminum (approximately 10-13 wt. %) in these regions. However, the aluminum contents in the dendritic regions may decrease as low as 2 wt. % [54].

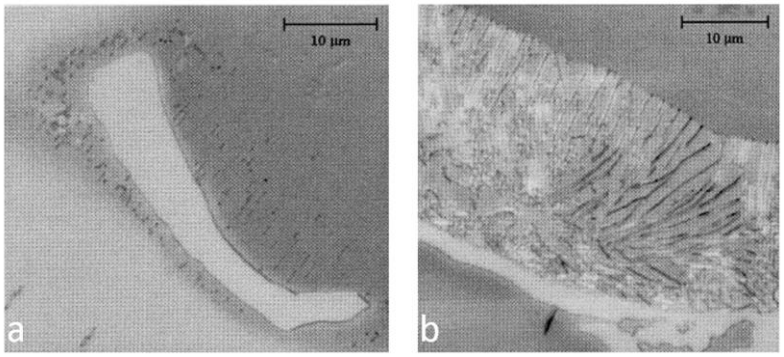

Fig. 2.11 (a) Continuous and (b) discontinuous precipitation in alloy AZ91E. [54]

Fig. 2.12 presents the typical microstructure images of AZ91 alloy poured with permanent mould cast method. It contains α-Mg with dissolved Al and Zn elements and divorced eutectic morphology comprised of the massive $Mg_{17}Al_{12}$ phase and supersaturated Mg solid solution. In the vicinity of the massive eutectic $Mg_{17}Al_{12}$ phase, discontinuous $Mg_{17}Al_{12}$ was also observed in the microstructure [14]. Divorced α-Mg-β-$Mg_{17}Al_{12}$ eutectic has a negative influence on the ductility of Mg-

Al alloys. As already stated, the presence of $Mg_{17}Al_{12}$ phase on the grain boundaries causes the intergranular cavitation and grain boundary sliding during high temperature creep, which finally results in the decrease in creep strength [27].

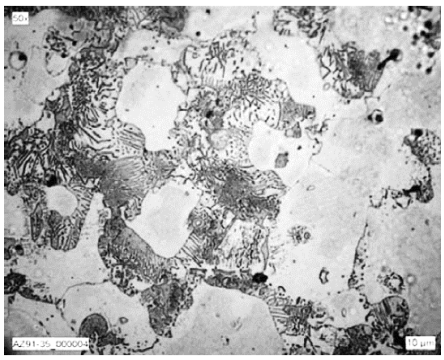

Fig. 2.12 Typical microstructure of the permanent mould cast AZ91 alloy [14]

The presence of massive β-$Mg_{17}Al_{12}$ eutectic phase and discontinuous precipitation in aluminum enriched regions inside of grains cause migration and sliding of grain boundaries during creep test, which results in the poor creep resistance of AZ series magnesium alloys. There are two possible ways to decrease or prevent this effect on creep behavior. The first one is the addition of elements having higher chemical affinity to Al than that of Mg. The other one is the element addition resulting in the formation thermally stable intergranular phase formation suppressing the grain boundary sliding. [43,44] While alloying elements such as Sr, Ca and RE represent to the former group, the alloying elements like Si, Bi and Sb belong to the second group. The addition of first group elements can have a possibility not only to reduce the amount of $Mg_{17}Al_{12}$ phase but also to form intermetallic compounds such as Al_2Ca, Al_4Sr and $Al_{11}RE_3$. The compounds formed after addition of second group elements such as Mg_2Si and Mg_2Bi decrease the grain boundary sliding at elevated temperatures [25,44]. According to the previous studies, grain boundary sliding mechanism is the main reason for deformation of Mg-Al alloys at elevated

temperatures. Therefore, in order to increase elevated temperature properties of aluminum based magnesium alloys, thermally stable intergranular phase formation suppressing the grain boundary sliding could be a solution [15].

2.6.2 Effect of Zn alloying on Magnesium Alloys

Due to low solid solubility of zinc in magnesium, it forms many intermetallic compounds. Mg-Zn phase diagram is given in Fig. 2.13 [30]. The maximum solubility of zinc is 6 % observed at 340 ^{0}C. Precipitation hardening is the main strengthening mechanism for magnesium alloys containing zinc [40,41].

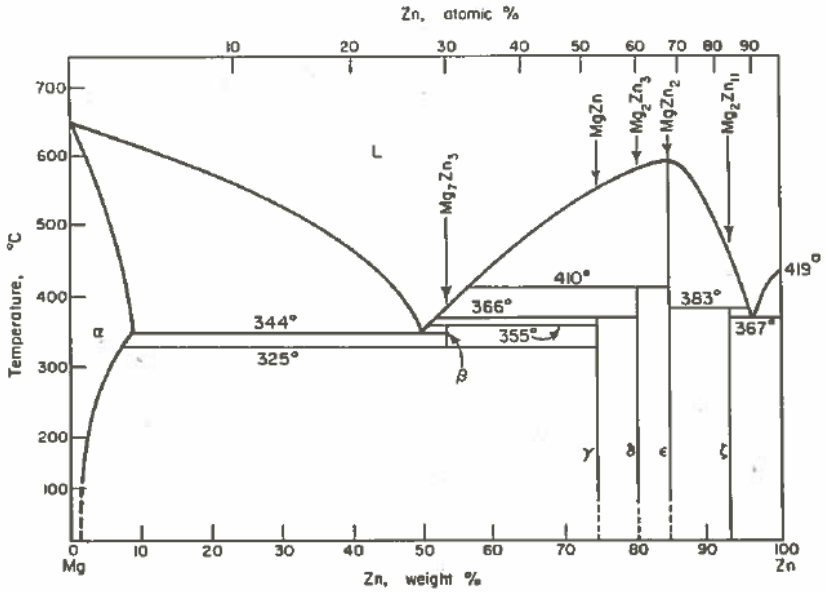

Fig. 2.13 Mg-Zn Equilibrium Binary Phase Diagram [20]

Zinc is preferred in Mg-Al system as a ternary element in order to increase RT mechanical properties and fluidity [40,41]. Since zinc addition to Mg-Al alloys

decreases the Al solubility in α-Mg, this increases the volume fraction of Al containing intermetallic phases, which brings increase in strength [28]. In addition to this, the small amount Zn addition to Mg-Al alloys increases the possibility of formation of fully divorced eutectic microstructure [27]. However, addition above the optimum limit may cause micro- and macro-cracks together with pores during solidification [51].

Addition of zinc to magnesium provides linear increase in the yield strength. The previous reports showed that the UTS and ductility values reach their maximum values around 4 % Zn and decrease with higher zinc levels. Zr and/or RE elements are used as minor additional elements when Zn is used for major alloying elements for aluminum free magnesium alloys. In addition, Zn can be added as for minor alloying elements in Mg-Al alloys. Although Zn addition increases strength, it is generally limited to 1% because of hot shortness formation in Mg-Al alloys. In addition to these properties, Zn can also be added to decrease the negative effect of iron on corrosion of magnesium alloys [25, 46].

On the other hand, Zn addition has a negative effect on the microporosity tendency of Mg-Al type castings in imperfect feeding conditions. Due to strong segregation power of zinc to the $Mg_{17}Al_{12}$ during eutectic growth, Zn leads to the eutectic solidification with a less isothermal interface by affecting formation and growth of eutectic on the α-Mg. Because of this reason, zinc addition could result in the porosity formation [54].

2.6.3 Effect of Mn Alloying on Magnesium Alloys

Manganese in magnesium alloys decreases the corrosion rate of the alloys coming from iron present in the system by forming less harmful intermetallic compound.

Due to very limited of solubility of Mn in magnesium, it is suggested to use up to 0.3% in aluminum containing magnesium alloys [30].

Ke et al. [102] found that Mn element has a key role in grain refinement of Mg-Al alloys for the heterogeneous nucleation of α-Mg grain. Al-Mn-C particle observed on the surface of Al_4C_3 nano particles were noted as potential nuclei for primary α-Mg [1].

2.6.4 Effect of Si Alloying on Magnesium Alloys

Decrease of mechanical properties for AZ series magnesium alloys above 120 ^oC limits their usage for high temperature applications. The main reason for this could be ascribed to softening of eutectic β-($Mg_{17}Al_{12}$) phase generally formed on the grain boundaries and intermetallic regions [52]. Si addition to Mg-Al alloys is aimed to improve creep properties with the formation of thermally stable Mg_2Si. Crystal structure of Mg_2Si is a FCC structure with lattice parameter a = 6.339 Å [47]. Mg_2Si phase is the only stable intermetallic compound in binary Mg-Si system, which shows high melting temperature (1080 ^0C), low density (1.99 g/cm^3), high hardness (460 $HV_{0.3}$) and low thermal expansion (7.5 x10 $^{-6}$ K^{-1}). Due to these reasons, Mg_2Si phase has been seen as a candidate phase to improve high temperature properties of magnesium alloys. Nevertheless, it was reported that Mg-Si binary alloys suffer from poor castability and low ductility [7]. In addition, modification of this phase also brings higher castability [1]. In order to compensate the negative aspects of this system, elements such as aluminum and zinc must be added [8,11,37,47]. Mg_2Si phase formed at grain boundaries during solidification restricts the free dendrite growth. Due to this reason, refinement in as-cast microstructure is also observed [1, 7, 9,48, 49].

The challenge for Si containing Mg-Al alloys is to avoid formation of undesirable and coarse Chinese script Mg_2Si phase formed at lower solidification rates, which causes the decrease in the mechanical properties [1,6,9]. Due to the lower cooling rate in in sand or permanent mould castings, the refining of Chinese script morphology Mg_2Si particles is crucial.

Due to the high congruent melting point of Mg_2Si phase, the only possible way for reasonable diffusion is seen as the α-Mg/ Mg_2Si interface [54]. Spheroidization tendency of Mg_2Si particles during solutioning is ascribed to diffusion of Si atoms along this interface [11,41]. In addition, it should also be mentioned that the dissolution of $Mg_{17}Al_{12}$ phase may affect the spheroidization process of Mg_2Si, since the diffusion of Al atoms may have an influence on Mg_2Si phase, which is generally formed together with $Mg_{17}Al_{12}$ precipitates near the grain boundaries during solidification in the as-cast condition [54]. Lü et al. [57] also pointed out spheroidization tendency of Mg_2Si after solution heat treatment at 420 ^oC for 24 h in comparison to 0.5 h of this treatment. The spheroidization tendency of permanent mold cast Mg-6Al-1.5Si alloy at these treatments is given in the optical microscope images (Fig. 2.14). As understood in Fig. 2.14 (b), 24 h solutionizing heat treatment resulted in the disconnection in branches of "Chinese script" phase and spherodiaztion at the tips of this phase [57]. Mazraeshahi et al. [52] reported that steady state creep rate of Si added AZ61 alloy decreased with increasing Si content. This increase was ascribed to the Mg_2Si phase formed both on Chinese script and modified morphologies as indicated in Fig. 2.15 [11,44].

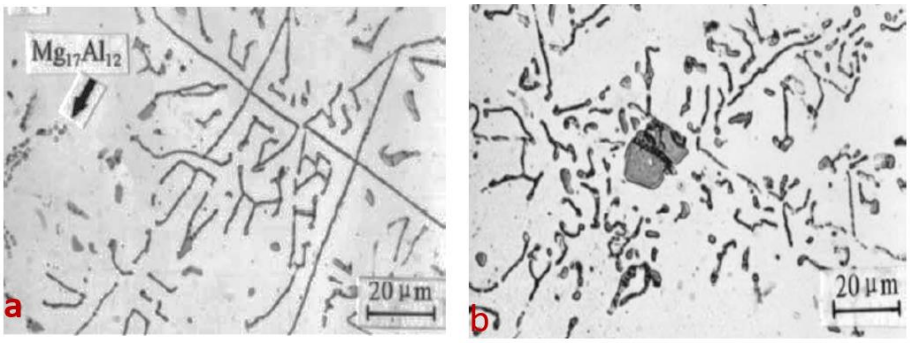

Fig. 2.14 Optical images of Mg-6Al-1.5 Si alloy with different solution treatment time (a) 0.5 h (b) 24 h [57]

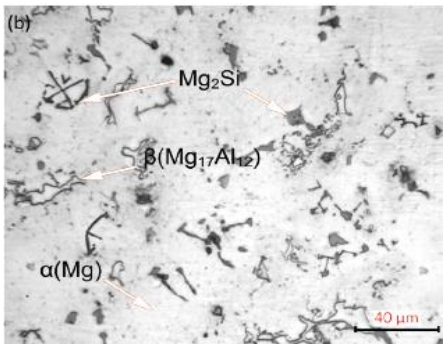

Fig. 2.15 Optical micrograph of AZ61-0.8Si alloy [52]

2.6.4.1 Effect of Si on Microstructure of Mg-Al Alloys

There are several elements such as Ca, P, Sr, Sb reported in the modification and/or refining of Chinese script Mg_2Si phase in Si containing Mg-Al alloys. Nevertheless, some studies claimed that Sb is not an effective modifier for Mg_2Si phase, that addition of Ca causes casting defects such as hot-crack, that addition of P generates ignition and controlling the amount of P in the melt is very difficult. It was also reported that Sr and Sn additions to Mg-Al-Si alloys result in the desirable

modification and refinement of Chinese script Mg_2Si phase [58]. It was noted that morphology change of Mg_2Si from Chinese script to polygonal shape brings improves both room and elevated temperature properties [35]. The example of Si addition effect to aluminum containing magnesium alloy could be observed for Mg-5Al-1Zn-1Si for permanent mould casting shown in Fig. 2.16. This micrograph consists of Chinese script Mg_2Si phase with interdendritic β-$Mg_{17}Al_{12}$ particles in α-Mg matrix. When solution treatment applied at 420 ^oC for 10 hours, most of the β-phase dissolved in the matrix and only Chinese script Mg_2Si was observed in the microstructure as shown in Fig. 2.16 (b). It can be concluded from this result that Mg_2Si has high thermal stability at elevated temperatures [13].

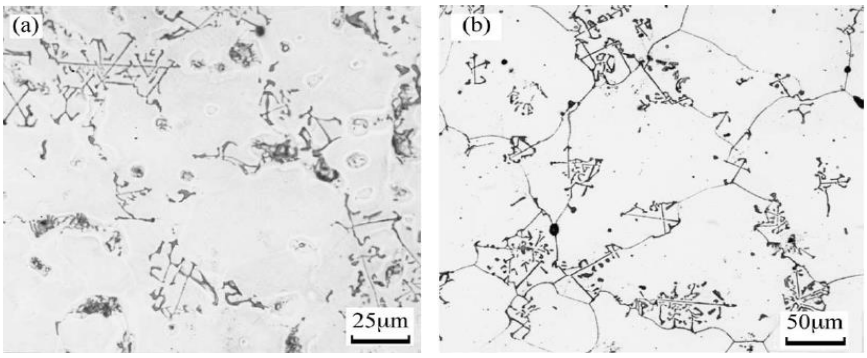

Fig. 2.16 Optical microstructural images in permanent mould castings (a) as-cast Mg-5Al-1Zn-1Si alloy (b) solution heat treated Mg-5Al-1Zn-1Si alloy [13,47]

2.6.4.2 Effect of Si on Strength of Mg-Al Alloys

The morphology of the Mg_2Si phase is the indicative for contribution effect to strengthening. The Chinese script Mg_2Si precipitate causes the separation of matrix, which leads to crack initiation sites. This effect results in the deterioration of tensile properties at RT and impact toughness with increasing silicon content. However,

polygonal or square-like morphology of Mg_2Si phase is beneficial to these properties. [11,37,50] The SEM image of tensile fracture surface of Mg-6Al-1Si tested at RT is given in Fig. 2.17 (a). The square like particle seen on the center of the SEM image is verified as Mg_2Si phase by EDS analysis. It can be concluded from this image that the grain boundaries on each side of Mg_2Si particle were pinched while main crack follow its path [48].

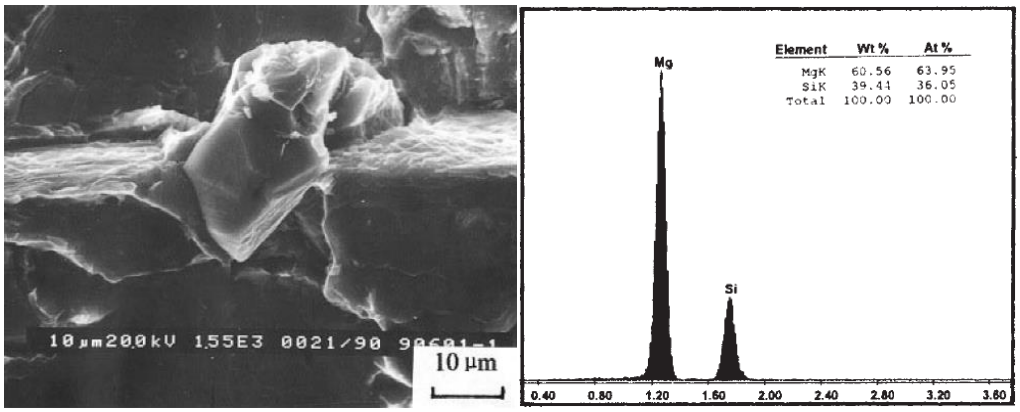

Fig. 2.17 Mg_2Si particle observed between two grains (a) SEM image (b) EDS result [48]

Due to the brittle nature of Chinese script morphology Mg_2Si precipitate, impact toughness of the alloy gradually decreases with increasing silicon content [48]. The increase of yield strength in Si added Mg-Al alloys can be ascribed to the dispersion strengthening of Mg_2Si particles and solid solution strengthening of Si elements in α-Mg matrix [60]. The reason for enhancement in creep resistance was attributed to the hindering of slip interface and dislocation climb at high temperature via Mg_2Si phase [59].

Due to the lattice constants and crystal structure difference between α-Mg and Mg_2Si phases, it was not expected to form coherent state between them. However, the increase in the strength could be attributed to the following reasons:

1) Enhancement in dislocation density: the thermal expansion coefficient difference between α-Mg and Mg_2Si and Mg_2Si could cause higher dislocation density in the microstructure. The increase in strength can be achieved by enhanced dislocation, which acts as a barrier for dislocation motion.
2) Load transfer path difference: The path of stress change from α-Mg to Mg_2Si phase could bring the enhancement in tensile strength due to higher strength of Mg_2Si than that of α-Mg [59].

The mechanical property variation with the addition of Si to AZ91 alloy was studied by Srinivasan et al. [40]. It was concluded that the coarse Chinese decreases the mechanical properties especially the ductility. The difference in mechanical properties at RT is presented in Fig. 2.18.

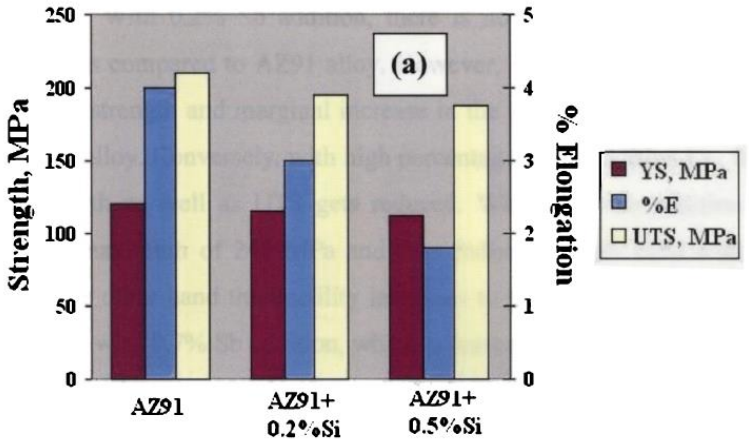

Fig. 2.18 Tensile property change of Si added AZ91 alloy [40]

2.6.4.3 Modification of Mg_2Si phase with Alloying Elements

Sr is known as perfect modifier for Si particles in Si containing Al alloys. Based on this information, Sr is also considered as a good modifier for Mg_2Si precipitates in Si containing Mg-Al alloys and verified by Wang et.al. [11, 15]. Effect of Sb, Sn, and Sr on the as-cast microstructure and mechanical properties of AZ61-0.7Si magnesium alloy was studied by Pans's group in CCMg. The result of this study has indicated that addition of 0.4 wt%Sb or 0.6wt% Sn to AZ61-0.7Si alloy could provide refinement in the Chinese script Mg_2Si phase in the microstructure. On the other hand, in this study, it was observed that small Sr addition can clearly result in both modification and refinement of Mg_2Si phase. (Fig. 2.19) The effect of Sr on this alloy was explained with easy segregation of Sr in Mg melt due to low solid solubility and formation of adsorption film layer on Mg_2Si phase surface [11].

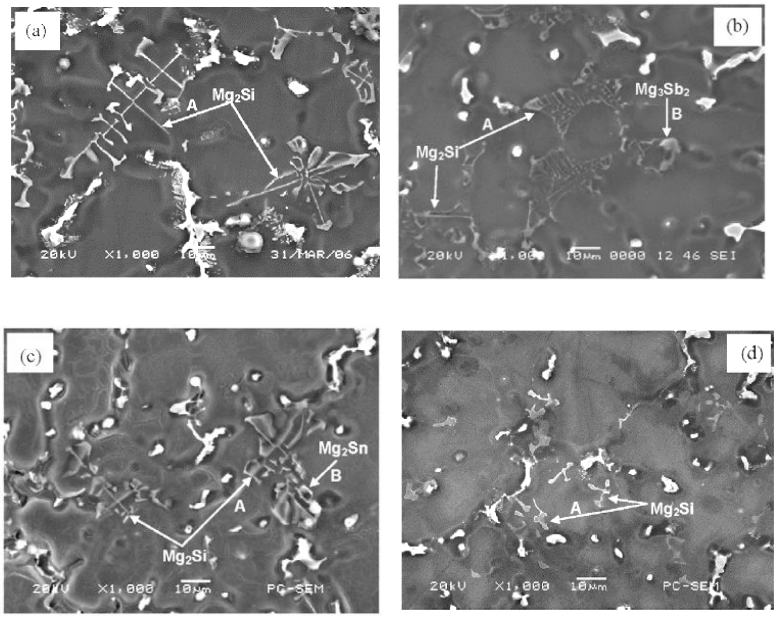

Fig. 2.19 SEM images for the AZ61–0.7Si alloy (a), AZ61–0.7Si–0.4Sb alloy (b), AZ61–0.7Si–0.6Sn alloy (c) and AZ61–0.7Si–0.09Sr alloy (d) [7,14]

The mechanical of the studied alloys (STJU-HM1 (5.0Al-0.90Zn-0.7Si-0.4Sb-0.2RE), AE42 and AZ91) are given in Table 2.5. The improvement in mechanical properties with the addition of Sb and Si could be attributed to the following reasons: 1) decrease in grain size 2) morphology change of Mg_2Si from Chinese script to polygonal shape 3) fine particle dispersion strengthening with Mg_2Si and Mg_3Sb_2 [56]

Table 2.5 Mechanical properties of permanent mould cast alloys [56]

Alloy	RT Tensile			150 ^oC Tensile			Apparent Toughness A_k (J)
	UTS (MPa)	YS (MPa)	El. (%)	UTS (MPa)	YS (MPa)	El. (%)	
SJTU-HM1	235	108	9	178	99	14	28
AE42	202	97	12	165	91	22	20
AZ91	234	110	3	175	96	20	15

The effect of Sb and Ca addition to Mg-5Al-1Zn-1Si on the mechanical properties could be compared with the help of Table 2.6. According to this table, Ca and Sb addition improve the yield strength, ultimate tensile strength, elongation and fracture toughness in comparison to base alloy. Increase in the ultimate tensile strength could be both due to the grain refinement and morphology change in Mg_2Si particles. Since coarse Chinese script Mg_2Si causes easy crack nucleation on the interface of Mg_2Si particles and α-Mg matrix, fine polygonal shape particles could possibly increase the elongation and ultimate tensile strength values [13,47]. Pekguleryuz et al. [9] has proposed that addition of low amount Ca (0.08-0.14%) to AS41 alloy helps to modify Mg_2Si phase to increase ductility and strength.

The optical microscope image of AZ91-0.5Si-0.1Sr given in Fig. 2.20 shows the morphological change of Mg_2Si phase from Chinese script to an irregular shape, which is indicated by an arrows on the figure. The average size (in terms of area) of the precipitates before and after refining was measured as 320 and 75 μm^2,

respectively. X-ray mapping performed on the area given indicated that Sr may be dissolved in Mg_2Si particles for modification [14].

Table 2.6 Mechanical properties at ambient temperature of Mg-Al-Zn-Si-X Alloy

Alloy [13]	Mg-5Al-1Zn-1Si	Mg-5Al-1Zn-1Si-0.5Sb	Mg-5Al-1Zn-1Si-0.25Ca
YS (MPa)	92	99	97
UTS (MPa)	223	235	240
El. (%)	11.6	12.7	17.8
Apparent fracture toughness, A_k (J)	21	30	24

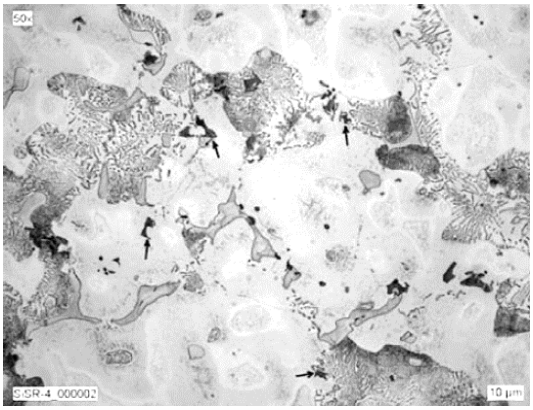

Fig. 2.20 Microstructure of AZ91 alloy containing 0.1% Sr [14]

2.6.5 Effect of Sr alloying on Magnesium Alloys

Sr is considered as a good modifier for Mg_2Si precipitates in Si containing Mg-Al alloys [14]. Moreover, Sr is another element like Si that can be added together with aluminum to improve the creep resistance and high temperature strength. It was also reported that grain refinement effect can be observed with minor Sr addition

[9,12,25,52,54]. The Sr solubility in the AZ91 matrix is low, approximately 0.11%, the excess Sr dissolving in the grain enriched in front of the grain growth interface during solidification. Thus, Sr forms the thin film formation on the boundaries of growing crystals causing a reduction of the grain growth rate, and therefore, the fine grain structure formed [12,18,51,53,64]. Nevertheless, RT tensile strength of the developed Mg-Al-Sr was lower than that of Mg-Al-Zn alloys [12]. In addition to this, Lee et al. [65] pointed that the effect of Sr addition to AZ91D alloy had a negligible effect on grain size. The main changes in the microstructure resulted from Sr addition were the refinement of the β-($Mg_{17}Al_{12}$) phase in the as-cast alloys and decrease in average grain size [12].

Pekguleryuz et al. [47] explained that surface active elements for alloying of magnesium is responsible to decrease its surface energy by segregating to the surface like the interface between matrix phase and second phase paticles, liquid metal surface or grain boundaries. The main driving force for surface segregation of the alloying elements was proposed to decrease the surface energy of the added alloy system. Pekguleryuz et al. [47] proposed that Sr, Ca, Ce, Nd and Sn could be the surface active elements to reduce the surface energy of magnesium and surface tension of magnesium.

Fig. 2.21 illustrates the effects of different alloying elements on surface tension of liquid magnesium. As seen in this figure, the surface tension of liquid magnesium decreases gradually with increasing Sr content. Sr brings the improvement in interdendritic feeding during solidification. Therefore, reduction or morphology change in shrinkage microporosity is expected with Sr addition. (Fig. 2.22) Pekguleryuz et al. [47] proposed that Sr eliminates the bulk microporosity formed during solidification by feeding interdendritic region. Interdendritic region feeding problem is faced with in long freezing range alloys such as AZ91 [47,66]. (Fig. 2.22)

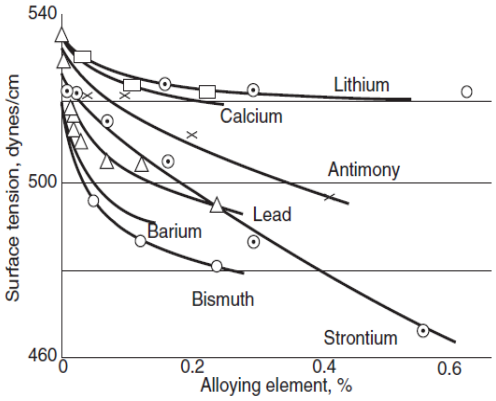

Fig. 2.21 Effect of alloying element on surface tension of liquid Mg [47]

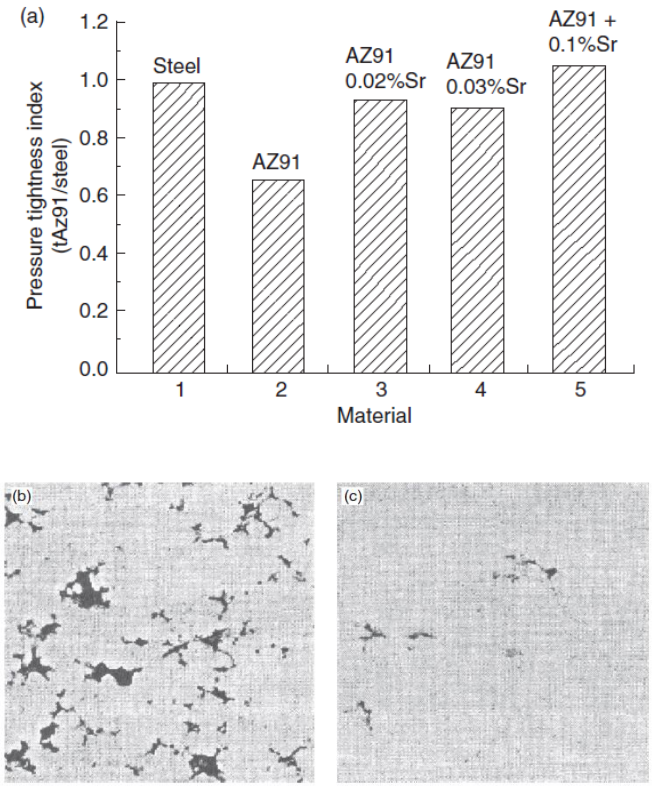

Fig. 2.22 (a) Pressure tightness comparison of AZ91,Sr added AZ91 in different levels and steel (b) die cast AZ91 (c) die cast AZ91-0.03%Sr [47]

Zhao et al. [12] indicated that solution strengthening may be one of the factors that Sr strengthens the AZ91 based alloy. EDS analysis of α-Mg matrix indicated that increase in Sr addition results in rising content of Sr on α-Mg matrix. Further addition would only cause the conglomeration of Sr on the grain boundaries due to its low solid solubility, which is detrimental for the elongation. Yang et al. [67] found that thermal stability of β-$Mg_{17}Al_{12}$ phase increased with both Sr and Ca addition dissolved into this phase as solid solution.

In another study, Wang et al. [11] showed that the typical microstructure of AS31 and effect of addition of 0.2 and 0.4 %Sr on AS31 microstructure shown in Fig. 2.23. AS31 magnesium alloy formed from α-Mg matrix, divorced eutectic β-$Mg_{17}Al_{12}$, massive primary Mg_2Si and Chinese script eutectic Mg_2Si with a coarse dendritic morphology (Fig. 2.23 (a)). The addition of 0.2 wt% Sr to AS31 alloy results in the morphology from Chinese script Mg_2Si to irregular blocky shape (Fig. 2.23 (b)). Chinese script Mg_2Si phase was almost eliminated with 0.4 wt% Sr addition (Fig. 2.23 (c)).

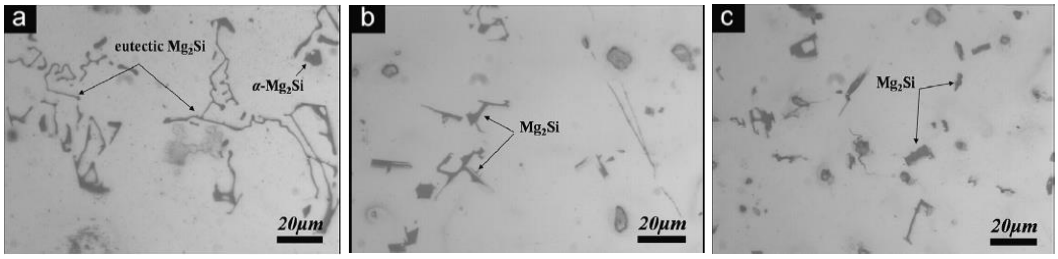

Fig. 2.23 As-cast microstructure of AS31 alloys and those with Sr addition: (a) 0, (b) 0.2, (c) 0.4. [11]

2.6.6 Effect of Ca alloying on Magnesium Alloys

Calcium addition is also known by improving creep resistance element for Mg-Al alloys [29,54]. In addition, it also increases the oxidation resistance of molten magnesium together with preventing the magnesium alloy's ignition [20,25,58,59]. In the perspective of internal quality improvement, Ca addition to zinc containing magnesium casting alloys such as AZ92 and AZ63 before pouring helps to reduce microporosity and decreases the solution heat treatment time. On the other hand, calcium addition is also the responsible for the formation of metallic foams skin containing bubbles. In addition to this, partially oxidized metal during melting settled down on the cope surface of the casting as a result of turbulence flow. High calcium amounts result in coarse grained castings and hot cracking susceptibility along grain boundaries [25,60]. However, Ca has a grain refinement effect on AZ91D magnesium alloy due to its impeding effect on grain growth of α-Mg during solidification by segregation on grain boundaries [54,69,80,95]. Ca also has a modification effect on Chinese script morphology Mg_2Si phase as seen in Fig. 2.24 [13].

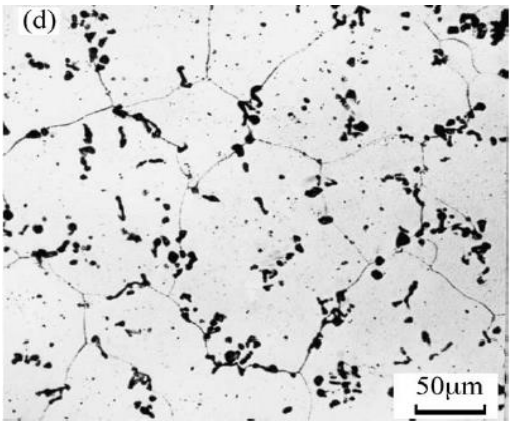

Fig. 2.24 Optical microstructural images in permanent mould castings heat treated Mg-5Al-1Zn-1Si-0.2Ca [13]

According to the study performed by Tang et al. [70], although Ca addition to AZ91D improves the mechanical properties, the possibility of hot crack formation in 1 wt.% Ca added AZ91D alloy in comparison to AZ91D increases approximately three times due to lower grain boundary tension of the liquid film for Ca containing phases. Moreover, feeding resistance of AZ91D worsens with Ca addition, which causes the decrese in filling capacity [58, 60].

Hirai et al. [73] investigated the effect of Ca addition on AZ91 alloy together with Sr addition. The optimal concentration for Ca and Sr addition has been found as 1.0 and 0.5 wt. %, respectively. The average grain size after this addition decreased from 65 to 19 μm. The study performed to see the effect of Ca addition on Mg-Si by Moussa et al. [63] indicated that segregation of Ca atoms at the advancing solid/liquid interface would hinder the growth of Mg_2Si phase during solidification. In addition to this, Ca atoms detected in Mg_2Si in this study proposed that Ca decreases the surface energy of Mg_2Si phase formation with lattice distortion due to much larger atomic radius of Ca atoms in comparison to Mg ad Si atoms. This effect brought to suppression of growth in preferred habit and growth of Mg_2Si phase [74].

Liu et al. [8] also found that the addition of minor Ca amount to Si containing magnesium alloys results in $CaSi_2$ phase formation. Moreover, the standard Gibbs free energy of $CaSi_2$ is lower than that of Mg_2Si, - 122.299 Kj/mol and - 61.345 Kj/mol, respectively. Therefore, it can be deduced that the formation of $CaSi_2$ particles wrapping inside of Mg_2Si particles during solidification could be heterogeneous nucleation sites for the formation of Mg_2Si phase [8].

2.6.7 Effect of Sn alloying on Magnesium Alloys

Tin (Sn) is preferred in small amounts to improve the ductility of magnesium alloys [30]. It has low diffusivity in magnesium ($10x10^{-14}$ m/s^2), low solid solubility in Mg and high liquid solubility in Mg melt (100 % at 800 ^0C). In addition to these, Mg_2Sn increases the creep resistance of magnesium alloys due to its high melting temperature [50].

Even though the solid solubility of Sn in magnesium is in high amount (~14.8%), enrichment of liquid ahead of Mg_2Si growing interface causes the restriction of Mg_2Si growth during solidification process. The disregistry factor between Mg_2Sn and Mg_2Si is 6.32%, which is less than the critical limit (15 %) for heterogeneous nucleation site formation. Due to this reason, Mg_2Sn phase could act as a nucleus for Mg_2Si particles. In addition, the other possible reason for modification of Mg_2Si with the effect of Sn addition could be due to the decrease in undercooling degree [7].

2.6.8 Effect of RE alloying on Magnesium Alloys

Rare Earth (RE) elements are added to magnesium as mischmetal or didymium. Since direct RE element addition is expensive, a cheaper solution has been found in the industry as “Mischmetal”, which is formed from mixture of several rare earth elements such as cerium (Ce), lanthanum (La) and neodynium (Nd). In addition to this, in order to meet individual addition of rare earth elements, many new master alloys are being developed such as gadolinium (Gd) and Nd master alloys. Due to very low solubility of rare earth elements in magnesium, they usually form intermetallic compounds with magnesium. RE additions also decrease the

solidification range of the alloys, provide feeding easier and also enhance the high temperature properties of magnesium alloys [9,25,40].

Although the RE elements actually decrease the mechanical properties such as yield and tensile stresses for a given zinc content, they enhance castability, weldability and creep properties [20]. Rare earth elements in magnesium alloys decrease the weld cracking possibility and porosity due to narrowing the freezing range of the alloys [25]. Although rare earth elements confer long term creep resistance up to about 250 ^{0}C, cast alloys show low tensile properties unless grain refined with zirconium. They contribute suppressing microporosity and offsetting the brittleness due to zinc in some alloys, but, do not themselves contribute to ductility. Amount of RE addition should be kept at least optimum level in order to minimized cost [20,29].

Liu et al. [8] proposed that adding rare earth elements (RE, eg. Gd, Y, Nd, Sm, Dy) to aluminum containing magnesium alloys improves elevated temperature and creep properties due to the reduction in β-($Mg_{17}Al_{12}$) phase and modification effect on this phase. In the perspective of creep resistance, formation of new thermally stable precipitates such as $Al_{11}RE_3$ and Al_2RE with high melting temperature brings the pinning effect on grain boundaries at elevated temperature, which results in improvement in creep resistance [8,52]. The addition of Ca and Gd to Mg-7Al-1Si alloy not only brings the formation of some new phases such as $CaSi_2$, CaMgSi and Al_2Gd but also provides obvious modification of β-$Mg_{17}Al_{12}$ phase and Mg_2Si particles. Al_2Ca phase has negative effect on mechanical properties [8].

2.7 Solidification of Alloys

Casting properties such as fluidity and hot tearing could be predicted and correlated by solidification behavior [30]. The ability of the metal's filling the mold and reproducing the features is defined as fluidity. As a general approach, pure metal and eutectic compositions have higher fluidity. In addition, fluidity is directly related with pouring temperature. Experiments with magnesium alloys show that fluidity and superheat have exponential relationship. Small alloy addition to magnesium decreases the fluidity of magnesium while fluidity recovers with higher amount of alloying with aluminum, zinc and RE. Silicon is the other element as reported to improve fluidity of magnesium [30]. It is very important to obtain and understand solidification characteristics of the alloys and alloying element on solidification behavior. Phase diagrams could also be used as basics however, wide variety of cooling rates due to non-equilibrium cooling conditions push to obtain actual data while the alloy solidifies in actual condition to understand the solidification sequence and the corresponding temperatures. At the same time, the degree of undercooling get form the cooling curve is the other vital factor to be controlled for the refinement of magnesium alloys [20, 25,27, 50, 64,74].

Another aim of the obtaining cooling curve is to find the freezing range of the studied alloys. Since this parameter gives a clue about the hot tearing susceptibility and fluidity of the alloys. Long freezing rage alloys are more susceptible to hot tearing. The reason is to keep in mushy state for a considerable period after pouring. This allows tensile/shear stress originating from contraction restraints, which results in propagating crack/tears. Aluminum containing magnesium alloys are less susceptible to hot tear than those with zinc and rare earth elements. In addition, decreasing aluminum content in Mg-Al alloys increases the tendency of hot tear. Additions of rare earth elements (RE) to Mg-Al alloys, especially above 1.2 wt% RE,

significantly increase hot tearing susceptibility. Since RE elements cause grain coarsening, it also decreases the fracture strain necessary for hot tear initiation.

Grain refining efficiency of an added nucleant could also be determined by using the cooling curves obtained during solidification of melt. The degree of undercooling is an indirect measure of efficiency of grain refinement. As indicated in 2.8.1.1, lower undercooling degress results in the decrease of the critical nucleus radius (r^*). Due to this reason, a smaller undercooling by a grain refiner addition with respect to the unrefined alloy shows the easy nucleation mechanism in the melt. The relative amount of the undercooling is a good indicative for the determination of grain refiner effectiveness [79].

The basic cooling curve parameters used on the thermal analysis are defined below and shown on an actual cooling curve in Fig. 2.25. θ_n helps to get information about the first nucleation temperature while $\Delta\theta_{rec}$, t_{rec} and LPP provides the degree of recalescence. LPP is related with both $\Delta\theta_{rec}$ and t_{rec} [80].

θ_n: initial temperature for start of primary dendrites nucleation
θ_{min}: unsteady state growth temperature
θ_g: recalescence of steady state growth temperature due to the release of latent heat of primary α-Mg
$\Delta\theta_{rec}$: recalescence undercooling, the difference between θ_{min} and θ_g
t_{rec}: duration of recalescence
LPP: liquidus peak parameter where $d\theta/dt>0$

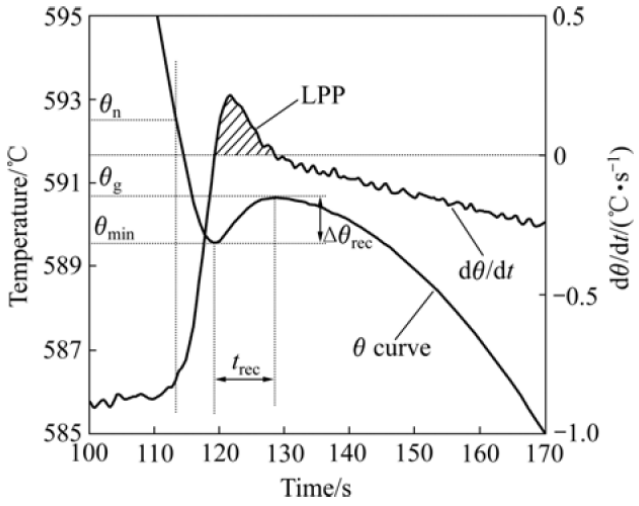

Fig. 2.25 Segment of cooling curve with illustration of critical parameters [80]

2.7.1 Solidification Sequence and Microstructure of Mg-Al-Zn Alloys

Mg-Al binary phase diagram provides the basic understanding of the phase constitution and equilibrium solidification behavior of the Mg-Al-Zn based alloys. The small zinc addition to binary Mg-Al alloys has no significant effect on the structure of these alloys. However, when Zn/Al ratio exceeds 1:3, a ternary Mg-Al-Zn phase formation is observed [30].

As-cast microstructures of AZ91 alloy under at different cooling rates 0.03 ^{0}C/s, 1 ^{0}C/s and die casting conditions are provided in Fig. 2.26 (a), (b), and (c), respectively. For the slowest cooling rate (near-equilibrium) condition, partially divorced eutectic microstructure [α-Mg + β-$Mg_{17}Al_{12}$] is observed. It is assumed that the lamellar β-$Mg_{17}Al_{12}$ formation is finished after solidification completion via discontinuous precipitation from α-Mg supersaturated solid solution. This lamellar structure is not detected in higher cooling rates condition as seen in Fig. 2.26 (b) and

(c). In addition, it is significant that β-$Mg_{17}Al_{12}$ precipitates in divorced morphology result in better mechanical properties than the lamellar structure [30]. The non-equilibrium solidification sequence for AZ91 alloy is listed in Table 2.7 [30]. The study conducted by Ohno et al. [81] has also shown three different phase transformation temperature performed with different equipments as provided in Table 2.8. These results are consistent with the data obtained in Table 2.7.

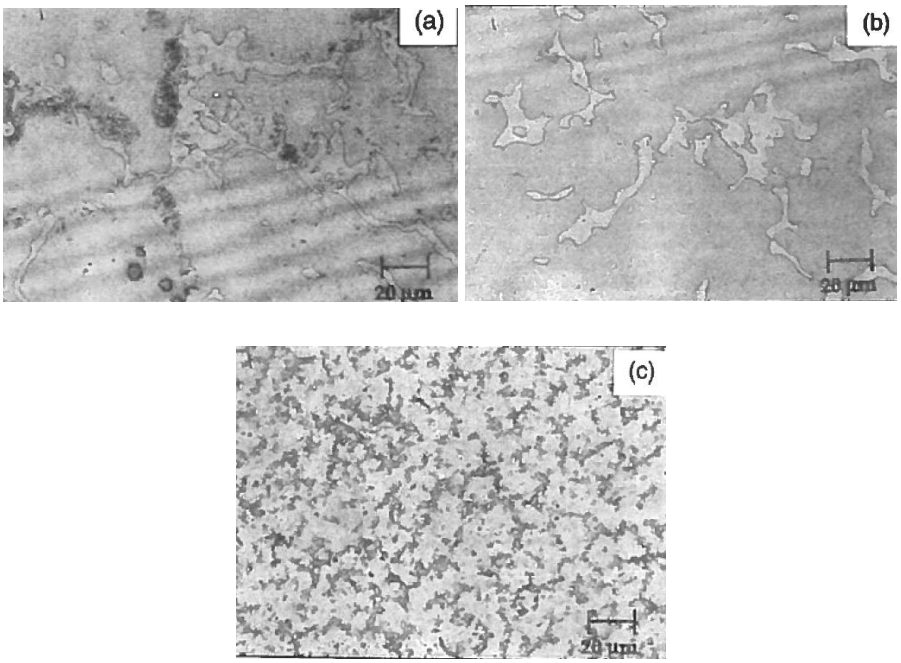

Fig. 2.26 Optical micrographs of the as-cast microstructure of AZ91 alloy under the cooling rates of (a) 0.03 ^{0}C/s (b) 1 ^{0}C/s and (c) die casting [30]

Table 2.7 Non-Equilibrium solidification sequence of AZ91 alloy [30]

Temperature	Transformation Reactions
T_L= 601-593 ^{o}C	Start of α-Mg nucleation: L= α-Mg + L
T_L-T_E	Growth of α-Mg phase: L= α-Mg + L
T_E = 434 ^{0}C	Divorced eutectic reaction: L = α-Mg + Mg + $Mg_{17}Al_{12}$

Table 2.8 Signal temperatures for AZ91 measured with a technique of DSC and DTA systems (^{0}C) [81]

	α-Mg nucleation	Divorced eutectic reaction $Mg_{17}Al_{12}$ precipitation temperature
DSC 1	598	434
DSC 2	595	433
DTA	599	436

Table 2.9 summarizes the solidification temperature range of the studied alloys, where the liquidus temperature of AZ91 markedly decreased with the addition of Sr and B, but no obvious change in solidus temperature was detected. The decrease in solidification range may be another reason to observe in the improvement of fluidity. The following conclusions can be the reasons of improvement in the fluidity [12].

Table 2.9 Solidification temperature ranges of AZ91, AZ91-0.5%Sr and AZ91-0.5%Sr-0.09%B [12]

Alloys	Solidus (^{0}C)	Liquidus (^{0}C)	Freezing Range (FR)
AZ91	435	596	161
AZ91-0.5%Sr	436	580	144
AZ91-0.5%Sr-0.09%B	437	580	143

2.7.1.1 Cooling Curve Analysis of Aluminum Based Magnesium Alloys

Fig. 2.27 indicates the typical cooling curve and its first derivative curve of AZ91 alloy under a cooling rate of 0.06^{0}C/s. The plateau temperatures (discontinuities) in the cooling curve and their corresponding valleys in the first derivative curve as in Fig. 2.27 (a) and Fig. 2.27 (b), respectively, the liquidus (T_L) and solidus (T_S) temperatures are easily obtained. In this cooling rate, T_L and T_S are determined as 600 and 435 ^{o}C for AZ91 alloy, respectively. Moreover, the liquidus and solidus

temperatures at different cooling rates are represented in Table 2.10 for AZ91 alloy. The cooling rates given in Table 2.10 corresponds to several magnesium casting methods: plaster casting (0.03-0.06 ^{0}C/s), sand casting (~0.4 ^{0}C/s), permanent mold casting (0.4-10 ^{0}C/s) and die casting (>50 ^{0}C/s). It can also be concluded form this table that the determination of solidus (T_S) at high cooling rates are nearly impossible due to the severe microsegregation at higher cooling rates. The solidus temperature (T_S) actually represents the non-equilibrium eutectic temperature (T_E) for the phase transformation of L = α-Mg + $Mg_{17}Al_{12}$ (β). This value is also comparable with the equilibrium eutectic temperature of 437 ^{o}C in Mg-Al binary phase diagram [30].

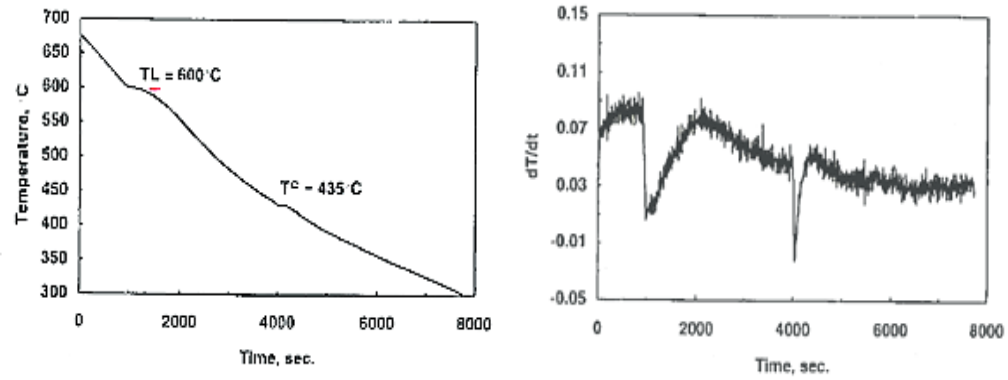

(a) (b)

Fig. 2.27 (a) Typical cooling curve for AZ91 alloy under a cooling rate of 0.06 ^{0}C/s (b) the first derivative of the cooling curve [30]

The cooling rate of sand casting magnesium for AZ91D alloy was reported between 0.22-0.32 ^{0}C/s. The cooling rate with chill block is evidently higher than without chill block system as expected as shown in the result given Fig. 2.28. The highest cooling rate (0.93^{0}C/s) was obtained by the side of chill location. Cooling rates, ε, in this study was defined as $\varepsilon = (T_L - T_E)/\Delta t$, where T_L and T_E are liquidus and

equilibrium eutectic temperatures, respectively. Δt was described as the elapsing time between these temperatures [28].

Table 2.10 Liquidus and solidus temperatures for AZ91 alloy under different cooling rates [30]

Cooling Rate (dT/dt, ^{0}C/s)	0.03	0.06	0.4	7.8	20.6	41.1
Liquidus (T_L, ^{0}C)	600.2	600	599.5	598	595.5	593.8
Solidus (T_S, ^{0}C)	435	435	430	328	-	-

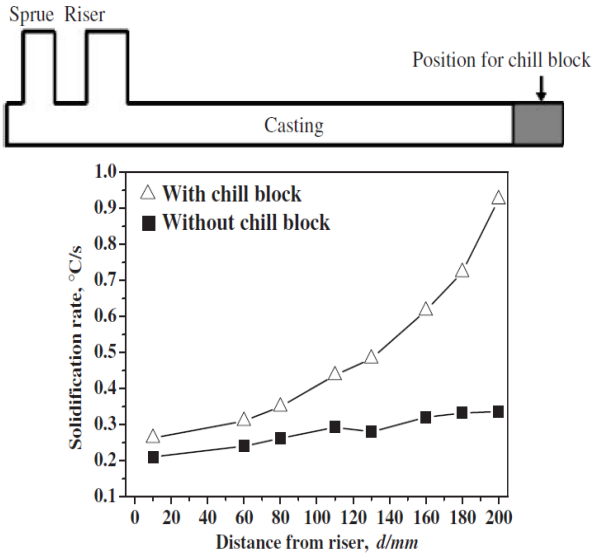

Fig. 2.28 Cooling rate determined as a function of distance from riser**.** The view given above the figure indicates the lateral section of the experimental plate in the sand molding system [28].

St John et al. has also reported the freezing range of AZ91 as 160 ^{o}C in comparison to 30 ^{o}C for A356 (Al-7wt%Si) aluminum alloy. In addition, volume fraction of eutectic is approximately 25% in magnesium while 50 % eutectic is measured in that of aluminum alloys. These may result in the formation of defect like structure such as gas porosity, shrinkage porosity and segregation [27].

Summary of the thermal data in the cooling curve for AZ91 alloy with and without carbon inoculation is summarized in Table 2.11 [80]. These results propose that grain size decreases with increasing θ_n and decreasing the values of $\Delta\theta_{rec}$, t_{rec} and LPP. The refinement mechanism with carbon inoculation was proposed as Al_2CO formed as a result of a reaction between Al and CO_2 appeared by decomposition of added magnesite [80].

Table 2.11 The thermal analysis data obtained from the cooling curves of AZ91 with and without carbon inoculation [80]

Alloy	θ_n (^{0}C)	θ_{min} (^{0}C)	θ_g (^{0}C)	$\Delta\theta_{rec}$ (^{0}C)	t_{rec} (s)	LPP	Average grain size (μm)
AZ91	598.9	592.4	592.8	0.4	5.8	0.39	175
AZ91-C	605.1	594.2	594.3	0.1	2.4	0.06	85

2.8 Grain Refinement of Magnesium Alloys

Grain refinement is known as the best method to increase mechanical properties of the alloys. The major advantages of grain refinement are as followed:

(a) homogenous porosity distribution with small interconnected holes
(b) increases feeding behavior while reducing segregation
(c) machinability improvement

(d) uniform mechanical properties
(e) increasing castability
(f) more homogeneous distribution of second phases
(g) surface finish improvement in as-cast surfaces and subsequent machining surfaces [24,59,70,71,81]

The grain size of polycrystalline materials is mainly determined with the number of potential nuclei in the melt, thermal and constitutional undercooling created at the advancing solid/liquid interface [83]. The main effect of solute element addition is to both control the growth of nucleation grains and the subsequent nucleation mechanism, which could be explained in terms of GRF value. The constitutional undercooling created by solute element addition hinders the grain growth by decreasing diffusion of alloying elements. Due to the high GRF values, some alloying elements such as Al, Zr, Sr, Si and Ca have been observed as obvious grain refiner for pure magnesium [85]. Lee et al. [54] also reported that Zr, Si and Ca additions to pure magnesium showed signifcat grain refinement. The grain refinement with these elements could be attributed to their GRF values (constitutional undercooling) during solidification, introducing of nucleant particles either with alloying or with secondary particle formation via reactions [65].

The calculated GRF values from binary magnesium phase diagrams are presented in Table 2.12. The GRF values for Zr, Si and Ca are higher than those of other elements such as Al, Sn and Y etc, which is mainly explained with the more powerful growth restriction for high GRF values. Therefore, it is expected to have a stronger grain refinement with the small addition amount [54,71].

2.8.1 Nucleation Theory

Grain nucleation mechanism must be discussed to understand the grain refinement. During the solidification of a metal, there is a temperature where the nucleation of solid (nucleus) starts and leads to growth of a grain. Each grain starts to grow in an order to form its own nucleus. Therefore, the number of grains is directly related with the number of nucleus forming at the nucleation temperature.

Table 2.12 The calculated GRF (m(*k*-1)) values from slope of liquidus line (m), equilibrium distribution coefficient (*k*) for various alloying elements in magnesium [54,71]

Element	m	*k*	m(*k*-1)	System
Zr	6.90	6.55	38.29	peritectic
Ca	-12.67	0.06	11.94	eutectic
Si	-9.25	~ 0.00	9.25	eutectic
Zn	-6.04	0.12	5.31	eutectic
Ge	-4.41	~ 0.00	4.41	eutectic
Al	-6.87	0.37	4.32	eutectic
Sc	4.02	1.99	3.96	peritectic
Sr	-3.53	0.006	3.51	eutectic
Ce	-2.86	0.04	2.74	eutectic
Y	-3.40	0.50	1.70	eutectic
Sn	-2.41	0.39	1.47	eutectic

There are two types of grain nucleation mechanism, which are homogeneous and heterogeneous, to initiate the solidification of a liquid metal. The nucleus starts to solidify from the bulk of the liquid in homogeneous nucleation. However, a foreign particle must exist in the liquid for heterogeneous nucleation. Brief information about these nucleation mechanisms are given in the subsection below [65,72,73]. In addition, it should be noted that the nucleation does not occur at the freezing temperature of metal due to the non-equilibrium nature of solidification.

2.8.1.1 Homogeneous Nucleation

The main issue for homogeneous nucleation is related with the energy to create a minute solid particle in the liquid. The clustering of small atom groups called as nuclei is the sign of liquid metal solidification. The nuclei formation starts at the temperature, T, which is lower than the equilibrium melting temperature, T_m. This means that undercooling acts as a driving force for nucleation. Due to this reason, the liquid metal must be undercooled to achieve liquid to solid phase transformation. The shape of the homogeneous nucleus shall be spherical with a radius, r, as indicated in Fig. 2.29. The composition of the formed nucleus has the same chemical composition with the bulk liquid.

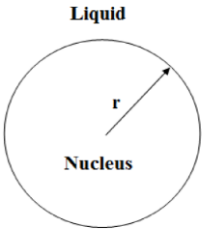

Fig. 2.29 Schematic representation of homogeneous nucleation [88]

The starting of the solidification needs a free energy change. Energy related with the formation of the spherical form nucleus is given below:

- ΔG_v = The net free energy necessary to phase transformation from liquid to solid
- γ_{sl} = The interfacial tension of the solid-liquid interface

The net bulk free energy is necessary for the formation of a spherical nucleus given below:

$$\Delta G_v = \Delta H - T\Delta S \quad (2\text{-}1)$$

Where,

ΔH = the change in enthalpy= latent heat of fusion per unit volume L_v

ΔS = change in entropy = $\frac{L_v}{T_m}$

L_v = Latent heat of fusion per unit volume

T_m = Melting point of the liquid

Equation (2-1) could also be replaced with the following equation:

$$\Delta G_v = L_v - T\frac{L_v}{T_m} \quad (2\text{-}2)$$

when the temperature $T < T_m$, ΔG_v becomes negative, which means the spontaneous transformation from liquid to solid occurs.

The bulk free enrgy for entire sphere,ΔG_v, is [88]:

$$\Delta G_v = \Delta T \frac{L_v}{T_m} \text{ x } \frac{4}{3}\pi r^3 \quad (2\text{-}3)$$

The bulk free energy per unit volume with a given undercooling from Equation (2-3) [79]:

$$\Delta G_v = \frac{L_v \Delta T}{T_m} \quad (2\text{-}4)$$

where, $\Delta T = T_m - T$

The surface energy defined by ΔG_S is expressed as positive due the necessity of energy for formation of a surface. The surface energy can also be defined as:

$$\Delta G_S = 4\pi r^2 \gamma_{sl} \quad (2\text{-}5)$$

Therefore, the energy necessary for the formation spherical particle could be defined as the summation of net bulk free energy, ΔG_v, and surface energy, ΔG_S:

$$\Delta G_r = -\Delta G_v \text{ x } \frac{4}{3}\pi r^3 + 4\pi r^2 \gamma_{sl} \quad (2\text{-}6)$$

Equation (2-6) explains the relationship between ΔG_r and r, which are the total free energy change and particle size at any time, respectively. As seen Fig. 2.30, which is the graphical representation of Equation (2-6), the volume related free energy change (ΔG_v x $\frac{4}{3}\pi r^3$) favors the nucleation while surface related free energy change ($4\pi r^2 \gamma_{sl}$) resist the nucleation. Fig. 2.30 could be divided into two sections: $r < r^*$, and $r > r^*$, where r^* is defined as the critical nucleus radius for the progress of nucleus growth. Over the range of $r < r^*$, ΔG_r increases on the positive region of the graph up to the maximum value at $r = r^*$. After this point, $\Delta G_{T\,(r)}$starts to decrease and finally go into the negative net energy change region. However, at the points $r < r^*$, the total free energy change is positive due to the surface energy domination, which brings thermodynamically non-spontaneous liquid to solid phase transformation. Due to this reason, particles having a size less than the critical nucleus radius ($r < r^*$) cannot survive in the melt, which means it dissolves in the melt. Nevertheless, nucleus having a particle size greater than r^* ($r > r^*$) could be able to grow to form a grain. Therefore, in order to obtain stable nucleus for solidification, particle size shall be equal and greater than the critical nucleus radius [65,73].

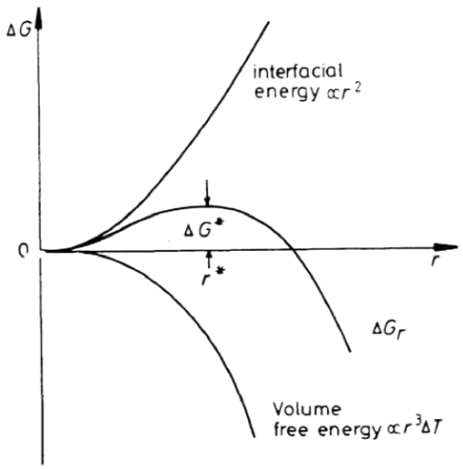

Fig. 2.30 Free energy change curve of homogeneous nucleation with a spherical radius particle having a radius r [79]

As seen in Fig. 2.30, ΔG_r reaches its maximum value at the critical nucleus size. The slope of the curve is equal to zero when the free energy change shows ΔG^*. Differentiation on both sides of Equation (2-7) with respect to the critical nucleus radius r_c gives the following Equation:

$$r^* = \frac{2\gamma_{sl}}{\Delta G_v} \tag{2-7}$$

Substitution of ΔG_v given in Equation (2-4) into the Equation (2-7) results in the formula given in (2-8). This equation shows that $r^*$and subsequently ΔG^* can be reduced by either increasing undercooling or lowering the interfacial surface energy.

$$r^* = \left(\frac{2\gamma_{sl}T_m}{L_v}\right)\frac{1}{\Delta T} \tag{2-8}$$

The necessary energy for the homogeneous nucleation, ΔG^*_{homo}, obtained from the substitution of r^* in (2-7) to (2-6) gives the following expression:

$$\Delta G^*_{homo} = \frac{16\pi\gamma^3_{N-L}}{3\Delta G_v^2} \tag{2-9}$$

2.8.1.2 Heterogeneous Nucleation

Due to the necessity of high activation energy barrier for nucleus formation in homogeneous nucleation, it takes places rarely. When any preferential sites such as impurity, mould walls, grain refiners and metal oxide inclusions present in the melt, crystallization is promoted by decreasing the energy barrier ΔG^*. According to the Equation (2-6), the only way is to decrease the interfacial surface energy. In the practical applications, heterogeneous nucleation mechanism dominates the solidification. Fig. 2.31 illustrates the mechanism of heterogeneous nucleation taking place at a mould wall. The number of atoms necessary to create a spherical cap as illustrated in Fig. 2.31 is lower than the full sphere for homogeneous nucleation given shown in Fig. 2.29.

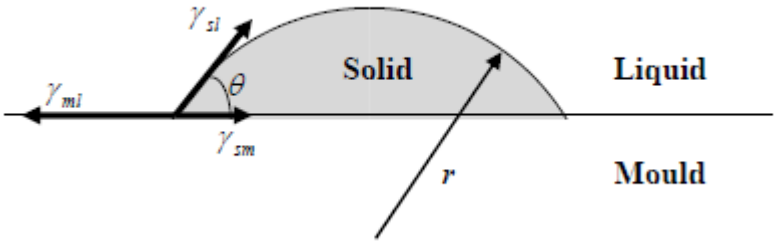

Fig. 2.31 Illustration of heterogeneous nucleation formation on a mould wall [79]

The presence of any discontinuities decreases the critical radius size (r^*). The modelling of heterogeneous nucleation according to Fig. 2.31 yields to (2-10) [79].

$$\gamma_{ml} = \gamma_{sm} + \gamma_{sl} \cos\theta \qquad (2\text{-}10)$$

Where:

γ_{ml}: Interfacial surface tension between mould and liquid interface

γ_{sm}: Interfacial surface tension between solid and mould interface

γ_{sl}: Interfacial surface tension between solid and liquid interface
θ: Wetting angle

The rearranging the Equation (2-10) for $\cos\theta$ brings the following formula:

$$\cos\theta = \frac{\gamma_{ml} - \gamma_{sm}}{\gamma_{sl}} \tag{2-11}$$

2.8.2 Undercooling and Nucleation Temperature from Solidification Curves

According to the formula given in (2-12) and (2-13), the critical nucleus r^*could be decreased with decreasing T_l, which results in the decrease of nucleation energy of crystal nucleus. These provide increase in probability of nucleation, which finally brings in the grain size and precipitate refinement.

$$r^* = \frac{2\sigma}{\Delta G_r} = \frac{2\sigma T_m}{L_m \Delta T} \tag{2-12}$$

$$\Delta T = T_m - T_l \tag{2-13}$$

2.8.3 Grain Refinement and Fading

It is a well-known fact that smaller grain size in polycrystalline materials improves the mechanical properties. In addition, grain refinement reduces the risk of casting defects such as segregation, porosity and hot tearing [89]. The proper grain refinement selection shall be based on the low addition amount consideration and refining effect even with long holding period. Therefore, the performance of the

casting could be improved with the usage of grain refinement. For many materials, the correlation between yield strength and grain size is established by Hall-Petch relationship [26,75]:

$$\sigma_y = \sigma_0 + k_y d^{-1/2} \tag{2-14}$$

where: σ_y= yield strength, σ_0 = friction stress, k_y= locking parameter, d=average grain size

Fine grain structure with a large grain boundary area provides the impeding effect for easy dislocation motion. According to the Equation (2-14), it is expected to have a higher yield strength for a fine grain structure in comparison to a coarse grained structure.

Inoculation means the introduction of nucleating agents into the melt either with directly adding a nucleus or with creating the nucleus by a chemical reaction in the melt. J. Campbell [91] and Murty et. al. [92] summarized some characteristics to obtain good refinement with suitable grain refiners:

1. The metallic or weakly covalent bonded structures such as borides, carbides and intermetallic compounds are desirable in comparison to strongly covalent bonded structures [93].
2. A good lattice match should be obtained between the nucleating solid and the grain refiner agent.
3. The grain refiner should not dissolve into the melt.
4. The grain refiner shall have a higher melting point than the alloy being solidified.
5. Nucleating particles in a sufficient amount should be spread uniformly.
6. The size of the nucleating particle shall be larger than the critical nucleus radius, which is directly related with the undercooling of the melt.

7. Grain refiner shall initiate the solidification with a very small undercooling.

The lattice match between a metal and refiner could be determined by Equation (2-15) to check the planar disregistry (δ) [76,77]:

$$\delta_{(hkl)_n}^{(hkl)_s} = \frac{1}{3}\sum_{i=1}^{3} \frac{\left| d_{[uvw]_s^i} \cos\theta_d - d_{[uvw]_n^i} \right|}{d_{[uvw]_n^i}} \quad (2\text{-}15)$$

Where:

s and n: Denotations for the substrate and the nucleated

(hkl): Low index plane

$[uvw]$: One of the three low index directions in (hkl)

θ_d: Angle between two low index directions in (hkl)

$d_{[uvw]}$: Lattice spacing in the direction of $[uvw]$

In order to obtain higher grain refinement efficiency, γ_{sm} defined in Equation (2-10) shall be lower, which also means desired a good lattice match achieved. A smaller planar disregistry particle is expected to have a better nucleating agent alternative. Lu et al [92] proposed that particles having a planar disregistry less than 12 % could act as a nucleating site. However, detailed information related with the crystallography of the nucleating particles such as lattice parameters, crystallographic structure, habit plane etc. is necessary for making an accurate lattice matching study, which is very difficult to obtain [13,64].

Addition of the solute elements into the melt is another way to obtain grain refinement. The mechanism of the refinement is the controlling of the nucleated grain growth with these elements [65]. Solute elements concentration at the interface rises with the diffusion of the added elements to the solid-liquid interface. This brings to the additional solute build-up at the constitutionally undercooled region, which provides a lower solidification temperature in comparison to low solute

regions in the melt. The constitutional undercooling in a diffusion layer ahead of solid/liquid interface hinders the grain growth with the formation of dendrite-like network in the front of melt [65, 18]. This situation can be described with using the growth restriction factor (GRF) valid for binary phase diagrams. The growth restriction factor (GRF) is defined as [94]:

$$GRF = mC_0(k\text{-}1) \tag{2-16}$$

Where:

m : Slope of the liquidus line

k: Equilibrium partition coefficient

C_0 : Initial solute concentration in the melt

It should be noted that Equation (2-16) is only valid at dilute concentration levels. [65] GRF values for all solute in the melt are additive [65]. As it is explained, the higher GRF values means higher constitutional undercooling, which provides smaller grain size in the casting. The GRF values for some elements in Mg binary system are provided in Table 2.13. Higher GRF values means slower onset of solidification and slower latent heat release. Thus, a higher undercooling before recalescence results in initiation of easier growth on more particles [46,68].

Table 2.13 Calculated GRF values for different solute elements in Mg Binary system [75,89]

Solute	Type of Binary System	GRF at C_0 (K)
Mn	Peritectic	0.32 at 2.01
Al	Eutectic	11.9 at 3
Zr	Peritectic	13.5 at 0.45
Ti	Peritectic	39.5 at 0.006

As indicated by J. Campbell [91], after the addition of grain refinement agent, it is not desired to see dissolution of the refiner in a short period. If this situation is observed, this indicates the grain refiner fading. Fading can be described as the efficiency loss of grain refiner after holding of the refiner in the melt in a long period of time. Due to the difference in density, the collapsing or floating of grain refining agents in the melt after long holding period decreases the efficiency of refinement [71,65].

The grain refinement methods for magnesium alloys can be divided into two parts: grain refining for Zr-containing and Zr-free magnesium alloys. Grain refinement is very important and essential in sand casting of magnesium alloys to achieve uniform mechanical properties and high yield strength [27]. In addition, fine and homogenous grain distribution results in uniform deformation and more isotropic mechanical properties within HCP structure [18].

2.8.4 Grain Refinement of Mg Alloys Free from Al

Zirconium (Zr) is a well-known grain refiner for Al free magnesium alloys. The main reason for this is similar lattice parameters and crystal structure of Zr in comparison to those of Mg. The typical lattice parameters with its crystal structure are provided in Table 2.14 for both Zr and Mg.

Table 2.14 Crystal structure and lattice parameters of Mg and Zr [20]

Element	Crystal Structure	Lattice Parameters (nm)
Mg	Hexagonal Cubic Packed (HCP)	a = 0.320 c = 0.520
Zr	Hexagonal Cubic Packed (HCP)	a = 0.323 c = 0.523

The planar disregistry calculation (δ) between Mg and Zr according to Equation (2-15) results in only 0.7 %, which is much smaller than the threshold value (15%) to

achieve proper nucleation agent. Due to this reason, Zr is very suitable grain nucleation agent for magnesium alloys. However, due the formation of Al_2Zr phase in Mg-Al alloys with addition Zr, nucleating potential of Zr could not be observed [71]. Kabirian and Mahmudi [95] has stated that Al_2Zr phase is formed with Zr addition to AZ91 alloy. The formation of this phase in as cast state causes the grain coarsening. Grain size also does not change during aging heat treatment because of the thermal stability of Al_2Zr phase.

Due to the necessity of grain refinement of aluminum containing magnesium alloys, an alternative grain refiner must be developed. Section 2.8.5 outlines the alternative grain refiner for Mg-Al alloys.

2.8.5 Grain Refinement of Mg Alloys Containing Al

Since there is no commercially available grain refiner for aluminum containing magnesium alloys, the current researches have been focused on to find available and effective grain refiner agents. In the recent studies, numerous grain refiners have been studied Al containing Mg alloys and summary of these studies are presented in Table 2.15. A detailed outline of the efficient methods is provided in the subsections. The grain refinement methods given in this section focused on the additions of grain refiners. Other techniques such as melt superheating, ultrasonic vibration are not mentioned due to the difficulty in industrial foundry application.

2.8.5.1 Hexachloroethane (C_2Cl_6) Addition

Hexachlorethane (C_2Cl_6) is used for the degassing of aluminum melts. Similar chemical reactions are to be expected during grain refinement of Mg-Al-Zn type alloys [21]. C_2Cl_6 has been preferred for grain refinement of Mg-Al Alloys for this reason. However, toxic gas release and burning risk after alloying with C_2Cl_6 limits its usage due to environmental and safety problems [96].

C_2Cl_6 is used as inoculant in the form of mixture of wax or fluorspar. However, in thick sections, the grain refining is not much effective as in thin sections. Therefore, much reduced mechanical properties are observed in these areas. This conclusion has also been obtained from the international material specifications. Separately cast test bars have much more higher mechanical properties with respect to the specimens cut from the castings as seen in Table 2.3 [30].

Table 2.15 Summary of grain refinement methods for Aluminum containing magnesium alloys

Technique	Mechanism	Advantage/Disadvantage	References
Hexachloroethane (C_2Cl_6) Addition	Al_4C_3 nucleating particle formation	**Advantage:** • Very efficient results **Disadvantage:** • Harmful gas release after addition	[38,82,84,85] [20,54,82,83]
Carbon Based Grain Refiners (C, Al-C, Si-C)	Al_4C_3 nucleating particle formation	**Advantage:** • Good wettability in Mg melt **Disadvantage:** • Production of grain refiner is very difficult	[77, 83 84 86, 87,88,89, 90 ,91]
Aluminum-Boron (Al-B) Master Alloy Addition	AlB_2 nucleating particle formation	**Advantage:** • Small amount addition is effective **Disadvantage:** • Fading information is not known	[107]
Al-Ti Based Grain Refiners (Al-Ti-B, Al-Ti-C)	TiB_2 and TiC nucleating particle formation together with restriction in grain growth	**Advantage:** • Easy to reach **Disadvantage:** • Coarse $TiAl_3$ particle formation	[69,70, 77, 79]

Kim et al.[108] found that the grain size of AZ91 alloy was decreased to 460 to 97 μm with 0.6% C_2Cl_6 addition. The general overview in the microstructural change is given in Fig. 2.32. The SEM photographs given in Fig. 2.32 (c, d) show that A and B contains two types (rod and polygonal type) Al_8Mn_5 particles on the microstructure after elemental analysis. In C_2Cl_6 added AZ91 alloy SEM microstructure contains a rounded particle marked as C on Fig. 2.32 (d). This particle contains Al, Mn, C and Fe according to the qualitative analysis [108].

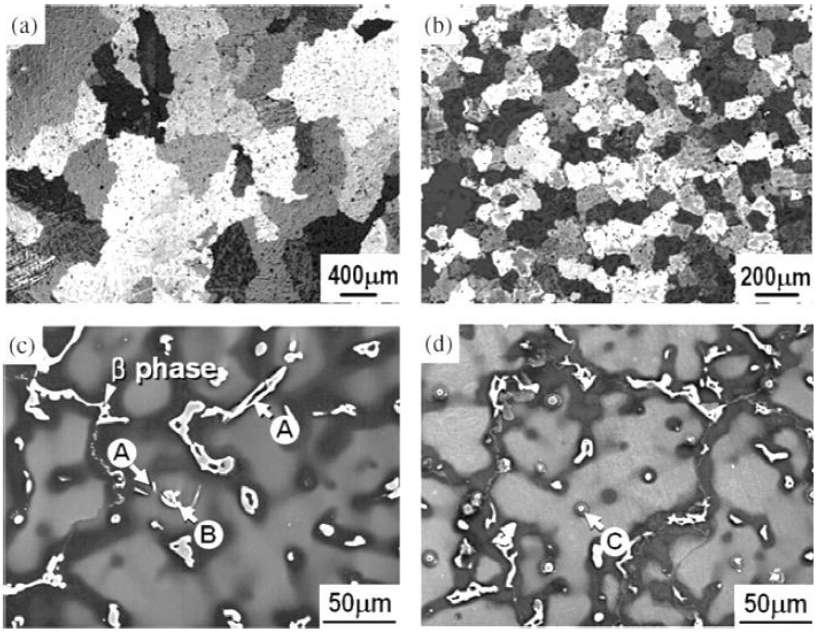

Fig. 2.32 Changes of microstructure of AZ91 alloy (a,c) without and (b,d) with an addition of 0.6% C_2Cl_6 [108]

2.8.5.2 Aluminium-Carbon or Carbon Grain Refiners

Carbon containing grain refiner addition to Mg-Al alloys is an effective method for grain refinement due to low operating temperature, less fading with long holding period easy processing for serial production, short processing time and crucible wear

[18,54, 96]. There are a lot of hypotheses explaining the grain refinement mechanism with carbon addition. However, Al_4C_3 nulcei formation inside of the grain is the most commonly agreed theory for Mg-Al alloys [108]. CaO et al. [109] also mentioned that the particles containing Al, C and O are observed in the central region of many magnesium grains. Activity calculation for Al_2CO showed that the formation of this phase in unfavorable in comparison to Al_4C_3 phase formation. The oxygen in this phase could come from the contamination during sample preparation [18,97].

Crystallographic calculations can be used to explain the potency of Al_4C_3 for primary α-Mg grains. The crystal structures of Al_4C_3 (a=0.32094 nm, c=0.52105 nm) and α-Mg (a=0.321 nm and c=0.21 nm) are both HCP lattice. According to the planar disregistry model of two-dimensional lattices proposed by Bramfitt [125] the critical value of disregistry between nucleant particles to behave as heterogeneous nuclei is 15 %. The smallest disregistry between α-Mg and Al_4C_3 is 3.35 %, which is much less than the critical value. Thus, Al_4C_3 particles can act as an effective heterogeneous nucleant for the AZ91 magnesium alloy. [77,98] In addition, according to the DTA curves obtained by Lei et al. [110], AZ91-1.8 %Mg-50%Al_4C_3 alloys show less undercooling degree and higher crystallization time. These are indication grain refinement and restriction of growth restriction of α-Mg phase in the solid/liquid interface, respectively.

In the other study [86] , Mg-3Al alloy modified by 0.2 wt.% C contains the Al-C-O particles in the microstructure. This may put forward Al_4C_3 particles formation acting as nucleants [111]. the other study conducted by Du et al. [86], addition of Mg-40%Al-10%C pellets into the AZ31 magnesium alloys effectively refines the grain and no obvious fading effect is observed for holding period between 5 to 120 min. This situation is mainly related with the stability of nuclei and the remaining of effective inoculant element during prolonged time. Generally, carbon inoculation to Mg-Al alloys is known as bringing the advantage of less fading. The minimum grain

size for 0.2 wt. % C added AZ31 alloy was measured 193 ± 25 μm with 20 min. holding time for the permanent mould cast samples. Most of the Al_4C_3 particles are in the range of 2 to 4 μm [86].

Motegi [100] studied the effect of high-purity carbon powder addition to AZ91E alloy by using carbon capsule. The powder is in five micrometers size. It was found that 0.08% C addition to AZ91E alloy resulted in comparable grain refinement with Cl_2C_6 addition as represented in Fig. 2.33. Grain size obtained with this addition amount was approximately 75 μm [83,101].

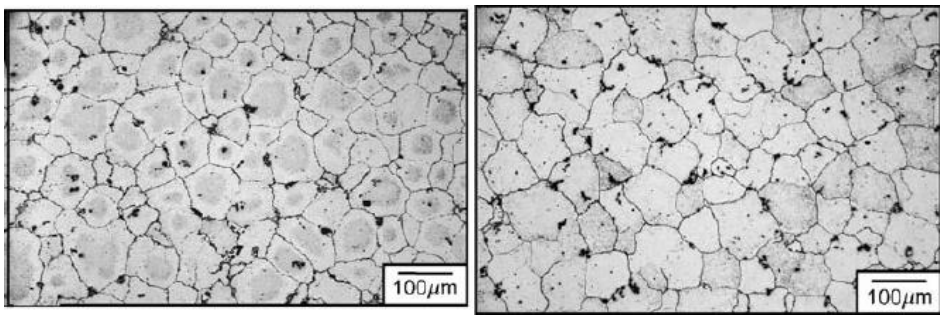

Fig. 2.33 Microstructure for grain size comparison (a) AZ91E-0.08%C (b) AZ91E with Cl_2C_6 addition [100]

Direct inoculation of carbon powder into magnesium melt has a risk of serious problems regarding to burning due to the explosive reaction and melt boiling risk. Therefore, Bae et al. [113] preferred to add carbon in the mixture form of $MnCO_3$ and C powder pellet. The optimum ratio between $MnCO_3$ and C was found as 7:3 to achieve optimum grain refinement. The grain size of AZ91 alloy was decreased from 460 to 52 μm with the addition of 1 wt. % this mixture [113].

2.8.5.3 Silicon Carbide (SiC) Grain Refiner

Silicon carbide (SiC) grain refiner has been extensively preferred as reinforcement agent for Al- and Mg-based composites. In the recent studies, it has also been seen a potential candidate for grain refinement in Mg-Al alloys such as AZ91, AZ31 and AZ63 used in different casting processes like stir casting, compocasting etc [114]. Moreover, Schiffl [115] has pointed out grain refinement with SiC particles was more powerful with lower aluminum content magnesium alloys (<6%) [102]. It was also noted that significant grain refinement could be achieved with combination of the heterogeneous nucleation of primary α-Mg phase and restricted grain growth [114]. The lattice misfit between α-Mg and SiC particles was noted as 4 %. In addition, wetting of Mg-Al melt with SiC particles is enough after obtaining a simple mechanically forced wetting [115].

Chen et al. [116] reported that addition of 0.2 wt. % SiC particles in the form of mixture with Mg powder into AM60B magnesium decreases grain size from 317 μm to 46 μm. After the microscopic examination, it can be concluded that decrease of β phase and formation of Mg_2Si and Al_4C_3 phases according to following reaction:

- $3SiC + 4Al = Al_4C_3 + 3Si$ (1)
- $2Si + Mg = Mg_2Si$ (2)

The study conducted by Huang et al. [114] proposed the ternary carbide Al_2MgC_2 instead of Al_4C_3 as a nucleant particle. The higher possibility was also explained by the closer crystal structure of Al_2MgC_2 to that of Mg than to that of Al_4C_3 [114]. The grain size of Mg-3Al alloy was decreased from 417 to 128 μm with the addition of 0.3% SiC. The grain refinement was explained on the basis of enhanced nucleation of α-Mg on the surface of ternary carbide Al_2MgC_2 together with the lower planar

disregistry factor (5.32%) [114]. Schiffl et al. [71,104] also pointed that Al_2MgC_2 is responsible for grain refinement with the following equation in AZ31 magnesium alloys:

- $2SiC + 2Al + 5Mg = 2Mg_2Si + Al_2MgC_2$ (3)

Another study conducted by Liu et al. [103] indicated that a novel Al_4C_3-SiC/Al master alloy addition to AZ31 and AZ63 alloy results in remarkable change in grain size. However, there was a slight effect on this addition on AZ91 alloy due to the higher Al content in the alloy composition. The average grain size of AZ31 and AZ63 was decreased from 1300 to 225 μm and from 300 to 200 μm, respectively, by the addition of 0.5 wt. % Al_4C_3-SiC/Al master alloy. In addition, additional grain refinement could not be achieved with further master alloy addition [103]. The reason for the grain refinement in this study was reported as Al_4C_3 formed at the surface of SiC particles coming from the master alloy [103]. Chen et al. [117] has also shown that addition of 0.2 % SiC to AZ91D magnesium alloy decreased the grain size form 311 μm to 71 μm as a result of formation of Al_4C_3. In this study, grain size with respect to different casting thicknesses and different locations have also summarized as shown in Fig. 2.34. The microstructure after 0.2% SiC addition in 16 mm casting thickness is very uniform within the edge and center region. However, non-uniformity in sole casting thicknesses above 16 mm increased with increasing casting thicknesses as indicated in Fig. 2.34. In order to visualize change in the grain size both with respect to region and casting thicknesses, Fig. 2.35 is provided for 0.2% SiC added AZ91D alloy [117].

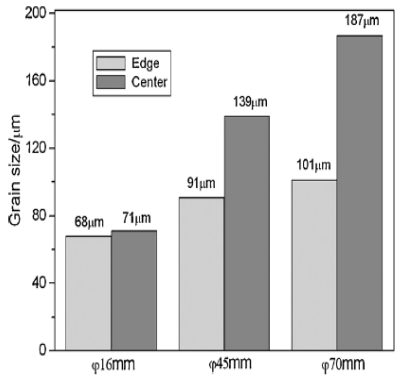

Fig. 2.34 Grain size of different areas 0.2 %SiC added AZ91D alloy for different diameters [117]

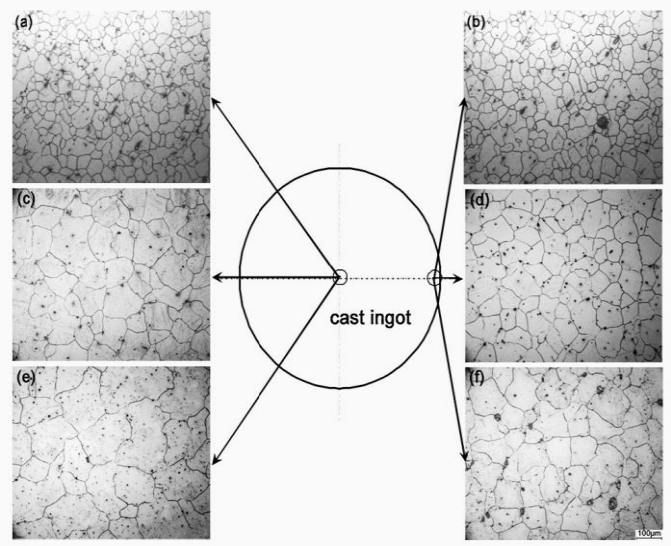

Fig. 2.35 Optical Micrographs of 0.2 % SiC added AZ91D alloy in different regions with a dimeter (a)-(b) 16 mm, (c)-(d) 45 mm and (e)-(f) 70 mm [117]

2.8.5.4 Boron Containing Grain Refiners (Al-B, Sr-B, Mg-B)

Another effective grain refiner for aluminum containing magnesium alloys has been shown as Al-B by Suresh et al. [107] The effect of Al-4B on the grain refining

efficiency AZ91E magnesium alloy was studied. The grain size was reduced from 100 μm to 30 μm (70 % reduction) with the addition of 0.032 wt.% B addition to AZ91 alloy produced by the permanent mold casting. The heterogeneous nucleation site was realized as AlB_2 particle which has lattice parameters of a= 0.300 nm and c=0.325 nm similar to that of Mg with lattice parameters of a=0.323 nm and c= 0.523 nm. In addition, due to the high melting point of AlB_2 (T_m=892 ^{0}C) particle, it is highly stable in magnesium melt to provide grain refinement [39,101].

In order to observe the effect of boron addition to AZ91 alloy, different amounts of boron (0.008, 0.02, 0.032 and 0.04 wt%) in the form of Al-4B were added by Suresh et. al [87]. Fig. 2.36 shows the micrographs of AZ91 alloy with varying boron additions in this study. The grain size of the base AZ91alloy, its microstructure given in Fig. 2.36 (a), is approximately 100 μm. After 0.032 wt% boron addition to AZ91 alloy, the smallest grain size was obtained with 30 μm as shown in Fig. 2.36 (c). Increase in boron addition to this level did not bring to any further grain refinement. It was explained by the saturation level of the nucleants with 0.032 wt% B addition [107]. The SEM micrograph and its EDS results taken inside of a grain given in Fig. 2.37 from AZ91-0.032%B alloy suggested that the particle responsible for grain refinement is AlB_2. This finding proposes the grain refinement of α-Mg grains is achieved with increasing nucleation sites with AlB_2 particles [12,107]. The mechanical properties of boron added AZ91 alloy is presented in Table 2.16.

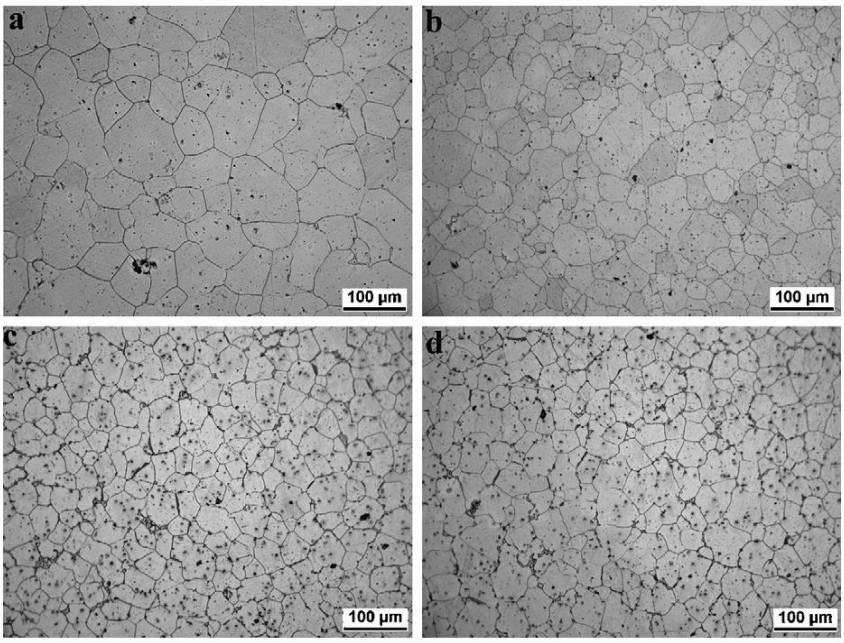

Fig. 2.36 Optical microstructure of AZ91 alloy refined with (a) 0.008 wt.%B (b) 0.02 wt%B (c) 0.032 wt.%B (d) 0.04 wt.%B [107]

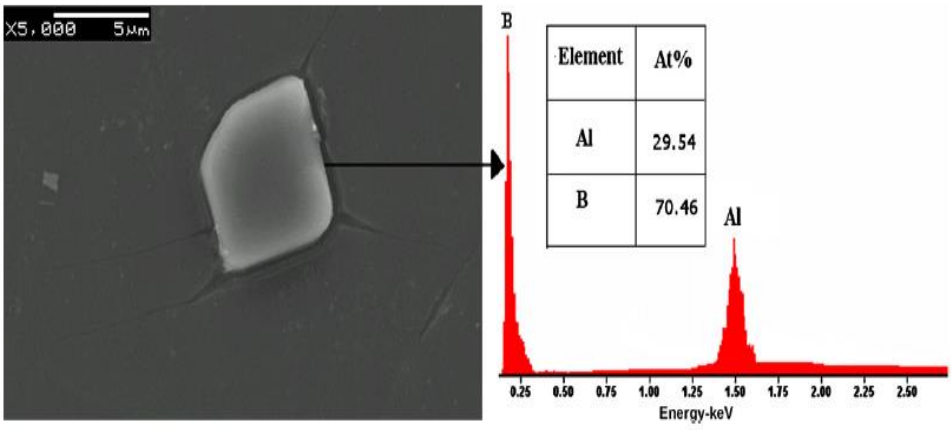

Fig. 2.37 SEM photograph and its EDS result of 0.0032 B added AZ91 alloy [107]

Table 2.16 Mechanical properties of AZ91 Mg alloy before and after boron additions in as-cast conditions [107]

Alloy	0.2% YS (MPa)	UTS (MPa)	El. %
AZ91	95	180	3.3
AZ91 + 0.008%B	102	197	3.9
AZ91 + 0.02%B	107	211	4.4
AZ91 + 0.032%B	110	226	4.8
AZ91 + 0.04%B	113	229	4.9

In another study performed by Liu et al. [83] indicated that addition of 1.8 et. %Mg-TiB_2 master alloy (50 wt.%Mg powder, 34.44 wt.%Ti powder, 15.56 wt.%B powder) results in grain size change of AZ91D alloy form 240 μm to 50 μm. Ti and B enriched particles observed in the center of grains were proposed as potent nucleating substrates for α-Mg [83].

2.8.5.5 Aluminum-Titanium (Al-Ti) Based Grain Refiners

Aluminum-Titanium-Boron (Al-Ti-B) based grain refiners have been getting popular due to microstructural characteristics containing TiB_2 particles which satisfies the requirements of edge to edge model given by Campbell [91]. TiB_2, Al_4C_3 and Al_2CO are the potential grain refiners for Mg alloys determined by the crystallographic studies performed by using the edge to edge model. Generally speaking, the misfit between the directions and planes should be less than 10% and 6%, respectively, for a good refinement [118]. The smallest disregistry number between TiB_2 and α-Mg was reported as 5.6 % for the crystallographic orientation between $(0001)TiB_2$ // (0001)Mg [38,71].

Since Ti is known as strong undercooling element (large GRF value in liquid magnesium), it is expected to hinder grain growth of α-Mg phase. When Ti and B are preferred together, not only TiB_2 particles act as nucleation sites but also excess Ti atoms could restrict the dendrite growth and accelerate the nucleation possibility [38]. Due to this reason, it is expected to have more grain refining efficiency in Ti-B or TiB_2-Ti in comparison sole B or Ti containing refiners [38,69]. TiB_2 particles have melting temperature higher than 3000 ^oC and present as solid particles in the molten alloy [70]. Thus, these particles can behave as heterogeneous nucleation sites for α-Mg grains theoretically [38,69]. In addition, as a result of dissolving $TiAl_3$ into the melt, Ti element in the form of Ti atoms is expected in the melts prior to pouring as a kind of solute element of the melt. These elements can restrict the grain growth due to being high grain restriction parameter of Ti (about $5.95x10^{-4}$), which is approximately four orders larger than that of Zr. It makes a very promising element for grain refinement [70].

TiB_2 particle size also affects the nucleation potency. The TiB_2 particle size in the Al-Ti-B master alloy used in this study is only 2-3 μm and thus, Chen et al. [38] suggests that they have large potency of nucleation. Based on the scenario given in these studies [38,69,70, 107] similar phenomena could be reason of the fading, which was explained by the density difference between the Mg and the grain refinement agent. The possibility of availability of denser TiB_2 (4,38 g/cm^3) particles on the Mg melt (1,74 g/cm^3) is decreasing due to settlement of TiB_2 particles with time on the bottom of crucible. Hence, fewer heterogeneous nucleating TiB_2 agent were available at longer holding times [100,107].

The grain size of base AZ31 alloy decreases from 1100 μm to 80 μm (93% reduction) with the addition of 0.3 wt. % Al-4Ti-5B grain refiner, respectively. The

key role of grain refinement has been found as TiB_2 which was confirmed from energy dispersive x-ray (EDX) and crystallographic dimensions [118].

The microstructures of solutionized sample with different Al-Ti-B master alloy additions are shown in Fig. 2.38. As seen on this figure, the grain size of AZ91 alloy decreases up to 0.3% Al-Ti-B master alloy addition and then increases again with exceeding this limit. Quantitative grain size examination results given in Fig. 2.38 indicates that the grain size of un-refined AZ91 alloy decreases from 422 μm to 79 μm with 0.3% Al-Ti-B master alloy. It can be reasonably suggested that the number of the TiB_2 particles increase as the master alloy addition amount increases. In addition to that, increase of atomic Ti concentration in the melt provides enhancement in the constitutional undercooling and restriction to grain growth [38]. The difference in grain size of Al-5Ti-1B added AZ91 ingots having a diameter 45 mm and 70 mm is lower than that of SiC added AZ91 alloy. This shows that the microstructural sensitivity of AZ91 alloy refined with Al-5Ti-1B master alloy is less than that of the alloy refined with SiC particles, which also indicates the lower sensitivity to cooling rate in different sections [38]. The summary of the grain size for different casting thicknesses for Al-5Ti-1B refined AZ91 alloy is given in Fig. 2.39.

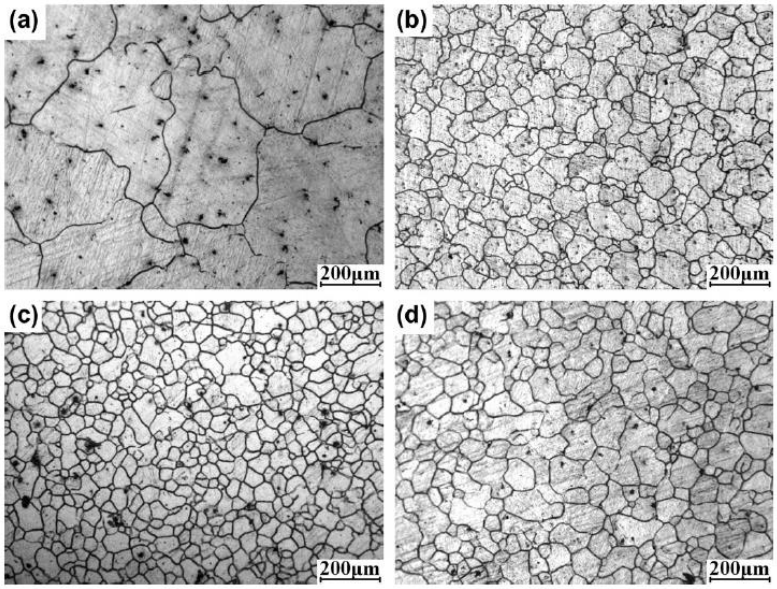

Fig. 2.38 Microstructures of the AZ91D alloys refined by (a) 0%, (b) 0.2%, (c) 0.3% and (d) 0.5% Al–Ti–B master alloy and then solutionized at 420 ^{o}C for 8 h [38].

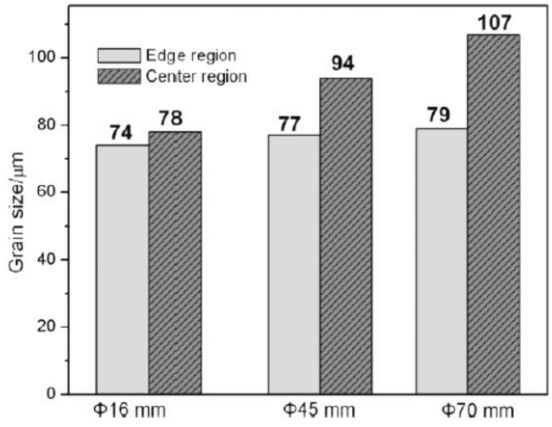

Fig. 2.39 Grain size summary of AZ91 alloy refined with 0.3% Al-5Ti-1B master alloy having a casting thickness (16, 45 and 70 mm) [38]

The recent studies show that saturation level for TiB_2 nucleation substrates was obtained with 0.3% Al-Ti-B addition as shown in Fig. 2.40. After this critical limit,

TiB_2 particles will agglomerate and settle down, resulting in the decrease of effective nucleation substrate number. In order to support this idea, specimen with 1% refiner prepared from the melt being close to bottom was examined with back scattered imaging technique and EDS analysis. According to these examinations, agglomerate particles rich in Ti elements were frequently detected as indicated by arrows in Fig. 2.41. Thus, the result indicates that TiB_2 particles are agglomerated and settled down under this condition [38].

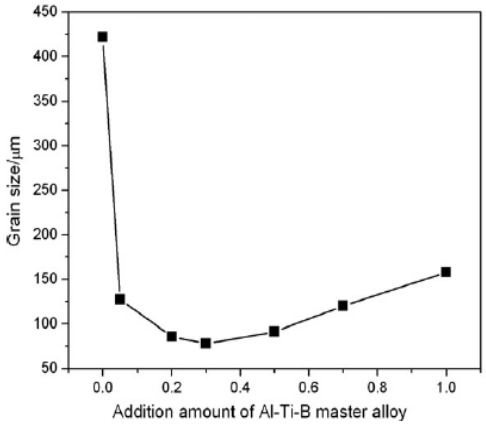

Fig. 2.40 Variation of grain size with addition amount of Al–Ti–B master alloy [38]

In one another study, Ti element was introduced into Al-C melt to increase the fluidity of the melt and improve the distribution of Al_4C_3 in the alloys. Meantime, a series of Al-Ti-C master alloys with low Ti to C ratios were prepared by melt reaction method [120]. Fig. 2.42 indicates the measured grain sizes of AZ31 with different grain refiner addition levels prepared by this method. The most effective grain refiner addition is 1% Al-1Ti-1C with decreasing grain size from 850 μm to 200 μm [120]. From this study, it can deduced that the size of Al_4C_3 particles in the Al_4C_3 containing Al-Ti-C master alloys plays a key factor for the refinement of Mg-Al based alloys [120].

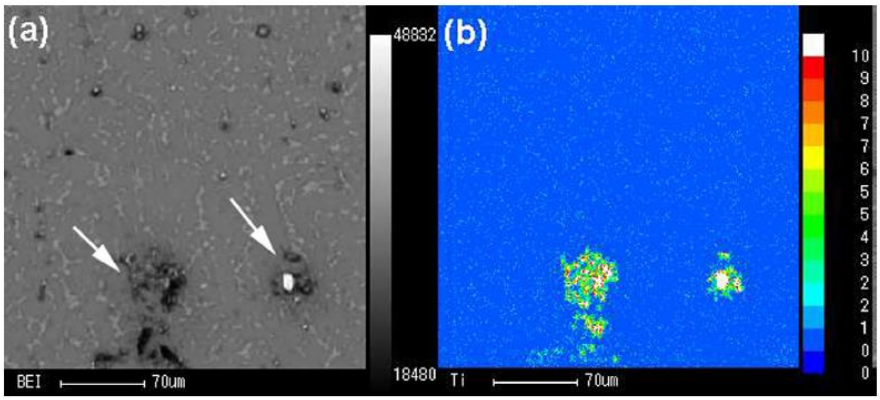

Fig. 2.41 (a) Back-scattered electron image of the specimen prepared from the melt being close to the bottom of crucible (the melt treated by 1% Al–Ti–B master alloy) and (b) Ti map. [38]

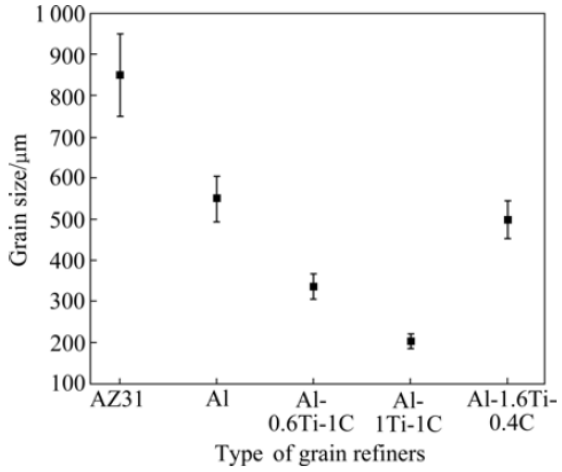

Fig. 2.42 Grain sizes of AZ31 in T4 solid solution state with and without addition of grain refiners [120]

Optical micrograph of AZ91E alloy is shown in Fig. 2.43. The average grain size of AZ91E without any grain refiner addition was measured as 1000 μm [100]. Grain size measurement results after different amount Al-5Ti-1B and Al-1Ti-3B addition to

AZ91E is summarized in Fig. 2.44. The figure also explains the effect of different holding times [118].

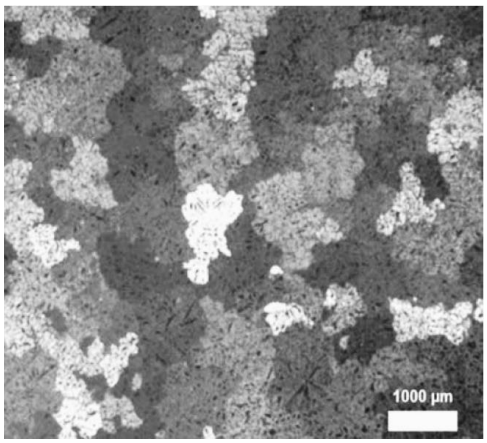

Fig. 2.43 Micrograph of AZ91E magnesium alloy [100]

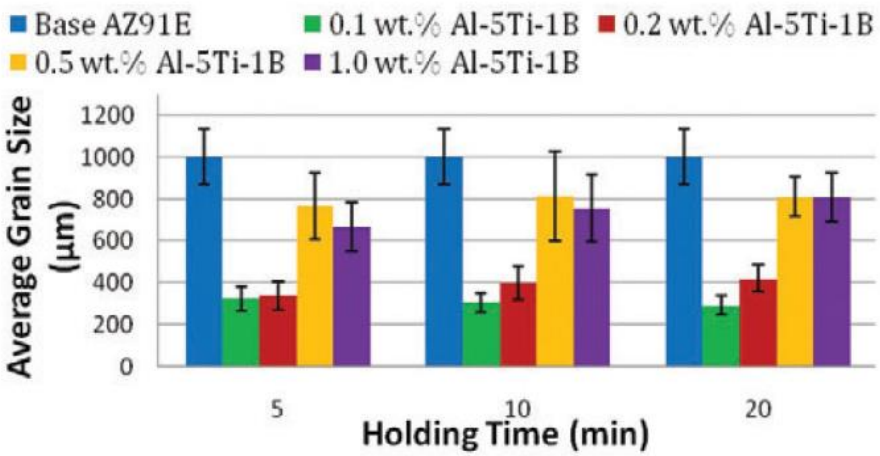

Fig. 2.44 Influence of Al-5Ti-B addition levels and holding time on the grain size of AZ91E magnesium alloy [118]

The smallest grain size was obtained by using Al-5Ti-1B grain refiner on the addition levels 0.1 and 0.2 wt% to AZ91E according to A. Elyased et al. [118]

Moreover, for these addition levels, A. Elyased et al. [118] reported that increasing holding time decreases the grain size. Grain size of the base AZ91E alloy was reduced from 1000 to 323 µm with 0.1 wt% Al-5Ti-1B addition for 5 minutes holding time. However, increasing the addition levels of Al-5Ti-1B to 0.5 and 1.0 wt. % resulted in rapid grain size increase, which becomes comparable to unrefined alloy after 20 minutes of holding. In order to understand the ınfluence of addition levels and holding times of Al-5Ti-1B grain refiner to AZ91E alloy, the micrographs are taken from the study of to A. Elyased [118] are given in Fig. 2.45. From the quantitative results given in Fig. 2.44 and micrographs at Fig. 2.45, 0.1 and 0.2 % Al-5Ti-1B addition shows a very little sign of fading [75,116].

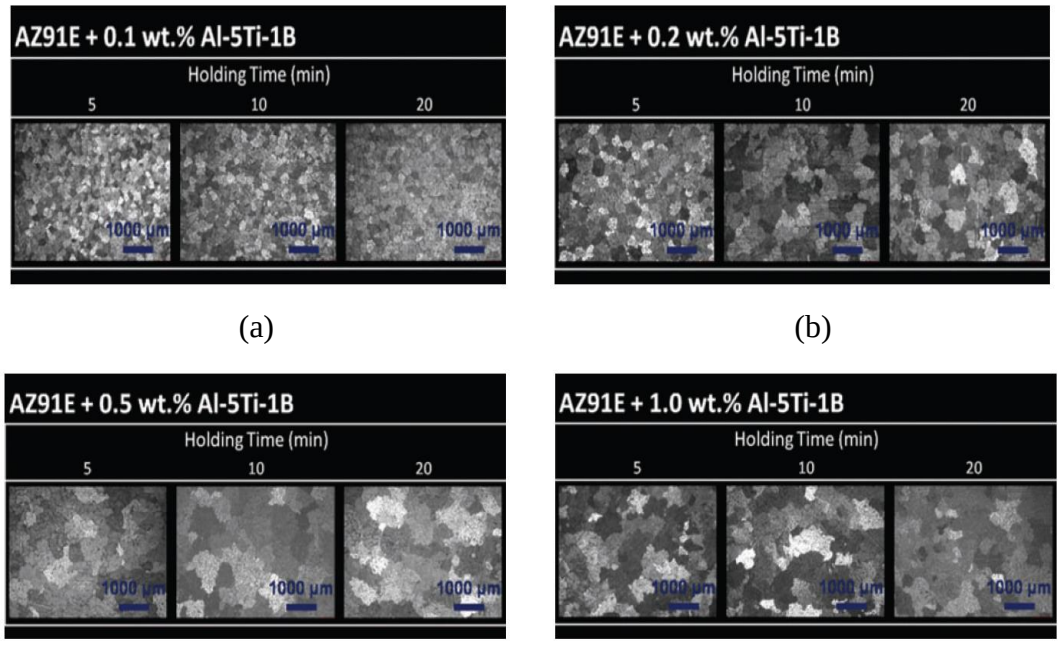

Fig. 2.45 Optical micrographs of AZ91E + Al-5Ti-1B alloys with different holding times (a) 0.1 wt% Al-5Ti-1B (b) 0.2 wt% Al-5Ti-1B (c) 0.5 wt% Al-5Ti-1B (d) 1 wt% Al-5Ti-1B [75,116]

Another study conducted by Wang et al. [85] indicated that Al-4Ti-5B was also effective grain refiner for AZ31 magnesium alloy. The reason to use Al-4Ti-5B instead of Al-5Ti-1B was to obtain higher amount of TiB_2 nucleating particles in the microstructure of the grain refinement. A minimum grain size was obtained as 80 μm with the addition of 0.3 wt. % Al-4Ti-5B [85].

Al-Ti-B based grain refiner addition decreased the severe hot tearing susceptibility of AZ91 alloy according to the study performed by Elsayed et al. [87] Although Al-5Ti-1B master alloy addition has a slight decrease in this susceptibility, Al-1Ti-3B results in significant reduction hot tears. The reason for slight reduction with Al-5Ti-1B addition is the large $TiAl_3$ behaving as stress concentration points formation during solidification [87]. However, fine TiB_2 and AlB_2 particles detected in Al-1Ti-3B alloy did not cause any blockage for feeding channels. In addition, excess of these particles bonded with the matrix and eutectic [87]. All of them cause the reduction of hot tearing susceptibility with homogeneous strain distribution during solidification [87].

2.9 Fractography Analysis

Fractographic analysis from the literature has been examined in order to characterize general fracture behavior of magnesium alloys. Aluminium containing and aluminium free magnesium alloys may show different fracture behavior depending on the microstucture and alloying elements. Due to hcp nature of magnesium, fracture mechanism of magnesium alloy is expected to be cleavage. The cleavage crystal plane for magnesium is (0001). The failure mode could not be defined easily as cleavage or quasi-cleavage fracture for all type of magnesium alloys. The fracture surface generally consists of large volume of cleavage and/or quasi-cleavage facets together with ridges and/or steps formed by tearing and secondary cleavage,

respectively. The fracture behavior depends on the silicon content and test condition [48].

In Mg-6Al alloy without Si addition, fracture surface contains elongated grains with indication of some ductile deformation and cracks usually initiating from the α-Mg/β-$Mg_{17}Al_{12}$ interface. Si addition changed the deformation type with bringing the fragility to the alloy together with the additional crack initiation sites by Chinese script Mg_2Si. The cleavage characteristics were detected on the fracture surface tested at RT as indicated in Fig. 2.46. [48] Fractography of Mg-6Al-Si alloys generally shows the brittle failure. However, fracture mode of these alloys is a rather complex in comparison to the others. No ductile microvoid coalescence was detected on failure surface [48].

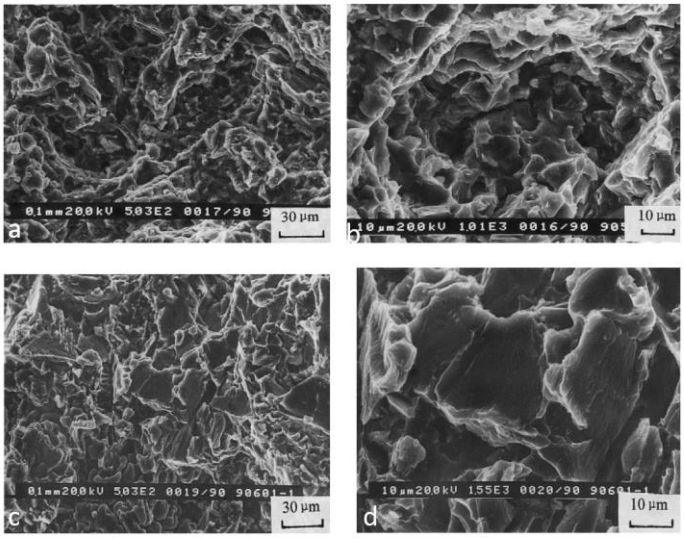

Fig. 2.46 SEM fractography of tensile fracture surfaces (b, d are respective local magnifications of a and c) (a), (b) Mg-6Al tested at RT (c), (d) Mg-6Al-1Si tested at RT [48]

The fracture surface of Mg-6Al alloy shown in Fig. 2.47 (a) indicates that crack propagation is generally seen along grain boundaries, particularly on the interface of $Mg_{17}Al_{12}$ phase and α-Mg matrix. The tiny hair-like microcracks are detected on the $Mg_{17}Al_{12}$ particle surrounding. The high elongation is expected due to the presence of grain lengthening near the failure surface. [48] The introduction of Si into Mg-6Al brings additional crack initiation sites, i.e. Mg_2Si precipitate phase, especially the coarse Chinese script morphology shown in Fig. 2.47 (b), which is the possible main reason for decrease in UTS at RT. Some secondary cracks were detected along the Chinese script morphology Mg_2Si and connected with main crack. It can be deduced form Fig. 2.47 (b) that the initiation, growth and coalescence of crack along the Chinese script Mg_2Si resulted in the main failure mechanism [48].

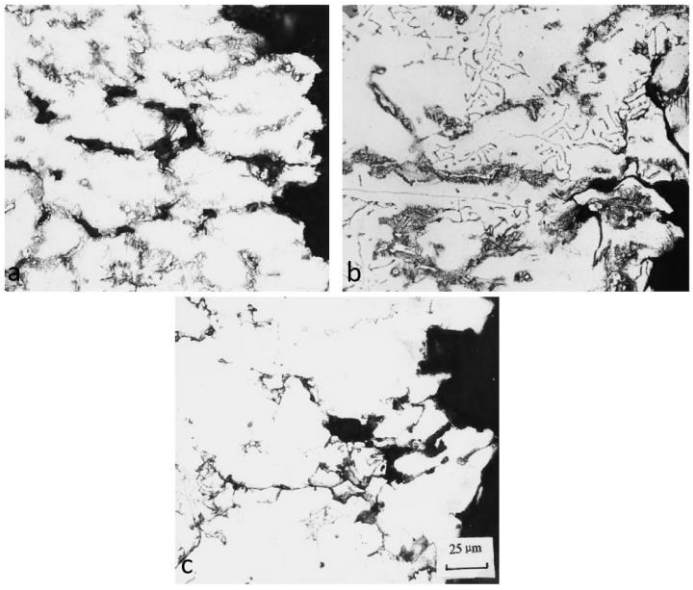

Fig. 2.47 Optical micrographs of metallographic sections perpendicular to the tensile surface (a) Mg-6Al tested at RT (b) Mg-6Al-1Si tested RT (c) Mg-6Al-1Si tested at 150 ^{o}C [48]

In order to see the positive effect of Si on the elevated temperature mechanical properties, Fig. 2.47 (c) could be an important indication. The fracture mechanism given in Fig. 2.47 (b) changed with the test at 150 ^{0}C. Even though some microcracks are seen along Mg_2Si in the section given in Fig. 2.47 (b), the main voids causing the failure is mainly located on near the $Mg_{17}Al_{12}$ phase. $Mg_{17}Al_{12}$ particles near to the fracture surface were broken due to the softening of $Mg_{17}Al_{12}$ phase [48]. Decrease in the number of facets and steps for the fractography analysis of Mg-6Al-1Si tested at 150 ^{o}C is obvious together with increase in tearing ridges and secondary cracks. Moreover, morphology of fracture surface is even rougher [48].

The study performed by Lee [122] indicated that interdendritic morphology in the shrinkage void and entrapped hole are observed in the fracture surface of AZ91 alloy (Fig. 2.48).

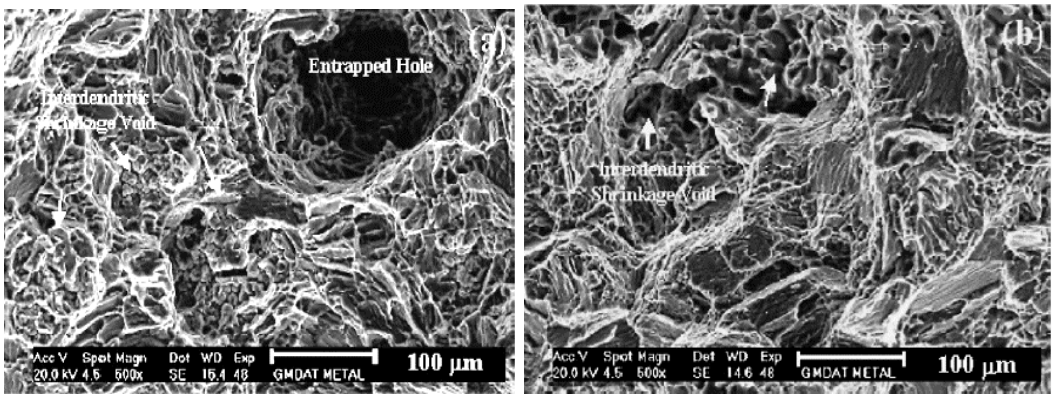

Fig. 2.48 Fracture surface of (a) die-cast and (b) gravity cast AZ91 alloy [122]

The fractography of AZ91 alloy is a cleavage type as shown in Fig. 2.49. The discontinuous β-($Mg_{17}Al_{12}$) phase at the grain boundaries are the main reason of

cleavage type of fracture and poor mechanical properties of the alloy such as ductility and elongation [17,25].

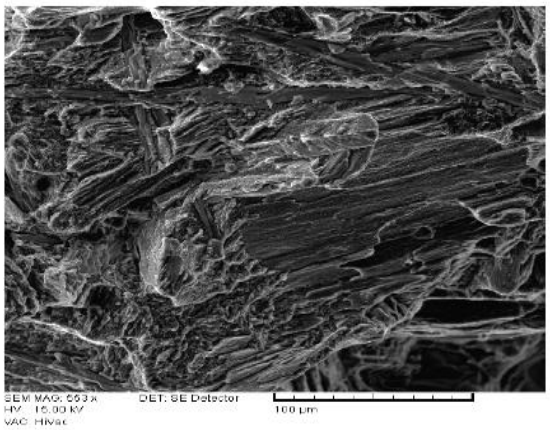

Fig. 2.49 Tensile test fracture surface of AZ91 alloy [17]

It was also reported by Li. et al. [70] that the fatigue microcracks in Mg-Al alloys is mainly originated from on the grain boundaries of α-Mg. Therefore, the second phase strengthened the grain boundaries for magnesium alloys is very important to obtain higher resistance to fatigue damages.

2.10 Objectives of This Work

In the light of literature review, the necessity of developing high temperature creep resistant aluminium based magnesium alloys has been arised in recent years to speed up the usage of them in the helicopter powertrain components. However, β-($Mg_{17}Al_{12}$) phase formation in Al containing Mg alloys limits the usage of these alloys at the temperatures above 120 ^{o}C due to the softening of this phase. Because of this, this thesis focused on the eliminating this disadvantage to replace Al free Mg alloys in industry. Al containing Mg alloy replacement could bring the decrease in

cost and easy handling during melting and pouring. Nevertheless, in the literature, there is a very limited knowledge about magnesium sand casting because of difficulties in mould preparation, moulding parameters and sand mould surface and liquid magnesium reactions. Most of the studies on magnesium casting are related with permanent mould casting method. On the other hand, the actual production method of complex helicopter casings is sand casting. The experiments in this thesis enable the obtaining sand casting mould preparation parameters for the actual production method and future studies. One of the most crucial objectives of this study was to set up a controlled atmosphere magnesium sand casting unit containing induction heating, vacuum attachment, gas flow controls and data acquisition. Another important technique was to develop controlling liquid flow rate during sand casting in the range of 0.6-1.1 m/s using SiC ceramic foam filter to eliminate bi-films and turbulent related porosities.

This thesis provides an important breakthrough to observe the combined effect of Ca-Sn and Sr-Sn elements on Si containing sand cast AZ91 alloys. The aim of the element additions is to improve creep properties in order to meet the creep requirements and supress the formation of creep susceptible β-($Mg_{17}Al_{12}$) phase formation in the microstructure. Together with suppression of this phase, it is purposed to obtain fine polygonal creep resistant Mg_2Si phase both inside of grain and at the grain boundaries. Investigation of simultaneous addition of Ca-Sn and Sr-Sn on the modification of 'Chinese Script' morphology Mg_2Si phase to fine polygonal shape provides to estimate which of them is more beneficial for desired homogeneous and fine microstructure. Since sand casting of modified AZ91alloys for gearbox housing of a helicopter is affected by microshrinkage due to various section thicknesses, Sr optimization is an effective technique to eliminate this problem via improving interdendritic liquid flow. The joint investigation on metallurgical characterizations such as porosity percentages, grain size measurements and microstructure analysis for the alloys on different casting

thicknesses provides a comprehensive understanding on final properties. In the literature, it is generally preferred in focusing one of those metallurgical characterizations. This thesis is valuable to combine them in one study. The grain refiner addition on these metallurgical properties and tensile properties at different specimen thicknesses were studied to observe the useful effect on the property improvement such as grain refinement, grain size homogenization in different section thicknesses, elimination of interdendritic porosity, modification of Mg_2Si from Chinese script to globular morphologies, suppression of β-($Mg_{17}Al_{12}$) phase by forming high temperature stable intermetallics such as MgSiSr, Mg_2Si containing Sr and Sn.

In addition, the correlation between grain size and undercooling is very rare in the current researches. The studies generally refer to DSC and DTA experiments for solidification analysis while this thesis uses the data directly obtained from the mould to obtain actual solidification behaviour. Therefore, this study leads to obtain correlation between grain size and undercooling degree in the real experiment conditions. The combined effect of alloying elements and grain refiner addition on the solidification curve was also one of the most interesting experimental outcomes studied in this work. The aim was to reveal the decrease in liquidus undercooling with alloying additions to the modified AZ91 alloy.

CHAPTER 3

EXPERIMENTAL PROCEDURE

3.1 Materials

This section of the thesis explains the materials used in the studies. The compositions of the Mg alloys, master alloys and grain refiner preferred in this study are presented.

3.1.1 AZ31D Magnesium Alloy

AZ31D magnesium alloy was received as ingots. The chemical composition of the alloy from ingot specified in material certificate is outlined in Table 3.1. This alloy was used as a base material to make the desired alloy systems in this thesis.

Table 3.1 Chemical composition of AZ31D magnesium alloy (wt. %)

Mg	Al	Zn	Mn	Si	Cu	Fe	Be	Total Others
Bal.	2.55	0.95	0.44	0.02	0.005	0.005	0.0006	0.3

3.1.2 Raw Materials Used in Master Alloy Preparation

Mg-30%Sr (wt. %) and Al-10%Sr (wt. %) master alloys were used in main master alloy preparation to achieve desired Sr concentrations. Mg-25%Ca (wt. %) are also preferred in the Ca element adjustment in the main master alloy preparation. EDS results of the master alloys are given in Table 3.2.

Table 3.2 Mg-30Sr, Al-10Sr and Mg-Ca master alloys EDS analysis results (wt. %)

Master Alloys	Mg	Al	Sr
Mg-30 Sr	67.7	-	32.3
Al-10Sr	-	88.2	11.8
Mg-25Ca		74.3	25.7

Commercially pure Al (99.7%), Si (99.7%) Sn (99.7%) and Zn (99.7%) were used to obtain desired Al, Si, Sn and Zn levels in the final alloy series.

3.1.3 Al-5Ti-1B Grain Refiner

The grain refiner was used in the form of thin rods. The chemical composition of the Al-5Ti-1B grain refiner is given in Table 3.3.

Table 3.3 Chemical composition of Al-5Ti-1B grain refiner (wt.%)

Al	Si	Fe	Ti	B	V	Total Others
93.73	0.06	0.1	5	1	0.1	0.1

3.1.4 Specifically Prepared Master Alloy for Alloys

In order to obtain desired chemical composition in the final alloy, specifically prepared Al based master alloys were preferred in this study. Two types of master alloys were chosen. One of them contains Mg, Al, Si, Ca and Sn (Master Alloy I) elements and the other one includes Al, Si, Sr and Sn elements (Master Alloy II). The main reason for using these master alloys was to prevent dissolution problem of high melting point Si elements by formation intermetallics with aluminum. Other elements were also added in these master alloys to obtain homogeneous chemical composition in the final alloy series.

Master alloy I was prepared with using Al-10Sr, pure Si, pure Sn, pure Al, Mg-30Sr and Mg-25Ca master alloys. On the same way, Master alloy II was prepared by using Al-10Sr, pure Si, pure Sn and pure Al. The target composition and the EDS analysis results of Master Alloy I and II are provided in Table 3.4. The Master alloy II was differentiated from the other with containing Ca element. Some differences were observed in the targeted and obtained results from EDS analysis due to dissolution problems during alloying. The EDS results of master alloys were taken into account to calculate the addition amounts in final alloy series.

Table 3.4 Targeted and EDS analysis results of Master Alloy I and Master Alloy II

	Mg	Al	Si	Sr	Sn	Ca
Master Alloy I Targeted composition	10.6	71.1	7.8	-	6.4	3.5
Master Alloy I EDS analysis result	8.3	70.5	5.8	-	6.2	4.0
Master Alloy II Targeted composition	-	80.4	10.5	5.9	3.4	-
Master Alloy I EDS analysis result	-	83.3	8.2	5.9	2.6	

3.1.5 Alloy Systems

Using AZ31D magnesium ingots as base materials, a series of magnesium alloys was prepared in this thesis given in Table 3.5 with the method of adding specially prepared master alloys and industrially available master alloys. This table summarizes the desired chemical compositions before the experiments. The ranges of elements were specifically given in the same way with industrial standard for magnesium alloys, ASTM B80-15. [78] Compositions of the alloys in T6 heat treated conditions measured by ICP-AES analysis method are given in Table 3.6.

Master Alloy I was used for Alloy I while Master Alloy II was used for both Alloy II and Alloy III. Alloy I was mainly chosen in order to investigate the effect of Ca on the modification effect of Mg_2Si phase while Alloy II was preferred to simulate the effect of Sr for the same purpose. Sn element was used for all alloy series except Alloy IV in order to increase ductility of the alloys. Alloy III contains 0.1 % Al-5Ti-1B master alloy to analyze the grain refinement in Alloy II. Alloy IV was prepared to obtain similar nominal composition with AZ91 magnesium alloy, which was seen as benchmark for aluminum containing magnesium alloys.

Table 3.5 Nominal compositions (wt.%) of magnesium alloys used in this study and AZ91E [78]

Alloy System	Mg	Al	Zn	Mn	Si	Sr	Ca	Sn
Alloy I	Balance	8.1 9.3	0.4 1.0	0.2 0.35	0.6 0.7	-	0.4 0.5	0.8 0.9
Alloy II	Balance	8.1 9.3	0.4 1.0	0.2 0.35	0.6 0.7	0.3 0.4	-	0.5 0.6
Alloy III	Balance	8.1 9.3	0.4 1.0	0.2 0.35	0.6 0.7	0.3 0.4	-	0.5 0.6
Alloy IV	Balance	8.1 9.3	0.4 1.0	0.2 0.35	-	-	-	-

Table 3.6 Measured composition (wt. %) of magnesium alloys used in this study via ICP-AES analysis

Alloy System	Mg	Al	Zn	Mn	Si	Sr	Ca	Sn	Ni	Cu
Alloy I	Bal.	9.2	0.84	0.30	0.60	0.02	0.45	0.84	0.014	0.023
Alloy II	Bal.	9.8	0.84	0.33	0.63	0.31	-	0.59	0.013	0.016
Alloy III	Bal.	8.7	0.83	0.33	0.69	0.32	-	0.50	0.015	0.015
Alloy IV	Bal.	8.9	1.17	0.34	-	0.03	-	-	0.016	0.012

3.2 Sand Casting Mould Preparation

3.2.1 Sand Casting Mould Model

The sand casting mould (see Fig. 3.1) was used for the experimental tensile test samples. The specimens in the mould are in different geometry and thickness to observe the effect of variable casting thicknesses on mechanical properties.

The drawing of the CNC machined mold from aluminum alloy is provided in Appendix C (C.1).The filter location and the pool above the filter were made after the mould preparation by hand. The filter was added by the aim in reduction of velocity and possible turbulence in the mold. The thermocouple location for thermal analysis is illustrated in Fig. 3.2. This area was specifically selected due to the thickest and one of the last solidifying region. In addition, CNC machined mold is provided in Fig. 3.3. The mold was made from two mirror halves containing the risers, gates, runners and specimens.

In this study, the as-cast and machined tensile specimens shown in Fig. 3.2 were used to examine the mechanical and metallurgical properties. In addition to these specimens, three additional samples shown in Fig. 3.3 were also taken in order to observe the mechanical property differences in thicker sections. The other reduced diameter specimens could be used in the fatigue tests for future studies.

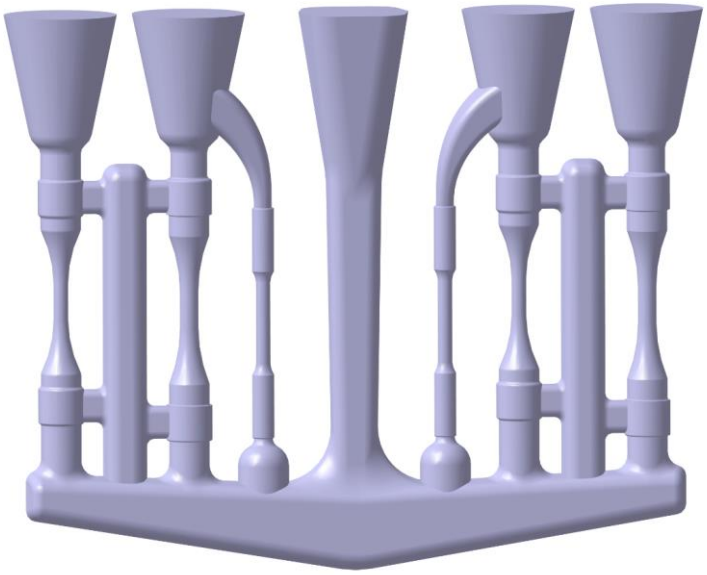

Fig. 3.1 The sand casting model without filter system

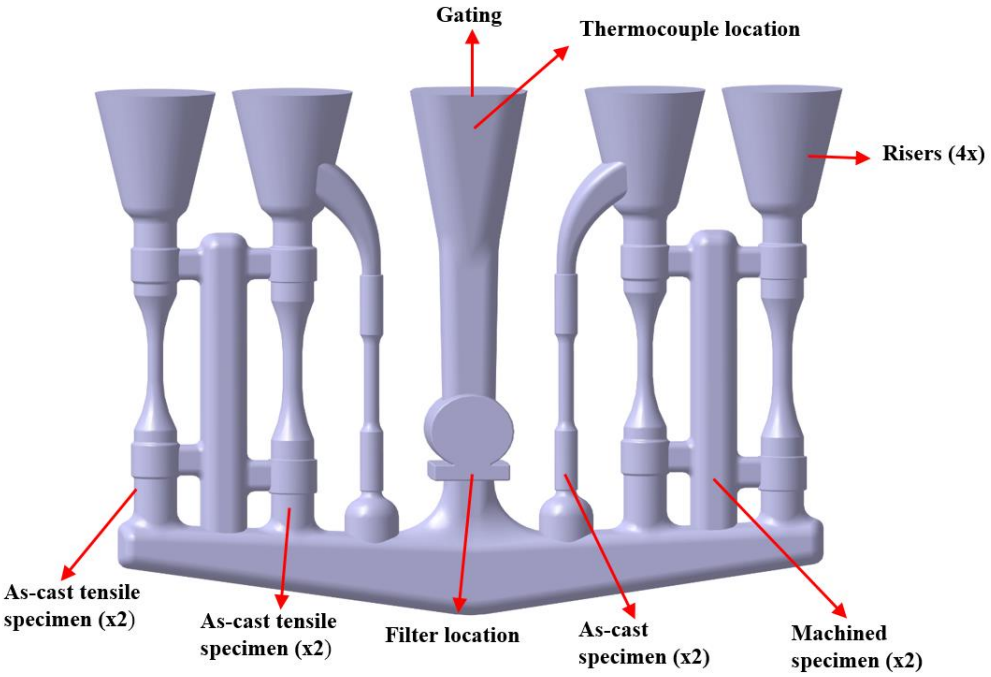

Fig. 3.2 The sand casting model for tensile test samples

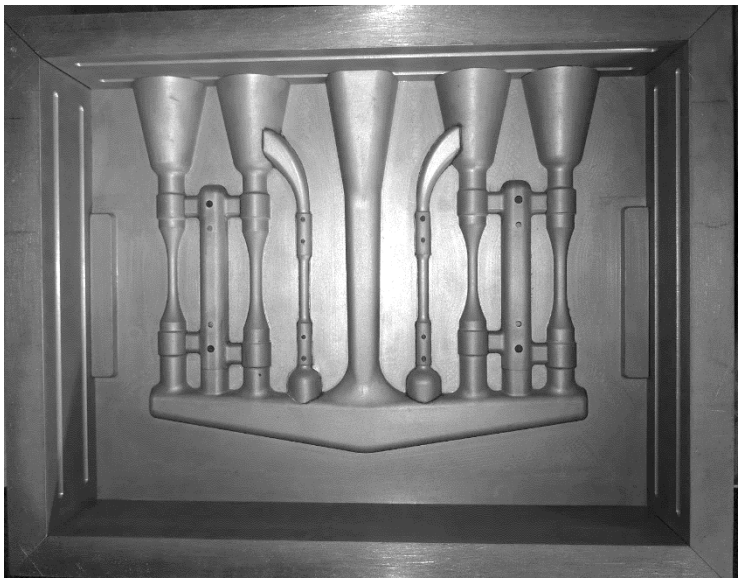

Fig. 3.3 CNC machined aluminum mould (half of the mould)

3.2.2 Validation Modelling of Sand Casting Mould

NovaCast-NovaFlow® casting simulation program was used to validate the moulding system. Although filter and pool above it were preferred to decrease casting velocity in the mould, it was not implemented on the program due to the unavailability of the filter containing simulation module. Therefore, the results provided from the simulation program in this thesis were obtained with using same 3D model while the positive effect of filter was not demonstrated. In addition, the material was selected as "AE42" magnesium alloy since there is no available other magnesium alloy in the program. Although some deviations exist in the simulation program, the simulation results are valuable in order to understand solidification behavior, casting velocity, liquid phase fraction and last solidified area in the mould.

Fig. 3.4 shows the velocity distribution in the mold. While light blue region represents the velocity range between 0.4-0.6 m/s, light yellow region shown by red circle indicates the region where velocity in the rage of 1.6-1.8 m/s. Since it is desired to have homogeneous distribution in velocity all around the mould, filter and pool above it was adapted to the mould system. This certainly decreased the casting velocity in thinner sections of specimens and the radiography results as shown in Fig. 4.7 being an indicative to obtaining desired level of velocity and turbulance. According to Fig. 4.7, gas porosities resulted from turbulance on the thinner section are minimized.

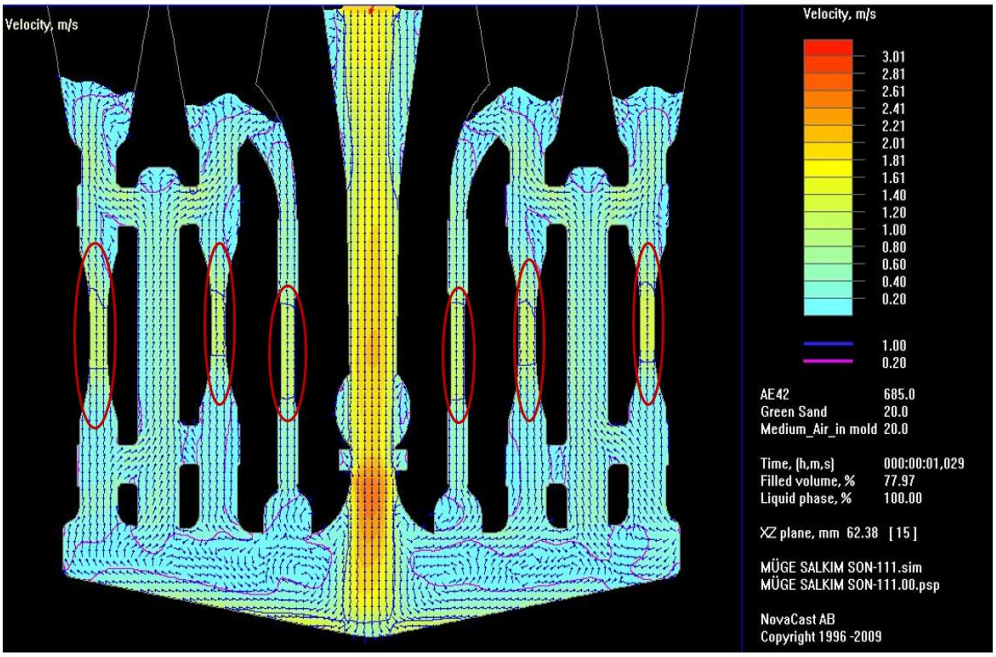

Fig. 3.4 A two dimensional velocity distribution in the mould obtained from NovaCast--NovaFlow ® simulation

Fig. 3.5 shows the shrinkage distribution after solidification. As a good indicative from moulding design, shrinkage was observed both in the gating and risering system. (red regions in Fig. 3.5)

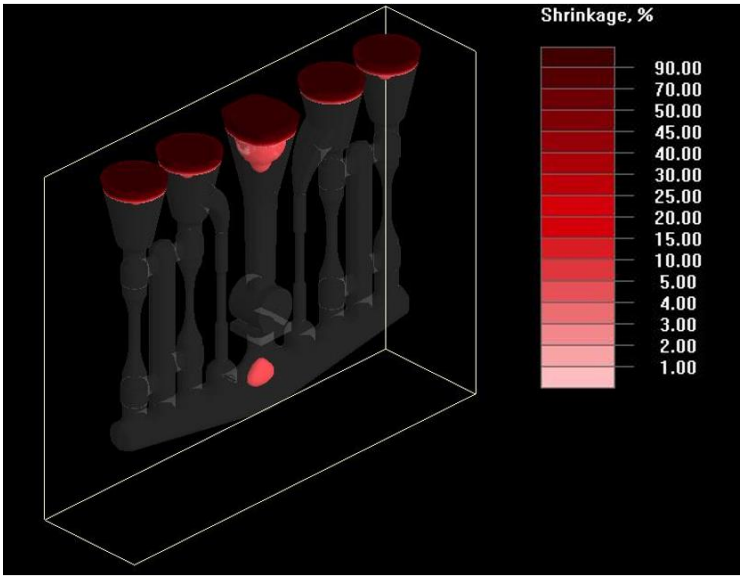

Fig. 3.5 Shrinkage distribution in the mould obtained from 3D NovaCast-NovaFlow® simulation

3.2.3 Sand Casting Mould Preparation

AFS 45-55 silica sand was selected for sand. The resin was chosen as Alkafen C-150 provided by Cukurova. It is a fenol formaldehyde based resin, which is hardened by CO_2. Resin hardenable with CO_2 was specifically selected in order to minimize moisture content in the mould and eliminate time restriction for hardening of resin during mold preparation. The mixing time resin-sand mixture was approximately 15 minutes. CO_2 gas was injected to mold via pores opened to the sand mold as shown in Fig. 3.6 (a) after pouring resin-sand mixture into the mold. The exposure time was

approximately 25 minutes. The picture of one half of the sand mold is provided in Fig. 3.6 (b). After mould preparation, zirconium graphite painting was applied to the surface in order to avoid chemical reaction between sand and magnesium melt during solidification. In addition, thermocouple installation location, gas vents for as-cast tensile specimens, filter insertion location with its pool as shown in Fig. 3.7 were opened up by hand after sand mould preparation steps. SiC ceramic foam filter with 20 mm thickness and 30 ppi pore size was preferred in this study due to its availability in industry. (Fig. 3.6 (c))

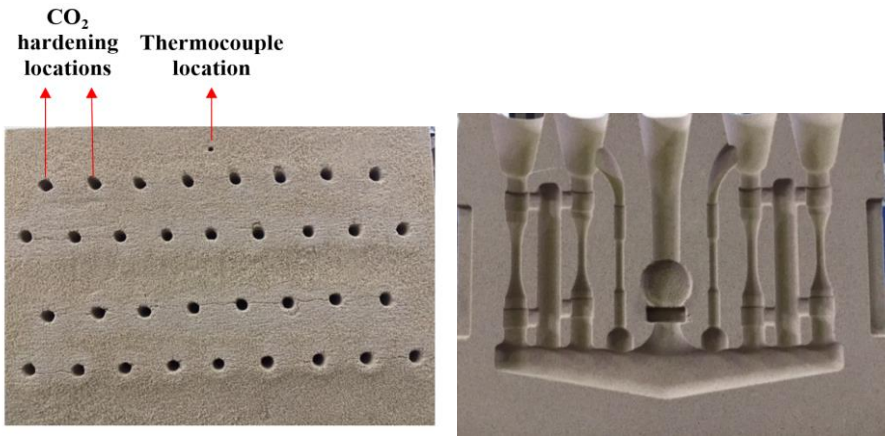

(a) (b)

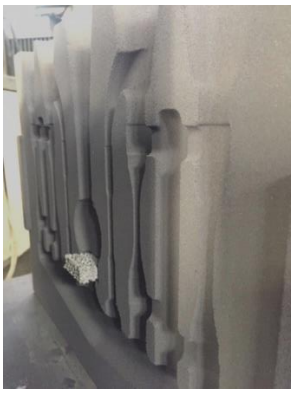

(c)

Fig. 3.6 (a) Hardening method with CO_2 for sand moulding (b) half of the sand moulding after hardening (c) filter inserted mould

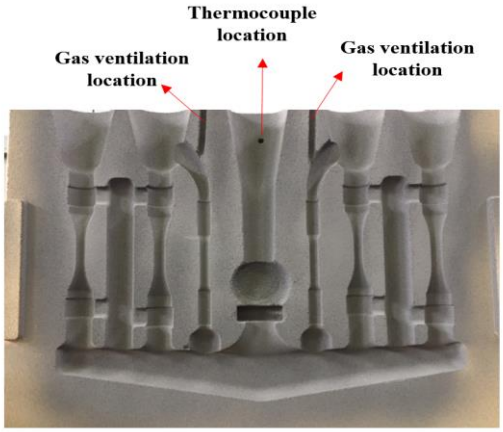

Fig. 3.7 Thermocouple and gas ventilation location in painted sand moulding

The appearance of casting brunch in the mould after casting is illustrated in Fig. 3.8. The mould was fully filled without any problem. Moreover, as it can be understood from the surface of the casting, the chemical reaction problem between sand and magnesium was avoided with precautions. Final appearance of the casting bunch after moulding cut off is shown in Fig. 3.8.

Fig. 3.8 Appearance of the casting bunch after casting in the mould (a) and after moulding cut off

3.2.4 Magnesium Sand Casting Experiment Unit

Since magnesium is very reactivity in molten state, several precautions were taken to avoid any burning and explosion problem. N_2-2%SF_6 gas mixture was used as a main protective gas during melting of magnesium in the induction furnace (Prothoterm Furnace.). In addition to this, pure CO_2 and SF_6 gases were also readily available near to N_2-2%SF_6 in case of any emergency. In order not to cause any cleanliness problem in the melting, flux was not preferred. Instead of this, N_2-2%SF_6 gas mixture was preferred for covering gas to cut any reaction between molten magnesium and mould atmosphere. The specifically designed closed atmosphere pouring cabin is shown in Fig. 3.9 in order to provide safe atmosphere during pouring and solidification. The sand moulding was placed into this system and closed before the experiment. At the beginning of the experiment, vacuum system was run and then N_2-2%SF_6 gas mixture injected to the system to ensure that minimum level of oxygen on the casting atmosphere. In order to guarantee the minimum level of oxygen on the moulding, N_2-2%SF_6 gas mixture was also merged directly to the mold before pouring. The stopper system in Fig. 3.9 was used in the experiment. The casting was started with the pulling the arm of the stopper system until the filling of the mold completed.

3.3 Magnesium Sand Casting Parameters

AZ31D master alloys together with necessary master alloy addition were inserted into the crucible and melting in the induction furnace was started. During melting, all temperature data was controlled by the data acquisition system. After melting of the alloy, temperature was raised to 720 ^oC in 30 minutes with controlled heating. Grain refiner addition and other alloying such as pure Zn, Mg-Sr etc. to make small adjustment in alloying, if necessary, were performed at this temperature. After this

step, 20 minutes holding at 720 ^{o}C was followed in order to ensure necessary dissolution of the elements. In the final step, the temperature was decreased to 690 ^{o}C and pouring into the mould was performed by stopper system.

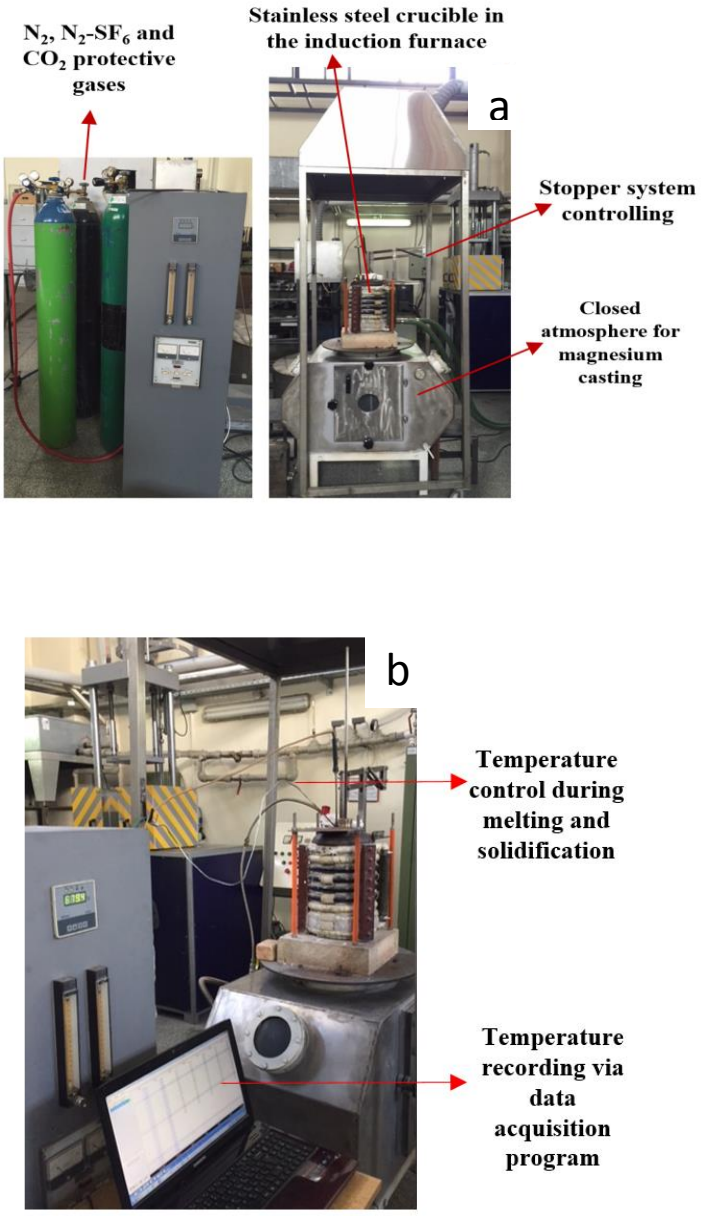

Fig. 3.9 Magnesium sand casting experiment unit (a) protective gases and melting and casting unit (b) temperature recording system

3.4 Thermal Analysis

Thermal analysis was performed to record and characterize the solidification behavior of the studied alloy systems. Thermal analysis was directly taken from the sand casting mold from the locations shown on Fig. 3.2, Fig. 3.6 and Fig. 3.7. Thermal data were collected until the temperature falling down to 400 ^{o}C or lower from the start of collection data. Data collected for every 1 second on an ORDEL 100 universal data loger device connected to a computer with Dali data acquisition software was analyzed using Microsoft EXCEL® and Matlab programs. A K type thermocouple was used in all experiments. Data was collected every 1 second on an ORDEL UDL 100 device connected to a computer with Dali data acquisition software.

Liquidus and solidus temperatures were determined by taking the derivative of the temperature-time cooling curve and evaluating the deviation in linearity during cooling. An example of a cooling curve together with its first derivative is illustrated in Fig. 3.10. In addition, undercooling was measured for each alloy system investigated to comment on the effect of undercooling on grain size. First derivative curve of each cooling curve was examined to define the degree of undercooling.

3.5 Specimen Preparation for Tensile Test

The tensile tests were conducted on both as-cast and machined specimens to understand the effect of thickness and casting surface condition on the mechanical properties. The as-cast tensile specimen examples cut from the casting bunch is given in Fig. 3.11. There was no additional operation on these specimens, which were directly subjected to the tensile test.

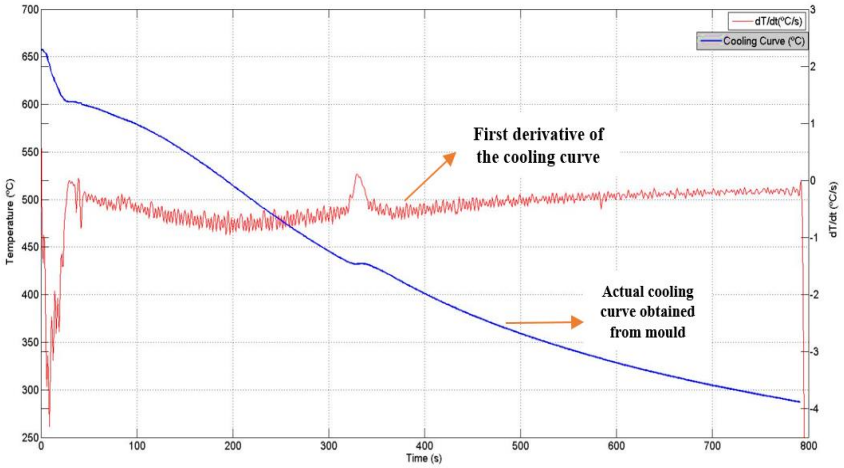

Fig. 3.10 Example of a cooling curve and its first derivative for Alloy I

Fig. 3.11 As-cast specimen examples for tensile test

The machined specimens were taken both from rectangular area shown on casting bunch and gating systems. The specimen locations for these specimens are provided

in Fig. 3.12. The specimens are grouped as machined tensile specimens and machined specimens taken from the gating. The specimens taken from the gating allow understanding the mechanical property difference in low and high possibility of casting defect regions.

The example specimens cut off from the casting bunch is shown in Fig. 3.13 (a). These specimens were subsequently machined and their final appearances are shown in Fig. 3.13. These specimens were grouped according to their location, as already mentioned, and their test results were evaluated accordingly.

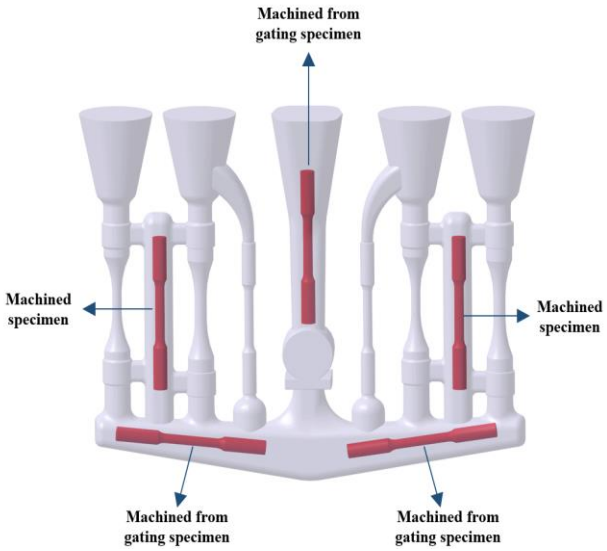

Fig. 3.12 Machined specimen locations taken from rectangular specimen and gatings (shown by red color)

(a) (b)

Fig. 3.13 Machined test specimens for tensile test examples (a) before machining (b) after machining

3.6 Heat Treatment of Specimens

All tensile test specimens were T6-heat treated before the test. Heat treatment parameters were selected after reviewing the standards and literature. Solutioning was perfomed in protective atmosphere (N_2-2%SF_6) due to the risk of oxidation and burning of Mg-Al alloys during heat treatment. Water quenching after solution heat treatment was performed at temperature about 60 ^{0}C. Aging treatment was performed directly after cooling to water quenched samples to RT. Since low temperatures were used in aging treatment, there was no protective atmosphere. The temperatures and times for heat treatment cycle used in this thesis are summarized below:

- Solution heat treatment at 420 ^{o}C for 12 hours
- Water quenched at 60 ^{o}C
- Aging treatment at 200 ^{o}C for 16 hours

3.7 Radiographic Inspection of Castings

Variations in compositions of castings required to see whether there is any deviation in terms of internal quality exists between the alloy systems. Radiographic inspection was performed to examine gas porosity, foreign materials internal cracks, voids and microshrinkage. It was tried to correlate the region of fracture in tensile test and radiographic inspection results.

Radiographic inspection was performed at Turkish Aerospace Industries, Inc. (TAI) Process Control Laboratory via film method. In addition, digital radiographic inspection was also conducted at METU Non-Destructive Testing Laboratories. The X-ray tube used in film method was ERESCO 65 MF4 (300 Kv 6mA Focal Spot size 3 mm, effective focal spot size 2,5mm). The brand of film was Carestream Industrex AA400 contactpak 30x40 cm. The shooting parameters were 50 kV 6 mA time 1:30, 70 kV 6 mA time 1:40, 70 Kv 6mA time 2:00.

Digital radiography result of Alloy I before filter insertion is given Fig. 3.14. The results of both radiographic film and digital radiography were evaluated. The reasons of gas porosity in as-cast specimens could be attributed to entrapment in the cross section changes in the mold geometry and N_2-%2SF_6 protective gas given to the mold just before the pouring. According to the radiographic inspection results, the smaller gage section (approximately, 8 mm) specimens are more susceptible to gas porosities. In addition, foreign materials were not detected in the specimens due to the addition of alloying element dissolution problems in the radiographic results. After evaluation, specimens with minimum and similar internal discontinuities were evaluated in this thesis. After the tests, porosity measurements were conducted just

below the fracture surface. The tensile test results were compared to the porosity percentages.

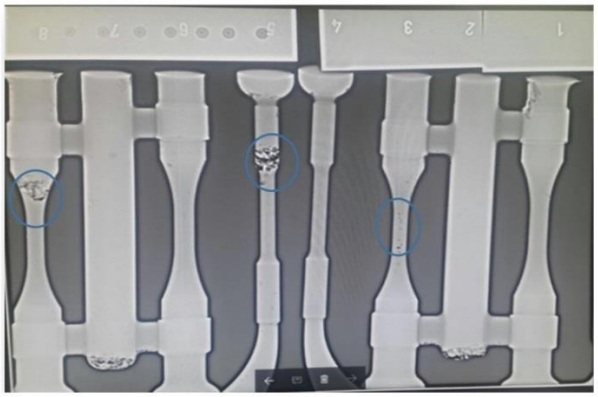

Fig. 3.14 Gas porosities present in cross section changes and smaller gage specimens

3.8 Tensile Testing

Tensile tests were performed to determine yield strength (YS), ultimate tensile strength (UTS) and elongation (% El.) of the specimens. All specimens were tested in T6 heat treated conditions. As-cast, machined and machined form gating systems specimens in each alloy system were used to compare mechanical properties of the alloy system. In as-cast surface specimens, where the gas porosities were not significant, tensile test results did not deviate significantly whether the specimen were reduced gage specimens or not. Machined specimens and machined specimens from the gating system had the same geometry. The tested specimens' geometries are represented in Fig. 3.15. Tensile test was conducted with an elongation rate 1 mm/min. for each alloy system as shown in Table 3.5. Yield strength of the alloys was determined with taking 0.2% offset from the stress-strain curve. Instron 5985 electromechanical test machine was used in the tests.

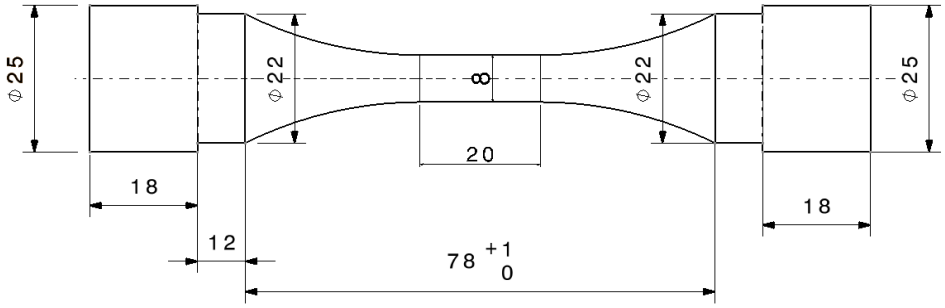

(a) As-cast specimen 8 mm reduced section diameter example

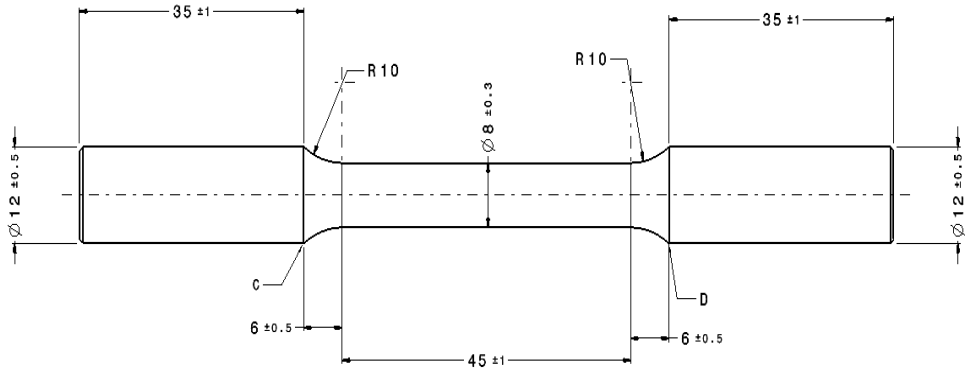

(b) As-cast tensile specimen geometry

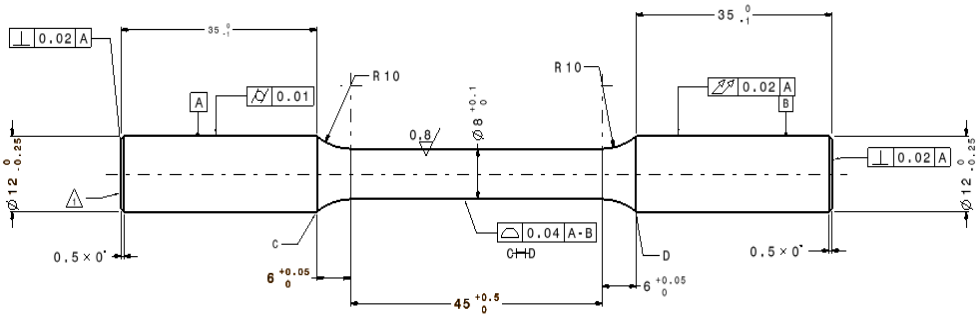

(c) Machined tensile specimen geometry

Fig. 3.15 As-cast and machined tensile specimen geometry used in the tensile tests (a) ASTM E466 [123] (b) and (c) ASTM B557 [124]

3.9 Microstructural Characterization

3.9.1 Optical Microscopy and Scanning Electron Microscope (SEM)

Microstructural samples were sectioned just below the fracture surface and mounted in could epoxy resin. Metallographic specimen preparation started with the grinding of samples from 120 to 1200 grit and then continued with polishing with 6 μm and 3 μm Al_2O_3 paste. This sample preparation was performed in each alloy system in as-cast and T6 (solutionizing + quenching + aging) conditions. The etchant for grain size general microscopic images was the mixture of 6 g picric acid, 50 ml acetic acid, 100 ml ethanol and 10 ml distilled water. [125]

The microstructural investigation and grain size measurement of metallographically prepared samples were performed on a Huvitz optical microscope and SOIF XJP-6A optical microscope. The SEM examinations were performed on a typical working distance 5 mm together with the accelerating voltage 18 kV, spot size of 5 and aperture set at 2 on Nova Nano SEM430 microscope. The fracture surfaces after tensile test were also studied in SEM.

The grain size measurement per ASTM E112 [126] and porosity analysis were investigated with the Dewinter Material Plus program and image analysis software on SOIF XJP-6A optical microscope, respectively. For the former, at least 50 measurements of T6 samples in different areas were conducted. For the latter, minimum 10 different regions were examined and average of them was recorded.

3.9.2 X-Ray Diffraction (XRD)

XRD analysis was performed to determine the phases present in each alloy system and effect of alloying additions to new phase formation. The analysis was performed on Bruker D8 Advance X-Ray diffractometer with Cu Kα radiation. The range of X-ray 2θ angle is 20-120^0. The step size was chosen as 0.02^O with a count time of 3 second for one step.

CHAPTER 4

EXPERIMENTAL RESULTS AND DISCUSSIONS

4.1 Cooling Curve and Undercooling Analysis

Cooling curve analysis was performed with the data taken from the thermocouple position shown in Fig. 3.2 and Fig. 3.7. The thermocouple read the temperature for every second. After getting the time and temperature data via data acquisition system explained in Section 3.4, cooling curves and their firs derivatives were plotted for each alloy system via Microsoft EXCEL® and Matlab® programs. In order to define exact phase transformation temperatures, the first derivative of each curve was obtained on Matlab®.

Fig. 4.1 shows the cooling curves of each alloy system. By analyzing these curves, it was deduced that AZ91 base alloy (Alloy IV) shows 0.4 ^{O}C undercooling for primary α-Mg phase nucleation as indicated in Fig. 4.2. After addition of Si, Ca, Sr and Sn (Alloy I), the degree of undercooling decreased to 0.2 ^{O}C, which indicates grain refinement achieved in comparison to AZ91 alloy. For Alloy II, the degree of undercooling is nearly same with Alloy I. However, undercooling degree of Alloy III is nearly 0 ^{O}C. The main reason for such decrease in undercooling for this alloy type could be attributed to Al-5Ti-B inoculation, which decreases the undercooling and helps to obtain finer grain size for higher mechanical properties. The plateau temperatures for Alloy I-III are shown in Fig. 4.3. The plateau temperatures obtained with the peak points from the first derivatives of the each ally system. The example

of Alloy IV (AZ91) is shown in given Fig. 4.4. The figures for other alloys are presented in Appendix A. (A.1) The critical temperatures obtained after analyzing these figures are listed in Table 4.1.

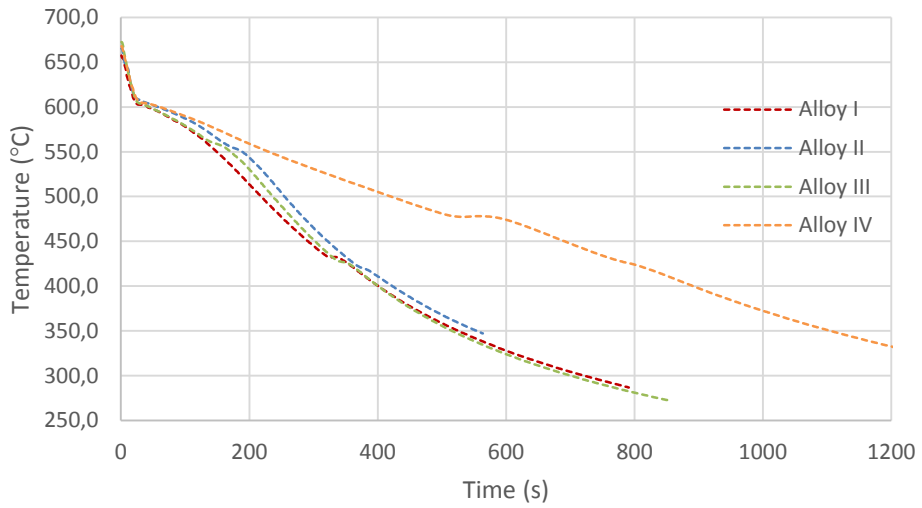

Fig. 4.1 Cooling curve comparison of the alloys

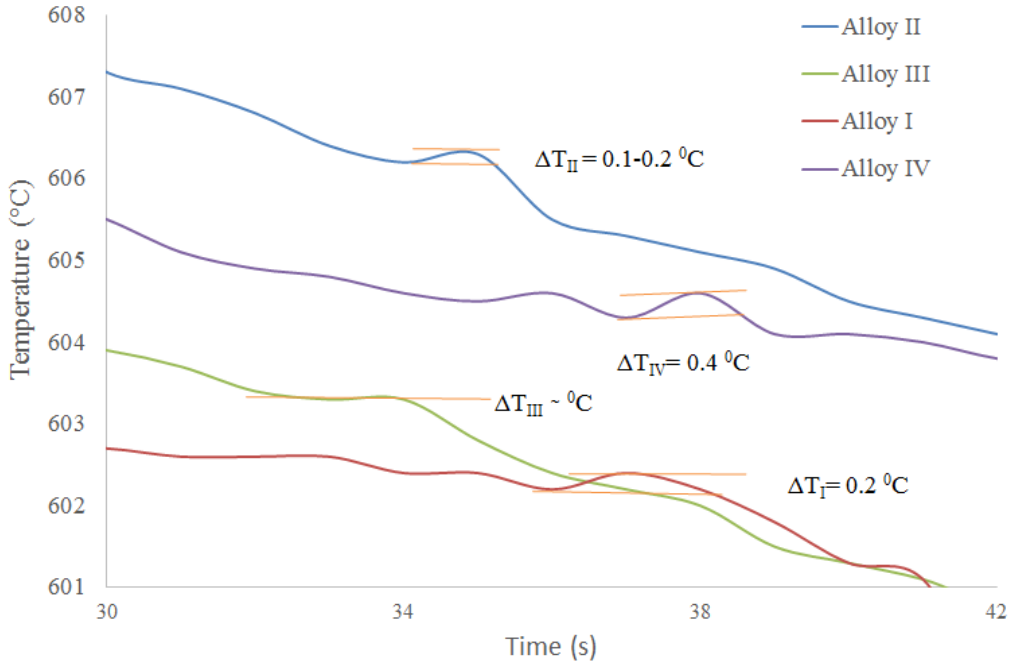

Fig. 4.2 Undercooling degree (ΔT) of the alloys

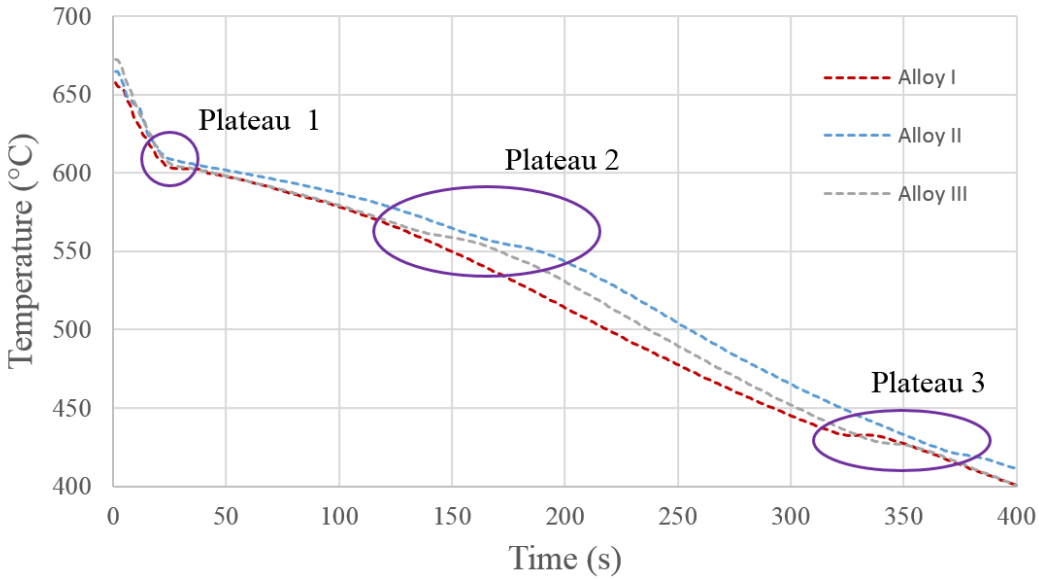

Fig. 4.3 The plateau and phase transformation temperature of the alloys

The solidification temperature was obtained as 604.1 ºC for Alloy IV (AZ91) where the first derivative of cooling curve indicates the first peak of the curve as shown in Fig. 4.4. The other two peak temperatures corresponding to the other phase transformations are listed in Table 4.1. The phases formed in AZ91 were α-Mg, Al_8Mn_5 and β-$Mg_{17}Al_{12}$, which were also verified by XRD and EDS analysis as explained in Section 4.1, 4.2, and 4.5.1. For Alloy I-III, the number of peaks obtained from the first derivatives was also three. The details of cooling curves and its first derivatives are given in the figures provided in Appendix A (A.1). The peaks in these figures represent the phase transformation temperatures of α-Mg, Mg_2Si and β-$Mg_{17}Al_{12}$ phases. These phases were also detected by XRD analysis. In addition, Al-Mn containing phases were also observed in SEM and EDS analysis. However, the lower amount of Al-Mn containing phase in the microstructures could be the reason not to see any peak related with this phase formation in the cooling curve. The summary of the phase transformation and their temperatures for all alloys is presented in Table 4.2.

The difference in the phase transformation and their times can be mainly attributed to the constitutional undercooling created by alloying element addition. In addition, dissolution of added elements in Mg_2Si phase such as Ca, Sr and Sn affect its formation temperature. The shift in solidus temperature could be due to the solute content increase via alloying [121].

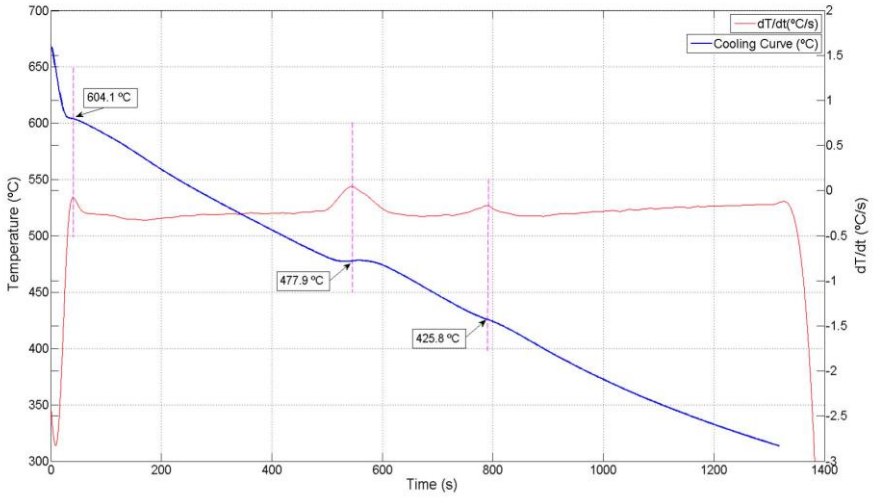

Fig. 4.4 Cooling Curve and its first derivative for Alloy IV (AZ91)

Table 4.1 Summary of the critical temperature and time data for each alloy obtained from fist derivative curves

Alloy	Peak #	Temp. Def.	Temp. (^{O}C)	Alloy	Peak #	Temp. Def.	Temp. (^{O}C)
I	1	T_n	636	II	1	T_s	635
		$T_l = T_{p1}$	602.6			$T_l = T_{p1}$	605.5
	2	T_{p2}	584		2	T_{p2}	554
	3	$T_s = T_{p3}$	432.4		3	$T_s = T_{p3}$	419.5
III	1	T_n	646.8	IV	1	T_s	647.8
		$T_l = T_{p1}$	602.8			$T_l = T_{p1}$	604.1
	2	T_{p2}	559.2		2	T_{p2}	477.9
	3	$T_s = T_{p3}$	427		3	$T_s = T_{p3}$	425.8
T_n: α-Mg nucleation start temperature (start of the first peak) T_l: liquidus temperature (peak point of the first peak T_{p1}, T_{p2}, T_{p3}: peak point of the first, second and third peak) T_s: solidus temperature (peak point of the third peak)							

Table 4.2 Solidus, liquidus and phase transformation temperatures of studied alloys with their corresponding reactions

Alloy	Temperature (^{O}C)	Transformation
Alloy I	T_l (T_{p1})= 602.6	α-Mg nucleation start: L= α-Mg + L
	T_{p2} = 584	Mg_2Si formation start: L = Mg_2Si + L
	T_s (T_{p3}) = 432.4	Solidification end: L= α-Mg + β-$Mg_{17}Al_{12}$
Alloy II	T_l (T_{p1})= 605.5	α-Mg nucleation start: L= α-Mg + L
	T_{p2} = 554	Mg_2Si formation start: L = Mg_2Si + L
	T_s (T_{p3}) = 419.5	Solidification end: L= α-Mg + β-$Mg_{17}Al_{12}$
Alloy III	T_l (T_{p1})= 602.8	α-Mg nucleation start: L= α-Mg + L
	T_{p2} = 559.2	Mg_2Si formation start: L = Mg_2Si + L
	T_s (T_{p3}) = 427	Solidification end: L= α-Mg + β-$Mg_{17}Al_{12}$
Alloy IV	T_l (T_{p1})= 604.1	α-Mg nucleation start: L= α-Mg + L
	T_{p2} = 477.9	Al_8Mn_5 formation start: L = Al_8Mn_5 + L
	T_s (T_{p3}) = 425.8	Solidification end: L= α-Mg + β-$Mg_{17}Al_{12}$

Liquidus and solidus temperatures were used to determine solidification (freezing range (FR) range of the alloys. The highest FR was measured for Alloy II as shown in Table 4.3. It is expected for Alloy II to have highest hot cracking possibility due to long mushy zone as indicated while Alloy I has the lowest hot cracking possibility. Al-5Ti-1B inoculation to Alloy II brought to decrease of freezing range from 186 to 175.8 ^{O}C as indicated in Table 4.3 [87]. It could be reasonably proposed from this result that AL-5Ti-1B inoculation to Alloy II improved the feeding behavior providing higher castability in accordance with these results. In addition, in the study performed by Zhao et al. [12], solidus and liquidus temperatures of AZ91 alloy were measured by DSC method as 435 and 591 ^{O}C, respectively. In this thesis, the temperatures for the same alloy were recorded as 604.1 and 425.8 ^{O}C, respectively. Due to the lower solidification rate in sand casting, the freezing range, which is directly related with the solidus and liquidus temperatures, is higher than the data provided in the literature as expected. In addition, since the temperature data taken directly from the mould, the difference in temperature could be seen as normal in comparison to DSC measurement in controlled atmosphere.

Table 4.3 Solidus, liquidus and freezing range of the studied alloys

Alloys	Solidus (^{O}C)	Liquidus (^{O}C)	Freezing range (^{O}C)
Alloy I	432.4	602.6	170.2
Alloy II	419.5	605.5	186
Alloy III	427	602.8	175.8
Alloy IV	425.8	604.1	178.3

Lee et al.[121] has also studied to define solidus and liquidus of AZ91E alloy with different grain refiner additions such as Al-5TiB_2, Al-Al_4C_3 ZnO. In adition, by identifying the FRs of the alloys, hot tearing susceptibilities for the studied alloys were interpreted and observed by tests. The freezing range of the studied alloys is illustrated in Fig. 4.5. The freezing rage of AZ91E magnesium alloy was measured as 164 ^{O}C, while the FRs with the addition of Al-5TiB_2, Al-Al_4C_3 and ZnO to AZ91E magnesium alloy was found as 165, 166, and 172 ^{O}C, respectively [26,120].

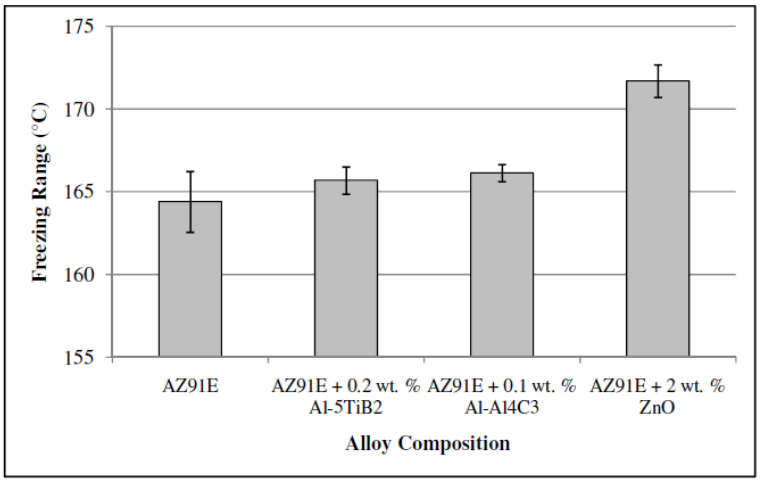

Fig. 4.5 Influence of different grain refiner addition on the freezing range of AZ91E [121]

The undercooling degree of AZ91E for magnesium alloy was found as 1 ^{O}C while that of AZ91E-0.1%Al-5Ti-1B addition with 10 minute holding time was measured as 0.2 ^{O}C [79]. These results are consistent with this thesis. The measured

undercooling for AZ91 and AZ91-0.7%Si-0.3%Sr-0.6%Sn + 0.1% Al-5Ti-1B allow was detected as 0.4 and~ 0-0.1 ^{O}C, respectively. The alloying element could also be responsible for the further decrease in undercooling.

4.2 XRD Analysis

X-Ray Diffraction (XRD) analysis of the studied alloys in as-cast condition was shown in Fig. 4.6. Alloy I consists of α-Mg, β-$Mg_{17}Al_{12}$, Mg_2Si phases while Alloy II and III consist of MgSiSr phase in addition the phases detected in Alloy I. Alloy IV (AZ91) contains α-Mg, β-$Mg_{17}Al_{12}$ and Al_8Mn_5 phases. The phases observed in XRD analysis were symbolized on the top of the peaks (Fig. 4.6).

According to the XRD analysis, 0.6-0.7 % Si addition to AZ91 alloy was resulted in the formation of Mg_2Si phase for Alloy I to Alloy III as seen in Fig. 4.6. For Alloy II and Alloy III, Sr addition also revealed the MgSiSr phase peaks. However, Ca addition did not cause any phase formation in Alloy I. In addition, 0.5-0.9% Sn addition to all alloy series and 0.1% Al-5Ti-B grain refiner addition to Alloy III did not bring any new phase formation according to XRD analysis.

4.3 Radiographic Inspection

Radiographic inspection was used to verify solidification characteristics in the mould, determine areas of possible gas porosities and resolve any foreign material existing in the specimens. After inspections, it was decided that main observable casting defect is gas porosities. In addition, adding filter into the mould system was decreased to turbulence especially in the transition area of thin and thick region, which is confirmed by the comparison digital radiographic results of Fig. 4.7 (a) and Fig. 4.7 (b).

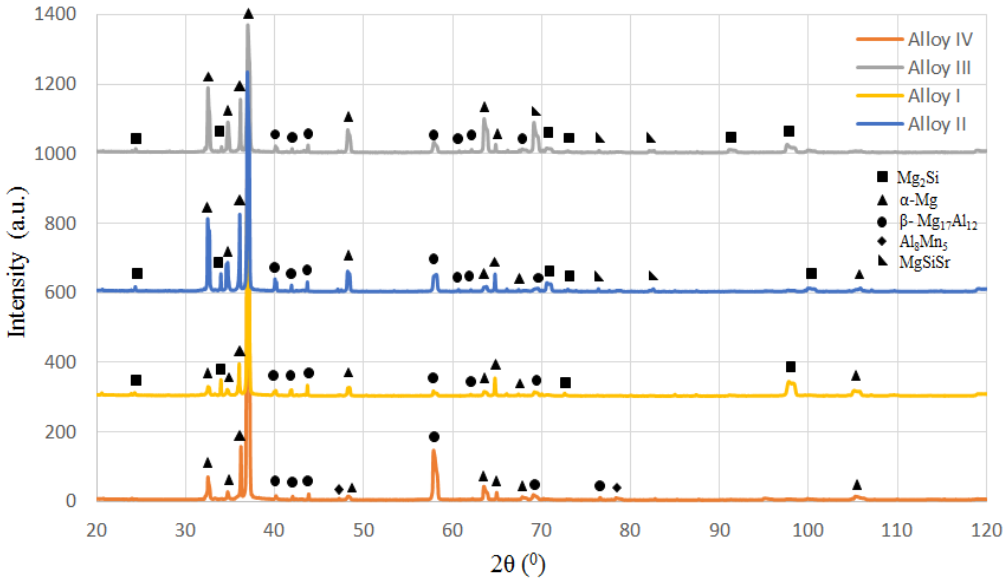

Fig. 4.6 XRD analysis of the alloys (Alloy I, II, III, IV)

The regions indicated by circles on Fig. 4.7 (a) represent the areas having gas porosities. These regions consist of the transition region between thin and thick region and gage section (thin test region) of as-cast specimen surfaces. By introducing filter and pool above it into the moulding system as shown in Fig. 4.7 (b), these gas porosities were minimized in the specimens in comparison to the previous system. The magnified region of the specimens in the filter added mould are shown in Fig. 4.8. As seen in this figure, some minor gas porosities were detected on the test region, they were so minor in comparison to unfiltered mould system. Due to this reason, all specimens tested in this thesis were taken from the filtered added mould system. Tested specimens have selected according to the radiographic inspection results and these specimens had similar radiographic results as much as possible.

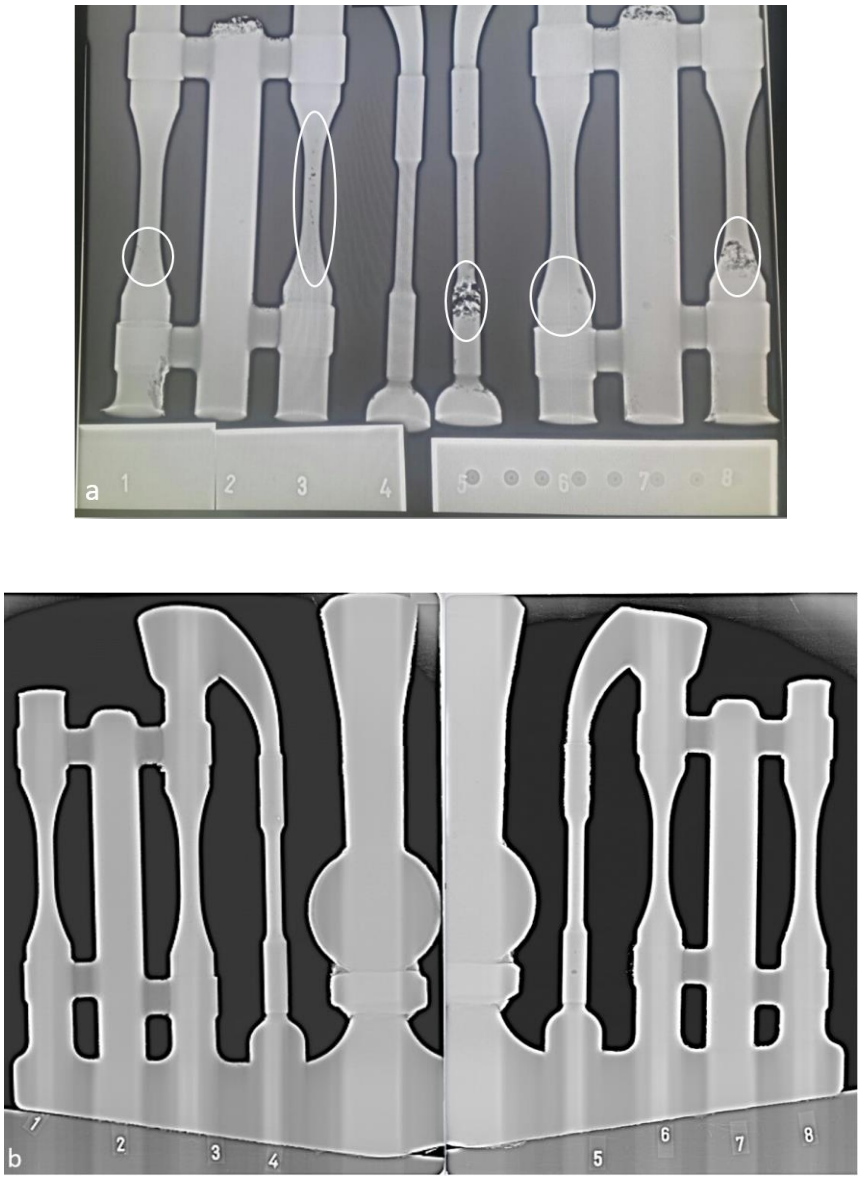

Fig. 4.7 Radiographic inspection of the specimens before (a) and after (b) filter addition

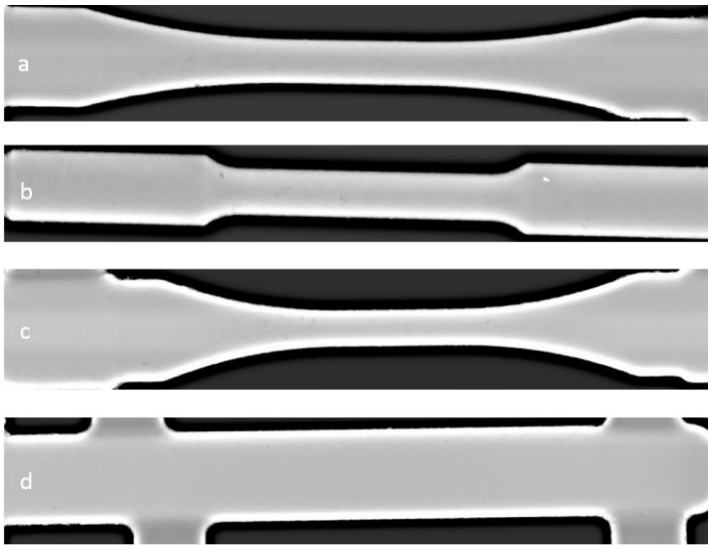

Fig. 4.8 Digital radiography results for magnified region of test specimens given in Fig. 4.7 (a) 10 mm reduced section as-cast surface specimen (b) 10 mm as-cast surface specimen (c) 10 mm reduced section as-cast surface specimen (d) 22 mm bar specimen to be machined

4.4 Tensile Test Results

Tensile tests were performed in machined, machined from gating and as-cast surface specimen in order visualize the effect of specimen conditions on mechanical properties. All specimens were tested in T6 heat treated condition. The as-cast specimens were directly subjected to the tensile tests after heat treatment without any subsequent operation. The geometry of the specimen are provided in Fig. 3.15. (10 mm reduced specimen was also used. Due to the similar mechanical properties were obtained with Fig. 3.15 (a), the geometry of this type specimen was taken as 10 mm reduced specimen.) The machined specimens were machined from 22 mm rectangular bar taken from the casting mould. (Fig. 3.12) The machined from gatings specimens had approximately 30 mm thicknesses. Therefore, three different specimen types provide to compare the effect of different casting thicknesses on mechanical properties. Since it is very important to control structural integrity of

casting component, this evaluation brings the opportunity whichever alloy series have more appropriate for more uniform mechanical property distribution over all casting regions.

Table 4.4 summarizes the tensile test results of alloys series in different specimen conditions after T6 heat treatment. As seen in this table, mechanical properties in as-cast surface condition has the highest mechanical properties in each alloy series while machined from gating specimen shows the lowest of that due to higher casting thickness. Higher casting thicknesses results in more susceptible to casting defects such as shrinkage and porosity, which affects dramatically the mechanical properties. Alloy IV has the highest UTS value in as-cast surface specimen condition and it decreases Alloy III, Alloy II and Alloy I in the sequence. However, Alloy III (Alloy II +0.1%Al-5Ti-1B) has superior UTS values both machined and machined from gating specimen conditions. Therefore, Alloy III shows desired highest structural integrity in these alloy series.

Table 4.4 Tensile test results of alloy series in different specimen conditions

Alloy	Specimen Condition	Mechanical Properties		
		UTS (MPa)	YS (MPa)	El. (%)
Alloy I	Machined (22 mm)	175	136	1.9
	Machined from gating (30 mm)	160	142	1.7
	As-cast (10 mm)	191	105	3.4
Alloy II	Machined (22 mm)	193	164	2.3
	Machined from gating (30 mm)	150	130	2.7
	As-cast (10 mm)	200	98	3.3
Alloy III	Machined (22 mm)	200	164	2.4
	Machined from gating (30 mm)	190	176	2.2
	As-cast (10 mm)	204	105	2.8
Alloy IV	Machined (22 mm)	157	150	0.9
	Machined from gating (30 mm)	146	137	0.8
	As-cast (10 mm)	207	102	1.4

The tensile strength comparison of each alloy series is provided in Fig. 4.9. As indicated in this figure, as-cast surface specimen has the highest ultimate tensile strength while those of machined and machined from gating specimen are decrease in order, respectively. The UTS value of Alloy IV in as-cast specimen surface condition is the highest and comparable to that of Alloy III.

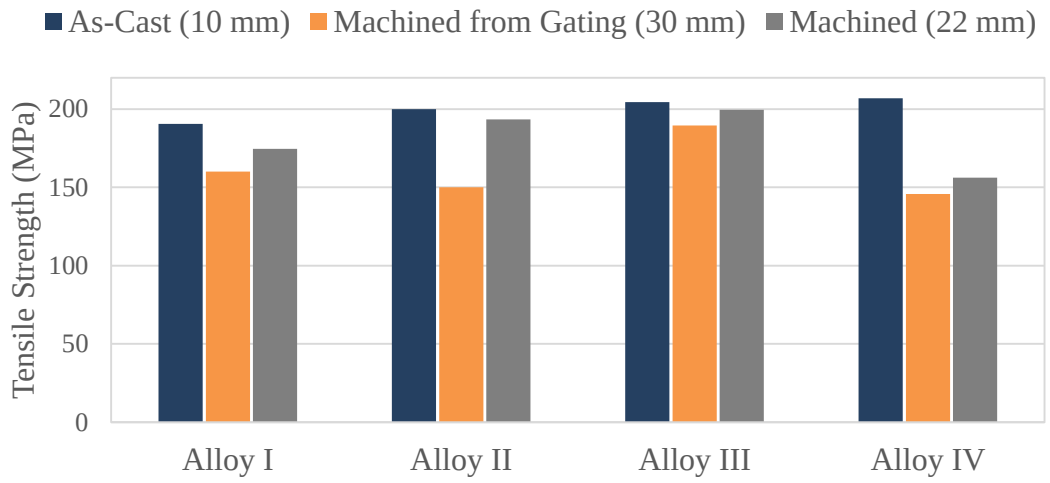

Fig. 4.9 Ultimate tensile strength (UTS) (MPa) comparison in T6 heat treated conditions for all alloy series

The yield strength values change considerably in different specimen conditions in each alloy series (Fig. 4.10). The change in yield strength values for Alloy I to III with respect to Alloy IV could be ascribed to the formation of Mg_2Si phase, which enhances the dislocation density. [59] Due to the path change of load transfer via introducing higher strength Mg_2Si phase, yield strength variation in different section thicknesses could be attributed the morphology and thickness alteration of this phase. In addition, variation in casting thicknesses in each alloy series resulted in yield strength differences in each alloy series. This could be predicated to the different solidification rate and alloying elements on the alloy series. It could be concluded

from Fig. 4.10 that variation in casting thicknesses resulted in variability of yield strength in studied alloy series.

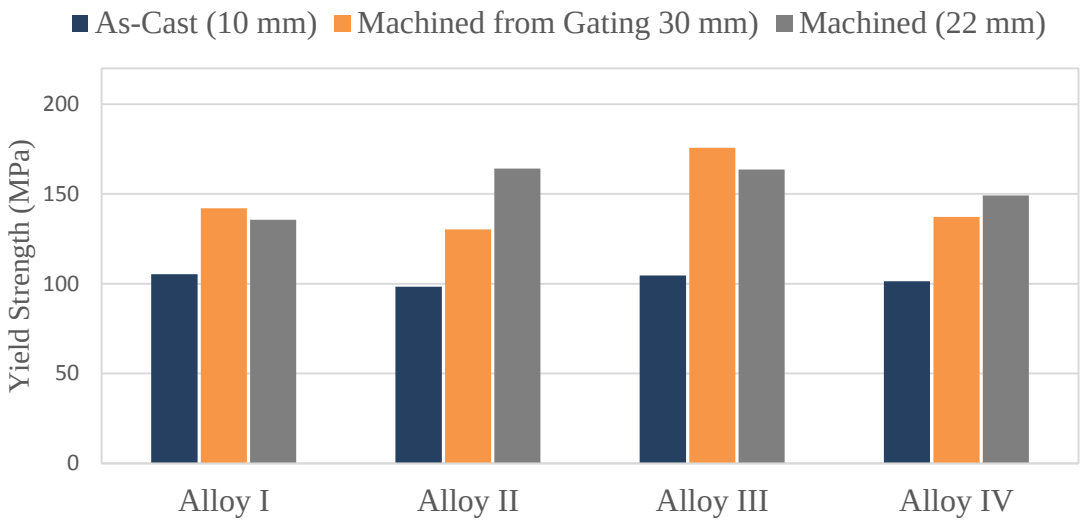

Fig. 4.10 Yield strength (YS) (MPa) comparison in T6 heat treated conditions for all alloy series

The elongation value comparison for different section thicknesses and between the alloy alloy series in this study is presented in Fig. 4.11. This figure shows the benefit of alloying and grain refinement in increase and homogeneity of elongation for variable casting thicknesses.

As already mentioned, researches conducted with sand casting process is very limited. One of the study performed by Universit et al. [46] showed that efficiency on grain refiner depends on the wall thicknesses of the specimen for 16 and 50 mm casting specimen thicknesses in Fig. 4.12 (a) and (b) represent the mechanical properties of 16 and 50 mm specimen diameter conditions, respectively. Nr.5 in these figures shows sand cast T6 heat treated AZ91E alloy with 0.6% C_2Cl_6 grain refiner

addition. Other conditions in this figure given with different Nr number specify the effect of different heat treatment condition on AZ91E alloy without any grain refiner.

The values of UTS, YS and El for AZ91E-0.6% C_2Cl_6 alloy in 16 mm diameter specimen were 302 MPa, 147 MPa and 5.2%, respectively, while those values for that alloy in 50 mm diameter specimen were found as 141 MPa, 110, and 1.1 %, respectively. [46] These results could be explained with inherent microporosity in thick sections. Due to this reason, thick sections of AZ91E castings even with C_2Cl_6 grain refiner need risers and chills to obtain higher cooling and and lower microporosity levels.

In this thesis, the disadvantage of variable mechanical properties in AZ91E alloy is eliminated with via alloying and Al-5Ti-1B grain refiner addition. It can also be concluded that Al-5Ti-1B was more beneficial in comparison to C_2Cl_6 as a grain refiner to obtain higher mechanical properties and more integrity in casting components poured with AZ91E magnesium alloy.

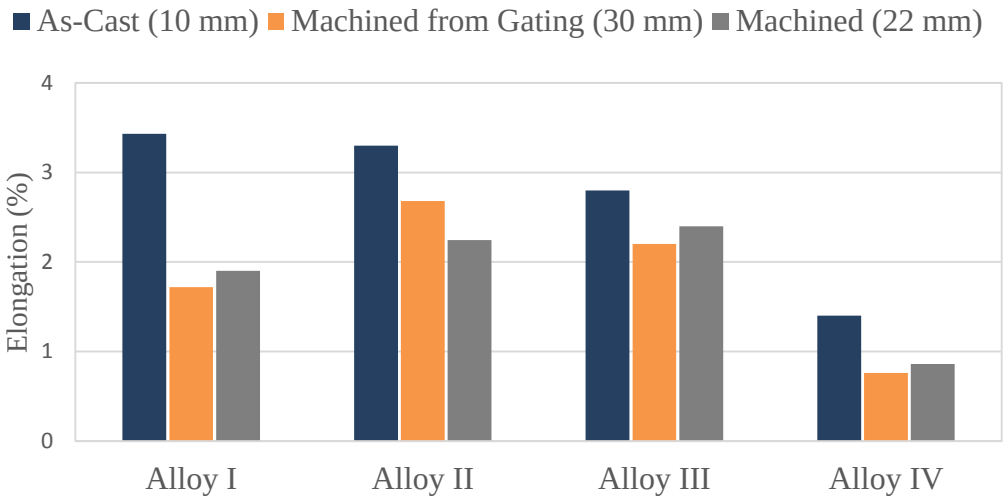

Fig. 4.11 Elongation (El.) (%) comparison in T6 heat treated conditions for all alloy series

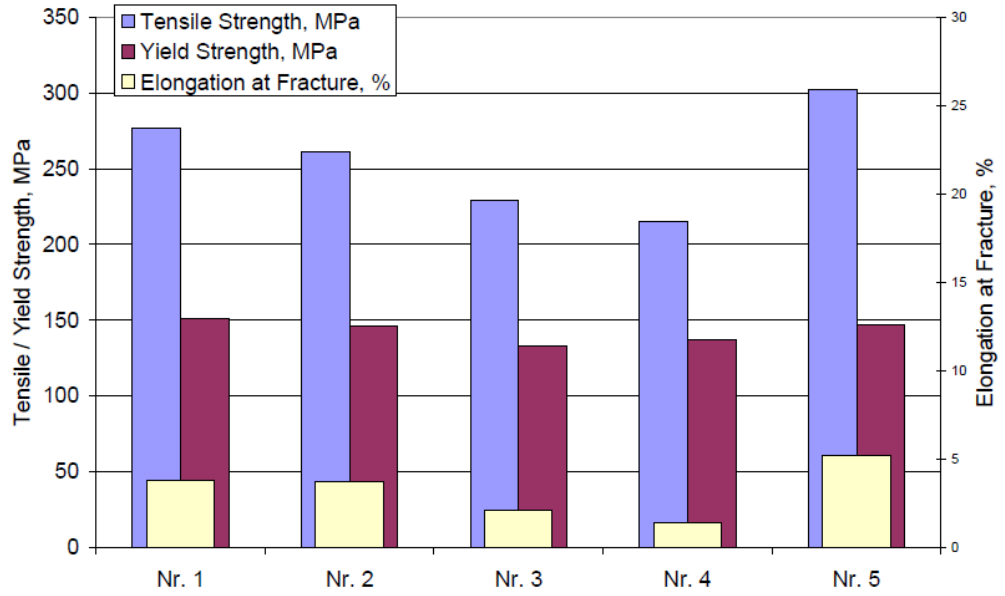

(a)

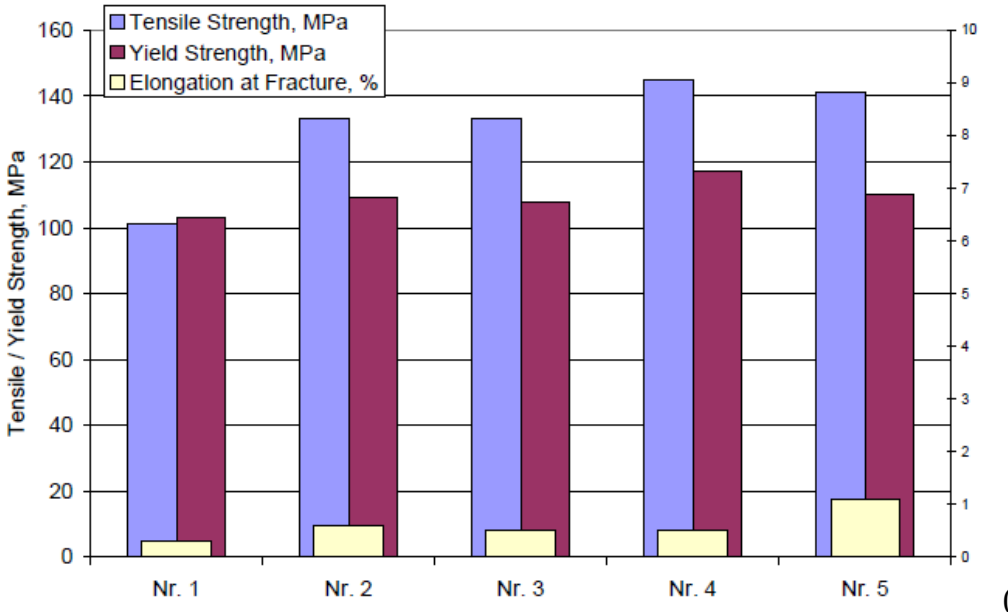

(b)

Fig. 4.12 Mechanical properties of AZ91 sand-cast samples after T6 heat treatment (a) 16 mm (b) 50 mm sample diameter [46]

4.5 Microstructural Analysis

4.5.1 Optical Microscope and SEM Analysis

This section explains the optical microstructural and SEM examination of the alloy series. The phases shown on the micrographs were identified by the correlation obtained from both XRD analysis results and EDS analysis via SEM.

Fig. 4.13 shows the optical images of as-cast Alloy I at different magnifications. As seen in Fig. 4.13 (a), the microstructure consists of massive discontinuous $Mg_{17}Al_{12}$, polygonal Mg_2Si and small Mg-Al-Mn-Fe-Zn containing particles. In addition, α-Mg is the base phase on each alloy system. At higher magnification (Fig. 4.13 (b)), polygonal Mg_2Si and small Mg-Al-Mn-Fe-Zn particle is more obvious. Together with polygonal Mg_2Si phase, Chinese script Mg_2Si was also detected in Fig. 4.13 (c). From this figure, it can be concluded polygonal or detached Mg_2Si particles with modified shape were observed in as-cast state of Alloy I together with some Chinese script Mg_2Si.

In order to identify the phase much more clearly, SEM investigation of Alloy I in as-cast condition was performed. The EDS analysis results of the locations shown in Fig. 4.14 are given Fig. 4.15. According to these results, region A was identified as β-$Mg_{17}Al_{12}$ although some Zn and Ca dissolved in this phase, which may bring improvement in creep resistance. Region B and C were determined as Mg_2Si and Al-Mn-Fe particles, respectively. In addition, region B was designated as polygonal Mg_2Si with some dissolution of Ca, Sn and Al elements. Ca and Sn elements could be attributed to assist modification to polygonal shape if its EDS results are compared with those of Chinese script Mg_2Si. Mg-Al-Mn-Fe-Zn particles, Region C,

are named as Al-Mn-Fe particle after this point in this thesis due to the similarity observed in the literature [38,74,82,84,85]. This particle has been thought as main nucleating agent in these type of alloys in the literature.

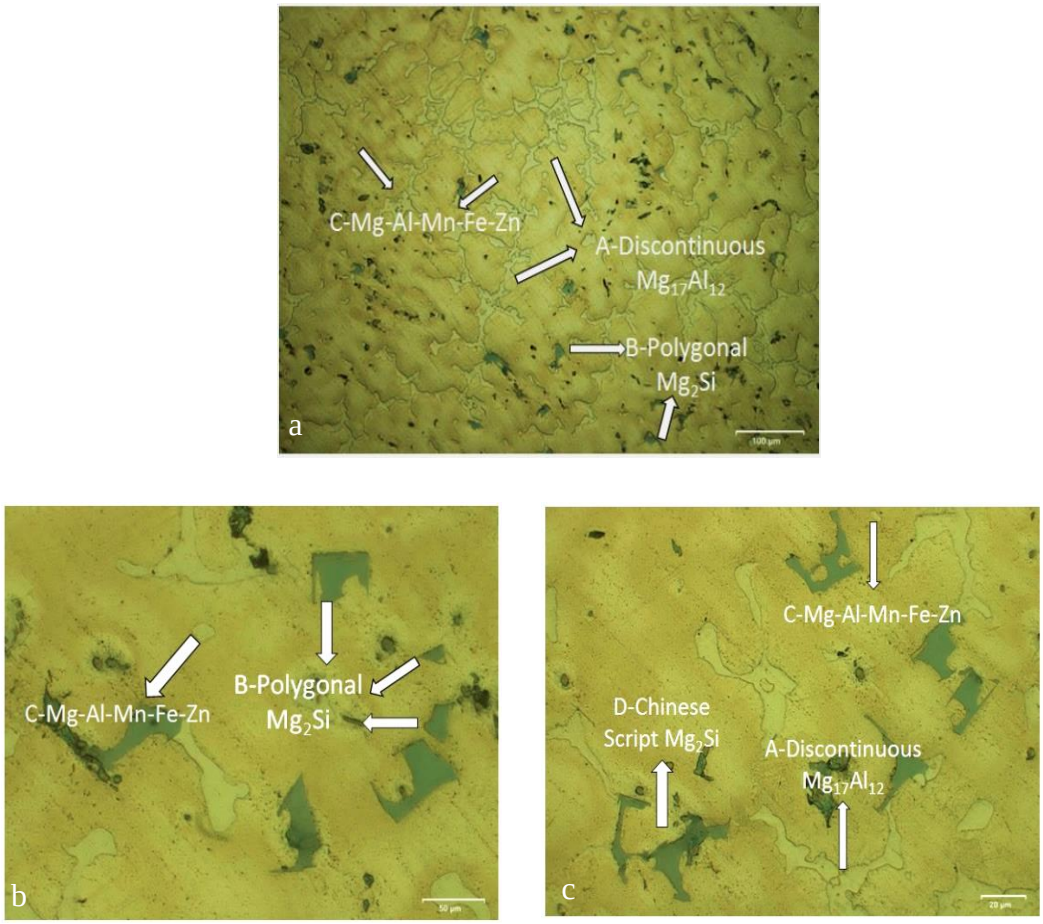

Fig. 4.13 Optical images of Alloy I in as-cast condition (a) General overview at lower magnification (b) Polygonal Mg_2Si and Mg-Al-Fe-Mn-Zn particle (c) Chinese script Mg_2Si phase (A-Discontinuous $Mg_{17}Al_{12}$, B-Polygonal Mg_2Si, C-Mg-Al-Mn-Fe-Zn particle, D-Chinese Script Mg_2Si)

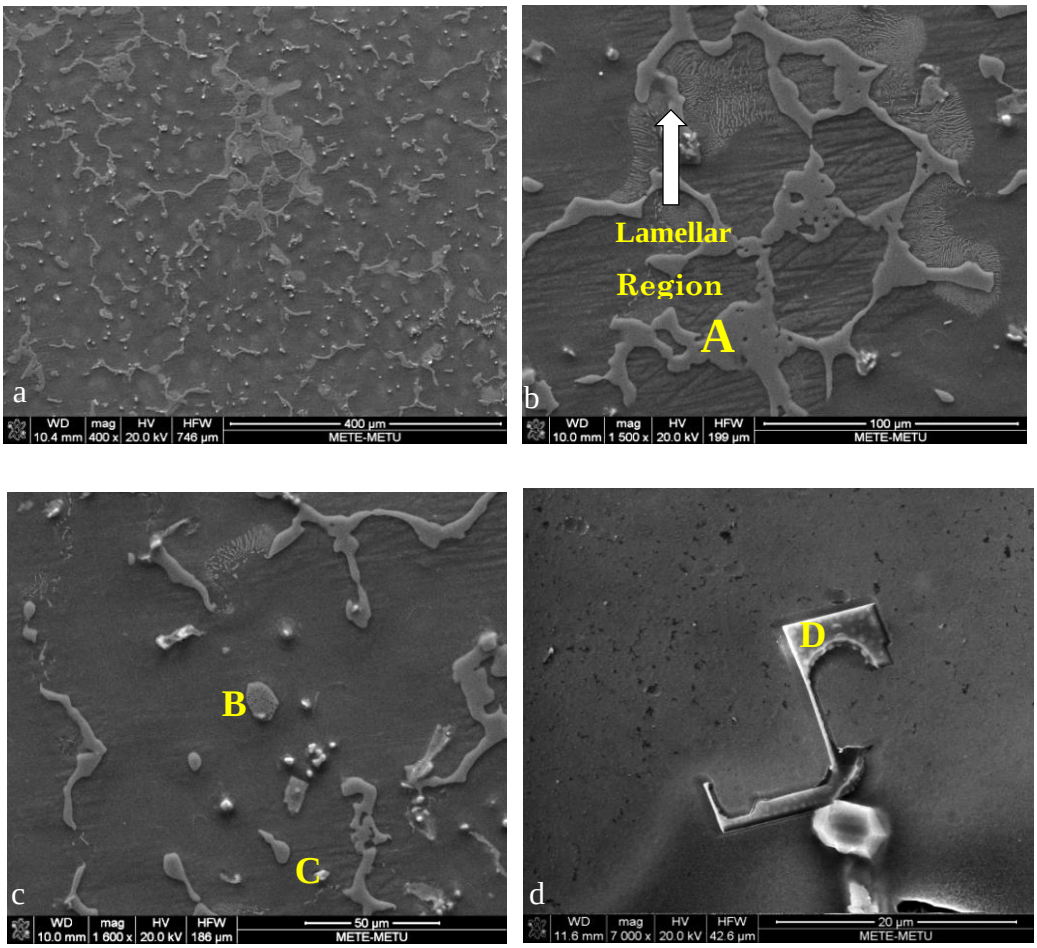

Fig. 4.14 SEM images of Alloy I in as-cast condition (a) general microstructural overview at higher magnification (b) massive discontinuous β-$Mg_{17}Al_{12}$ showing EDS analysis region 'A' (c) polygonal Mg_2Si phase and Mg-Al-Mn-Fe-Zn showing EDS analysis region 'B' and 'C' (d) Chinese script Mg_2Si showing EDS analysis region 'D'

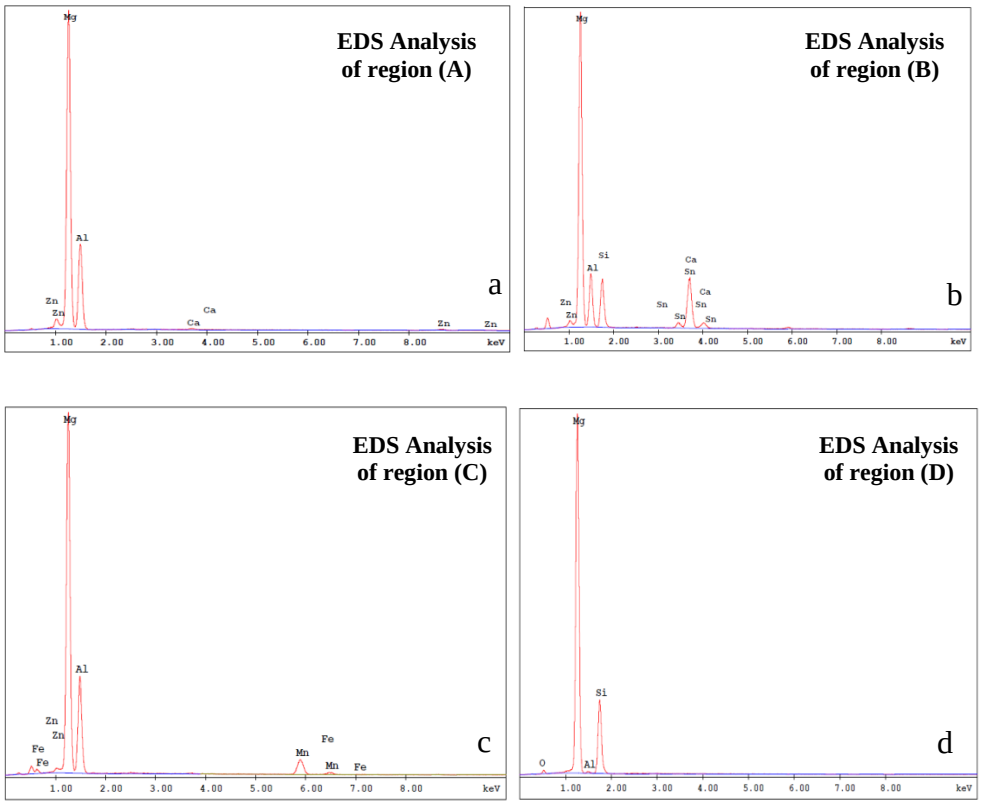

	Region A	Region B	Region C	Region D
Element	wt.%	wt.%	wt.%	wt.%
Mg	56.09	48.71	54.99	65.29
Al	40.72	16.99	31.45	0.87
Ca	0.58	13.55	-	-
Zn	2.61	2.14	1.55	-
Si	-	14.39	-	33.84
Sn	-	4.21	-	-
Mn	-	-	11.75	-
Fe	-	-	0.25	-

Fig. 4.15 EDS analysis results of the locations shown in Fig. 4.14 (a), (b), (c), and (d) showing the EDS analysis results of A, B, C, and D regions, respectively

After T6 treatment to Alloy I, optical microstructure images at different magnifications are provided in Fig. 4.16 (a), (b), and (c). At the highest

magnification given in Fig. 4.16 (c), spheroidization tendency of polygonal and Chinese script Mg_2Si are clearly observed, which could bring increase in elongation and UTS values in tensile test [13,47]. In these optical images, it was concluded that dissolution of local massive discontinuous β-$Mg_{17}Al_{12}$ is obtained with solutioning and aging treatment. In addition, Al-Mn-Fe particles were not detected by optical microscope after the heat treatment.

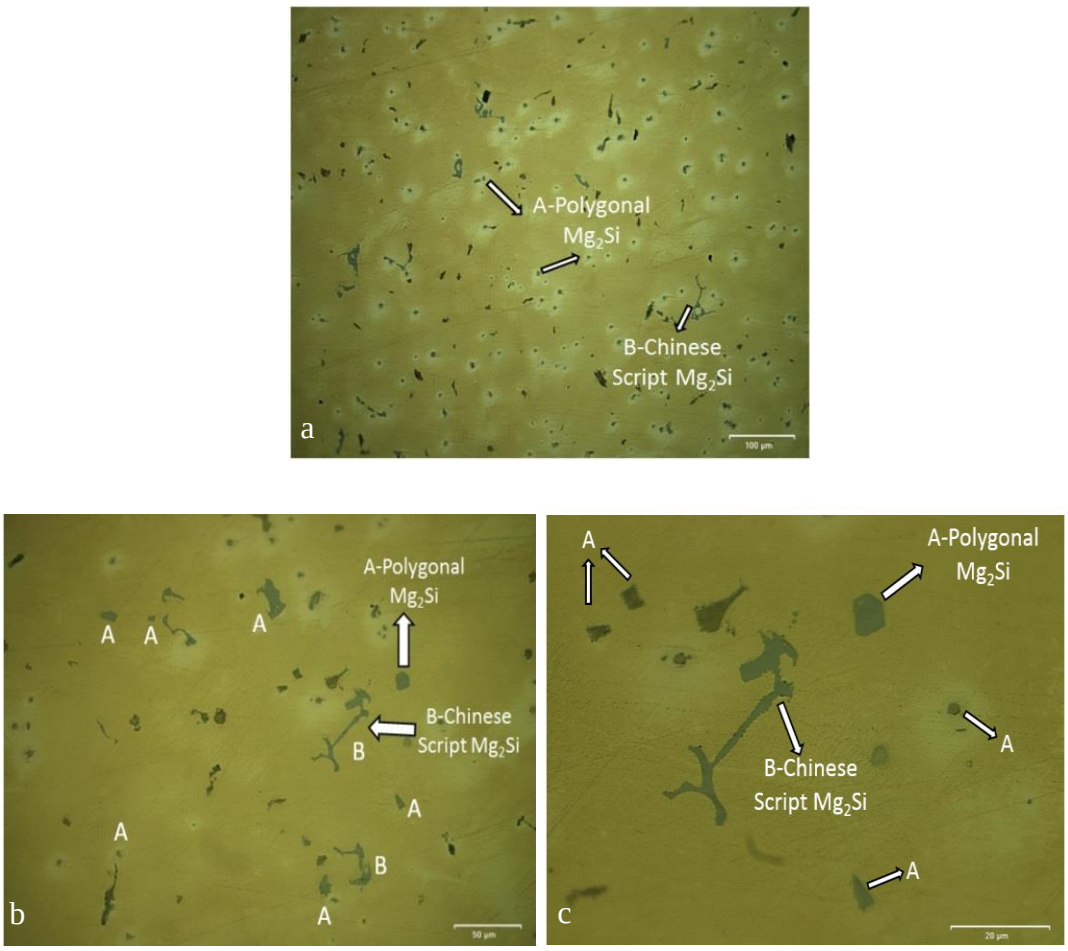

Fig. 4.16 Optical images of Alloy I in T6 heat treated condition at different magnifications (a-c, lower to higher, respectively) showing both polygonal and Chinese script morphology Mg_2Si phases (A-Polygonal Mg_2Si, B-Chinese Script Mg_2Si)

The SEM images and EDS analysis results of Alloy I after T6 treatment are given in Fig. 4.17 and Table 4.5, respectively. Region A in Fig. 4.17 (a) was described as β-$Mg_{17}Al_{12}$ with some dissolved Ca according to the EDS analysis results given in Table 4.5. Moreover, region B in Fig. 4.17 (b) was designated as Al-Mn-Fe particle with the help of EDS results provided in the same table.

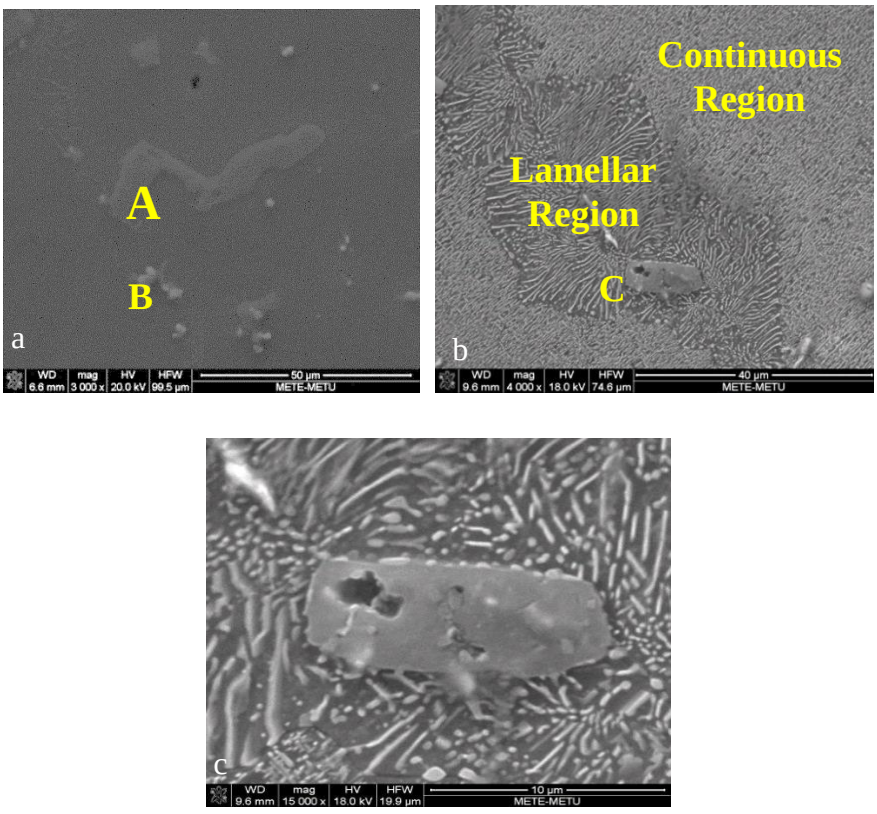

Fig. 4.17 SEM images of Alloy I in T6 heat treated condition (a) SEM image containing both Al-Mn-Fe particle (B) and discontinuous β-$Mg_{17}Al_{12}$ phase (A) (b) Lamellar and continuous region of α-(Mg)-β-$Mg_{17}Al_{12}$ precipitate together with polygonal Mg_2Si phase (c) polygonal Mg_2Si phase (C) given in (b) at higher magnification

Fig. 4.17 (b) shows lamellar (α-(Mg)–β-$Mg_{17}Al_{12}$), continuous precipitate region (α-(Mg)–β-$Mg_{17}Al_{12}$) and area-C identified as polygonal Mg_2Si. This polygonal Mg_2Si particles located at the grain boundary will be certainly responsible to increase in creep strength and RT mechanical properties in comparison to Chinese script Mg_2Si and discontinuous β-$Mg_{17}Al_{12}$ phase located at the same region. Fig. 4.18 shows the optical images after etching in T6 heat treated condition.

Table 4.5 EDS analysis results of the corresponding regions provided in Fig. 4.17

	Region A	Region B	Region C
Element	wt.%	wt.%	wt.%
Mg	61.44	3.37	62.07
Al	35.25	57.22	2.73
Ca	0.61	-	0.92
Zn	2.70	-	0.89
Si	-	-	26.54
Sn	-	-	6.85
Mn	-	38.97	-
Fe	-	0.29	-

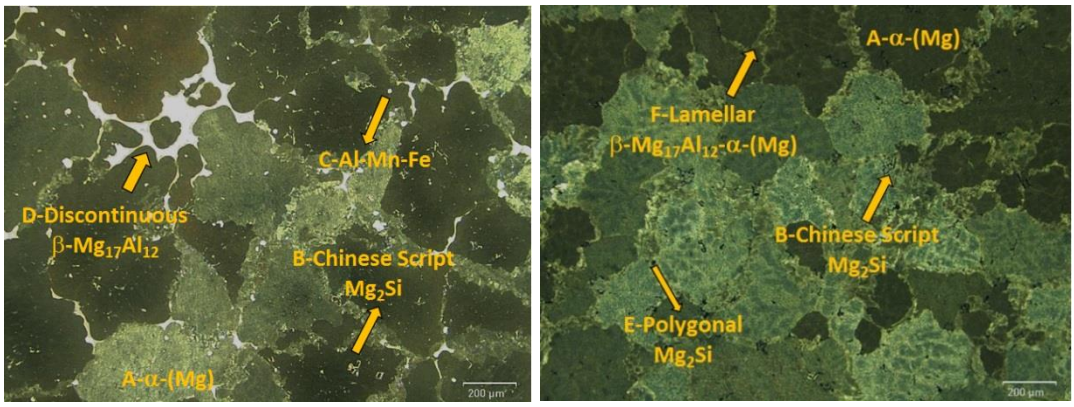

Fig. 4.18 Optical images of Alloy I alloy in T6 heat treated condition showing all phases (A-α-(Mg), B- Chinese script Mg_2Si, C-(Al-Mn-Fe) particle, D-discontinuous β-$Mg_{17}Al_{12}$, E-polygonal Mg_2Si, F-lamellar α-(Mg)-β-$Mg_{17}Al_{12}$) after etching

For Alloy II, optical images in as-cast condition show homogeneous distribution of polygonal Mg_2Si phase in the microstructure. (Fig. 4.19 (a)) The sizes of polygonal Mg_2Si phases change between 5 to 20 μm as seen in Fig. 4.19 (b)-(c). In addition, amount of modified polygonal or polygonal like shape Mg_2Si phase increased in comparison to Alloy I. Another observation deduced from these figures is that some of the Mg_2Si phases form on the discontinuous β-$Mg_{17}Al_{12}$ phase, which means these phases growing simultaneously during solidification. (Red circles indicated on Fig. 4.19 (b)-(c)) Small size Al-Mn-Fe particles were also found in the microstructure verified by EDS analysis. (Table 4.6)

In the recent studies, although modification effect of Ca, Sr and Sn elements on Mg_2Si phase has been studied separately, simultaneous addition of Sr and Sn elements has not been studied yet. This result indicates that simultaneous Sr and Sn dissolution also causes the morphological modification of detrimental Chinese script Mg_2Si. Region D indicated in Fig. 4.20 (b) has the similar composition with the Al-Mn-Fe particle observed in Alloy I. As already indicated, this particle has been thought as heterogeneous nucleation site in Mg-Al alloys.

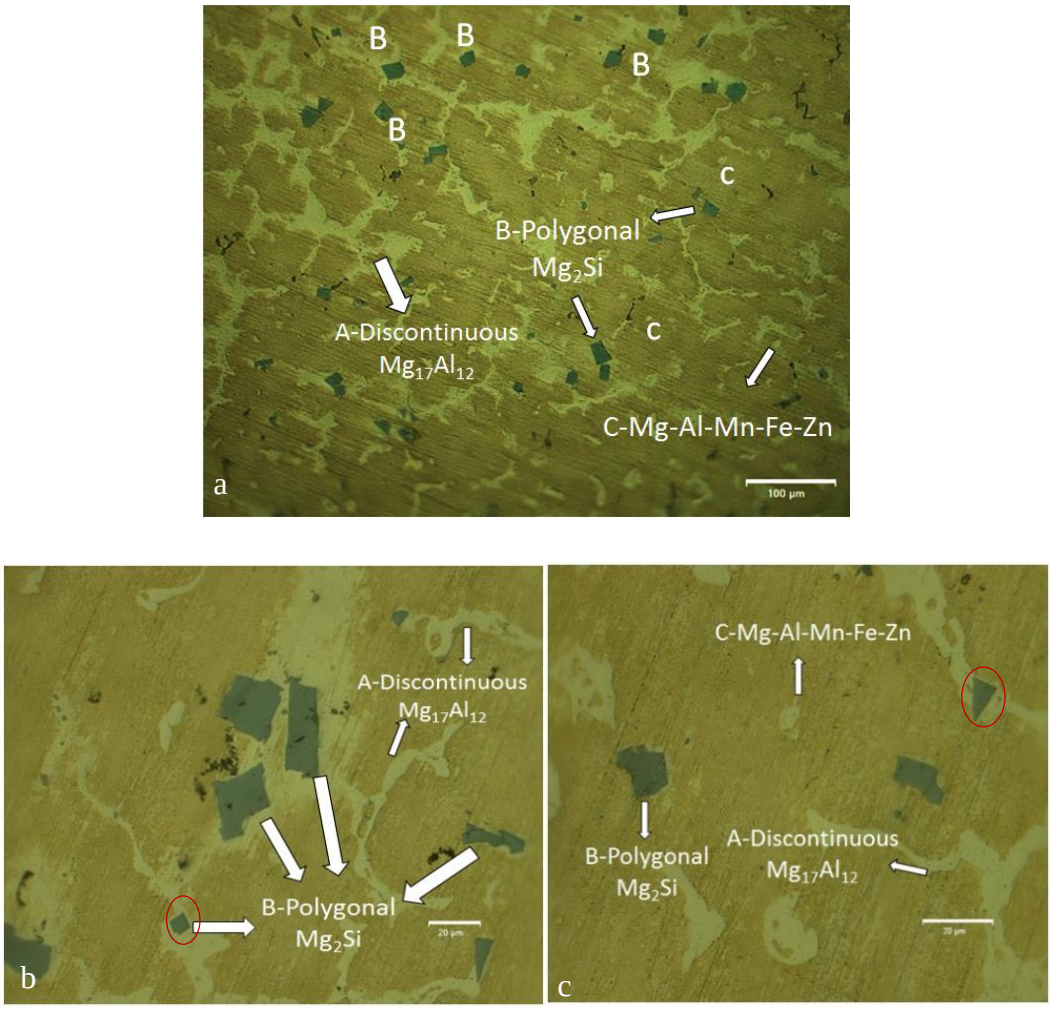

Fig. 4.19 Optical images of Alloy II in as-cast condition (a) general view of the optical microstructure (b) size variation of polygonal Mg_2Si (c) illustration of simultaneous formation of Mg_2Si and discontinuous β-$Mg_{17}Al_{12}$ phase (A-Discontinuous $Mg_{17}Al_{12}$, B-Polygonal Mg_2Si, C-Mg-Al-Mn-Fe-Zn particle,)

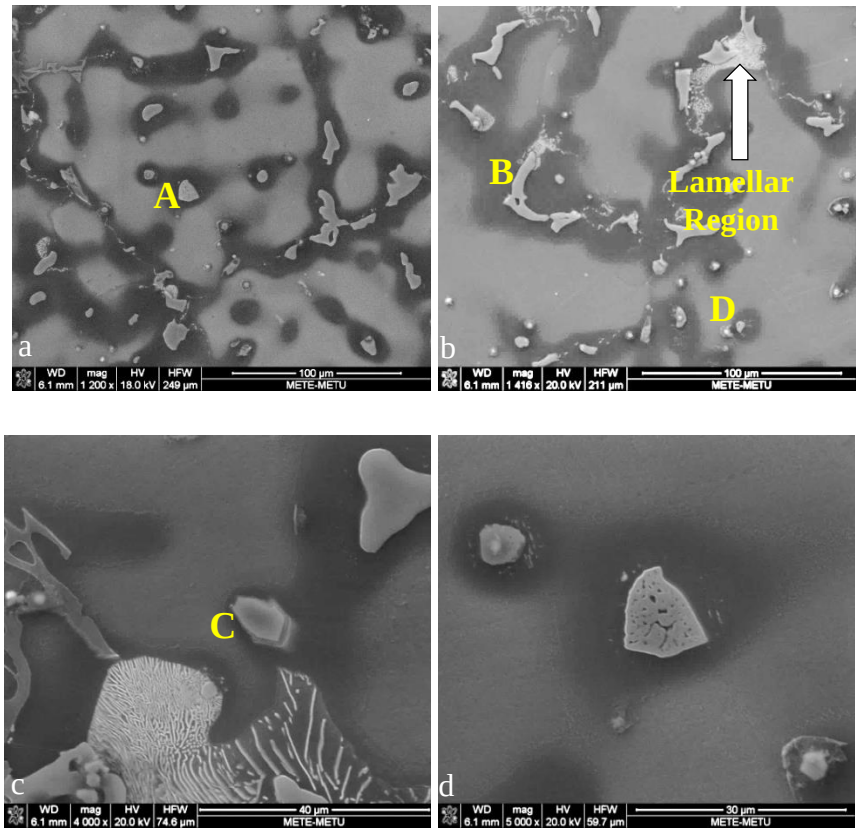

Fig. 4.20 SEM images of Alloy II in as-cast condition (a) general microstructural overview containing region 'A' (oval β-$Mg_{17}Al_{12}$) (b) general microstructure showing lamellar region and'B' region (discontinuous β-$Mg_{17}Al_{12}$) and region 'D' (Al-Mn-Fe particle) (c) polygonal Mg_2Si in region 'C' (d) oval β-$Mg_{17}Al_{12}$ (A) phase shown in (a) at higher magnification

Table 4.6 EDS analysis results of the regions shown in Fig. 4.20

	Region A	Region B	Region C	Region D
Element	wt.%	wt.%	wt.%	wt.%
Mg	61.21	55.15	39.72	33.09
Al	34.28	39.18	1.97	45.76
Zn	4.28	4.63	-	-
Si	0.28	1.04	24.67	-
Sn	-	-	1.19	-
Sr	-	-	32.45	-
Mn	-	-	-	20.75
Fe	-	-	-	0.4

The optical images of T6 heat treated Alloy II is presented in Fig. 4.21 (a)-(c). Fig. 4.23 (a) shows all phases present in the microstructure, which are α-(Mg) (matrix), Chinese script and polygonal Mg_2Si, Mg-Al-Mn-Fe-Zn (Al-Mn-Fe) particle, and discontinuous β-$Mg_{17}Al_{12}$. As seen in Fig. 4.21 (b) and (c), thinner and small Chinese script morphology in the microstructure is not fully same with the Mg_2Si provided in the recent studies. Polygonal and Chinese script Mg_2Si are also detected together as shown in Fig. 4.21 (c). Finer size and more homogeneous distribution of polygonal Mg_2Si were observed in Alloy II in comparison to Alloy I.

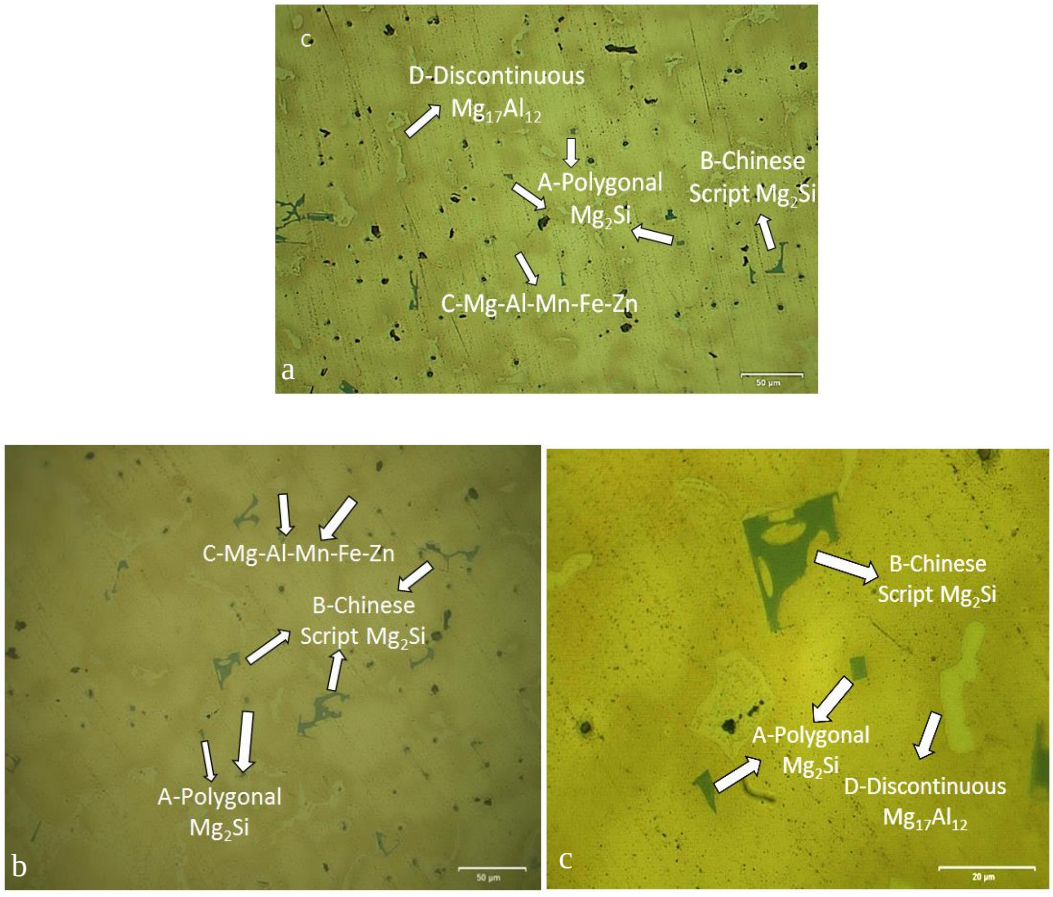

Fig. 4.21 Optical images of Alloy II in T6 heat treated condition at different magnifications (a-c, lower to higher, respectively) (A-Polygonal Mg_2Si, B-Chinese script Mg_2Si, C-Mg-Al-Mn-Fe-Zn particle, D-Discontinuous $Mg_{17}Al_{12}$)

In SEM images of T6 treated Alloy II, three different Mg_2Si morphologies were determined: detached Mg_2Si particles from Chinese script morphology Fig. 4.22 (a), Chinese script Mg_2Si with polygonal region in Fig. 4.22 (b) and Mg_2Si in polygonal shape in Fig. 4.22 (c). In addition, discontinuous β-$Mg_{17}Al_{12}$ phase containing Si, Sr and Sn elements (Fig. 4.22 (d)) was detected on the grain boundary. As also observed in Alloy I, Al-Mn-Fe particles with some dissolved Mg and Zn (Fig. 4.22 (e)) were found. The EDS analysis results of these phases shown by A, B, C, D and E in Fig. 4.22 are summarized in Table 4.7.

The detachment of particles from the Chinese script Mg_2Si phase could be attributed to diffusion of Si atoms on the way of α-Mg/Mg_2Si interface during solutioning and aging treatment. [11,41,43,49] The reason for this is predicated the effect of Al diffusion where both β-$Mg_{17}Al_{12}$ and Mg_2Si formed simultaneously at the grain boundaries. The morphology observed in Fig. 4.22 (b) could be separated into pieces as detached and polygonal Mg_2Si with longer period solutioning treatment according to the current studies. [57] The formation of fine round Mg_2Si formation at the grain boundaries could increase both room and elevated temperature mechanical properties [7,11,14,15,34]. In addition, it should be noted that dissolved Sr and Sn element in Chinese script morphology Mg_2Si is lower than the polygonal Mg_2Si. (Table 4.7) The reason for not being full modification to polygonal shape could be attributed to dissolved amount of these elements in the Chinese script Mg_2Si phase. The lamellar region (α-Mg-β-$Mg_{17}Al_{12}$) formed near discontinuous β-$Mg_{17}Al_{12}$ phase decreased and changed to continuous precipitate (Fig. 4.22 (d)). It was reported that discontinuous precipitation in AZ91 alloy may be responsible for the lower creep resistance due to its higher surface area for grain boundary sliding [5].

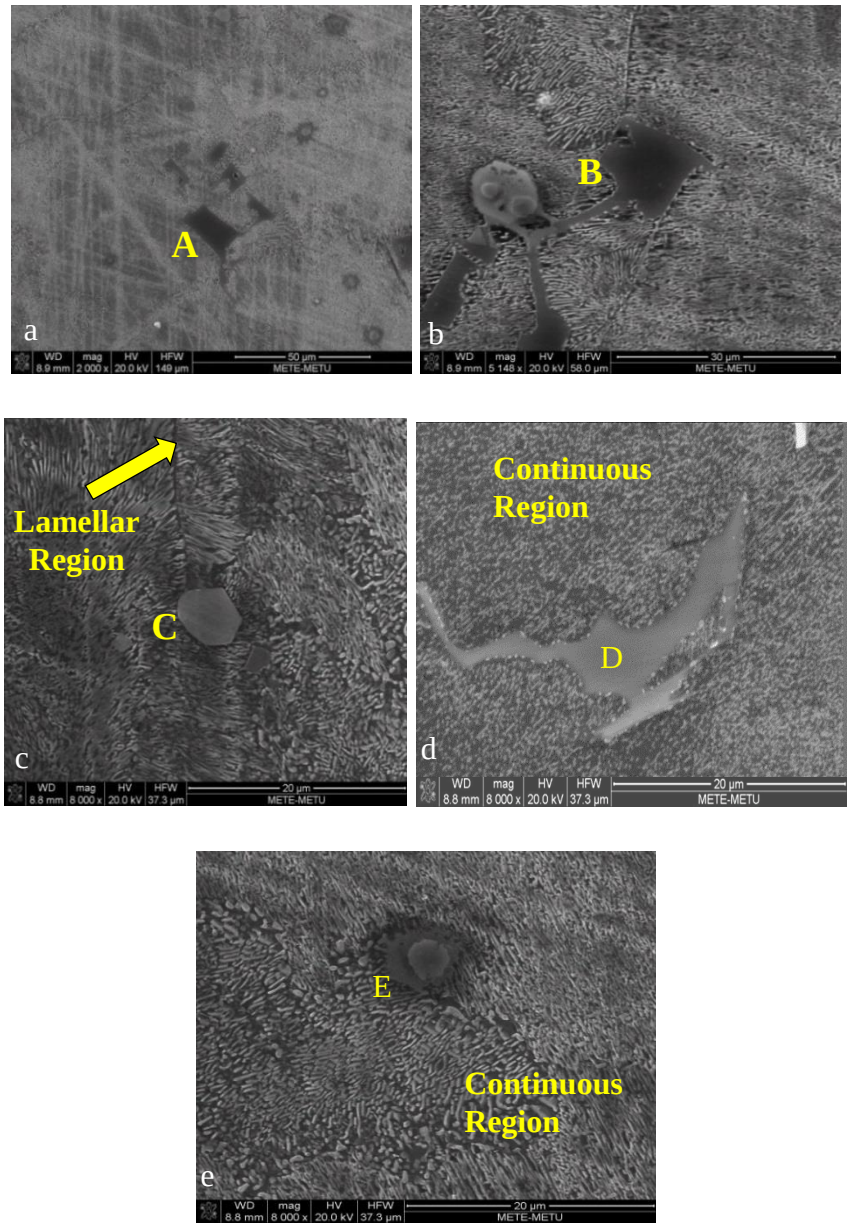

Fig. 4.22 SEM images of Alloy II in T6 heat treated condition (a) detached Chinese script Mg_2Si (A) phase after heat treatment (b) Chinese script Mg_2Si (B) phase containing polygonal region (c) Polygonal Mg_2Si (C) phase (d) discontinuous β-$Mg_{17}Al_{12}$ (D) located at grain boundary (e) Al-Mn-Fe (E) particle at grain boundary

Table 4.7 EDS analysis results of the regions shown in Fig. 4.22

	Region A	Region B	Region C	Region D	Region E
Element	wt.%	wt.%	wt.%	wt.%	wt.%
Mg	38.43	39.65	42.47	52.45	20,39
Al	1.26	1.12	2.07	41.10	50.26
Zn	-			2.50	
Si	26.43	52.26	40.62	2.94	
Sn	4.56	0.76	1.26	0.34	
Sr	29.62	6.21	13.58	0.67	
Mn					29.60
Fe					0.35

The optical images of T6 treated Alloy II after etching indicates all constituent phases in the microstructure. (Fig. 4.23) The alloy consists of α-Mg matrix, Chinese script and polygonal Mg_2Si located both at grain boundaries and inside of grain, Al-Mn-Fe particles and both discontinuous and lamellar β-$Mg_{17}Al_{12}$ containing region. The amount of β-$Mg_{17}Al_{12}$ phase is lower than that of Alloy I. In addition, massive distribution of this phase was not detected in the microstructure. This would certainly result in creep resistance increase over Alloy I.

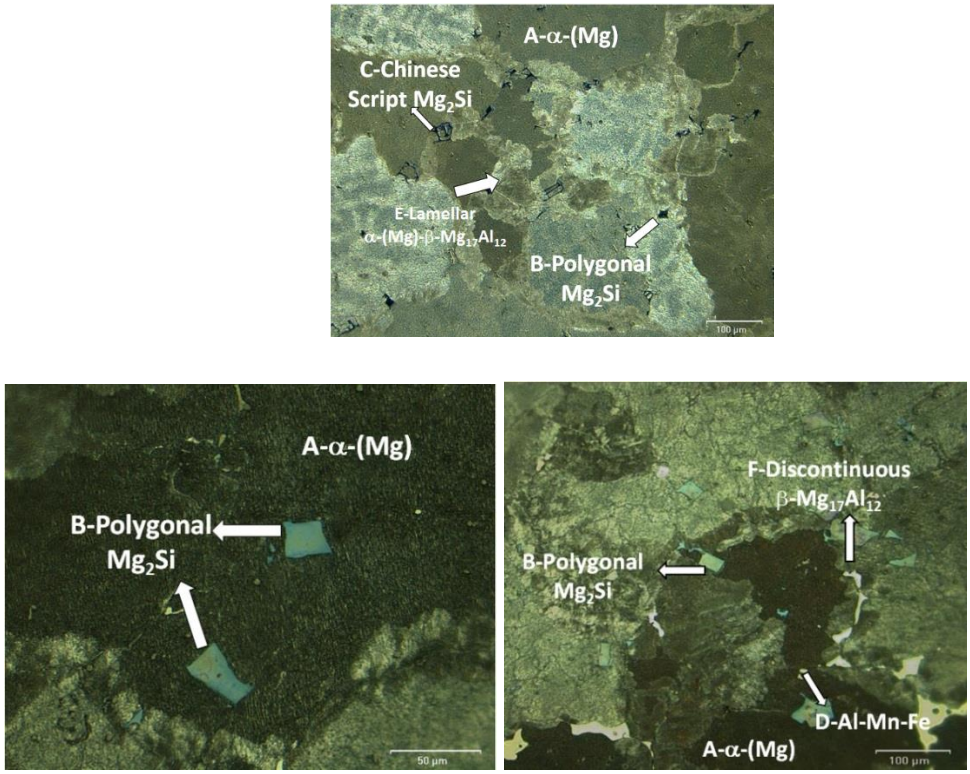

Fig. 4.23 Optical images of Alloy II alloy in T6 heat treated condition showing all phases (A-α-(Mg), B-Polygonal Mg_2Si, C-Chinese script Mg_2Si, D-(Al-Mn-Fe) E-Lamellar particle α-(Mg)-β-$Mg_{17}Al_{12}$ and F-Discontinuous β-$Mg_{17}Al_{12}$)

The microstructural images of Alloy III (Alloy II+0.1%Al-5Ti-1B) obtained from optical microstructure in as-cast state are demonstrated in Fig. 4.24. There is no difference in terms of phases observed in microstructure in comparison to those of Alloy II. The main difference is observed in the size and distribution of Mg_2Si and discontinuous β-$Mg_{17}Al_{12}$ phases. Finer polygonal and thinner Chinese script Mg_2Si phases were observed in the as-cast microstructure. As in the other alloy series, Al-Mn-Fe particles were observed in the central locations of the grains. The SEM image showing all these phases together are presented in Fig. 4.25. Since similar elemental compositions were observed with Alloy II (Table 4.6), the results of these phases were not attached. Lamellar structure of α-(Mg)-β-$Mg_{17}Al_{12}$ was observed around discontinuous β-$Mg_{17}Al_{12}$ phase while optical image did not demonstrate this

structure. With the addition of Al-5Ti-1B grain refiner, distribution of Al-Fe-Mn particles was also more homogenous and uniform if it is compared with the Fig. 4.20 (a) and (b).

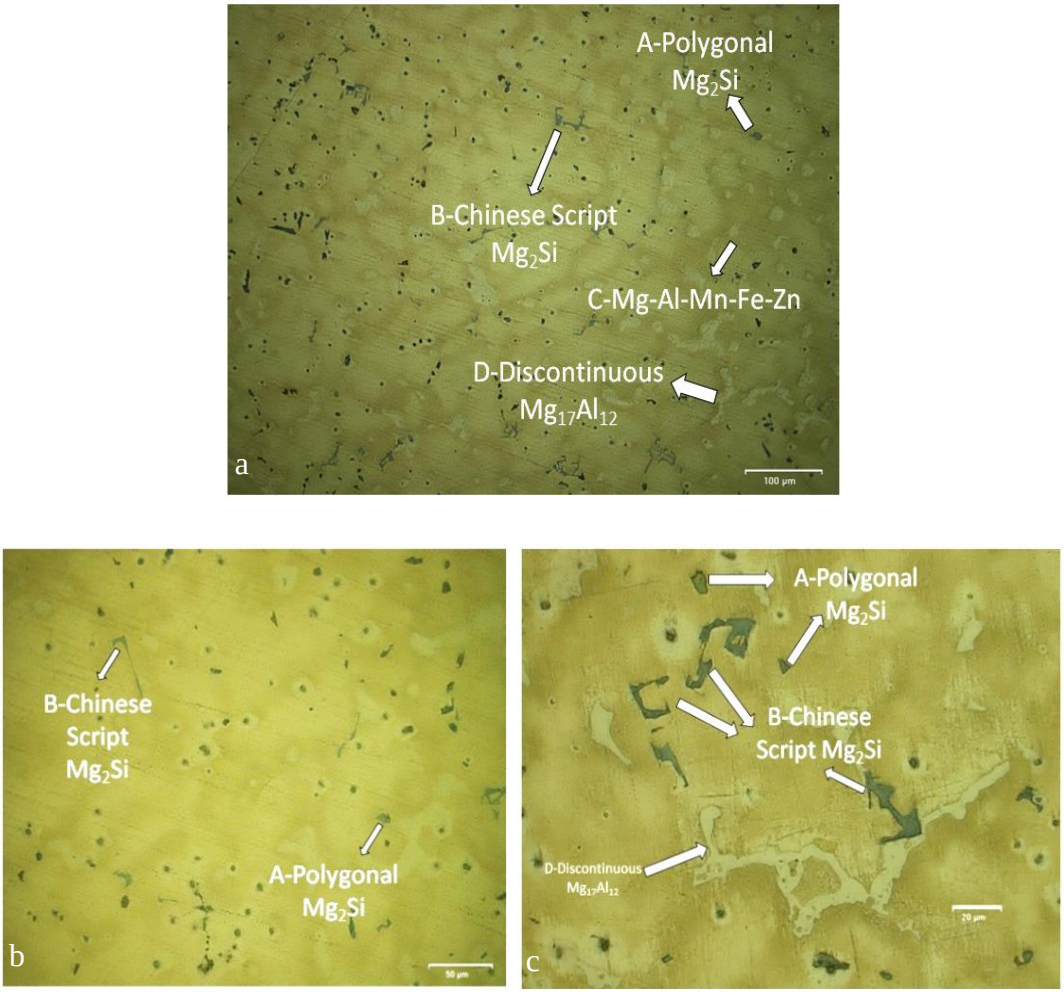

Fig. 4.24 Optical images of Alloy III in as-cast conditions (A-Polygonal Mg_2Si, B-Chinese script Mg_2Si, C-Al-Mn-Fe particle, D-Discontinuous $Mg_{17}Al_{12}$)

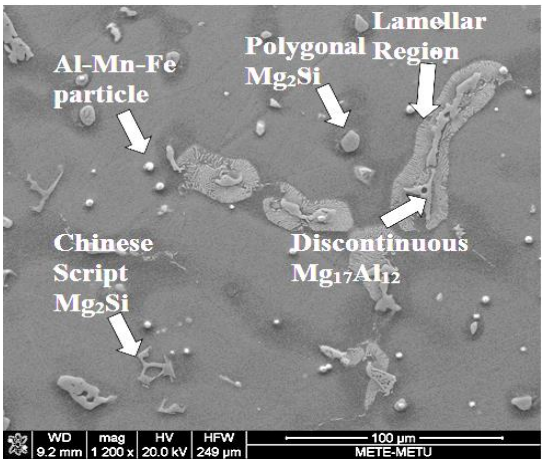

Fig. 4.25 SEM image showing all phases in as-cast sate of Alloy III

The optical images of T6 treated Alloy III before and after etching are shown in Fig. 4.26 and Fig. 4.28, respectively. In addition to polygonal and Chinese script Mg_2Si, acicular Mg_2Si was detected in Alloy III as shown in Fig. 4.26 (b). The thinner and detached Chinese script Mg_2Si phases were identified in this figure. The detachment of Chinese script branches could be attributed to solutioning and aging treatment in T6 condition. Fig. 4.26 (c) indicates the size of polygonal Mg_2Si phase in Alloy III decreased up to 5 μm together with its homogenous distribution given in Fig. 4.26 (a).

SEM images and EDS analysis results of the phases for Alloy III are shown in Fig. 4.27 and Table 4.8, respectively. Mg_2Si phase was observed in different morphologies: Chinese script, polygonal and acicular shape. The alloying elements dissolution amounts provided in Table 4.8 could be the possible reason for morphological difference in this phase. Main elements responsible for this change are Sr and Sn. In addition, lamellar α-(Mg)-β-$Mg_{17}Al_{12}$ was detected especially in grain boundaries while its amount is lower than those formed near discontinuous β-$Mg_{17}Al_{12}$ phase for other alloy series. Homogeneous distribution of Al-Mn-Fe particles in Fig. 4.27 (a) was also recorded for Alloy III.

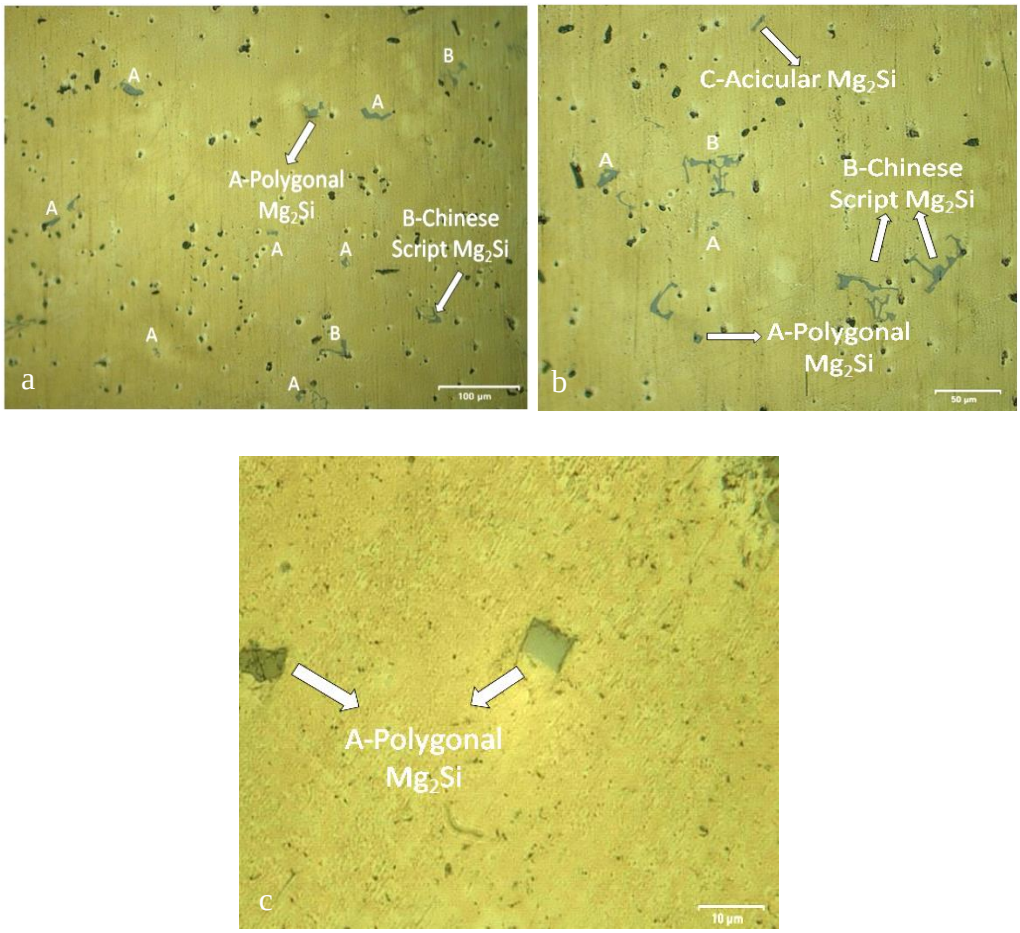

Fig. 4.26 Optical images of Alloy III in T6 heat treated condition (a) general optical microstructural overview (b) acicular Mg_2Si phase together with polygonal and Chinese script Mg_2Si phase (c) fine polygonal Mg_2Si phases at inside of grain (A-Polygonal Mg_2Si, B-Chinese script Mg_2Si, C-Acicular Mg_2Si)

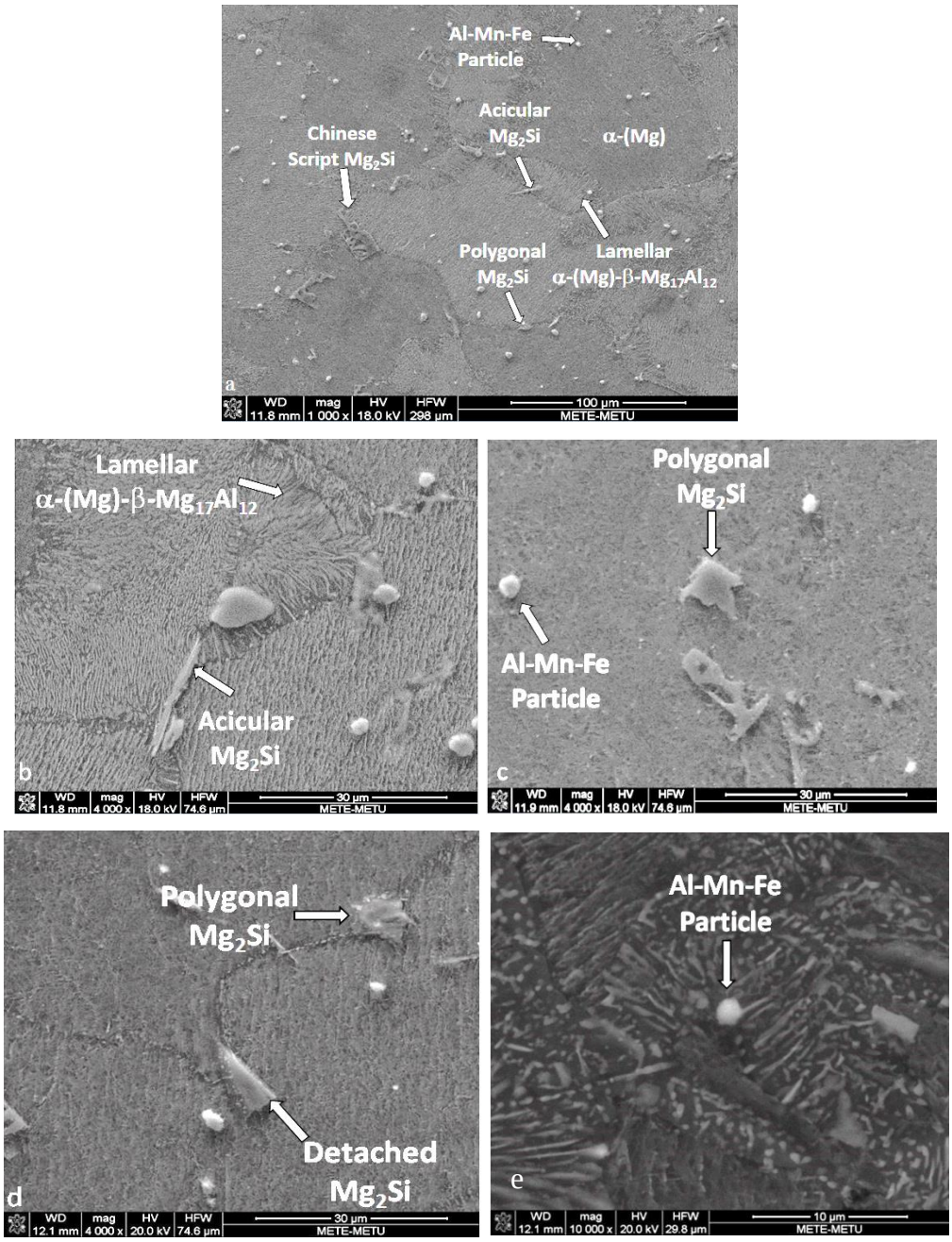

Fig. 4.27 SEM images of Alloy III in T6 heat treated condition from different fields (a) general SEM overview containing different phases (b) acicular Mg_2Si and lamellar α-(Mg)-β-$Mg_{17}Al_{12}$ (c) polygonal Mg_2Si and Al-Mn-Fe particle (d) polygonal Mg_2Si and detached (e) Al-Mn-Fe particle

Table 4.8 EDS analysis results of the phases shown in Fig. 4.27

	Chinese Script Mg_2Si	Polygonal Mg_2Si	Acicular Mg_2Si	α-Mg	Al-Mn-Fe
Element	wt.%	wt.%	wt.%	wt.%	
Mg	68.13	57.52	36.47	89.70	5.26
Al	-	0.76	10.07	8.92	59.94
Zn	0.42	-		1.08	-
Si	26.82	24.72	30.62	-	-
Sn	0.34	3.72	4.26	0.18	-
Sr	0.67	13.28	18.58	0.12	-
Mn	-	-	-	-	34.38
Fe	-	-	-	-	0.42

The optical images of Alloy III after etching (Fig. 4.28) reveal the polygonal and thin Mg_2Si phase at the grain boundaries. In addition to this, Al-Mn-Fe containing particles were also detected at near the groundaries. The formation of Mg_2Si phase would increase the creep resistance of the alloy by pinning the grain boundary movement and preventing diffusion in the matrix.

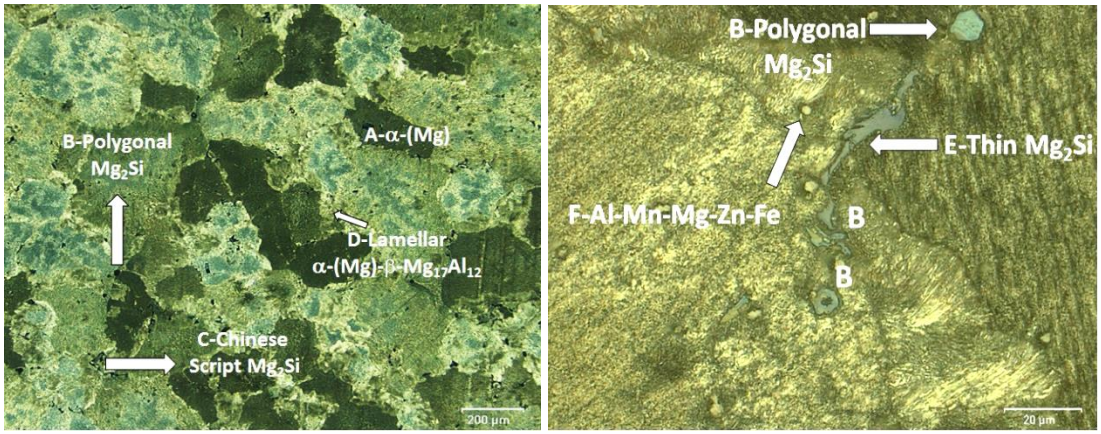

Fig. 4.28 Optical images of Alloy III alloy in T6 heat treated condition showing all phases (a) general microstructural overview (b) grain boundary region at higher magnification (A-α-(Mg), B-Polygonal Mg_2Si, C-Chinese script Mg_2Si, D-Lamellar α-(Mg)-β-$Mg_{17}Al_{12}$, E-Thin Mg_2Si, F-(Al-Mn-Mg-Zn-Fe)) particle after etching

For the benchmark purposes, AZ91 (Alloy IV) alloy was also examined through optical microscope and SEM. Optical images for AZ91 in as-cast state (without any heat treatment) are given in Fig. 4.29. As expected, massive discontinuous network of β-$Mg_{17}Al_{12}$ was observed at the grain boundaries. In addition to this, Al_8Mn_5 phase was also detected in accordance with the EDS analysis taken form the regions provided in Fig. 4.30. The EDS analysis results are provided in Table 4.9. Some amounts of dissolved Mg and Zn elements were also detected in Al_8Mn_5 phase. Phase transformation for Al_8Mn_5 phase under Scheil condition were suggested by Khan [127] according to the following reactions with their corresponding transformation temperatures:

$$L = \alpha\text{-(Mg)} + Al_8Mn_5 \text{ at } 593°C \quad (4)$$

$$L = \alpha\text{-(Mg)} + \beta\text{-}Mg_{17}Al_{12} + Al_8Mn_5 \text{ at } 431°C \quad (5)$$

Phase transformation temperature for this phase was found as 477.9 ºC as indicated in Fig. 4.4 and Table 4.2. Interestingly, small amount of Si element was also discovered in the EDS analysis of Al_8Mn_5, which possibly comes from the impurity element of the base metal. Al-Mn-Fe particles were also observed in AZ91 alloy as in other alloy series. However, as an interpretation according to all SEM images comparison, the amount and distribution is the lowest and more non-homogenous, respectively. The reason could be attributed to the considerable amount of β-$Mg_{17}Al_{12}$ formation, which may result in deficiency of Al element to form this particle during solidification. Moreover, as also indicated by Ohno et al. [81], the darker regions formed at the surroundings of discontinuous β-$Mg_{17}Al_{12}$ phase is saturated in terms of Mg verified by the EDS analysis result (Table 4.9) on this region (Fig. 4.30 (a)).

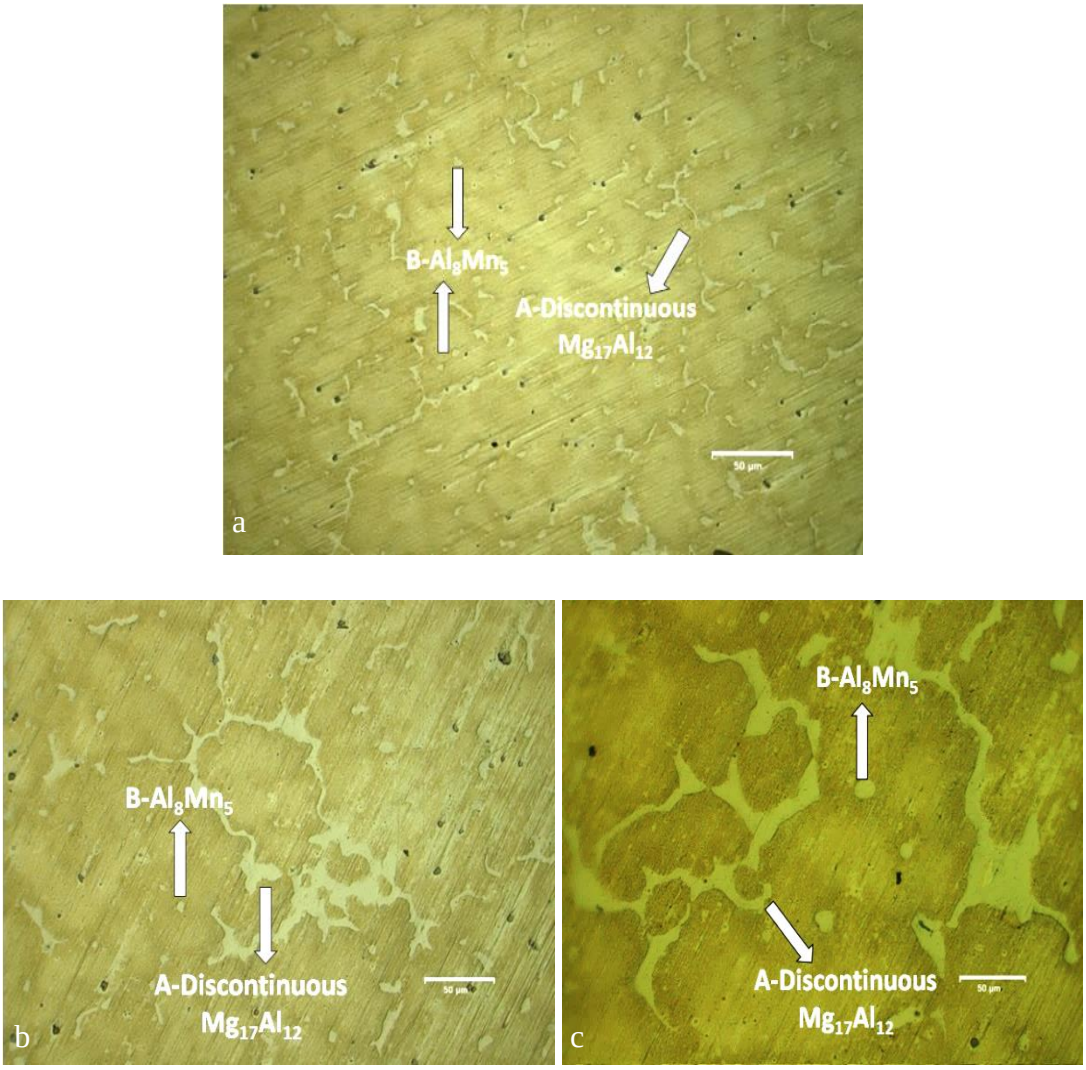

Fig. 4.29 Optical images of AZ91 (Alloy IV) in as-cast conditions at different magnifications **(**a) general optical microscope view (b) massive discontinuous β-$Mg_{17}Al_{12}$ phase network and Al_8Mn_5 phase (c) higher magnification view of (b) (A) β-$Mg_{17}Al_{12}$ phase amd B- Al_8Mn_5

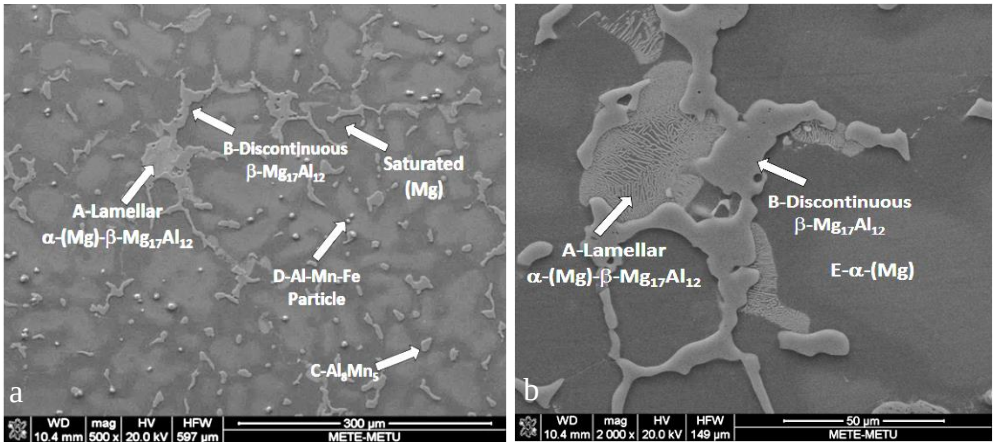

Fig. 4.30 SEM images of Alloy AZ91 (Alloy IV) in as-cast (a) general overview (b) at higher magnification on the field of discontinuous and lamellar region (A-Lamellar α-(Mg)-β-$Mg_{17}Al_{12}$ and B-Discontinuous β-$Mg_{17}Al_{12}$, C-Al_8Mn_5, D-(Al-Mn-Fe) particle, E- α-(Mg))

Table 4.9 EDS analysis of the areas shown in Fig. 4.31

Ele.	Lamellar $Mg_{17}Al_{12}$	Discontinuous β-$Mg_{17}Al_{12}$	Al_8Mn_5	Al-Mn-Fe	α-Mg	α-Mg (saturated)
	wt.%	wt.%	wt.%	wt.%	wt.%	wt.%
Mg	80.56	61.59	19.50	16.25	88.78	93.15
Al	18.07	33.03	49.94	45.72	12.22	6.85
Zn	1.37	5.37	0.58	0.72		
Si			0.40			
Mn			29.57	36.2		
Fe				1.11		

Optical images of AZ91 alloy after T6 heat treatment are provided in Fig. 4.31. In optical images, discontinuous β-$Mg_{17}Al_{12}$ phase is not clearly observed and only shrinkage and porosities seen as black on α-Mg matrix (Fig. 4.31 (a)) was noted on microstructure of T6 treated AZ91. However, at higher magnifications, lamellar α-Mg-β-$Mg_{17}Al_{12}$ structure was determined both on grain boundary and inside of grain region (Fig. 4.31 (b) and Fig. 4.31 (c), respectively).

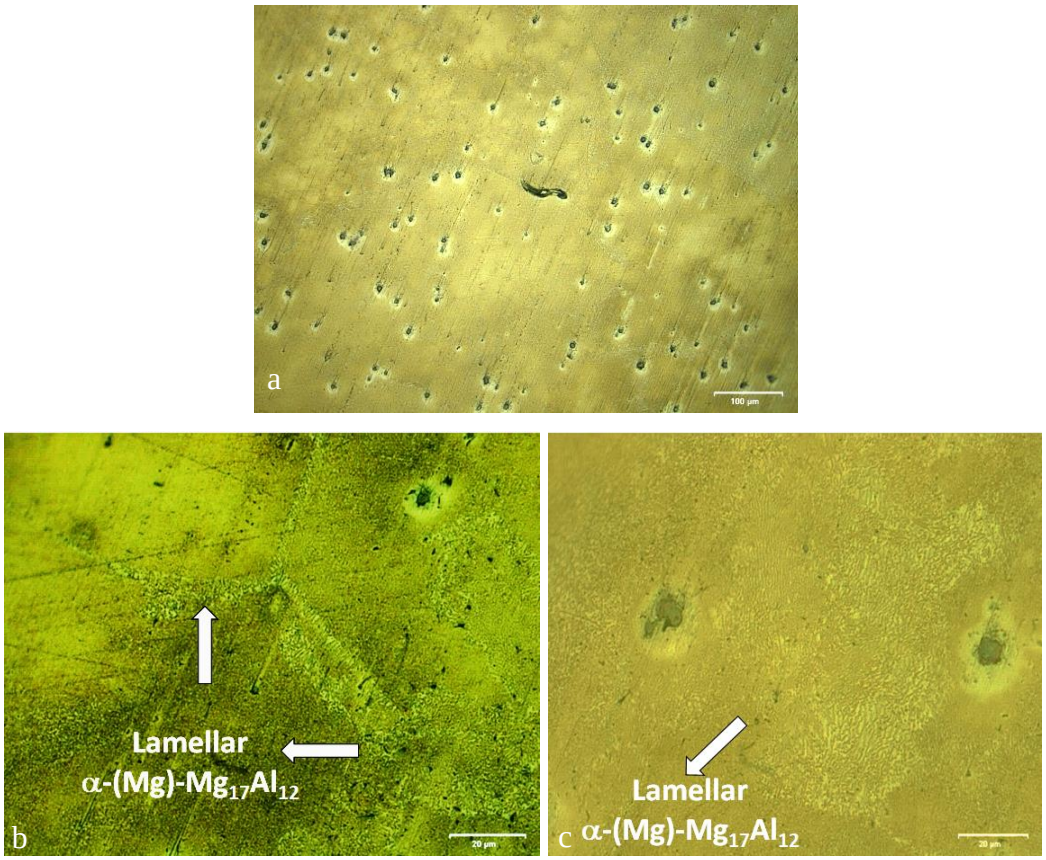

Fig. 4.31 Optical images of AZ91 (Alloy IV) in T6 heat treated conditions at different magnifications (a) general overview (b) lamellar α-Mg-β-$Mg_{17}Al_{12}$ on grain boundary region (c) lamellar α-Mg-β-$Mg_{17}Al_{12}$ at inside of α-Mg grain

Fig. 4.32 shows the SEM images of Alloy IV after heat treatment. As seen on this figure, huge lamellar α-Mg-β-$Mg_{17}Al_{12}$ region, massive β-$Mg_{17}Al_{12}$ phase and Al_8Mn_5 phase exist in the microstructure. In addition to this, Al-Mn-Fe containing particle was detected. Fig. 4.33 shows the optical image of AZ91 alloy (Alloy IV) consisting of all phases detected in SEM analysis.

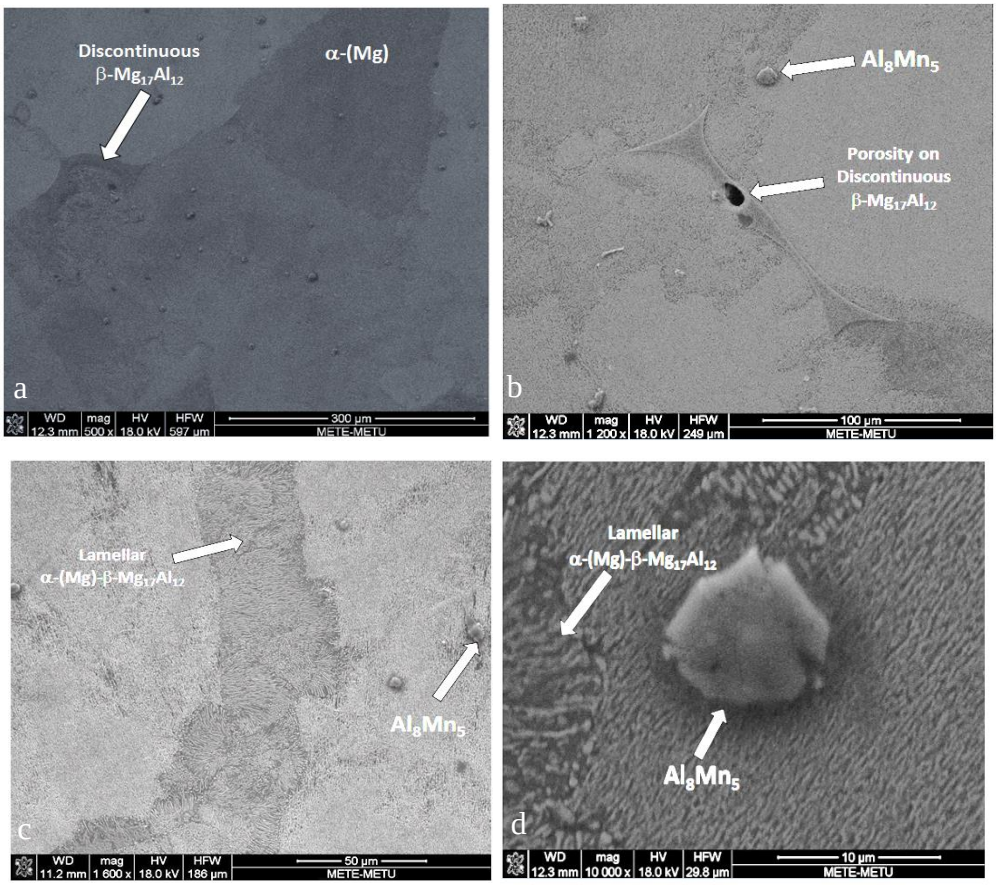

Fig. 4.32 SEM images AZ91 (Alloy IV) in T6 heat-treated condition (a) general overview of discontinuous β-$Mg_{17}Al_{12}$ phase region (b) higher magnification of discontinuous β-$Mg_{17}Al_{12}$ phase region with porosity on it (c) wide lamellar α-(Mg)-β-$Mg_{17}Al_{12}$ region on grain boundary (d) Al_8Mn_5 phase at inside of α-(Mg) grain

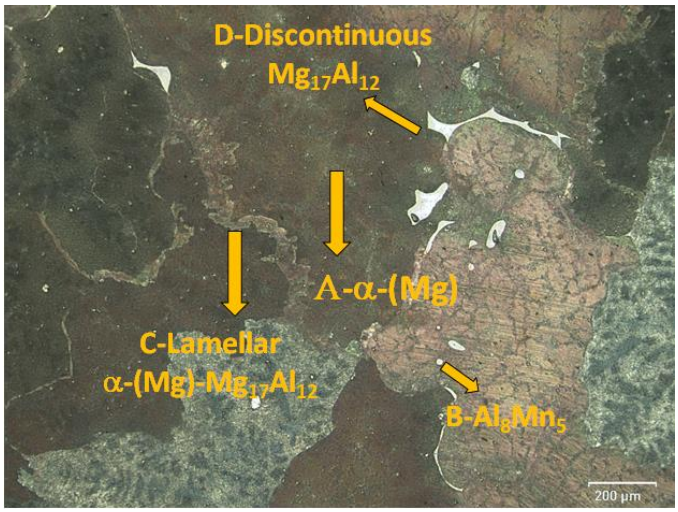

Fig. 4.33 Optical image of AZ91 (Alloy IV) alloy in T6 heat treated condition showing all phases (A-α-(Mg), B-Al_8Mn_5,C-Lamellar-(α-(Mg)-$Mg_{17}Al_{12}$), D-Discontinuous $Mg_{17}Al_{12}$) after etching

4.5.2 Elemental Mapping Analysis

In order to visualize dissolution of elements in the phases, elemental mapping analysis was performed for Alloy III in T6 heat treated condition. The main reason to perform this analysis is the observation of coincided peaks of some elements such as Si and Sr in the EDS analysis results. Due to this reason, elemental mapping by SEM and EDS around some phases were seemed as necessary. Since Alloy III showed the most desirable result in terms of desired microstructure, grain size and porosity, this alloy in T6 heat treated condition was chosen for this analysis.

Mapping analysis of polygonal Mg_2Si phase in Alloy III for Mg, Si and Sr is shown in Fig. 4.34. As seen in this figure, Sr agglomerated on Mg_2Si phase and deficiency of Mg phase in comparison to main α-Mg phase was also detected. From this result, it could be clearly stated that Sr casued the modification of Chinese script Mg_2Si phase to the modified polygonal shape.

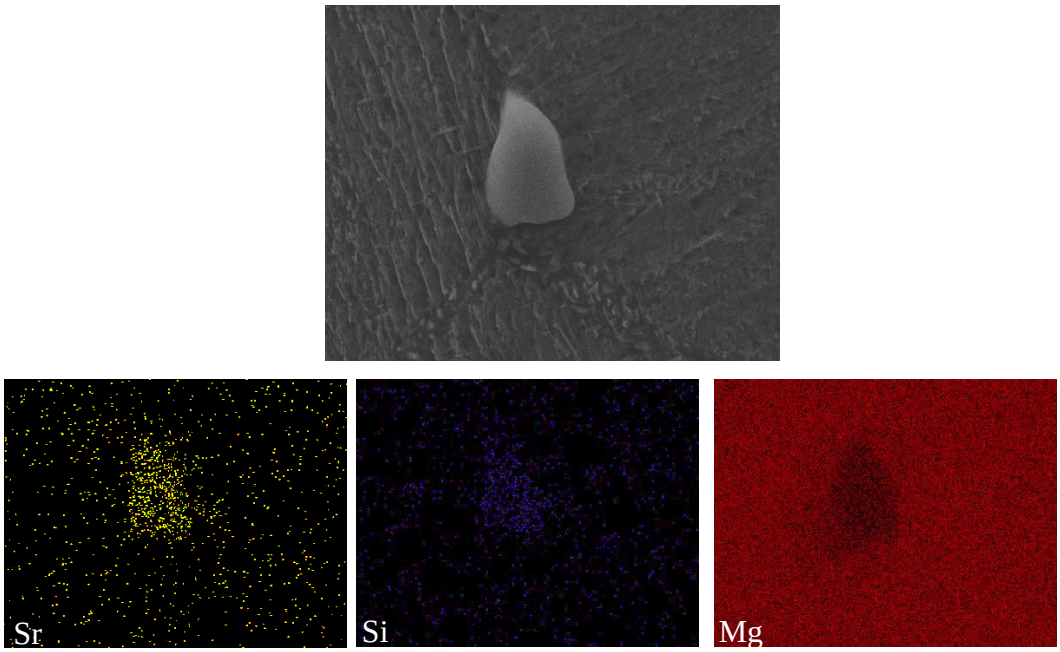

Fig. 4.34 Mapping analysis of polygonal Mg_2Si phase in T6 heat treated Alloy III for Mg, Si, and Sr

In another area for mapping analysis containing different phases in T6 treated Alloy III is presented in Fig. 4.35. This region contains polygonal and detached Mg_2Si phase, Al-Mn-Fe particle and α-Mg matrix. Mg and Si mapping analysis result validated Mg_2Si phase regions. Sr dissolution on polygonal Mg_2Si phases was verified with Sr mapping results. Sn element mapping indicated that Sn element mostly accumulated on near the Mg_2Si phases. Ti mapping did not give any conglomeration region to comment on the effect of 0.1% Al-5Ti-1B addition. The reason not to observe any this type of conglomeration region could be ascribed to very low addition amount of the grain refiner. In order to compare the elemental mapping analysis region containing Chinese script Mg_2Si phase, Fig. 4.36 is provided. As same with Fig. 4.35, Chinese script Mg_2Si phase contains Sr element even though the density of Sr around it is lower. Together with this, Mn and Al concentration on the mapping analysis also verified Al-Mn-Fe particle region.

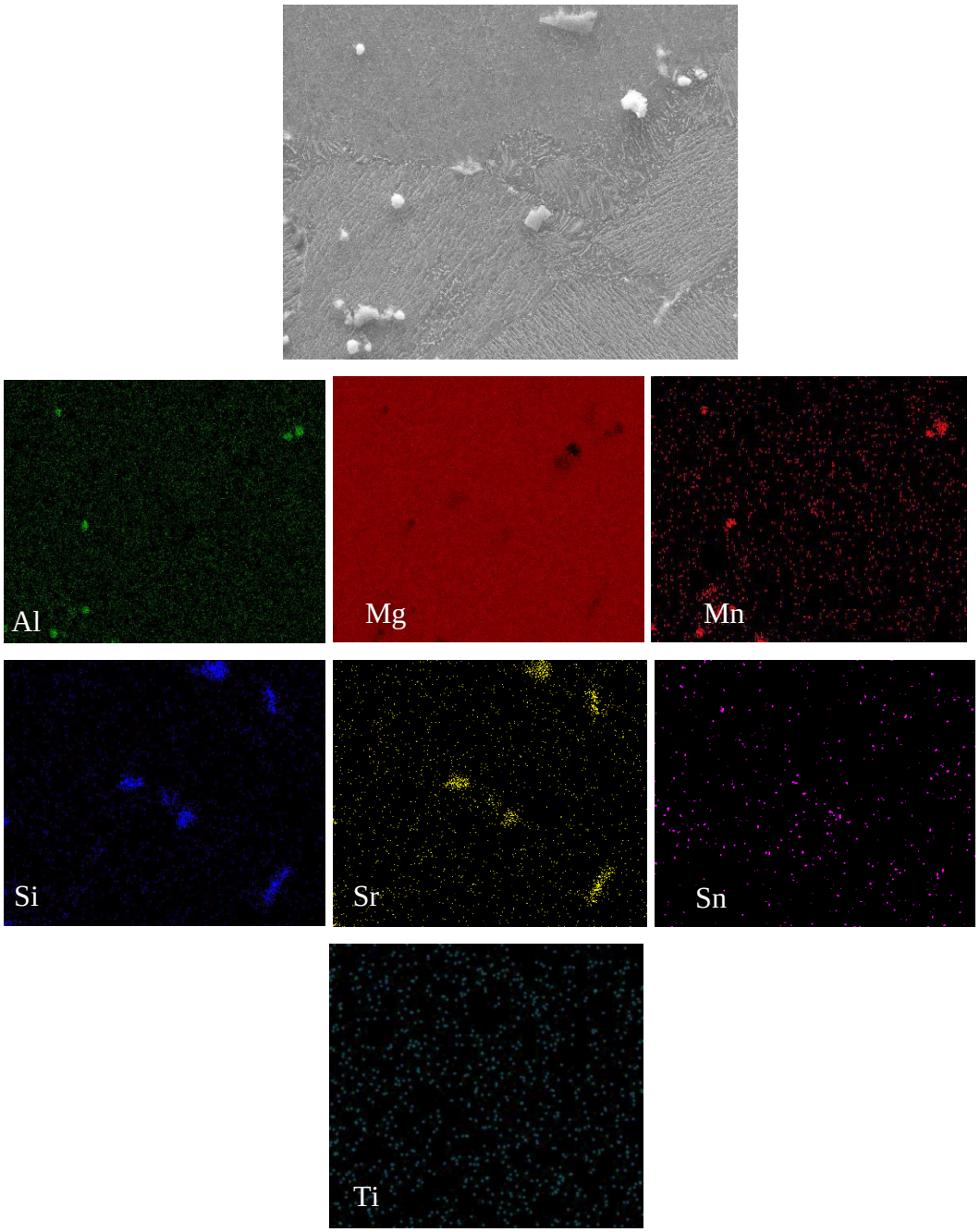

Fig. 4.35 Mapping analysis of T6 heat treated Alloy III for Al, Mg, Mn, Si, Sr, Sn, and Ti elements in the regions of modified Mg_2Si and Al-Mn-Fe particles

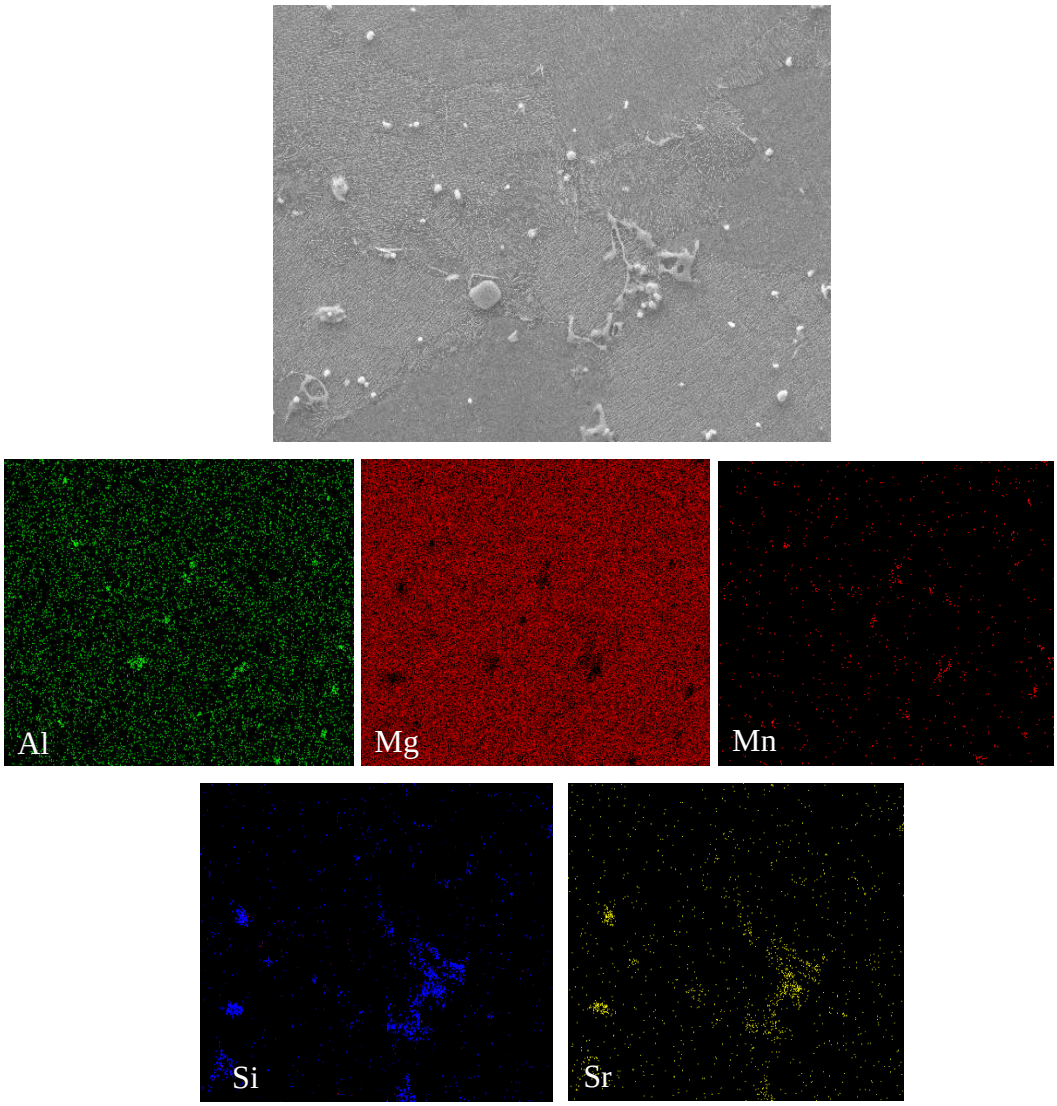

Fig. 4.36 Mapping analysis of T6 heat treated Alloy III for Al, Mg, Mn, Si, Sr, Sn, and Ti elements in the regions of Chinese script Mg_2Si and Al-Mn-Fe particles

4.5.3 Grain Size Measurement

The average grain size of alloy series in T6 heat treated condition with respect to their test surface condition are summarized in Table 4.10. These measurements were performed after tensile test just below the fracture surfaces. In addition, standard deviation of the measurements was indicated in this table. Grain size measurement

example for Alloy III in as-cast surface condition is given in Fig. 4.37. Measurements were performed with Dewinter Material Plus program with 4.1. Image Analysis software on SOIF XJP-6A optical microscope. The standard, ASTM E112, was used in the measurements via this software in the program.

Table 4.10 Average grain sizes of alloy series used in this study with their standard deviations in different specimen surface condition in T6 heat treated condition

Alloy	Tensile Test Specimen Surface Condition in T6 Heat Treatment	Average Grain Size (μm)	Standard Deviation (μm)
Alloy I	As-cast (10 mm)	222	93
	Machined (22 mm)	231	81
	Machined from gating (30 mm)	257	59
Alloy II	As-cast (10 mm)	181	49
	Machined (22 mm)	222	126
	Machined from gating (30 mm)	214	88
Alloy III	As-cast (10 mm)	139	39
	Machined (22 mm)	131	54
	Machined from gating (30 mm)	168	71
Alloy IV	As-cast (10 mm)	378	387
	Machined (22 mm)	676	446
	Machined from gating (30 mm)	1298	405

The lowest grain size was achieved by Alloy III with as-cast surface specimen condition as indicated in Table 4.10. In addition to this, the lowest standard deviation was observed in this type specimen. Highest degree of grain size was observed for Alloy IV (AZ91) in machined from gating specimen type, which approximately 6 times higher than that of Alloy III. Simultaneous addition of Si, Ca and Sn elements (Alloy I) to AZ91 alloy also brought a decrease in grain size together with more homogeneous distribution in each specimen condition. Grain size of AZ91 alloy was also reduced with combined addition of Si, Sr and Sn elements (Alloy II). Grain size of Alloy II is lower than that of Alloy I, which is expected to bring higher mechanical properties in Alloy II. Lowest grain size in each alloy series was

obtained in as-cast specimen surface type. (with T6 heat treatment and without any machining operation.)

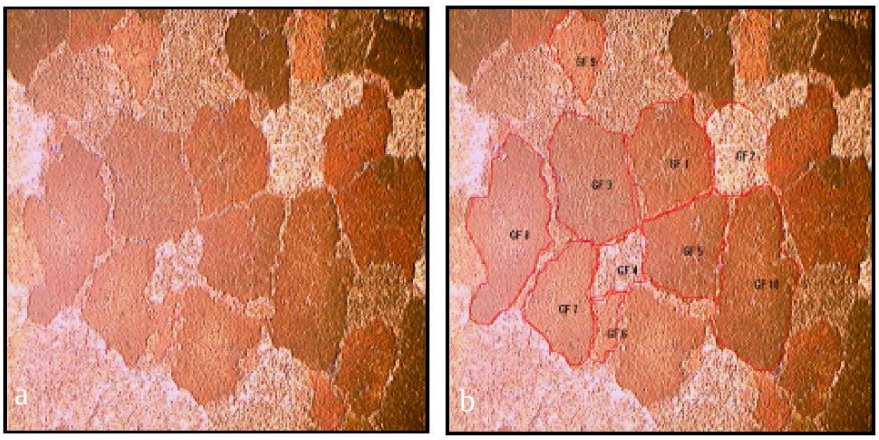

Fig. 4.37 Grain size measurement of Alloy III in as-cast surface region (a) measurement region and (b) measurement of grain sizes by red circles

In order to visualize the grain size of each alloy series in different surface condition, optical microstructural images are provided in Fig. 4.38 - Fig. 4.41. In these optical images, a circular cross section just below the tensile specimen surface was prepared and used to investigate the grain size variation from surface to center region. The lowest grain size variation was obtained in Alloy III (Fig. 4.40) while the highest grain size variation was observed in AZ91 alloy as shown in Fig. 4.41. This situation could also be analyzed by the standard deviation provided in Table 4.10. The specimen surface condition also reflects the different thicknesses whereas-cast, machined and machined from gating specimen are 10, 22, and 30 mm, respectively. Since each section had a different cooling rate due to thickness variations during solidification, the grain size variation in each alloy series was also expected. However, keeping the grain size variation same in different section thicknesses is very important to ensure structural integrity over one component. Aluminium containing magnesium alloys suffer from this and due to this reason, the usage of these alloys have limited in aerospace industry [23, 27]. In the studied alloy series,

obtaining minimum variation in different casting thicknesses, i.e. different specimen conditions, in one alloy series is very challenging due to this reason. The minimum variation in grain size was achived in Alloy III. (Fig. 4.40) In comparison to Alloy II, the only difference was 0.1%Al-5Ti-1B grain refiner addition for Alloy III. Effect of grain refiner on uniform grain size distribution was observed in the studied Alloy II as shown in Fig. 4.40 [24,59,70,71].

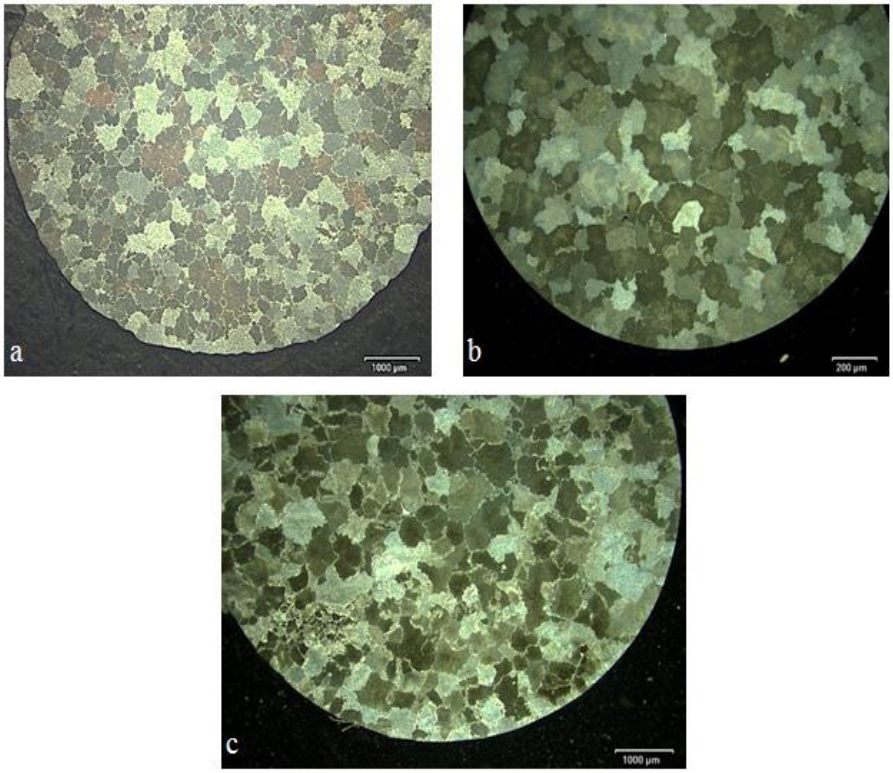

Fig. 4.38 Grain size distribution of Alloy I in T6 heat treatment from different specimen conditions after tensile test (a) as-cast surface specimen, (b) machined specimen and (c) machined from gating specimen

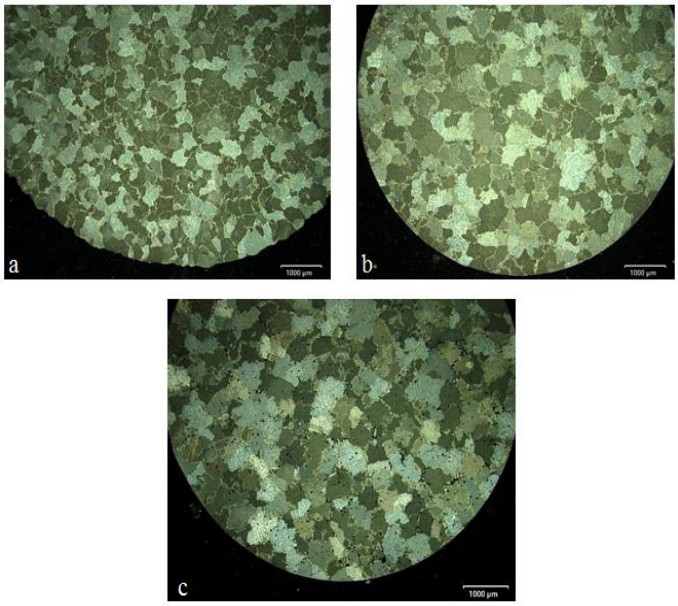

Fig. 4.39 Grain size distribution of Alloy II in T6 heat treatment from different specimen conditions after tensile test (a) as-cast surface specimen, (b) machined specimen and (c) machined from gating specimen

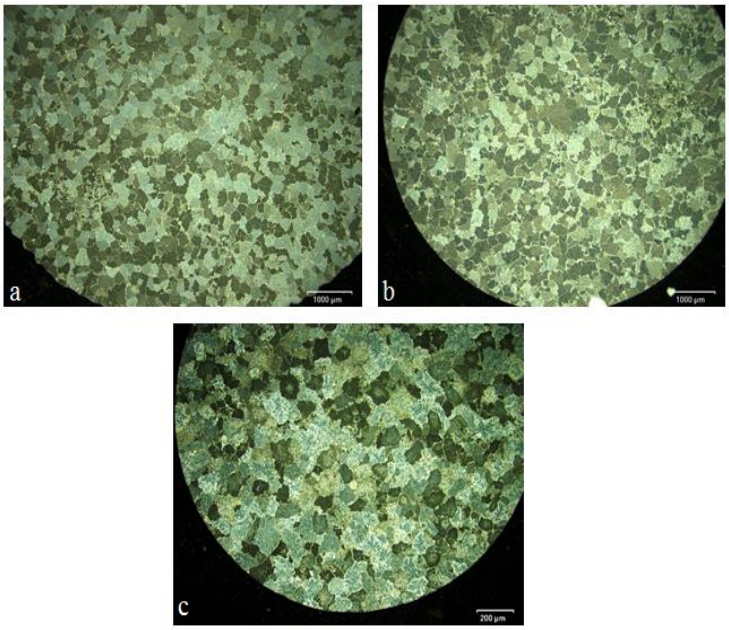

Fig. 4.40 Grain size distribution of Alloy III in T6 heat treatment from different specimen conditions after tensile test (a) as-cast surface specimen, (b) machined specimen and (c) machined from gating specimen

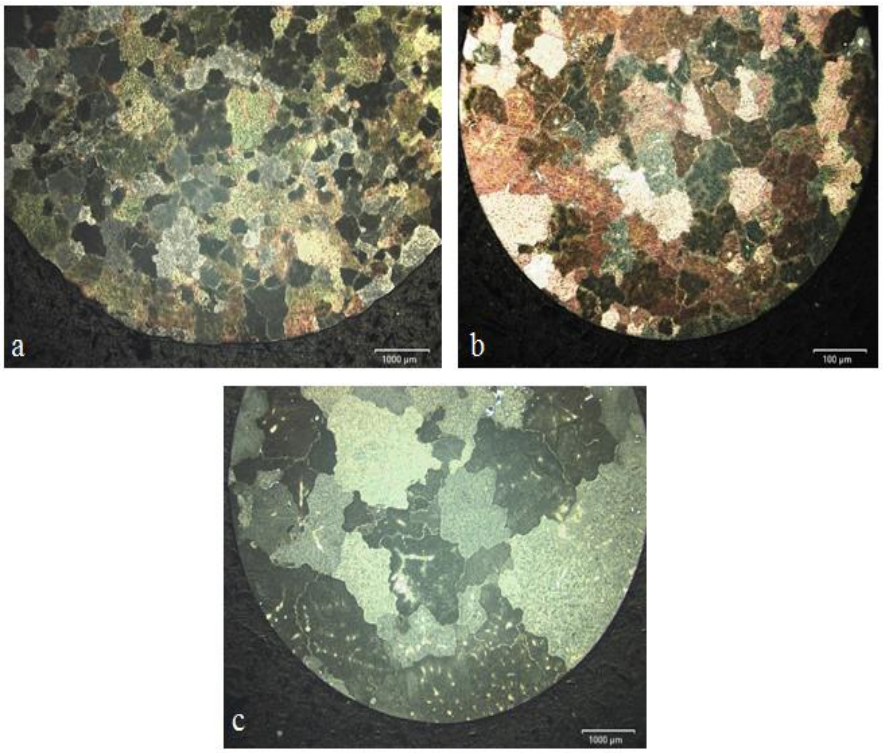

Fig. 4.41 Grain size distribution of Alloy IV (AZ91) in T6 heat treatment from different specimen conditions after tensile test (a) as-cast surface specimen, (b) machined specimen and (c) machined from gating specimen

Fig. 4.42 compares grain size distribution of as-cast surface specimen for the alloy series in T6 heat treated condition. From this figure, the lowest grain size of Alloy III could be easily distinguished in the studied alloys. In order to support this figure, comparison of numerical average grain size results is presented in Fig. 4.43. (The exact values of these results are provided in Table 4.10.) As shown on this figure, the lowest grain size and less variation these were obtained in Alloy III. On the contrary, grain size of Alloy IV (AZ91) was the highest together with excessive deviation within the measurement area. This situation results in the interruption of structural integrity, which finally affects the mechanical behavior of the component adversely.

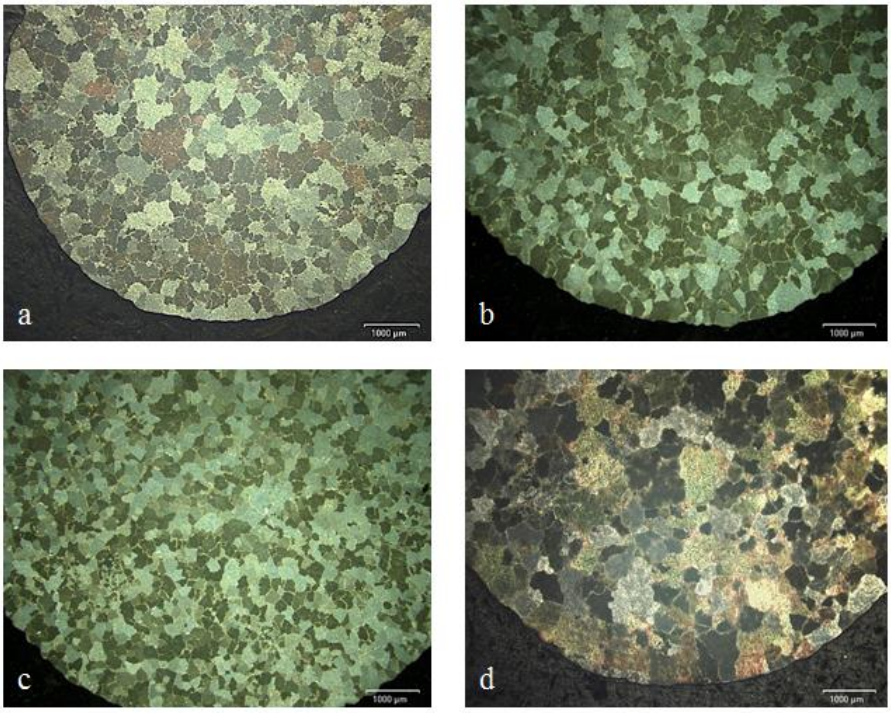

Fig. 4.42 Grain size of as-cast surface specimen (a) Alloy I, (b) Alloy II, (c) Alloy III and (d) Alloy IV in T6 heat treated condition

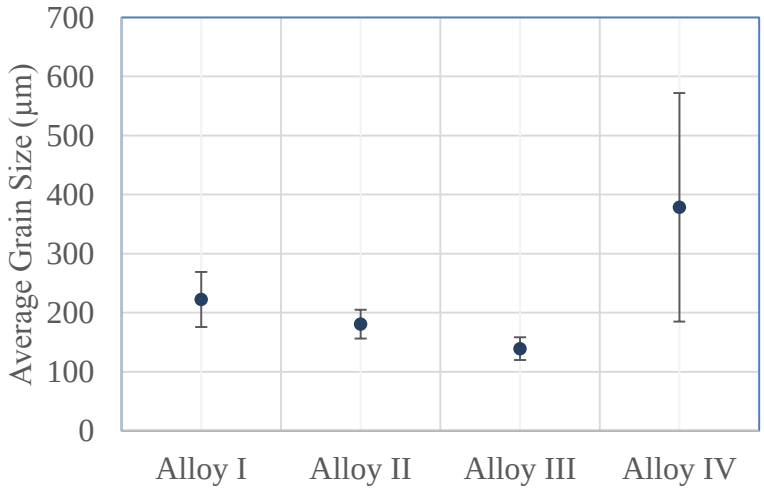

Fig. 4.43 Average grain size (µm) of as-cast surface alloy series

Fig. 4.44 and Fig. 4.45 show the optical microscope images and measurement results of machined specimen (22 mm casting thickness) grain sizes, respectively. The grain

sizes are higher in comparison to as-cast surface specimens (10 mm casting thickness). However, the average grain size changes in a similar way with as-cast surface specimens. Alloy III had the finest grain size while grain sizes increases in the order of Alloy II, Alloy I and Alloy IV.

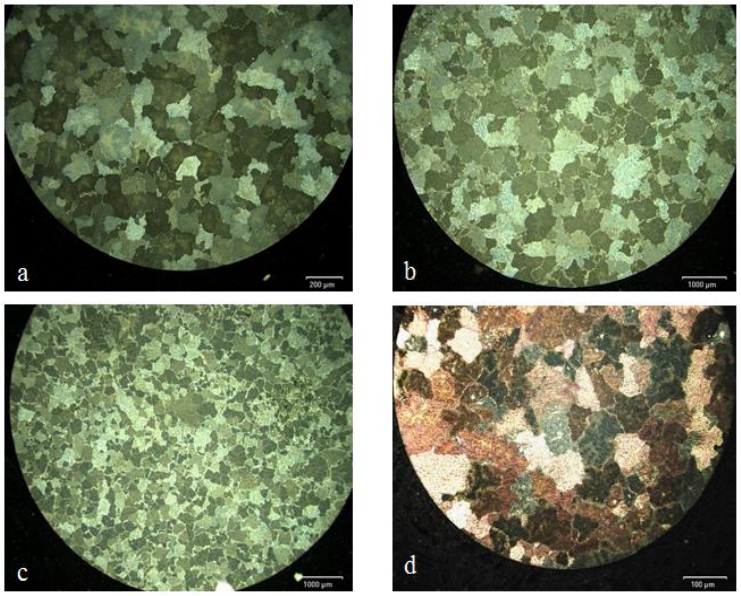

Fig. 4.44 Grain size of machined specimen (a) Alloy I, (b) Alloy II, (c) Alloy III, and (d) Alloy IV in T6 heat treated condition

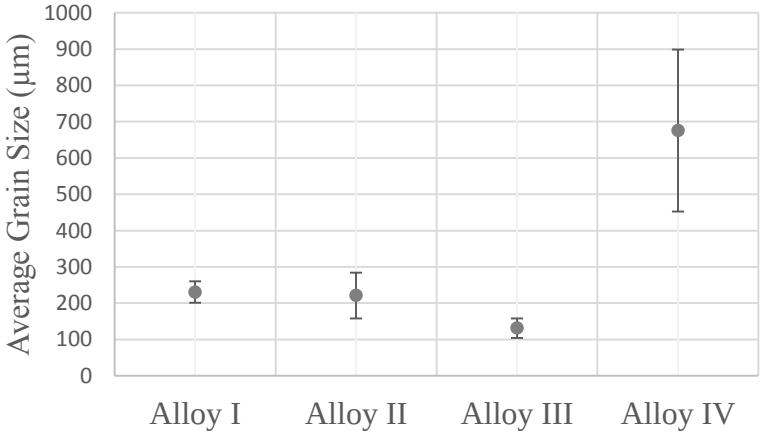

Fig. 4.45 Grain size (µm) of machined alloy series

Fig. 4.46 visualizes the grain size comparison of machined from gating specimen while Fig. 4.47 shows graphically the average grain sizes of them. As it is expected, the highest grain sizes were measured in the specimens taken from gating due to their highest casting thicknesses (30 mm) with respect to both as-cast surface specimen (10 mm) and machined specimens (22 mm). It is worth to note that the variation of grain size in Alloy IV is remarkable while that of Alloy III is negligible. This situation could be ascribed to the alloying elements and Al-5Ti-1B grain refiner addition. This would bring more homogeneous distribution in grain size even in thicker region.

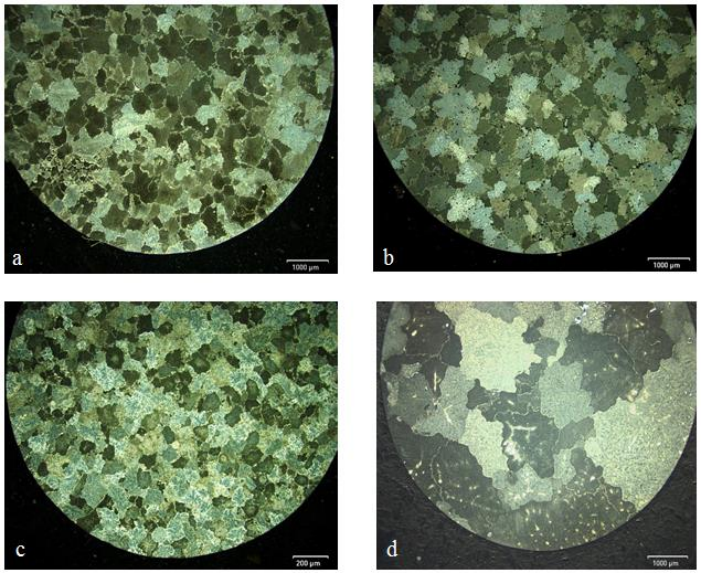

Fig. 4.46 Grain size of machined from gating specimen (a) Alloy I, (b) Alloy II, (c) Alloy III and (d) Alloy IV in T6 heat treated condition

Fig. 4.48 summarizes the average grain size measurement results of the alloys in all tensile specimen conditions after T6 heat treatment. At first glance to this figure, the grain size variation decrease of Alloy I-Alloy III could be remarkable. The second point to be emphasized is that Alloy III has the lowest variation and similar behavior in grain size in all tensile specimen conditions.

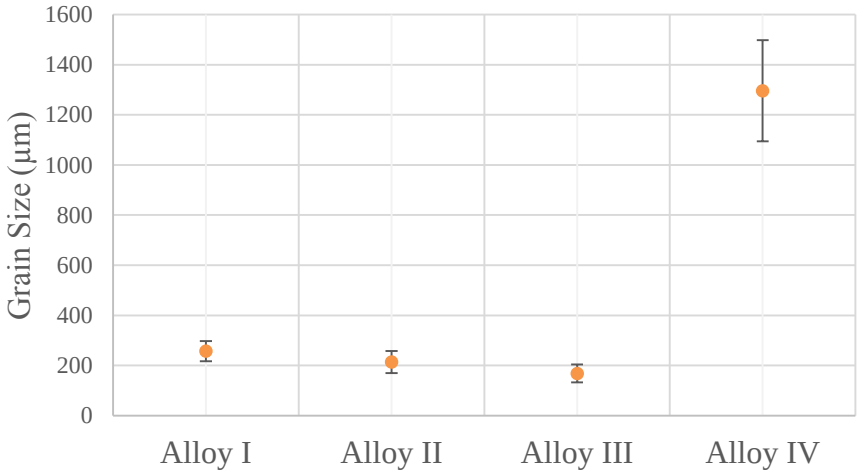

Fig. 4.47 Grain size (µm) of machined from gating alloy series

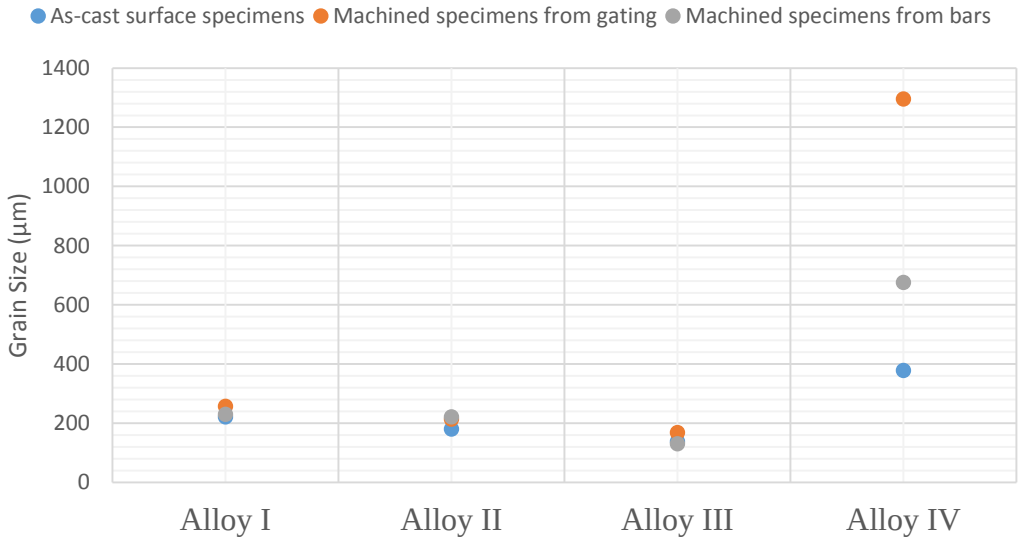

Fig. 4.48 Average grain size (µm) of studied alloys for all specimen types

4.5.4 Porosity Measurement

The porosity is another factor affecting tensile test results directly. The porosity measurements were performed after tensile tests just below the fracture surface as such in the grain size measurements. The one example from the measurement is

provided in Fig. 4.49 in order to represent the methodology. Red areas on Fig. 4.49 (b) represent porosities where approximate porosity percentage on this figure was found as 1.4%. Minimum 10 different areas on all specimen types for each alloy series were measured and average of them was given in the following respective figures.

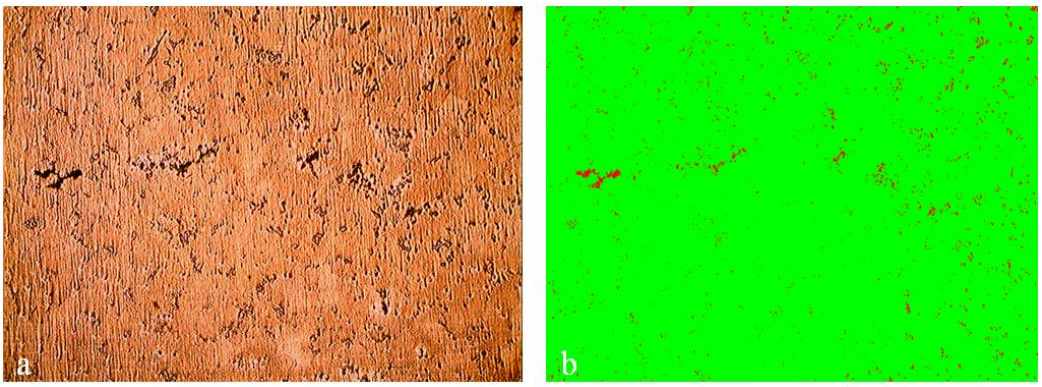

Fig. 4.49 Example of porosity measurement from as-cast surface specimen **o**f Alloy III (a) porosity measurement area (b) porosity measurement colorization on this region

Fig. 4.50 gives the average porosity percentages of studied alloy series in as-cast surface specimen condition. The porosity percentages of Alloy I (around 4.2%) was comparable higher than the others. In addition, Alloy II, III, and IV have nearly same porosity percentages. It can be concluded from this result that achievable porosity percentage in 10 mm section thickness (as-cast surface specimen condition) is about 2.5 %. It is not so meaningful to interpret these results within these alloy series because of small fluctuations.

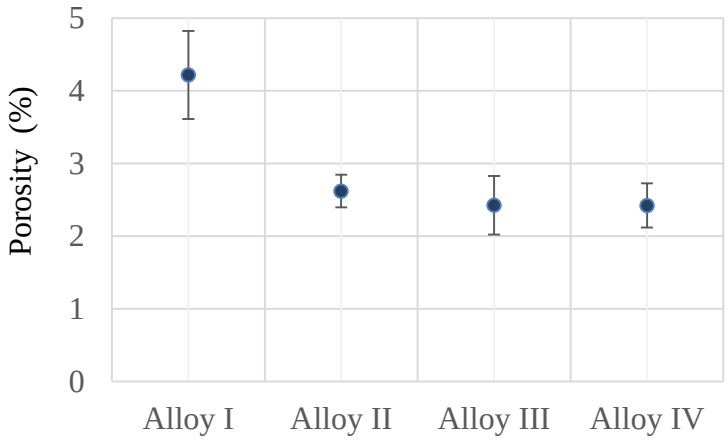

Fig. 4.50 Porosity values of alloy for as-cast specimen conditions

In comparison to as-cast specimen surface condition, machined specimens from 22 mm bar have higher porosity percentages as shown in Fig. 4.51. Higher porosity percentage could be attributed to thicker section. Meanwhile, since thicker regions are responsible to lower cooling rate, it would also be expected to a more porous structure. The highest porosity percentage was observed in Alloy I same as in as-cast specimen condition while remarkable difference was noted among the other. This deviation could be ascribed to the grain refiner addition in Alloy III and alloying element addition in Alloy II. Grain refinement with Al-5Ti-1B in Alloy III could increase feeding behavior by reducing segregation during solidification, which may cause homogeneous distribution of porosity and break the interconnection between the porosities. [24,59,70,71]

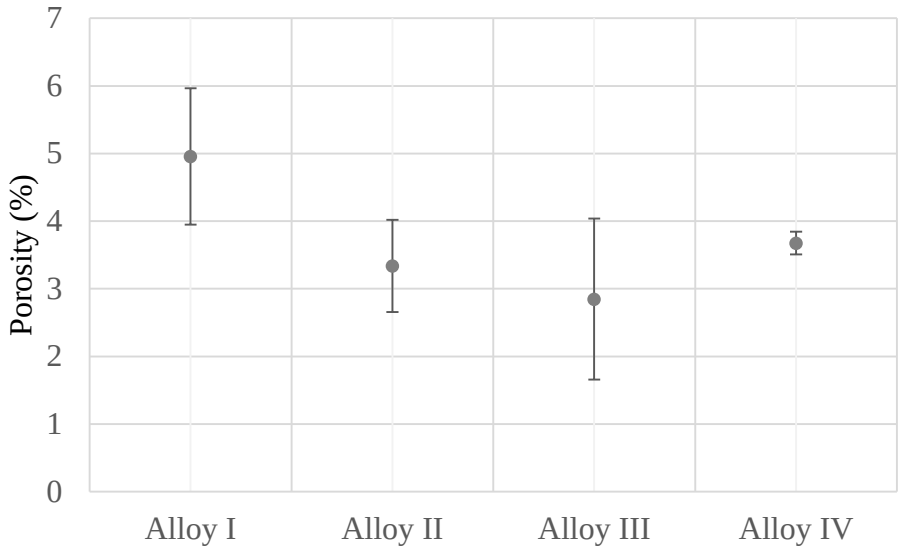

Fig. 4.51 Porosity values of alloys for machined specimens

The porosity percentages of the specimens taken from gating are represented in Fig. 4.52. It should be noted according that the difference in porosity percentages between Alloy III (or Alloy II) and Alloy IV (AZ91) increased in comparison to other specimen conditions. The increase of porosity in thicker section for AZ91 (Alloy IV) could be interpreted with increase of microporosity tendency. This situation was suppressed in Alloy II and Alloy III by addition of alloying elements such as Si, Sr and Sn and Al-5Ti-1B grain refiner. This certainly brings in improvement in integrity of casting having varying section thicknesses.

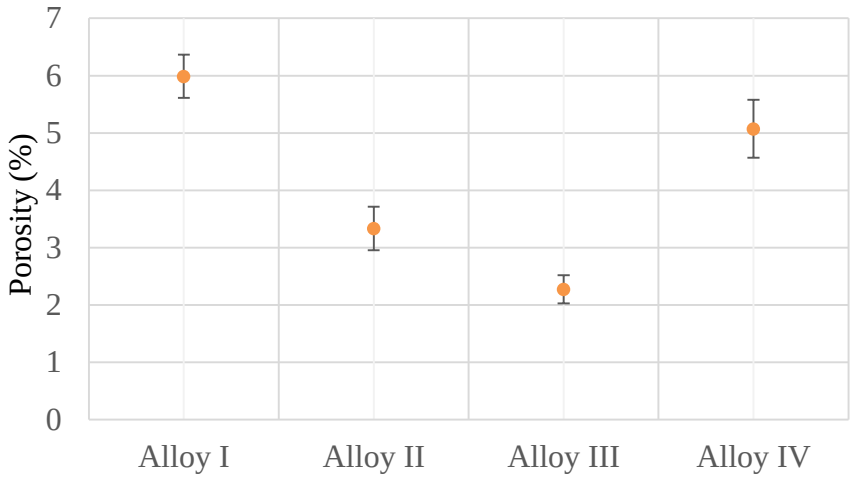

Fig. 4.52 Porosity values of alloys for machined from gating specimens

Fig. 4.53 summarizes all porosity percentages of the alloy series in different specimen conditions. As already explained, the variations in porosity percentages are easily observed via this figure between each alloy system in addition to specimen conditions within each alloy system. Alloy I and Alloy IV have higher porosity percentages with respect to Alloy II and Alloy IV. Since microporosity tendency of AZ91 would already expected in thicker section, the deviations within Alloy IV for different specimen conditions could be understandable. This variation would be related with longer solidification and feeding problem of AZ91. Ca containing Alloy I also suffered with this problem as indicated on Fig. 4.53. However, Sr containing alloys (Alloy II and Alloy III) had much less deviation in different specimen conditions. The reason could be attributed to the effect on Sr on interdendritic feeding and decreasing surface energy in liquid magnesium. The addition of 0.1% Al-5Ti-1B grain refiner to Alloy II improves solidification characteristics and results in more homogeneous distribution in porosity within different specimen conditions.

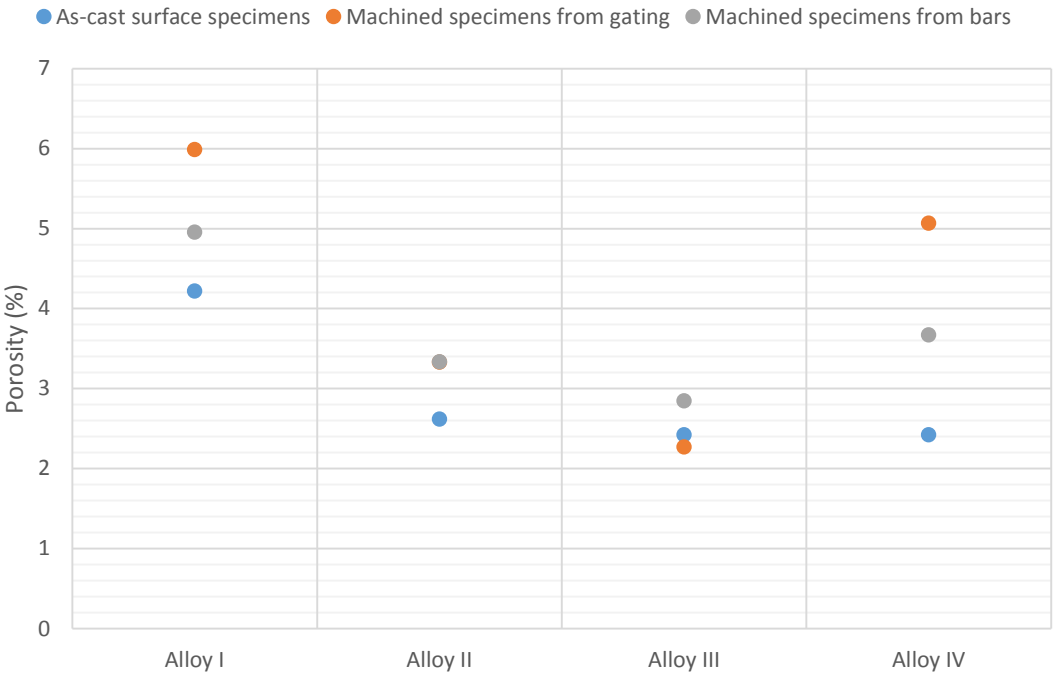

Fig. 4.53 Porosity percentage cof studied alloys for all specimen types

Porosity measurement results of AZ91E alloy and AZ91E alloy at different level of Al-SiC grain refiner are presented in Fig. 4.54 [88]. The minimum porosity was measured as 1.8 % with AZ91E-0.1 %Al-SiC while 2 % was obtained for AZ91E alloy. The increasing the addition level of Al-SiC grain refiner resulted in higher percentage of porosity. The situation was ascribed to the increase of freezing range, which causes difficulty in feeding the interdenditic region. It was expected to have higher porosity due to the longer time in mushy zone (solid-liquid phase together) with longer freezing range.

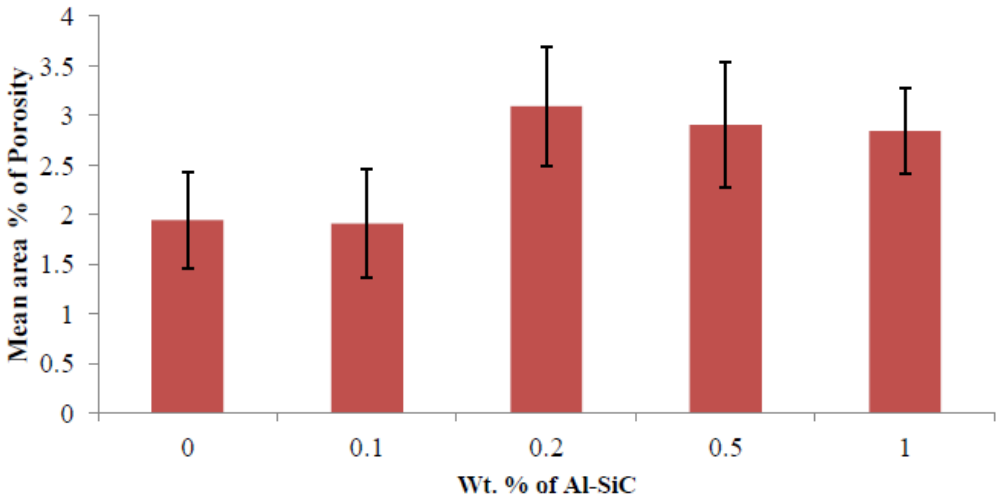

Fig. 4.54 Mean area percentage of interdendritic porosity in AZ91E alloy and grain refined alloys [88]

4.6 Fractography Analysis

Fractography analysis was performed in as-cast surface specimen in T6 treated conditions in order to estimate root cause of fracture. In addition, effect of alloying element additions on the fracture morphology were also interpreted from the fractography images. Due to HCP nature of magnesium, failure mode of Mg alloys is expected brittle via cleavage or quasi-cleavage (mixture of brittle and ductile fracture regions) fracture mechanism.

Fig. 4.55 shows the fracture surface images of Alloy I at different magnifications. As seen in Fig. 4.55 (a), fracture started from surface and went through to center region. In addition, gas porosity resulted from entrapped gas was detected on the fracture surface. Some amount of deformation was observed between matrix and second phase particles at the grain boundaries resulted in the formation of microvoid and tear dimple formation. In addition to this, cleavage planes were also detected on the

surface. The white particles observed on the surfaces contain Mg, Al, Ca and Zn element according to the EDS results. Since the fracture path completed on this area, it could be concluded that Ca containing β-$Mg_{17}Al_{12}$ at the grain boundary is the main responsible phase for fracture.

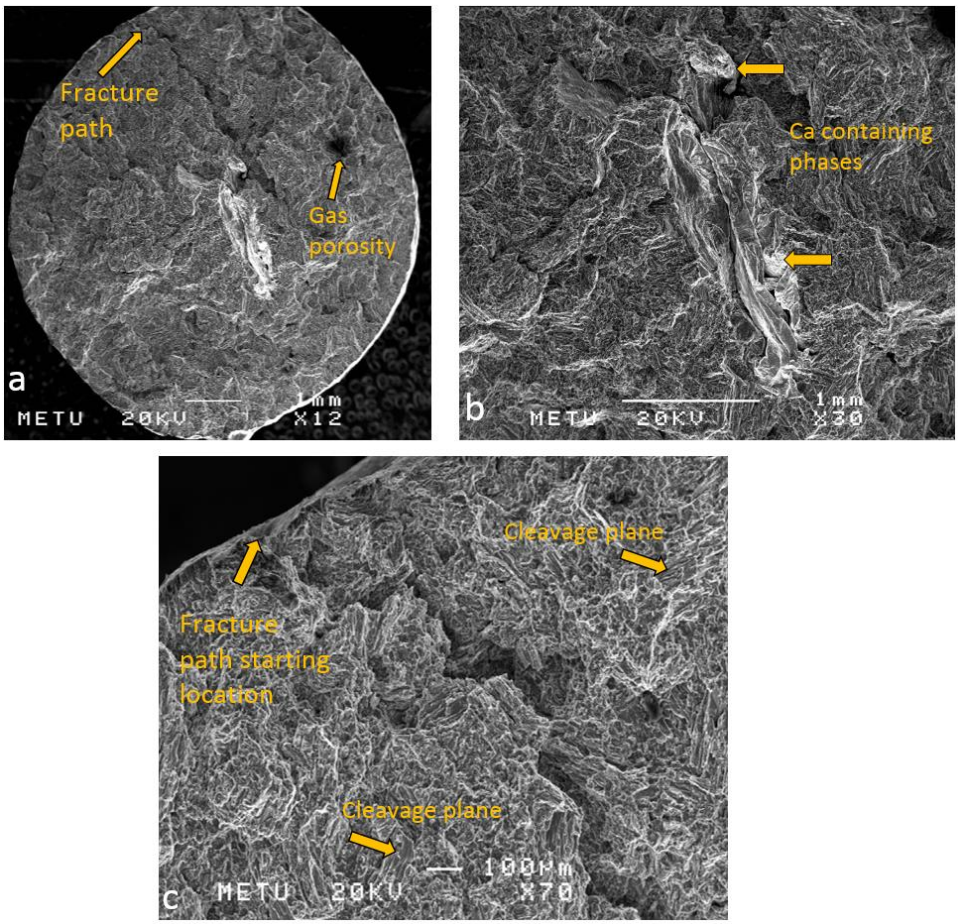

Fig. 4.55 Fracture surface images of Alloy I in as-cast surface specimen condition showing different regions

Fracture surface images of Alloy II are provided in Fig. 4.56. In comparison to Alloy I, more cleavage planes and river patterns were observed on fractography surfaces. Alloy II also consists of both brittle and ductile regions. This means two type of fracture mechanism exist in different locations. In addition, modified Mg_2Si phase

containing Sr and Sn elements according to the EDS analysis results as seen in Fig. 4.56 (c). Due to its hardness and strength, it did not distort during fracture and increase in the volume of cleavage planes around it was also observed. In some locations, as same with Alloy I, gas porosity and microvoid areas were also observed. In addition, in the grain boundary regions, Al containing phases (β-$Mg_{17}Al_{12}$) were observed in addition to modified Mg_2Si phase. These phases at the grain boundaries could be attributed to the main strengthening phase at RT.

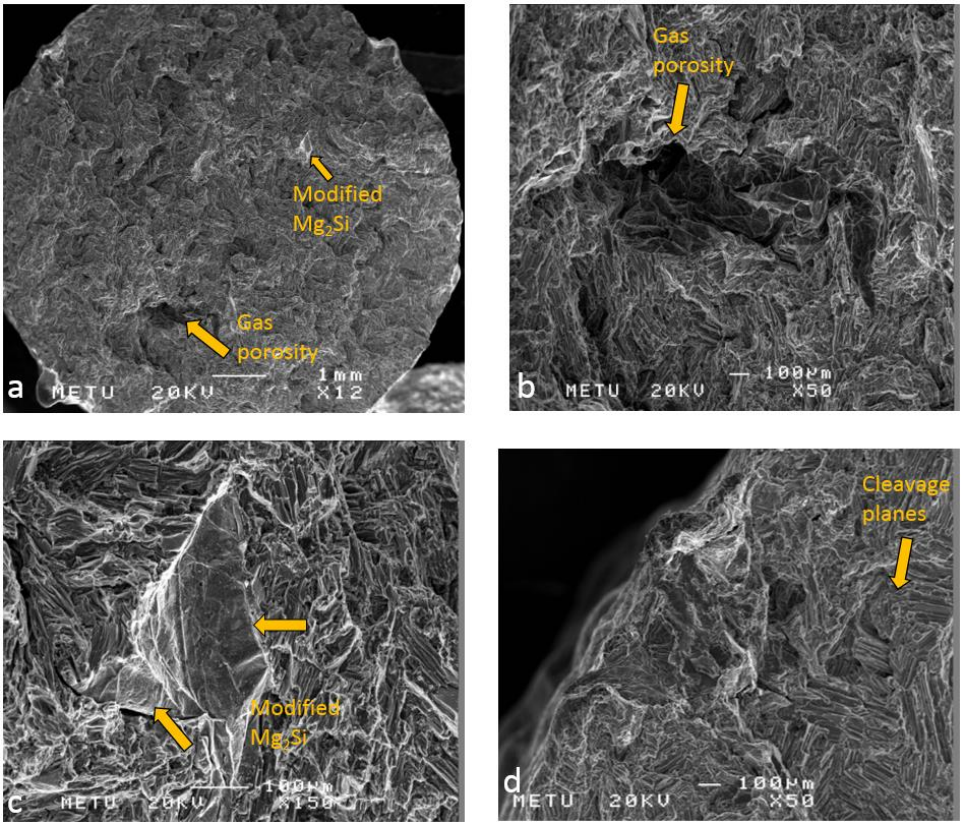

Fig. 4.56 Fracture surface images of Alloy II in as-cast surface specimen condition showing different regions

As same with Alloy I and Alloy II, Alloy III also behaves in quasi-cleavage type of fracture. However, refinement of grains with Al-5Ti-1B addition allows more elongated grains in comparison to Alloy II in overall fracture surface. Cleavage

planes at higher magnification were clearly observed as seen in Fig. 4.57 (e) Microvoids, gas porosities, smaller modified Mg_2Si phases containing Sr and Sn elements as a result of EDS analysis were also detected in Alloy III fracture surface (Fig. 4.57). Some plastic deformation and dimples were detected in the sample although the specimen fails in brittle fracture manner.

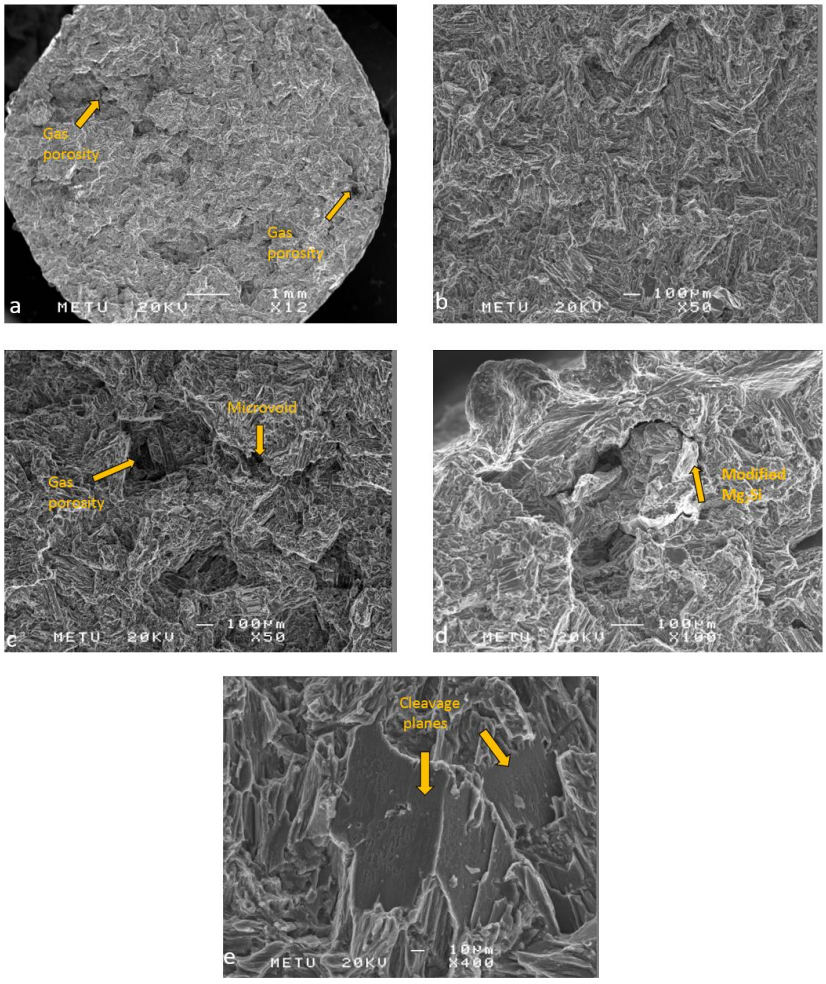

Fig. 4.57 Fracture surface images of Alloy III in as-cast surface specimen condition showing different regions

The fracture surface images of Alloy IV are given in Fig. 4.58. The fracture behavior of AZ91 is purely cleavage as understood from the cleavage steps of different sizes and river patterns. The discontinuous β-($Mg_{17}Al_{12}$) phase at the grain boundaries are

the main reason of cleavage type of fracture and lower elongation value [17,25]. In comparison to other studied alloys in this thesis, there was no plastic deformation indication observed in the fracture surface of AZ91 (Alloy IV).

This situation would reflect the lower elongation values obtained from tensile test (Table 4.4). In addition, it should be noted that the examined specimens was taken from the as-cast surface specimen condition (thinnest specimen). When the thickness was increased, the level of cleavage would expeced to be worse. The elongation value of machined from gating specimen is nearly half of that as-cast surface specimens. As a conclusion alloying element additions to AZ91 alloy as in Alloy I, Alloy II and Alloy III brought to change of fracture behavior from cleavage to quasi-cleavage. This situation could also be verified with elongation values as already mentioned.

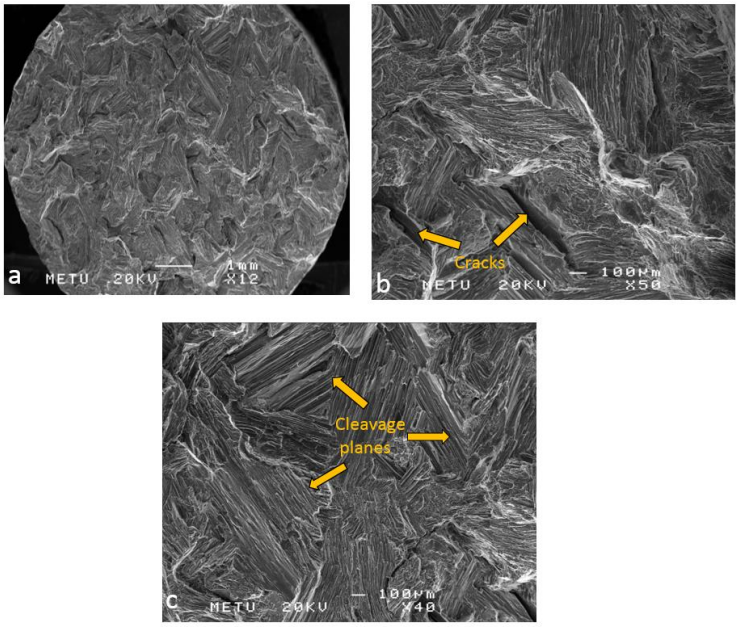

Fig. 4.58 Fracture surface images of Alloy IV in as-cast surface specimen condition showing different regions

Due to the massive and coarse discontinuous β-$Mg_{17}Al_{12}$ intermetallics at grain boundaries, AZ91 alloy is very suspectible to brittle fracture. Microcrack initiation is generally observed in these locations due to the nature of brittleness of this phase. Srinivasan [40] showed the tensile fractography image of AZ91 at room and elevated temperature as given in Fig. 4.59. As also stated by Srinivasan [40], type of fracture for AZ91 is cleavage with some secondary crack stated as "A" in Fig. 4.59 (a). Cleavage planes and river patterns were also observed in the fracture surface. (B and C, in Fig. 4.59 (a), respectively) Improvement in ductility was observed in the fracture surface of the specimen tested at 150 ºC while cleavage planes and secondary cracks were also indicative of brittle type of fracture. (Fig. 4.59 (b)) Main reason could be proposed as introduction of new slip planes with softening and weaking of β-$Mg_{17}Al_{12}$ phase at grain boundaries.

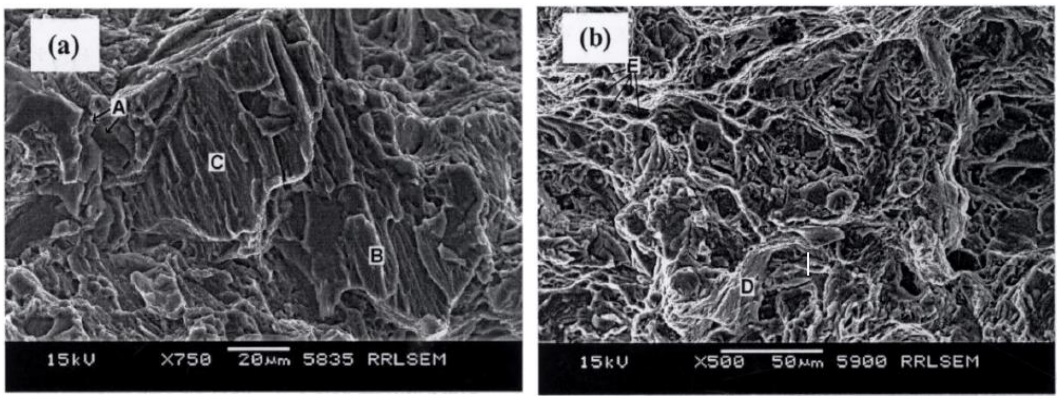

Fig. 4.59 Tensile fractography of AZ91 alloy at (a) RT (b) 150 ºC (A) secondary crack (B) cleavage plane (C) river pattern (D) plastic deformation (E) dimples [40]

CHAPTER 5

CONCLUSIONS AND SUGGESTIONS FOR FUTURE WORK

The development of creep resistance Al based Mg alloys for sand casting was studied with the addition of different alloying elements. The alloys used in this thesis were categorized into four groups:

- Alloy I: AZ91-0.7%Si-0.5%Ca-0.9%Sn
- Alloy II: AZ91-0.7%Si-0.3%Sr-0.6%Sn
- Alloy III: AZ91-0.7%Si-0.3%Sr-0.6%Sn + 0.1% Al-5Ti-1B
- Alloy IV: AZ91

Alloy IV was selected in order to obtain general data of base AZ91 magnesium alloy by using the experimental procedure and parameters for this thesis. Si was selected as a major alloying element to obtain creep resistant microstructure by forming Mg_2Si phase for all alloys except Alloy IV. Alloy I was created to observe the modification effect of simultaneous addition of Ca and Sn elements on Mg_2Si phase. Alloy II were generated to see that of Sr and Sn elements on this phase. In addition to this, after obtaining more desirable microstructure in Alloy II in comparison to Alloy I, 0.1%Al-5Ti-1B grain refiner addition to Alloy II was performed to increase integrity, decrease grain size and obtain more homogenous grain size distribution.

The aim of this thesis was to obtain creep resistant microstructure in Mg-Al alloys together with comparable tensile strength at RT with industrially available magnesium alloys used in aerospace sand casting applications. The main drawback

of AZ91 alloy in terms of creep resistance is the formation of massive and continuous network of thermally unstable β-$Mg_{17}Al_{12}$ phase at the grain boundaries. The undissolved β-$Mg_{17}Al_{12}$ after heat treatment coarsens and weakens the grain boundary at temperatures above 120 ^{0}C, which finally causes the activation of grain boundary sliding mechanism [1,10, 25, 41, 42, 48]. Therefore, the alloying additions for Alloy I, Alloy II, and Alloy III were focused on eliminating this disadvantage. Si addition to AZ91 alloy was specifically preferred to obtain high melting temperature (1080 ^{0}C) and high hardness (460 $HV_{0.3}$) and low density (1.99 g/cm^3) Mg_2Si formation on the microstructure. However, this addition causes the formation of undesirable Chinese script Mg_2Si phase for RT mechanical properties. In order to illustrate this effect, the optical microstructures of AZ91-0.7%Si in both as-cast and T6 heat treated condition were presented in Appendix B (B.1 to B.4). The complicated morphology of this phase is very prone to crack initiation site at RT.

The alloying element selection was firstly focused on changing morphology of Chinese script Mg_2Si. In the literature, Ca, Sr and Sn elements were found as some possible modification elements for this phase. It was obtained from optical microstructure and SEM-EDS analysis results that the modification effect of Sr element in Alloy II on this phase more obvious than that of Ca in Alloy I. In addition to this, the amount of undissolved β-$Mg_{17}Al_{12}$ after heat treatment was obviously lower in Alloy II. The size and distribution of modified Mg_2Si phase is lower and more homogeneous, respectively, as observed in optical and SEM images. EDS analysis proves the dissolution of Sr and Ca elements in both β-$Mg_{17}Al_{12}$ and Mg_2Si phase. The morphology of β-$Mg_{17}Al_{12}$ in these alloy series is thinner than that of AZ91. The main reason for morphology change of Mg_2Si phase from Chinese script to polygonal shape could be ascribed to the dissolution of Sr and Sn elements. This was also verified by elemental mapping analysis performed for Alloy III. The accumulation of Sr and Sn elements was easily detected around and inside of Mg_2Si. As already indicated by Pekguleyuz et al. [47], Sr segregates to the surface with decreasing surface energy and tension for magnesium alloys. Accumulation of Sr

elements especially inside of modified Mg_2Si phase also supports this idea. Also, it was indicated that Sr increases the interdendritic feeding during solidication. It was also verified in Alloy II and Alloy III. The measured porosity percentage in Sr containing alloys is considerably lower.

Cooling curve data obtained from the mould system brought the advantage of freezing range comparison and determination of actual phase transformation temperatures of the alloy systems used in this thesis. Although lowest freezing range was observed in Alloy I, measured porosity percentages were higher than other alloys in all casting thicknesses. In addition to this, fracture surfaces of tensile test specimens reveals Ca containing phases and Ca accumulation could be the main possible reasons. Due to this reason, it was concluded that Ca alloying is not suitable as Sr alloying in sand casting Al based magnesium alloys. In addition, the decrease of freezing range with the adition Al-5Ti-1B grain refiner was also deduced cooling curves. This grain refinement brought more homogeneous distribution of porosity in variable casting thicknesses. The decrease in undercooling degree from on the order of 0.4 ^oC (AZ91) to negligible degree (~ 0 ^0C) was obtained with grain refiner addition. This result also reflects the efficient grain refinement was obtained.

Radiographic examination after filter installation revealed the decrease in gas porosity coming from turbulent flow. According to the radiographic examination results comparison before and after filter addition to the mould, it could be reasonably proposed that this modification resulted in decrease of liquid metal velocity. Since homogeneous filling and low liquid metal velocity are desired to obtain minimum internal casting defect, it was verified with the aid of filter modification.

In terms of mechanical properties, most desirable results were obtained from Alloy III. If the values are compared in Alloy series used in this thesis, the integrity was optimum for Alloy III for variable casting thickness such as as-cast surface,

machined from rectangular bar and machined from gating specimen types (representative of 10, 22, and 30 mm section thicknesses, respectively.) The most significant change was observed with the addition of 0.1%Al-5Ti-1B grain refiner to Alloy II. In literature, TiB_2 was shown as possible nucleating agent when the addition amount increased about 1% [38, 67, 69, 71]. There are several reasons for Al-Ti-5B grain refiner to be a promising refinement agent in Mg alloys. The smaller planar disregistry factor of TiB_2 and α-Mg (5.6%), higher melting point of TiB_2 particle and large GRF value of Ti could be given for main reasons for selection Al-5Ti-1B grain refiner in Alloy III. The addition of this grain refiner to Alloy II showed that highest mechanical properties together with lowest grain size and minimum porosity. It was expected to see TiB_2 particles on SEM image. However, due to the lower additional level, it could be reasonably proposed these particles were not detected. Ti addition would cause hindering grain growth of α-Mg phase because of its large GRF value [70]. This may reflect to obtain lowest grain size and highest mechanical properties.

The summary of all the major findings and the conclusions obtained from this thesis is listed below:

1. The useful effect of SiC ceramic filter with 20 mm thickness and 30 ppi addition to the moulding system was verified with gas porosity decrease in the specimens radiographically. This result is predicated to the reduction in turbulance flow during filling the mold.

2. The as-cast microstructure of AZ91 alloy consists of α-Mg solid solution, Al_8Mn_5 phase, massive β-$Mg_{17}Al_{12}$ phase together with lamellar discontinuous precipitation of $Mg_{17}Al_{12}$ at the neighborhood of grain boundaries.

3. 0.7%Si addition to AZ91 alloy causes the formation of coarse Chinese Script Mg_2Si phase both at grain boundary and inside of the grains.

4. Addition of 0.5%Ca and 0.9%Sn to AZ91-0.7%Si alloy did not cause any new phase formation. However, modified polygonal Mg_2Si phase was observed at inside of grains, grain boundaries and on β-$Mg_{17}Al_{12}$ phase. Simultaneous growth of Mg_2Si and β-$Mg_{17}Al_{12}$ was deduced from optical microscope and SEM analysis. EDS results reveal the dissolution of Ca and Sn elements dissolved in polygonal Mg_2Si phase. This dissolution introduces the morphology change from Chinese script to polygonal.

5. Addition of 0.3%Sr and 0.6%Sn to AZ91-07%Si alloy causes the formation of MgSiSr phase formation. As same with 0.5%Ca and 0.9%Sn addition to that alloy, modified polygonal Mg_2Si was formed after introduction to these elements. The size of polygonal Mg_2Si phase was lower than that of AZ91-07%Si-0.5%Ca-0.9%Sn alloy. The distribution of this phase is also more homogeneous in comparison to that alloy.

6. 0.1% Al-Ti-B grain refiner addition to AZ91-0.7%Si-0.3%Sr-0.6%Sn yields to obtain the lowest grain size and most homogeneous distribution in the studied alloys. This result was ascribed to strong undercooling effect of Ti (meaning large GRF for liquid magnesium).

7. In the all alloy system studied in this thesis, Al-Mn-Fe particles were detected inside of grain. These particles were suggested as nucleation sites during solidification. It was also observed that distribution of these particles more homogeneous with 0.1% Al-Ti-B addition to AZ91-0.7%Si-0.3%Sr-0.6%Sn alloy.

8. The undercooling degree of AZ91 alloy was measured as 0.4 ^{0}C. The alloying decreased this value about 0.2 ^{0}C. Moreover, 0.1% Al-5Ti-1B added AZ91-0.7%Si-0.3%Sr-0.6%Sn alloy system showed negligible undercooling.

9. The highest mechanical properties were obtained for AZ91-0.7%Si-0.3%Sr-0.6%Sn-0.1%Al-5Ti-1B. The as-cast surface specimens (10 mm casting thickness) of AZ91 and this alloy have nearly same UTS values. However, variability in mechanical properties was clearly detected in AZ91 magnesium alloy while integrity was achieved with other alloy systems. The most remarkable integrity for varying casting thicknesses was observed in AZ91-0.7%Si-0.3%Sr-0.6%Sn + 0.1% Al-5Ti-1B magnesium alloy.

10. Beneficial effect of Sr addition on the interdendritic feeding was observed in accordance with the porosity percentages. Lower porosity percentages were obtained in AZ91-0.7%Si-0.3%Sr-0.6%Sn in comparison to AZ91-0.7%Si-0.5%Ca-0.9%Sn alloy. Highest porosity percentage was measured in the latter alloy system in this alloy system while the expectation would be AZ91 alloy.

11. The positive effect of grain refiner addition on porosity percentage was proven with AZ91-0.7%Si-0.3%Sr-0.6%Sn + 0.1% Al-5Ti-1B alloy system.

12. Fractography revealed AZ91 alloy is completely cleavage fracture behavior while other alloying sytems contains brittle and cleavage fracture regions. Alloying with Si, Sr, Ca and Sn elements to AZ91 alloy resulted in some evidence of ductility. In addition, elongation values validated the fracture morphology. The elongation values of AZ91 were almost one one third of other alloying systems in some specimen conditions.

In the scope of this thesis, future works for the studied alloys could be summarized as follows:

1. The developed creep resistant microstructure of AZ91-0.7%Si-0.3%Sr-0.6%Sn should be tested in the similar conditions of high temperature casting components used in aerospace and automotive industries.

2. Different addition amount of Al-5Ti-1B grain refiner to AZ91-0.7%Si-0.3%Sr-0.6%Sn should be carried out to find optimum amount together with optimum time for holding.

3. A detailed TEM study shall be performed to understand the dislocation and creep mechanism of developed alloy with and without Al-5Ti-1B grain refiner addition.

4. Since magnesium casting components preferred in high temperature applications are also exposed to fatigue loads, fatigue test results at different stress levels should evaluated.

5. Since corrosion is main drawback of magnesium alloys, corrosion behavior of all studied alloy systems shall be studied in order to compare their response to corrosion.

REFERENCES

[1] A. A. Luo, “Recent magnesium alloy development for elevated temperature applications,” *Int. Mater. Rev.*, vol. 49, no. 1, pp. 13–30, 2004.

[2] A. Luo and M. O. Pekguleryuz, “Cast magnesium alloys for elevated temperature applications,” *J. Mater. Sci.*, vol. 29, no. 20, pp. 5259–5271, 1999.

[3] N. D. Saddock, “Microstructure and Creep Behavior of Mg-Al Alloys Containing Alkaline and Rare Earth Additions” Ph. D. Thesis, The University of Michigan Materials Science and Engineering, Michigan,2008.

[4] H. Friedrich and B. Mordike, *Magnesium Technology. Metallurgy, design data, applications*. 2006.

[5] B. Amir Esgandari, H. Mehrjoo, B. Nami, and S. M. Miresmaeili, “The effect of Ca and RE elements on the precipitation kinetics of Mg17Al12phase during artificial aging of magnesium alloy AZ91,” *Mater. Sci. Eng. A*, vol. 528, no. 15, pp. 5018–5024, 2011.

[6] S. Fleming, “An Overview of Magnesium based Alloys for Aerospace and Automotive Applications ” M.S. Thesis, Rensselaer Polytechnic Institute Mechanical Engineering, pp. 1–36, Troy, 2012.

[7] Y. Mingbo, P. Fusheng, C. Renju, and S. Jia, “Comparison about effects of Sb, Sn and Sr on as-cast microstructure and mechanical properties of AZ61-0.7Si magnesium alloy,” *Mater. Sci. Eng. A*, vol. 489, no. 1–2, pp. 413–418, 2008.

[8] J. Liu, W. Wang, S. Zhang, D. Zhang, and H. Zhang, “Effect of Gd-Ca combined additions on the microstructure and creep properties of Mg-7Al-1Si alloys,” *J. Alloys Compd.*, vol. 620, pp. 74–79, 2015.

[9] M. O. Pekguleryuz and A. A. Kaya, “Creep resistant magnesium alloys for

powertrain applications," *Adv. Eng. Mater.*, vol. 5, no. 12, pp. 866–878, 2003.

[10] A. Srinivasan, J. Swaminathan, U. T. S. Pillai, K. Guguloth, and B. C. Pai, "Effect of combined addition of Si and Sb on the microstructure and creep properties of AZ91 magnesium alloy," *Mater. Sci. Eng. A*, vol. 485, no. 1–2, pp. 86–91, 2008.

[11] B. Wang, X. Wang, J. Zhou, G. Zhang, and F. Liu, "Effects of solution heat treatment on microstructure and mechanical properties of Mg-3Al-1Si-0.3Mn-xSr alloy," *Mater. Sci. Eng. A*, vol. 618, pp. 210–218, 2014.

[12] H. L. Zhao, S. K. Guan, and F. Y. Zheng, "Effects of Sr and B addition on microstructure and mechanical properties of AZ91 magnesium alloy," *J. Mater. Res.*, vol. 22, no. 9, pp. 2423–2428, 2007.

[13] G. Y. Yuan, Z. L. Liu, Q. D. Wang, and W. J. Ding, "Microstructure refinement of Mg – Al – Zn – Si alloys," *Mater. Lett. 56*, vol. 56, no. September, pp. 53–58, 2002.

[14] A. Srinivasan, U. T. S. Pillai, J. Swaminathan, S. K. Das, and B. C. Pai, "Observations of microstructural refinement in Mg-Al-Si alloys containing strontium," *J. Mater. Sci.*, vol. 41, no. 18, pp. 6087–6089, 2006.

[15] P. Cao, M. Qian, and D. StJohn, "Grain refinement of commercial purity Mg-9%Al alloys by superheating," *Magnes. Technol.*, no. January, 2005.

[16] T. A. Leil, "Development of New Magnesium Alloys for High Temperature Applications," Ph. D. Thesis,Clausthal University of Technology Faculty of Natural and Materials Sciences,Münich, 2009 .

[17] K. M. Asl, "Improving the Properties of Magnesium Alloys for High Temperature Applications," *Magnes. Alloy. - Des. Process. Prop.*, no. Mm, pp. 265–280, 2011.

[18] C. Song, Q. Han, and Q. Zhai, "Review of grain refinement methods for as-cast microstructure of magnesium alloy," *China Foundry*, vol. 6, no. 2, pp. 93–103, 2009.

[19] M. J. F. Gándara, "Recent growing demand for magnesium in the automotive industry," *Mater. Tehnol.*, vol. 45, no. 6, pp. 633–637, 2011.

[20] E. F. Emley, Principles of Magnesium Technology, London: Pergamon, 1966.

[21] S. Mathaudhu, A. Luo, Essential Readings in Magnesium Technology. London, Spinger, 2007.

[22] "Fansteel Wellman Dynamics." [Online]. Available: http://fansteel.com/folder/Wellman/html/foundry_products.html. [Accessed: 10-May-2018].

[23] U. Manchester, Magnesium Technology, London: The Institute of Metlas, 1987.

[24] S. K. Saha, "A Study of Grain Refinement of AZ91E and Mg-9 Wt.% Al Alloys Using Zinc Oxide," M. S. Thesis, Mechanical and Industrial Engineering Ryerson University, Toronto, 2014.

[25] T. Rzychoń, A. Kiełbus, and J. Szala, "Microstructure and quantitative analysis of cast ZRE1 magnesium alloy," *Archives of Foundry Engineering*, vol. 7, no. 1, pp. 175–178, 2007.

[26] W. Callister and D. Rethwisch, *Materials science and engineering: an introduction*, vol. 94. 2007.

[27] D. H. Stjohn, A. K. Dahle, T. Abbott, M. D. Nave, and M. Qian, "Solidification of Cast Magnesium Alloys," *Essent. Readings Magnes. Technol.*, no. 55, pp. 193–198, 2014.

[28] C.-Y. Cho, J.-Y. Uan, and T.-C. Tsai, "Effect of Cooling Rate on Mg17Al12 Volume Fraction and Compositional Inhomogeneity in a Sand-Cast AZ91D Magnesium Plate," *Mater. Trans.*, vol. 47, no. 8, pp. 2060–2067, 2006.

[29] L. A. Dobrzański, T. Tański, L. Čížek, and Z. Brytan, "Structure and properties of magnesium cast alloys," *J. Mater. Process. Technol.*, vol. 192–193, pp. 567–574, 2007.

[30] M. Sahoo, S.P. Thomas, Technology for Magnesium Castings : Design, Products and Applications, American Foundry Society, Schaumburg, 2011.

[31] ASTM International, "ASTM B951 − 11 Standard Practice for Codification of Unalloyed Magnesium and Magnesium- Alloys , Cast and Wrought," *Am. Soc. Test. Mater.*, pp. 1–7, 2015.

[32] ASTM International, “B296-3 Standard Practice for Temper Designations of Magnesium Alloys , Cast and,” *Am. Soc. Test. Mate* vol. 03, pp. 2–4, 2015.

[33] ASTM International, “B661-12, Standard Practice for Heat Treatment of Magnesium Alloys,” *Am. Soc. Test. Mater.*, vol. 02, pp. 1–7, 2015.

[34] M. Furui, Y. Ebata, H. Yamada, S. Ikeno, K. Sakakibara, and S. Saikawa, “Grain Boundary and Intragranular Reactions during Aging in Mg-Al System Alloys Poured into Sand and Iron Molds,” *Mater. Trans.*, vol. 52, no. 3, pp. 285–291, 2011.

[35] A. Srinivasan, J. Swaminathan, M. K. Gunjan, U. T. S. Pillai, and B. C. Pai, “Effect of intermetallic phases on the creep behavior of AZ91 magnesium alloy,” *Mater. Sci. Eng. A*, vol. 527, no. 6, pp. 1395–1403, 2010.

[36] L. Čížek and M. Greger, “Mechanical properties of magnesium alloy AZ91 at elevated temperatures,” *Journal of Achievements in Materials and Manufacturing Engineering*, vol. 18, no. 1, pp. 203–206, 2006.

[37] Z. Ning, P. Cao, H. Wang, J. Sun, and D. Liu, “Effect of Cooling Conditions on Grain Size of AZ91 Alloy,” *J. Mater. Sci. Technol.*, vol. 23, no. 5, pp. 645–649, 2007.

[38] T. J. Chen, R. Q. Wang, Y. Ma, and Y. Hao, “Grain refinement of AZ91D magnesium alloy by Al-Ti-B master alloy and its effect on mechanical properties,” *Mater. Des.*, vol. 34, pp. 637–648, 2012.

[39] SAE International, Metallic Materials Properties Development Standarization (MMPDS-08),Battelle Material Institute,2013.

[40] A. Srinivasan, “Influence of Si, Sb and Sr additions on the microstructure, mechanical properties and corrosion behaviour AZ91 Magnesium alloy,” *Thesis (Ph.D)*, no. April, p. 225, 2008.

[41] SAE Aerospace, “AMS 4437, Magnesium Alloy Castings, Sand 8.7Al - 0.70Zn (AZ91C-T6) Solution Heat Treated and Aged,” *Aerosp. Mater. Specif.*, no. 02, pp. 1–7, 2014.

[42] SAE Aerospace, “AMS 4446, Magnesium Alloy, Sand Castings 8.7Al - 0.70Zn - 0.26Mn (AZ91E-T6) Solution and Precipitation Heat Treated,”

Aerosp. Mater. Specif., pp. 1–8, 2012.

[43] SAE Aerospace, "AMS 4439, Magnesium Alloy Castings 4.2Zn - 1.2 Rare Earths - 0.7Zr (ZE41A-T5) Precipitation Heat Treated," *Aerosp. Mater. Specif.*, no. 09, pp. 1–8, 2012.

[44] SAE Aerospace, "AMS 4427, Magnesium Alloy Castings, Sand 4.0Y - 2.3Nd - 0.7Zr (WE43B - T6) Solution and Precipitation Heat Treated," *Aerosp. Mater. Specif.*, no. 06, pp. 1–9, 2012.

[45] SAE Aerospace, "AMS 4429, Magnesium Alloy Castings, Sand 2.8Nd - 1.4Gd - 0.4Zn - 0.6Zr (EV31A - T6) Solution and Precipitation Heat Treated," *Aerosp. Mater. Specif.*, no. 05, pp. 1–8, 2012.

[46] T. Universit, B. Freiberg, Z. Erlangung, S. Erchov, N. Gutachter, and F. Prof, "Research on the Mechanical Properties of the Sand Cast Magnesium Alloy AZ91 Danksagung," Ph. D. thesis, Technischen Universität Bergakademie, Freiburg, 2001.

[47] M. O. Pekguleryuz, K. U. Kainer, and A. A. Kaya, *Fundamental of magnesium alloy metallurgy*. 2013.

[48] Y. Z. Lu, Q. D. Wang, X. Q. Zeng, W. J. Ding, and Y. P. Zhu, "Effects of silicon on microstructure, fluidity, mechanical properties and fracture behaviour of Mg-6Aln alloy," *Mater. Sci. Technol.*, vol. 17, no. 2, pp. 207–214, 2001.

[49] J. Medved and P. Mrvar, "Thermal Analysis of the Mg-Al Alloys," *Mater. Sci. Forum*, vol. 508, pp. 603–608, 2006.

[50] D. H. Kang, S. S. Park, and N. J. Kim, "Development of creep resistant die cast Mg-Sn-Al-Si alloy," *Mater. Sci. Eng. A*, vol. 413–414, pp. 555–560, 2005.

[51] M. Sumida, "Microstructure development of sand-cast AZ-type magnesium alloys modified by simultaneous addition of calcium and neodymium," *J. Alloys Compd.*, vol. 460, no. 1–2, pp. 619–626, 2008.

[52] E. Mohammadi Mazraeshahi, B. Nami, S. M. Miresmaeili, and S. M. Tabatabaei, "Effect of Si on the creep properties of AZ61 cast magnesium

alloy," *Mater. Des.*, vol. 76, pp. 64–70, 2015.

[53] R. Günther, C. Hartig, and R. Bormann, "Grain refinement of AZ31 by (SiC)P: Theoretical calculation and experiment," *Acta Mater.*, vol. 54, no. 20, pp. 5591–5597, 2006.

[54] A. K. Dahle, Y. C. Lee, M. D. Nave, P. L. Scha, and D. H. Stjohn, "Development of the as-cast microstructure in magnesium - aluminium alloys," *J. Light Met.*, vol. 1, pp. 61–72, 2001.

[55] Y. Guangyin, S. Yangshan, and D. Wenjiang, "Effects of bismuth and antimony additions on the microstructure and mechanical properties of AZ91 magnesium alloy," *Mater. Sci. Eng. A*, vol. 308, pp. 38–44, 2001.

[56] Y. Guangyin, L. Manping, D. Wenjiang, and A. Inoue, "Mechanical Properties and Microstructure of Mg – Al – Zn – Si-base Alloy," *Materials Tranasactions*, vol. 44, no. 4, pp. 458–462, 2003.

[57] Y. Z. Lu, Q. D. Wang, X. Q. Zeng, Y. P. Zhu, and W. J. Ding, "Behavior of Mg – 6Al – xSi alloys during solution heat treatment at 420 ° C," *Materials Science and Engineering*, vol. 301, pp. 255–258, 2001.

[58] F. Pan, M. Yang, and X. Chen, "A Review on Casting Magnesium Alloys: Modification of Commercial Alloys and Development of New Alloys," *J. Mater. Sci. Technol.*, vol. 32, no. 12, pp. 1211–1221, 2016.

[59] H. Yong and R. Li, "Effects of silicon on mechanical properties of AM60 magnesium alloy," *China Foundry*, vol. 9, no. 3, pp. 244–247, 2012.

[60] M. Yang, F. Pan, R. Cheng, and A. Tang, "Effects of solutionized Al-10Sr master alloys on grain refinement of AZ31 magnesium alloy," *J. Alloys Compd.*, vol. 461, no. 1–2, pp. 298–303, 2008.

[61] N. Jiang, L. Chen, L. Meng, C. Fang, H. Hao, and X. Zhang, "Effect of neodymium, gadolinium addition on microstructure and mechanical properties of AZ80 magnesium alloy," *J. Rare Earths*, vol. 34, no. 6, pp. 632–637, 2016.

[62] S. Kong, F. Application, and P. Data, "(12) United States Patent," vol. 2, no. 12, pp. 12–15, 2011.

[63] L. Wu, F. S. Pan, M. B. Yang, J. Y. Wu, and T. T. Liu, "As-cast

microstructure and Sr-containing phases of AZ31 magnesium alloys with high Sr contents," *Trans. Nonferrous Met. Soc. China (English Ed.*, vol. 21, no. 4, pp. 784–789, 2011.

[64] D. H. Lee, Y.C., Dahle, A.K., St.John, "Grain Refinement of Magnesium," *Magnes. Technol.*, pp. 211–218, 2000.

[65] Y. C. Lee, A. K. Dahle, and D. H. Stjohn, "The role of solute in grain refinement of magnesium," *Metall. Mater. Trans. A Phys. Metall. Mater. Sci.*, vol. 31, no. 11, pp. 2895–2906, 2000.

[66] X. Q. Zeng, Y. X. Wang, W. J. Ding, A. A. Luo, and A. K. Sachdev, "Effect of strontium on the microstructure, mechanical properties, and fracture behavior of AZ31 magnesium alloy," *Metall. Mater. Trans. a-Physical Metall. Mater. Sci.*, vol. 37A, no. 4, pp. 1333–1341, 2006.

[67] W. Yan, X. Shoumei, L. Wenhui, and Z. Zhiwen, "Effect of Si, Ca and Sr on the creep-resistance of AZ91D alloy," *Mater. Sci. Forum*, vol. 488–489, pp. 767–770, 2005.

[68] Y. Chen, H. Liu, R. Ye, and G. Liu, "Effects of the addition of Ca and Sb on the microstructure and mechanical properties of AZ91 magnesium," *Mater. Sci. Eng. A*, vol. 587, pp. 262–267, 2013.

[69] S. F. Liu, B. Li, X. H. Wang, W. Su, and H. Han, "Refinement effect of cerium, calcium and strontium in AZ91 magnesium alloy," *J. Mater. Process. Technol.*, vol. 209, no. 8, pp. 3999–4004, 2009.

[70] S. S. Li, B. Tang, X. Y. Jin, and D. Ben Zeng, "An investigation on hot-cracking mechanism of Sr addition into Mg-6Al-0.5Mn alloy," *J. Mater. Sci.*, vol. 47, no. 4, pp. 2000–2004, 2012.

[71] D. H. StJohn, M. Qian, M. A. Easton, P. Cao, and Z. Hildebrand, "Grain refinement of magnesium alloys," *Metall. Mater. Trans. A Phys. Metall. Mater. Sci.*, vol. 36, no. 7, pp. 1669–1679, 2005.

[72] J. Du, J. Yang, M. Kuwabara, W. Li, and J. Peng, "Improvement of grain refining efficiency for Mg-Al alloy modified by the combination of carbon and calcium," *J. Alloys Compd.*, vol. 470, no. 1–2, pp. 134–140, 2009.

[73] K. Hirai, H. Somekawa, Y. Takigawa, and K. Higashi, “Effects of Ca and Sr addition on mechanical properties of a cast AZ91 magnesium alloy at room and elevated temperature,” *Mater. Sci. Eng. A*, vol. 403, no. 1–2, pp. 276–280, 2005.

[74] M. E. Moussa, M. A. Waly, and A. M. El-Sheikh, “Effect of Ca addition on modification of primary Mg2Si, hardness and wear behavior in Mg-Si hypereutectic alloys,” *J. Magnes. Alloy.*, vol. 2, no. 3, pp. 230–238, 2014.

[75] D. H. Stjohn, M. T. Frost, A. Magnesium, and C. Limited, “Zirconium alloying and grain refinement of magnesium alloys,” *The Minerals, Metals & Materials Society*, vol. 4, no. 3, January, 2003.

[76] Y. D. Wang, G. H. Wu, W. C. Liu, S. Pang, Y. Zhang, and W. J. Ding, “Influence of heat treatment on microstructures and mechanical properties of gravity cast Mg-4.2Zn-1.5RE-0.7Zr magnesium alloy,” *Trans. Nonferrous Met. Soc. China (English Ed.*, vol. 23, no. 12, pp. 3611–3620, 2013.

[77] M. B. Yang, F. S. Pan, J. Shen, and L. Bai, “Comparison of Sb and Sr on modification and refinement of Mg2Si phase in AZ61-0.7Si magnesium alloy,” *Trans. Nonferrous Met. Soc. China (English Ed.*, vol. 19, no. 2, pp. 287–292, 2009.

[78] ASTM International, “ASTM B80 Standard Specification for Magnesium-Alloy Sand Castings,” *Am. Soc. Test. Mater.*, pp. 1–12, 2015.

[79] A. Elsayed, “Novel grain refinement of AZ91E magnesium alloy and the effect on hot tearing during solidfication,” M.s. thesis, Ryerson University Mechanical Engineering, Toronto, 2010.

[80] L. Gao, S. M. Liang, R. S. Chen, and E. H. Han, “Correlation of recalescence with grain refinement of magnesium alloys,” *Trans. Nonferrous Met. Soc. China (English Ed.*, vol. 18, no. SPEC. ISSUE 1, pp. s288–s291, 2008.

[81] M. Ohno, D. Mirkovic, and R. Schmid-Fetzer, “Liquidus and solidus temperatures of Mg-rich Mg-Al-Mn-Zn alloys,” *Acta Mater.*, vol. 54, no. 15, pp. 3883–3891, 2006.

[82] L. Lu, A. K. Dahle, and D. H. StJohn, “Heterogeneous nucleation of Mg-Al

alloys," *Scr. Mater.*, vol. 54, no. 12, pp. 2197–2201, 2006.

[83] S. Liu, Y. Zhang, H. Han, and B. Li, "Effect of Mg-TiB2master alloy on the grain refinement of AZ91D magnesium alloy," *J. Alloys Compd.*, vol. 487, no. 1–2, pp. 202–205, 2009.

[84] A. K. Dahle and L. Arnberg, "The Effect of Grain Refinement on the Fluidity of Aluminium Alloys," *Mater. Sci. Forum*, vol. 217–222, pp. 259–264, 1996.

[85] Y. Wang, X. Zeng, and W. Ding, "Effect of Al-4Ti-5B master alloy on the grain refinement of AZ31 magnesium alloy," *Scr. Mater.*, vol. 54, no. 2, pp. 269–273, 2006.

[86] J. Du, M. Wang, M. Zhou, and W. Li, "Evolutions of grain size and nucleating particles in carbon-inoculated Mg-3% Al alloy," *J. Alloys Compd.*, vol. 592, pp. 313–318, 2014.

[87] A. Elsayed, C. Ravindran, and B. . Murty, "Effect of Al-Ti-B Based Master Alloys on Grain Refinement and Hot Tearing Susceptibility of AZ91E Magnesium Alloy," *Mater. Sci. Forum*, vol. 690, pp. 351–354, 2011.

[88] A. Azad, "Grain refinement of magnesium alloy AZ91E," M. S. Thesis, The University of British Columbia Mechanical Enginering, Canada, 2012.

[89] T. R. Ramachandran, P. K. Sharma, and K. Balasubramanian, "Grain refinement of light alloys," *68th World Foundry Congr.*, pp. 189–193, 2008.

[90] G. . Dieter, *Mechanical Metallurgy*, SI Edition. London: McGraw Hill., 1988.

[91] J. Campbell, *Casting*. Woburn, 1993.

[92] L. Lu, A. K. Dahle, and D. H. Stjohn, "Grain refinement efficiency and mechanism of aluminium carbide in Mg-Al alloys," *Scr. Mater.*, vol. 53, no. 5, pp. 517–522, 2005.

[93] R. Mitra and Y. R. Mahajan, "Interfaces in discontinuously reinforced metal matrix composites: An overview," *Bull. Mater. Sci.*, vol. 18, no. 4, pp. 405–434, 1995.

[94] L. Lu, A. K. Dahle, J. a. Taylor, and D. H. StJohn, "Theoretical and practical considerations of grain refinement of Mg-Al Alloys," *Mater. Sci. Forum*, vol. 488–489, pp. 299–302, 2005.

[95] F. Kabirian and R. Mahmudi, “Effects of zirconium additions on the microstructure of as-cast and aged AZ91 magnesium alloy,” *Adv. Eng. Mater.*, vol. 11, no. 3, pp. 189–193, 2009.

[96] T. Motegi, E. Yano, Y. Tamura, and E. Sato, “Clarification of Grain Refining Mechanisms of Superheat-Treated Mg-Al-Zn Alloy Castings,” *Mater. Sci. Forum*, vol. 350–351, pp. 191–198, 2000.

[97] Q. Jin, J. P. Eom, S. G. Lim, W. W. Park, and B. S. You, “Reply to comments on ‘grain refining mechanism of a carbon addition method in a Mg-Al magnesium alloy,’” *Scr. Mater.*, vol. 52, no. 5, pp. 421–423, 2005.

[98] R. Kumar, “Grain Size Control of Magnesium,” *Br. Foundaryman*, vol. 66, pp. 39–42, 1973.

[99] D. Schwam, “The Effect of Cooling Rate on Grain Size of Magnesium Alloys Cast in a Permanent Mold,” *AFS Trans.*, vol. 112:08-163, 2008.

[100] T. Motegi, “Grain-refining mechanisms of superheat-treatment of and carbon addition to Mg-Al-Zn alloys,” *Mater. Sci. Eng. A*, vol. 413–414, pp. 408–411, 2005.

[101] H. Ding and X. Liu, “The grain refinement efficiency of Ni-C on Mg-Al alloys,” *Mater. Lett.*, vol. 63, no. 6–7, pp. 635–637, 2009.

[102] M. A. Easton, A. Schiffl, J. Y. Yao, and H. Kaufmann, “Grain refinement of Mg-Al(-Mn) alloys by SiC additions,” *Scr. Mater.*, vol. 55, no. 4, pp. 379–382, 2006.

[103] H. Guang, L. Xiangfa, and D. Haimin, “Grain refinement of Mg-Al based alloys by a new Al-C master alloy,” *J. Alloys Compd.*, vol. 467, no. 1–2, pp. 202–207, 2009.

[104] Y. Liu, X. Liu, and B. Xiufang, “Grain refinement of Mg-Al alloys with Al4C3-SiC/Al master alloy,” *Mater. Lett.*, vol. 58, no. 7–8, pp. 1282–1287, 2004.

[105] A. Luo, “Heterogeneous nucleation and grain refinement in cast Mg(AZ91)/SiCp metal matrix composites,” *Can. Metall. Q.*, vol. 35, no. 4, pp. 375–383, 1996.

[106] M. Qian and P. Cao, “Discussions on grain refinement of magnesium alloys by carbon inoculation,” *Scr. Mater.*, vol. 52, no. 5, pp. 415–419, 2005.

[107] M. Suresh, A. Srinivasan, K. R. Ravi, U. T. S. Pillai, and B. C. Pai, “Influence of boron addition on the grain refinement and mechanical properties of AZ91 Mg alloy,” *Mater. Sci. Eng. A*, vol. 525, no. 1–2, pp. 207–210, 2009.

[108] Y. M. Kim, C. D. Yim, and B. S. You, “Grain refining mechanism in Mg-Al base alloys with carbon addition,” *Scr. Mater.*, vol. 57, no. 8, pp. 691–694, 2007.

[109] P. Cao, M. Qian, and D. H. Stjohn, “Native grain refinement of magnesium alloys,” *Scr. Mater.*, vol. 53, no. 7, pp. 841–844, 2005.

[110] S. Liu, Y. Chen, and H. Han, “Grain refinement of AZ91D magnesium alloy by a new Mg-50%Al4C3master alloy,” *J. Alloys Compd.*, vol. 624, pp. 266–269, 2015.

[111] W. L. and J. P. Jun Du, Jian Yang, Mamoru Kuwabara, “Effects of Manganese and/or Carbon on the Grain Refinement of Mg-3Al Alloy,” *Mater. Trans.*, vol. 49, no. 1, pp. 139–143, 2008.

[112] E. Yano, Y. Tamura, T. Motegi, and E. Sato, “Effect of carbon powder on grain refinement of an AZ91E magnesium alloy,” *Mater. Trans.*, vol. 44, no. 1, pp. 107–110, 2003.

[113] J. H. Bae, Y. M. Kim, C. D. Yim, H. Kim, and B. S. You, “Effect of inoculation method of refiner on the grain refinement of AZ91 alloy,” T*MS (The Minerals, Metals & Materials Society)*, vol. 02, pp. 275–279, 2013.

[114] Y. Huang, K. U. Kainer, and N. Hort, “Mechanism of grain refinement of Mg-Al alloys by SiC inoculation,” *Scr. Mater.*, vol. 64, no. 8, pp. 793–796, 2011.

[115] A. Schiffl and M. A. Easton, “Influence of SiC Particles on the Grain Refinement of an Mg-Al Alloy,” *Mater. Sci. Forum*, vol. 618–619, pp. 445–448, 2009.

[116] T. J. Chen, Y. Ma, W. B. Lv, Y. D. Li, and Y. Hao, “Grain refinement of AM60B magnesium alloy by SiC particles,” *J. Mater. Sci.*, vol. 45, no. 24, pp. 6732–6738, 2010.

[117] T. J. Chen, X. D. Jiang, Y. Ma, Y. D. Li, and Y. Hao, “Grain refinement of AZ91D magnesium alloy by SiC,” *J. Alloys Compd.*, vol. 496, no. 1–2, pp. 218–225, 2010.

[118] A. Elsayed, C. Ravindran, and B. S. Murty, “Effect of aluminum-titanium-boron based grain refiners on AZ91E magnesium alloy grain size and microstructure,” *Int. J. Met.*, vol. 5, no. 2, pp. 29–41, 2011.

[119] G. P. Jones and J. Pearson, “Factors affecting the grain-refinement of aluminum using titanium and boron additives,” *Metall. Trans. B*, vol. 7, no. 2, pp. 223–234, 1976.

[120] G. Han, X. F. Liu, and H. M. Ding, “Grain refinement of AZ31 magnesium alloy by new Al-Ti-C master alloys,” *Trans. Nonferrous Met. Soc. China (English Ed.*, vol. 19, no. 5, pp. 1057–1064, 2009.

[121] K. Lee, “A Study on Grain Refinement of AZ91E Magnesium Alloy,” 2011.

[122] C. D. Lee, “Effect of grain size on the tensile properties of magnesium alloy,” *Mater. Sci. Eng. A*, vol. 459, no. 1–2, pp. 355–360, 2007.

[123] ASTM, “E466-15 Standard Practice for Conducting Force Controlled Constant Amplitude Axial Fatigue Tests of Metallic Materials,” *Am. Soc. Test. Mater.*, p. 6, 2006.

[124] ASTM, “ASTM B557 − 15 Standard Test Methods for Tension Testing Wrought and Cast Aluminum- and,” *Astm Int.*, vol. i, pp. 1–16, 2015.

[125] A. Maltais, D. Dubé, M. Fiset, G. Laroche, and S. Turgeon, “Improvements in the metallography of as-cast AZ91 alloy,” *Mater. Charact.*, vol. 52, no. 2, pp. 103–119, 2004.

[126] ASTM, “ASTM E112-13: Standard test methods for determining average grain size,” *ASTM Int.*, pp. 1–28, 2013.

[127] M. N. Khan, “Solidification study of commercial magnesium alloys,” M.S. Thesis, Concordia University Mechanical Engineering, Montreal, 2009.

APPENDIX A

DETERMINATION OF PHASE TRANSFORMATION TEMPERATURES

A.1. Cooling Curves of Alloys Obtained from Mould

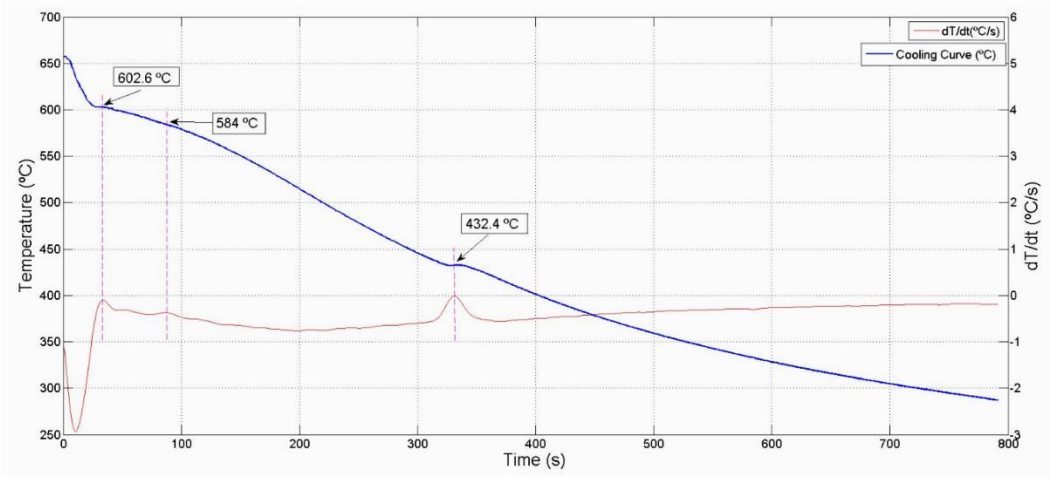

Fig. A.1 Cooling curve of Alloy I and its first derivative

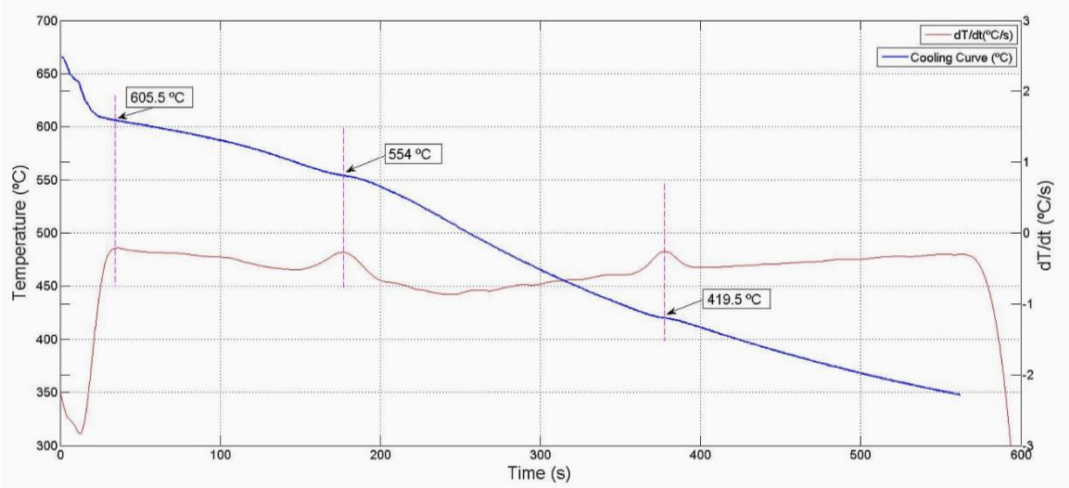

Fig. A.2 Cooling curve of Alloy II and its first derivative

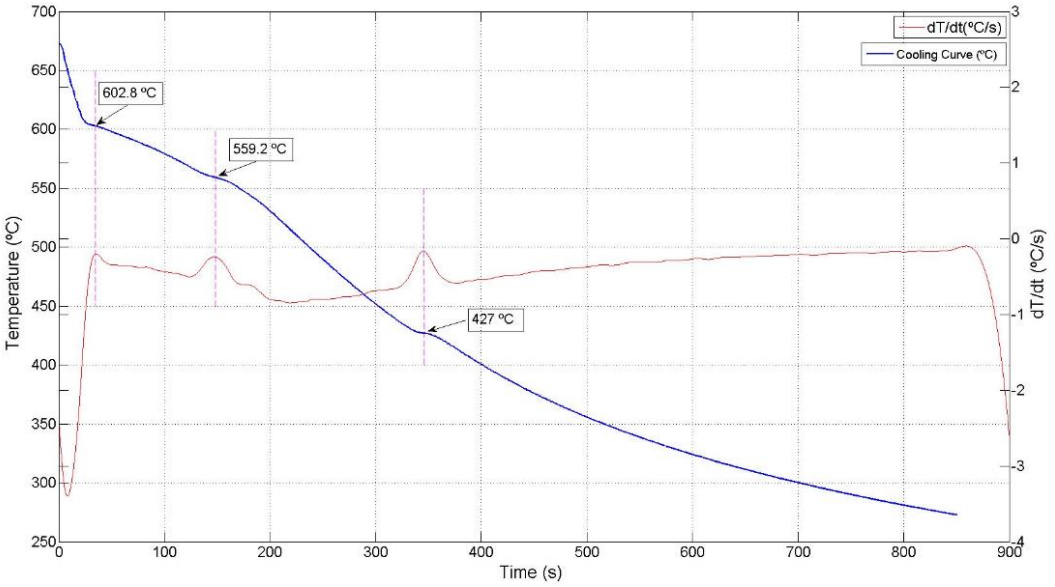

Fig. A.3 Cooling curve of Alloy III and its first derivative

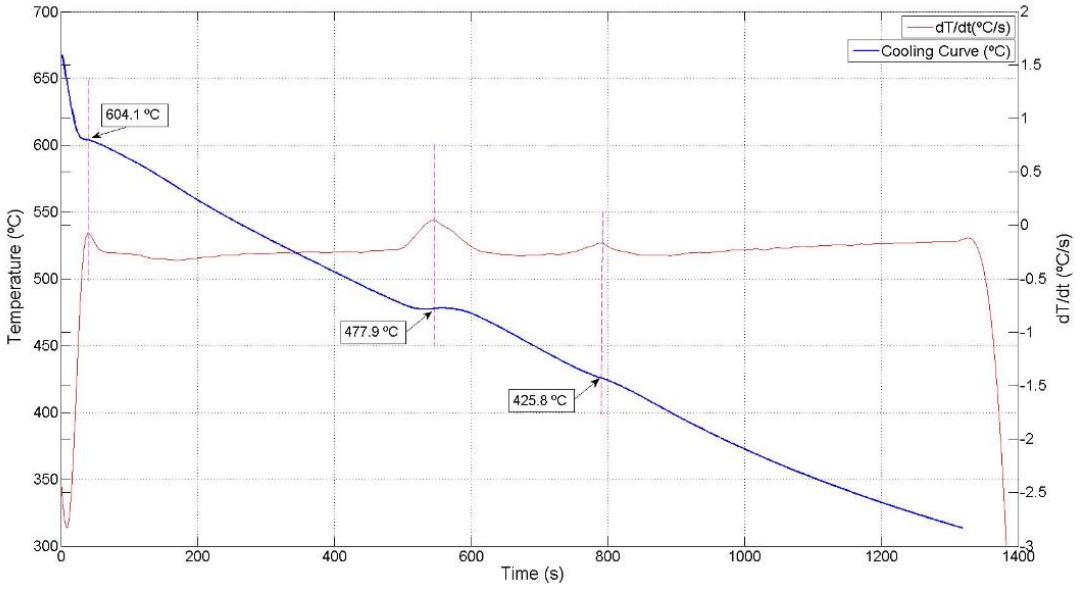

Fig. A.4 Cooling curve of Alloy IV (AZ91) and its first derivative

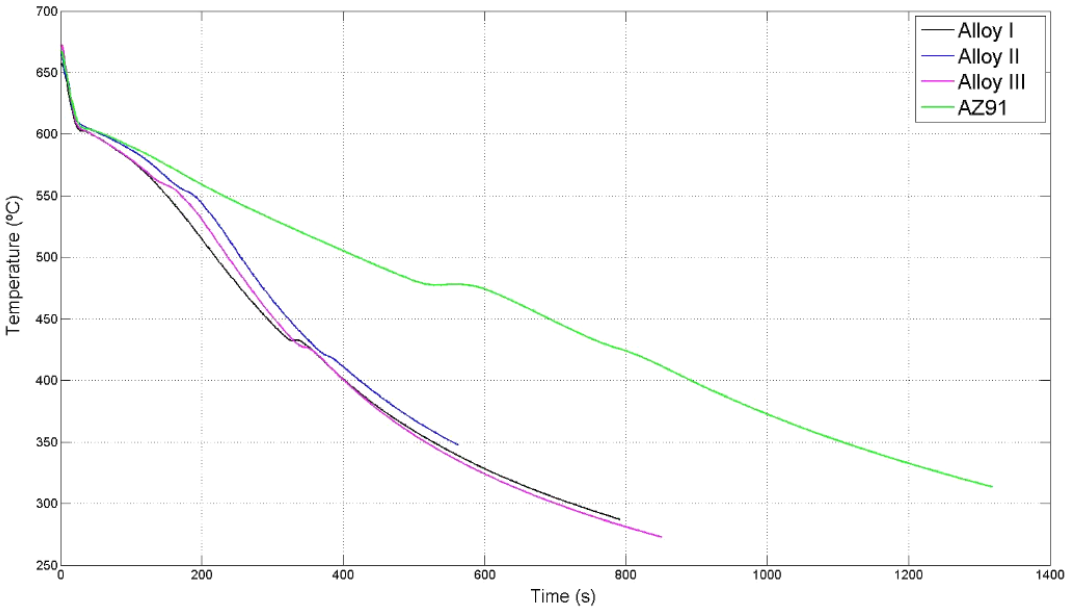

Fig. A.5 Cooling curve of comparison of alloy series used in this thesis

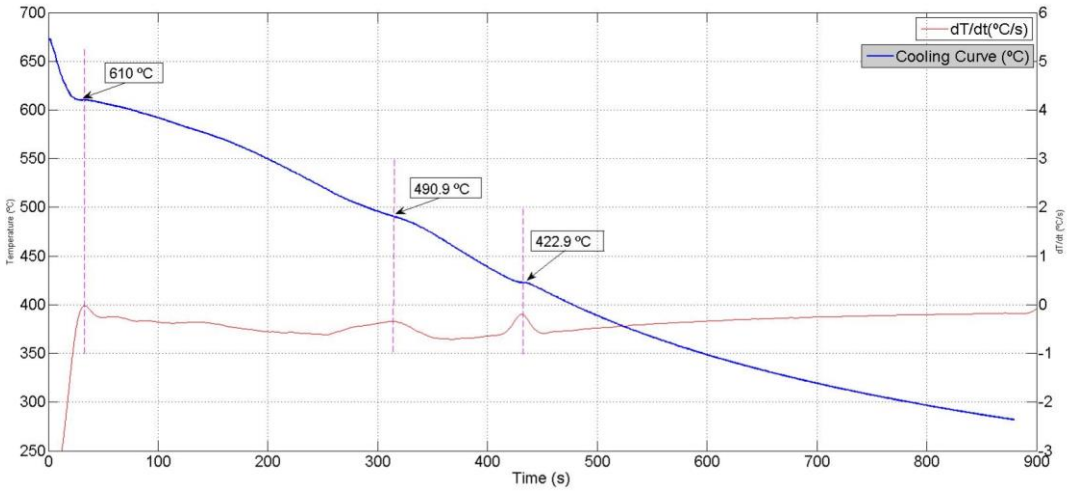

Fig. A.6 Cooling curve of Alloy IV (AZ91)-0.7%Si and its first derivative

APPENDIX B

DETERMINATION OF PHASE TRANSFORMATION TEMPERATURES

B.1. As-Cast Microstructure of Alloy IV (AZ91)-0.7%Si Before Etching

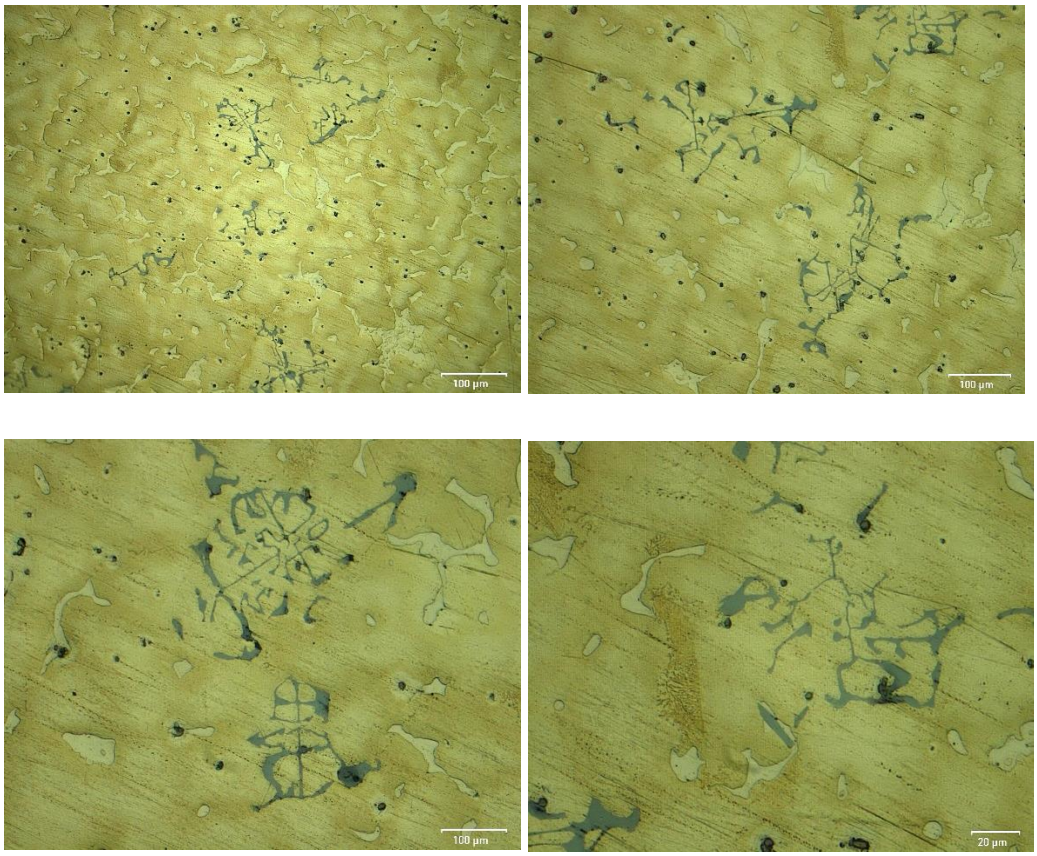

Fig. B.1 Optical microstructure of as-cast Alloy IV (AZ91) 0.7%Si at different magnifications

B.2. T6 Heat-treated Microstructure of Alloy IV (AZ91)-0.7%Si

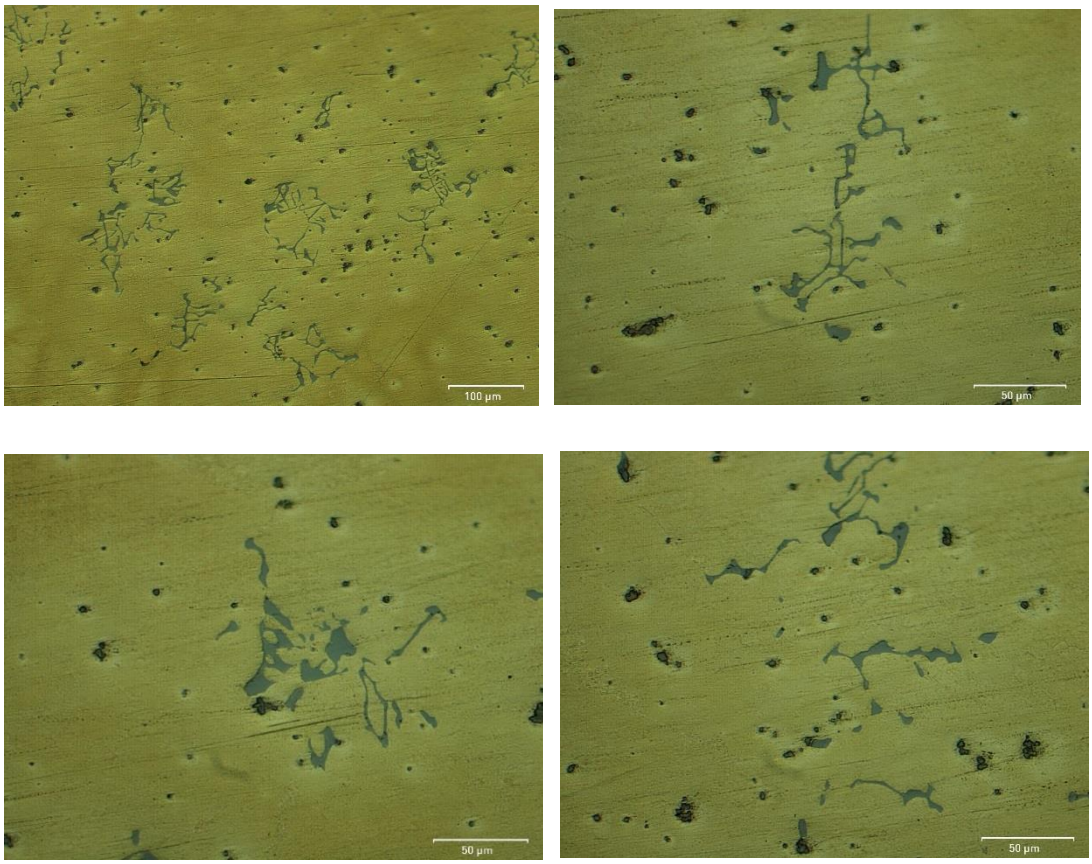

Fig. B.2 Optical microstructure of T6-heat treated Alloy IV (AZ91)-0.7%Si at different magnifications

B.3. As-Cast Microstructure of Alloy IV (AZ91)-0.7%Si After Etching

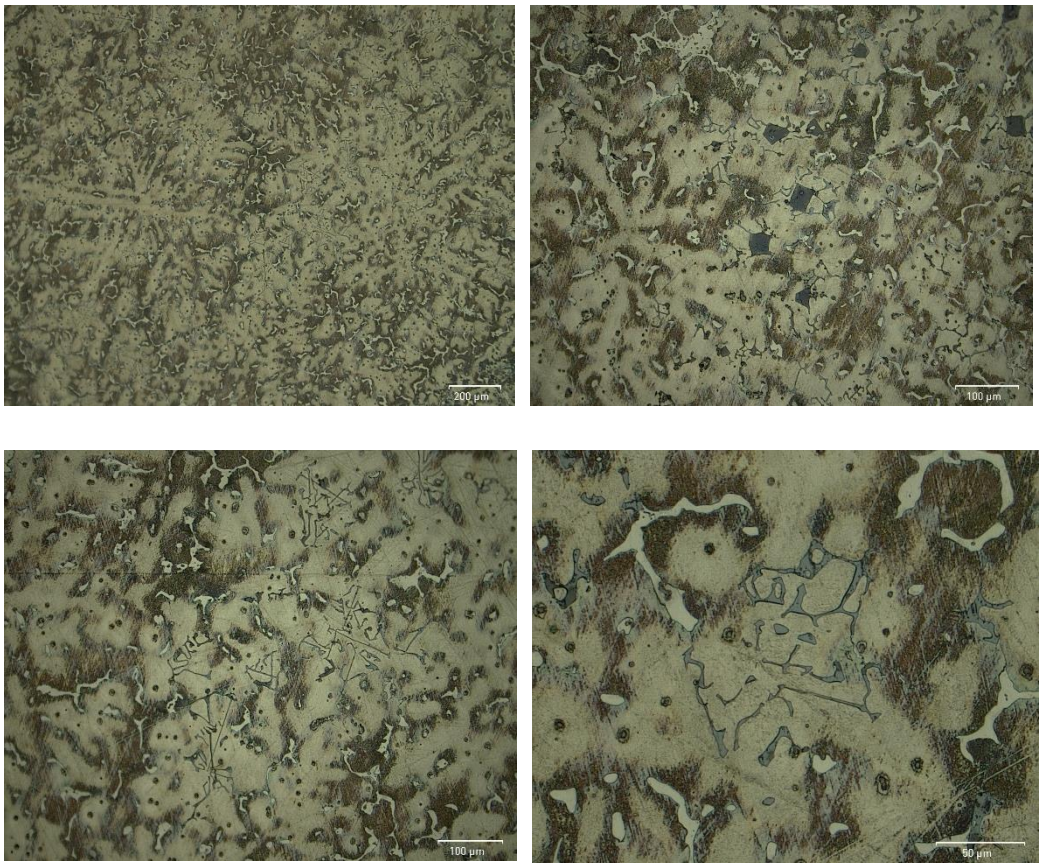

Fig. B.3 Optical microstructure of as-cast Alloy IV (AZ91)-0.7%Si at different magnifications after etching

B.4. T6 Heat-treated Microstructure of Alloy IV (AZ91)-0.7%Si After Etching

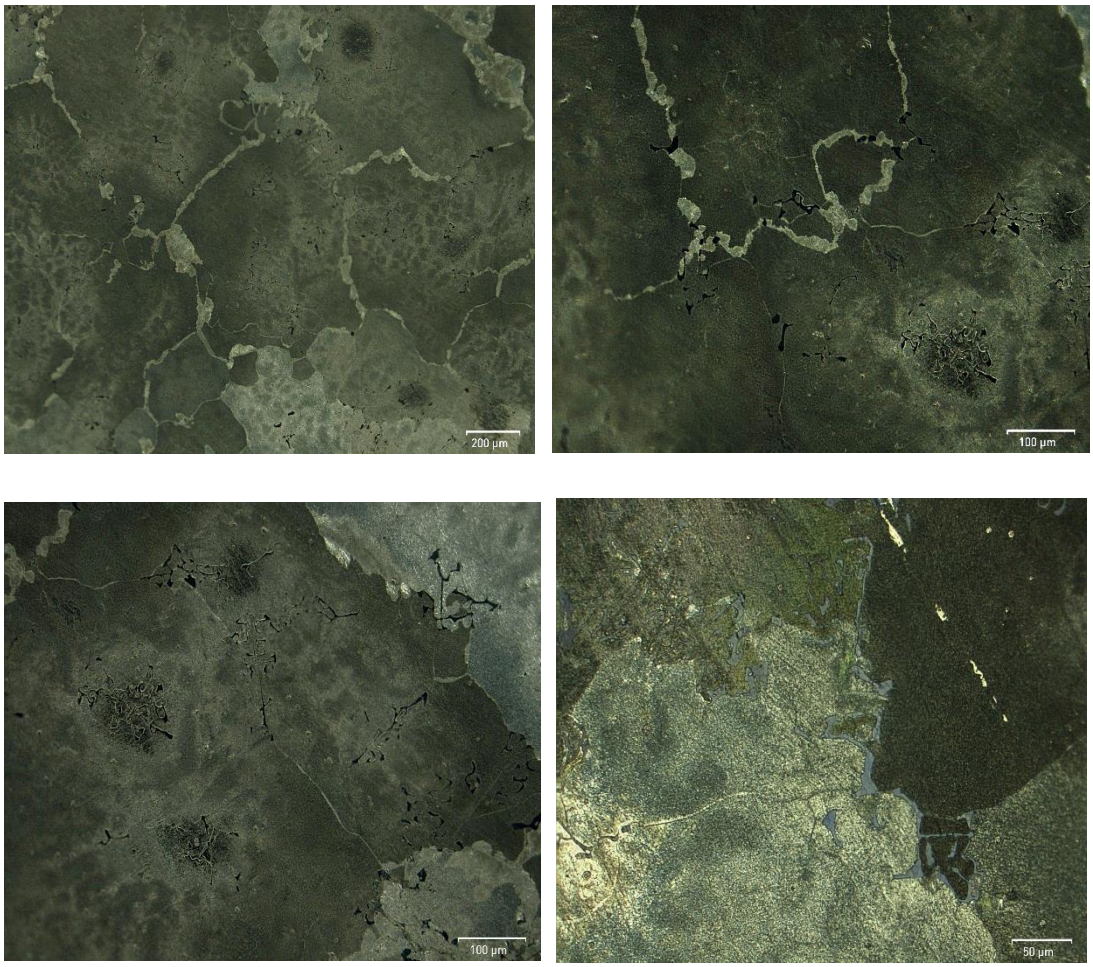

Fig. B.4 Optical microstructure of T6-heat treated Alloy IV (AZ91)-0.7%Si at different magnifications after etching

APPENDIX C

TECHNICAL DRAWINGS

C.1. Technical Drawing of CNC Machined Aluminium Sand Casting Mould

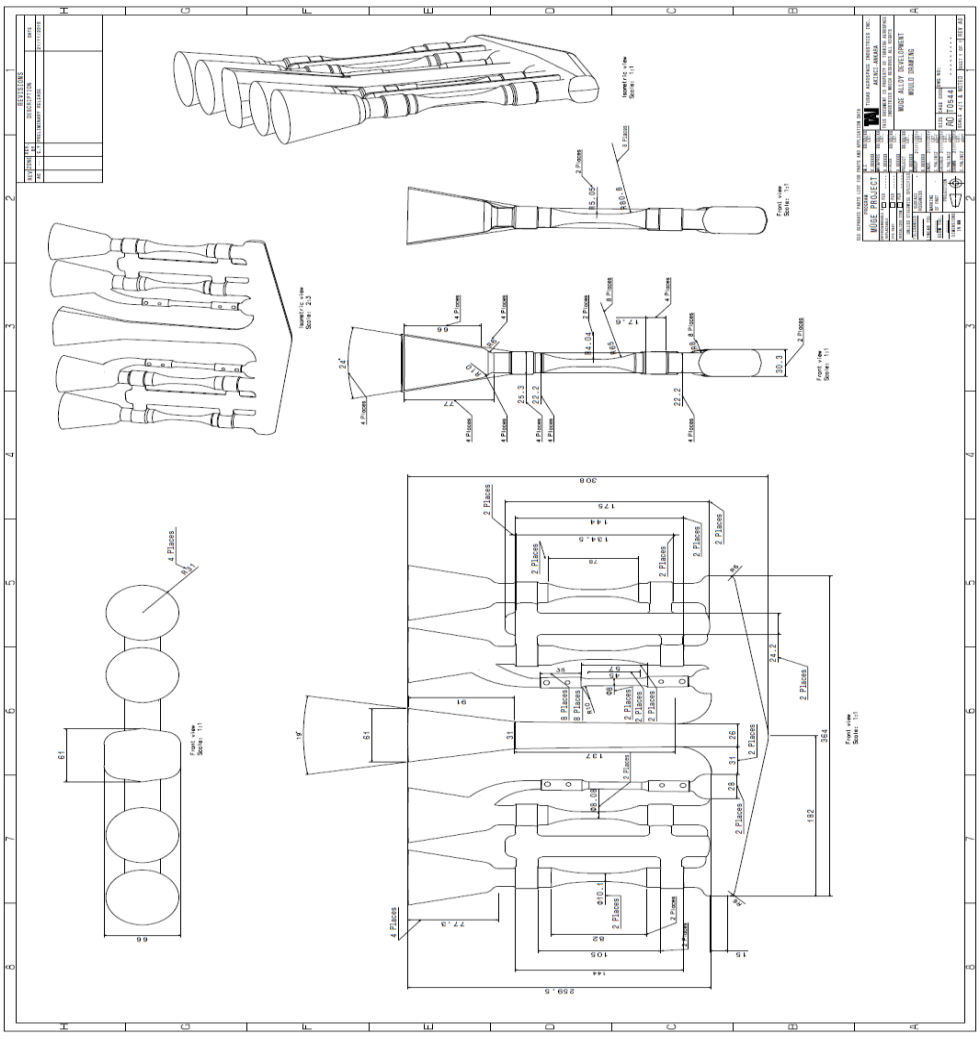

Fig. C.1 Technical drawing of CNC machined aluminum sand casting mould